UNIVERSITAT DE BARCELONA

Development of opto-mechanical sensors based on silicon nanopillars for biological applications

Elena López Aymerich

UNIVERSITAT DE BARCELONA

Tesi Doctoral

Development of opto-mechanical sensors based on silicon nanopillars for biological applications

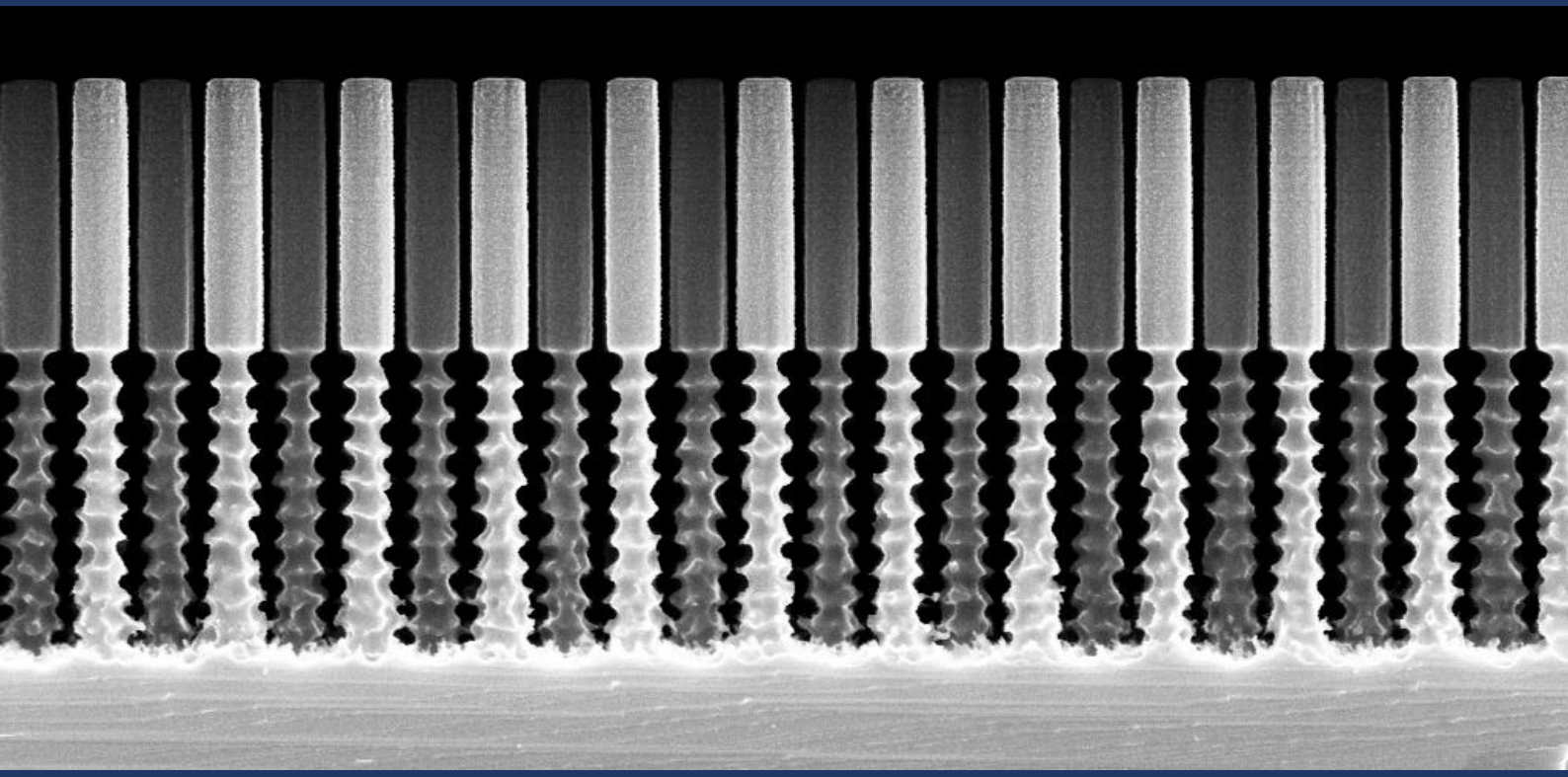

Elena López Aymerich

Development of opto-mechanical sensors based on silicon nanopillars for biological applications

Memòria presentada per optar al grau de doctor per la Universitat de Barcelona

Programa de doctorat en Nanociències

Autora: Elena López Aymerich

Directors: Prof. Dr. Albert Romano Rodríguez (UB)
Prof. Dr. Winnie Edith Svendsen (DTU)

Tutor: Prof. Dr. Albert Romano Rodríguez

UNIVERSITAT DE BARCELONA

Als meus pares, que sempre m'han recolzat en tot el que m'he proposat,

i a l'Oli, amb qui he compartit tots els dies d'aquesta etapa i les que vinguin.

Acknowledgements

Firstly, I would like to thank my main supervisor, Professor Albert Romano Rodríguez, for giving me the opportunity to take my first steps in research. His help and support from the beginning of my bachelor final project until the end of this thesis have been priceless for me.

I would like to thank Professor Winnie Edith Svendsen, co-supervisor, as well for her help and support, for welcoming me to her group and letting me be part of it during my research stays during my Ph.D. and within the scope of the StretchBio project afterwards.

In addition, this thesis has received funding from the European Union's Horizon 2020 research and innovation programme under grant agreement No 964808.

The colleagues and friends from the different departments at the Faculty of Physics and the Nanoscience Institute of the University of Barcelona. I would like to especially remember those at the Department of Electronics and Biomedical Engineering and, in particular to, those who have been and still are at the laboratory for micro and nanosystems.

I would like to thank all the people as well from DTU who have made a country such as Denmark feel like home for so many months. The members of the NaBIS group at DTU's Bioengineering department who have received me with open arms every time I was coming back for a research stay. I do not want to forget as well all the staff members of DTU Nanolab. Their assistance and advice have been precious to me and for the success of this thesis. I would like to specially thank Conny Hjort and Thomas Pedersen who have been and still are my mentors and friends inside the cleanroom.

I believe it is important to remember your origins and for this reason, I would like to dedicate a big thank you to my parents. They brought my sister and I up with love and determination to give us a good education and preparation for our future. Without their perseverance and dedication, I would have never been able to reach what I have reached. I don't want to forget my sister, who opened so many doors for me and has always been my example to follow. Moltes, moltes gràcies als tres, us estimo molt.

Finally, I would like to give my biggest thank you to Oliver Scheuregger, Oli. Who has been there every day since the beginning of this thesis. Always encouraging me and supporting me to continue and pursue my goals. We have lived together the best and the worst moments of these last years, and I cannot be more grateful for having had him with me all this time. I love you a lot.

Abstract

The scope of this thesis is the advancement on the theoretical simulation and nanofabrication of photonic crystals based on a periodic array of silicon pillars. This research is intended to be part of the preliminary research within the framework of an ambitious project for the development of mechanical biosensors for *in vivo* monitoring of tissues' growth and regeneration based on photonic crystal structures. This application introduces limitations and requirements on the photonic structures. Among other requirements, the system should work within the near infrared (NIR) wavelength range of the electromagnetic spectrum, and the materials used for the fabrication should be biocompatible.

The main two goals of this thesis have been the evaluation of the feasibility of such structures to behave as mechanical biosensor and the development and optimisation of a fabrication route and guidelines for the successful fabrication of sensor prototypes. This thesis compiles the work done and results obtained for the fulfilment of these two goals.

The theoretical evaluation of the structures has been carried out using well known finite element modelling and finite-difference time domain programs for the simulation of the band diagrams and transmission spectra of the analysed devices, respectively. The outcome of these simulations has been used to set the main photonic crystal parameters suitable for this project, such as the radius of the pillars, the pitch between them and their length. These simulations have been performed considering air and water backgrounds.

The simulations have shown, as well, that the introduction of defects into the main photonic crystal structure allow tuning the optical response of the system. Two types of defects have been considered: line and point defects (or cavities). The first ones, consisting in the variation of the size of the pillars in one row, introduces extra transmission bands inside the photonic band gap of the crystal. On the other hand, adding a point defect into this system a transmission peak appears within the photonic bandgap. An important result from the simulation is that this peak is sensitive to small perturbations of the cavity shape and size. Therefore, the proper design of the photonic crystal with defects can bring a system that can be sensitive to perturbations of its geometry.

The fabrication process has been built based on the results of the simulations. The nanofabrication of the structures has a crucial role for the success of the project. For this reason, the second part of the thesis has been devoted to developing a very well detailed and establish an optimised process flow for the fabrication of the arrays. In addition, this process has proved to be robust and versatile among different sensor designs.

The fabrication process is based on an electron beam lithography exposure, followed by a lift-off for creating a hard mask to be used for the dry etching of the pillars. This last step is the one that has been more broadly studied and optimised because it has the highest impact on the resulting structures. The shape and roughness of the pillars and the consistency of the etching over different samples and structure configurations have been analysed in depth to determine the optimal conditions of the dry etching process. A thorough analysis of the surface elements and compounds left after the fabrication process has been performed as well to ensure the biocompatibility of the structures.

Finally, a short attempt to fabricate more exotic structures to enhance the photonic performance of the devices has been carried out. The results have shown that it is possible to further nanostructure the bottom of the photonic crystal pillars to improve the vertical light confinement within the photonic crystal structure.

Table of contents

Table of contents ..... **I**
List of Figures ..... **IV**
List of Tables ..... **XIV**
List of Abbreviations ..... **XVIII**

CHAPTER 1. INTRODUCTION, BACKGROUND AND GOALS OF THIS WORK 1
1.1. Framework of the thesis 1
1.1.1. The problem inspiring this thesis 1
1.1.2. The project behind the thesis 3
1.2. Goals of this thesis 8
1.3. Structure of this thesis 10

CHAPTER 2. THEORY OF PHOTONIC CRYSTALS 15
2.1. Photonic crystals theory 15
2.1.1. Master equations in dielectric materials 16
2.1.2. Translational symmetries 20
2.1.3. Photonic Band Diagram 23
2.1.4. Photonic Band Gap 26
2.2. Linear and point defects 29
2.2.1. Linear defects 30
2.2.2. Point defects 32
2.3. Computational methods 32
2.3.1. Finite Element Method 33
2.3.2. Finite Difference Time Domain Method 35
2.4. Proposal of simulation activities 37

CHAPTER 3. THEORY OF NANOFABRICATION 41
3.1. The cleanroom 41

3.2. Lithography 43
3.2.1. Resist deposition 43
3.2.2. Exposure 46
3.2.3. Development 52
3.3. Thin film growth and deposition techniques 53
3.4. Etching techniques 57
3.4.1. Basics of RIE and ICP 59
3.4.2. The Bosch and pseudo-Bosch processes 60
3.5. Characterisation techniques 63
3.5.1. Scanning electron microscopy 64
3.5.2. Thin film characterisation: Ellipsometry 66
3.5.3. Atomic and chemical content analysis: X-ray Photoelectron Spectroscopy (XPS) .. 68
3.6. Proposal of fabrication strategy 69

CHAPTER 4. SIMULATION RESULTS 73
4.1. Two-dimensional photonic crystal 73
4.1.1. Band diagram simulation 74
4.1.2. Band diagram discussion 77
4.1.3. Transmission-Reflection spectra simulation 83
4.1.4. Transmission spectra discussion 87
4.2. Introduction of defects in two-dimensions 92
4.2.1. Line defects 93
4.2.2. Point defects 101
4.3. Photonic crystal slabs 104
4.3.1. Impact of the pillar length 107
4.3.2. Impact of the claddings 110

CHAPTER 5. FABRICATION RESULTS 119
5.1. Cleanroom processes 119
5.1.1. Pre-processing of SOI wafers 121
5.1.2. The lithographic process 122
5.1.3. Hard mask creation, etching and post-processing 124
5.2. Fabrication requirements 125

5.2.1. Shape and reproducibility 125
5.2.2. Presence of fabrication residues 126
5.2.3. Adaptability and scalability towards mass-production 127
5.3. Optimisation of the RIE step 128
5.3.1. Type of carrier and attaching approach 129
5.3.2. Gas flows in the chamber 135
5.3.3. Platen and Coil powers 138
5.3.4. Etching rates 143
5.3.5. The impact of the load 144
5.3.6. Impact of the dry etch on the surface materials 149
5.4. Creation of bottom cladding 159
5.4.1. Etching of buried silicon oxide 159
5.4.2. Undercutting silicon pillars 162

CHAPTER 6. CONCLUSIONS 167
6.1. Conclusions of this thesis 167
6.1.1. Simulation conclusions 167
6.1.2. Fabrication conclusions 171
6.2. Further work 173

Bibliography 177

List of Figures

Figure 1.1. (a) scheme of the proposed sensing system. A waveguide acting as linear defect (in green) made with smaller pillars and a cavity (in orange) are introduced in the main photonic crystal structure (in black); (b and c) scheme of how the light is transferred in the initial system (a) and in a system where the central pillar of the cavity is bent from its original position. As a result the light outcome of the system changes due to the deformation of the cavity. 5

Figure 1.2. Scheme of a drosophila melanogaster fly and how an epithelia coming from its wing is placed on top of the proposed system for the measurement of the tensions in a large surface. 6

Figure 1.3. Representation of what is expected to happen when an ill tissue is placed on the system (a) and what would happen when an effective drug is applied on it (b). 7

Figure 2.1. (a) Scheme of a system with different dielectric materials (represented by their dielectric permittivity ε_i); (b) Electric (red) and magnetic (green) fields propagating in the wavevector (yellow) direction as it is considered in this problem. 18

Figure 2.2. (a) Schematic representation of a one-dimensional photonic crystal in which several unit cells are depicted; both the lattice vector expressed as **a** and the lattice constant expressed as a. (b) Representation of the relation between the direct and the reciprocal space of a one-dimensional photonic crystal. 23

Figure 2.3. (a) Representation of a band diagram, where in red the different bands are shown. (b) Representation of a light cone. In grey the area of leaky modes is shown while in white the area of transmitted modes is represented. 24

Figure 2.4. Representation of the direct space for a hexagonal distribution of pillars. The lattice vectors for a structure like this are represented by $\mathbf{a_1}$ and $\mathbf{a_2}$. Then the reciprocal space representation of the same structure is shown with the reciprocal space lattice vectors represented by $\mathbf{b_1}$ and $\mathbf{b_2}$. Finally, the first Brillouin Zone calculation and symmetry points are shown as the intersection in the centre of the lines that connect the central point with the closer neighbouring pillars..... 30

Figure 2.5. (a) First Brillouin Zone boundaries for a perfect two-dimensional photonic crystal structure. The arrows show the direction of the wavevector variation during the band gap evaluation. (b) Projection of the M symmetry point onto the defect direction creating a new symmetry point K' due to the creation of a line defect to the structure. 32

Figure 2.6. Scheme of the approximation to the solution done with FEM methods. In dashed green the actual solution to the problem. In red the interpolation result obtained from a FEM simulation. On the **x** line are presented the nodes limiting the different space element in which the space is divided. An example of the flow followed by FEM simulations is shown too..... 35

Figure 2.7. Scheme of the time and space dependent solution of the electric and magnetic fields depending on the time step considered. The offset by half a time unit is expressed by the shift in the position of the nodes in the magnetic field wavevector line relation to the electric fields line..... 37

Figure 3.1. Images of the DTU Nanolab cleanroom facilities: (top left) the cleanroom building; (top right) electron beam lithography cassette loading; (bottom left) automatic resist spin coaters; (bottom right) automatic electron beam resist developer. 44

Figure 3.2. Sketch of the three main steps of the spin coating process: (a) wafer clamp and beginning of rotation (**ω**); (b) resist dispense; and (c) increase of rotation spin and resist flatten..... 47

Figure 3.3. Sketch of the curves used to determine the beam spot size on the substrate depending on the aperture size and the current used during the exposure. 50

Figure 3.4. (a) Scheme of a teardrop diagram showing the interaction volume and the outcoming particles and photons of this interaction. (b) Sketch of the distribution of the forward and backscattered electrons as a function of the distance to the incident beam and the electrons energy..... 52

Figure 3.5.(a) Example of a point spread function for silicon-on-insulator (SOI) wafer with a buried oxide (BOX) layer of 1 µm, a device layer of 1.5 µm and a resist thickness of 180 nm. The simulation has been carried out assuming a beam energy of 100 keV (as used in this thesis) it has been done using TRACER® software. (b) Dose modulation of a mask after the proximity effect correction using the point spread function in the left image done with BEAMER®. The different colours correspond to different modulations of the base dose with blue representing the minimum modulation and red the maximum..... 53

Figure 3.6. (a) Scheme of the silicon oxide growth curves used during a wet oxidation as a function of the oxidation time. (b) Sketch of the final oxidation layer and the upper silicon consumed during the oxidation. 56

Figure 3.7. Schemes of the different metal coverage depending on the resist profiles. 58

Figure 3.8. Sketches of the different etching profiles obtained with (a) wet etching processes and (b) dry etching processes. 61

Figure 3.9. Scheme of the (a) CCP chamber and the (b) ICP chamber. 62

Figure 3.10. Sketch of the Bosch process. (Top) The three main steps are here described: deposit (left), break (middle), and etch (right). (Bottom) The final result sketch after the repetition of these three. 65

Figure 3.11. Schematic of the distribution of the gas flows and powers during the etch process. Representation of the variation of the parameters depending on time for (a) a (cyclic) Bosch process and (b) a pseudo-Bosch process. 66

Figure 3.12. Representation of the interactions of the primary electrons with the substrate atoms: (a) the generation of SE when releasing an atom from the outer orbitals; (b) BSE electrons due to the atom nucleous electromagnetic potential; (c) creation of a photon due to the relaxation of an excited electron. 68

Figure 3.13. Schematic of how light interacts with the layers during ellipsometric measurements. 71

Figure 4.1. Image of the unit cell used for the simulation of band diagrams extracted from one of the COMSOL Multiphysics® programs created. In the figure the different geometry parameters are depicted as well as the different domains considered for the two-dimensional simulations. 78

Figure 4.2. Image of the simulated unitary cell as shown in the COMSOL Multiphysics® software. (a) Delimitation of the periodic Bloch conditions for the two-dimensional simulations; (b) Example of the free triangular mesh created for the finite element division of the cell. 79

Figure 4.3. (a) Scheme of the hexagonal structure of the reciprocal space and the three main points in the reciprocal space. With coloured arrows the m iteration path in the software is shown. (b) Band diagram corresponding to a photonic crystal structure with 100 nm radius pillars and 300 nm pitch for TM polarised light in air background. In red the different simulated bands are marked for the different **k** directions. In light green the bandgaps between the bands are shown too. 81

Figure 4.4. Robustness maps of the simulations carried out with a constant pillar radius of 100 nm and a pitch radius changing from 300 nm to 650 nm. The pillar material is silicon. These robustness maps correspond to (a) air and (b) water as background. 82

Figure 4.5. Evolution of the gap-to-midgap figure of merit as a function of the radius-to-pitch ratio of the simulated structures. The results obtained when considering an air or water background are shown in figures a) and b), respectively. 84

Figure 4.6. Band diagrams of a photonic structure of 100 nm radius and 500 nm pitch considering TM polarised light. In (a) an air background is considered while in (b) an aqueous background is used. The light red (a) and blue (b) bands correspond to the opened bandgaps. 86

Figure 4.7. Scheme of the constructed geometry when using MEEP. In dashed lines the limits of the simulation region. Inside the simulation region, the representation in two dimensions of the photonic crystal using black circles. The black colour representing the areas of high refractive index while the white background represents the low refractive index area. 88

Figure 4.8. Scheme of the simulation built with the MEEP package. In red the source used shows the direction of the wavevector pointing towards the hexagonal grid created. In green the two flux regions used to evaluate the incoming and outcoming fluxes through the hexagonal grid. Surrounding the cell, the perfectly matched layer is shown dashed. 89

Figure 4.9. Example of one of the transmission spectra in air for a photonic crystal with a pitch of 600 nm and pillars with radii of 120 nm. In shadowed grey the absorption region of the silicon is delimited while the photonic crystal region is shown in orange. 92

Figure 4.10. Overlap of the results of the bandgaps and the transmission spectra. Results for a photonic crystal with 500 nm pitch and 100 nm radius in (a) air and (b) water. Shadowed the principal band gap can be seen. 95

Figure 4.11. Transmission spectra of a structure of 14x14 unit cells of a photonic crystal with a 500 nm pitch and 100 nm radius. In red the transmission considering an air background and in blue considering a water background. Shadowed in grey the adsorbing region of silicon is marked. Shadowed in red and blue the bandgap regions for the air and water simulations are marked. 95

Figure 4.12. (a) Scheme of the supercell simulation carried out in COMSOL Multiphysics®. In red the pillars used as defect are marked; (b) Sketch of the projection of the M point onto the direction of the line defect. A new point of the reciprocal lattice is obtained from this projection (K'). 98

Figure 4.13. Projected band diagram of a missing row of pillars in a structure of 500 nm pitch and 100 nm radius in an air (a) and water (b) backgrounds. 98

Figure 4.14. Transmission spectra resulting from the FDTD simulation of a photonic crystal with a row of pillars missing in air (red) and water (blue). It can be observed how within the

bandgap a new transmission window is introduced thanks to the defect (shadowed in red and blue). In grey the area where silicon is adsorbent is shadowed. 99

Figure 4.15. Overlapping of the results obtained both with the COMSOL Multiphysics® and FDTD simulations in air (a) and water (b). In dashed lines it can be seen how the transmission window resulting in the FDTD simulation and the band introduced in the bandgap agree as shown as well in Table 4.6. 100

Figure 4.16. Projected band diagrams for different line defects in air (a) and water (b). The bands introduced in the bandgap resulting from a line defect of pillars with 80 nm radius (pink), 60 nm radius (blue), 40 nm radius (green) or no pillars (red) are marked. 101

Figure 4.17. Projected band diagrams for a line defect created by pillars of 40 nm with widths of (a) 250 nm, (b) 375 nm, (c) 500 nm (corresponding to the green line in Figure 4.16), (e) 625 nm, and (f) 750 nm in air background. Dashed lines corresponding to the different bands created by the defect are marked. 103

Figure 4.18. (a) Scheme of the structure simulated to evaluate the impact of cavities in the system. (b) The transmission spectra of the structure represented in figure a considering an air background (red) and water background (blue). Shadowed in grey the silicon absorption region is marked as well as shadowed in red and blue the resonance peaks for the cavities can be seen. 106

Figure 4.19. (a) Transmission spectra of the system shown in Figure 4.18 b for a water background. The displacements correspond to the movement of the left pillar creating the cavity to the left (negative values) and to the right (positive values); (b) representation of the peak position as a function of the displacement for both air and water background. 107

Figure 4.20. (a) Scheme of the three-dimensional simulation used in COMSOL Multiphysics®. In blue the pillar within the cell is shown. In addition, the areas acting as top and bottom claddings are marked as well as the PML top and bottom layer; (b) Sketch of one light cone considering an air cladding. In grey the region of leaky modes is marked while in white the area of guided modes can be seen. 109

Figure 4.21. Band diagrams of a pillar of height 1000 nm and 100 nm radius in air (a) and water (b) considering a unit cell of 500 nm pitch. Above the light cone line, the areas shadowed in red, and blue correspond to the leaky modes' regions. Below the light cone line, the simulated guided bands can be seen. 111

Figure 4.22. Resulting robustness maps and gap-to-midgap ratio evolution in front of the silicon pillar length for air (a, b) and water (c, d) background considering a structure with a stand-alone silicon pillar. 113

Figure 4.23. Sketches of the three configurations considered for the cladding distribution: (a) silicon pillars standing on a silicon oxide slab; (b) Silicon pillars on top of silicon oxide pillars and (c) silicon pillars in between two layers of silicon oxide pillars. 115

Figure 4.24. Resulting robustness maps and gap-to-midgap ratio evolution in front of the silicon pillar height for air (a, b) and water (c, d) background considering a structure with a bottom silicon oxide slab of 1000 nm with silicon pillars on top. 116

Figure 4.25. Resulting robustness maps and gap-to-midgap ratio evolution in front of the silicon pillar length for air (a, b) and water (c, d) background considering a bottom silicon oxide pillar of 1000 nm. 118

Figure 4.26. Resulting robustness maps and gap-to-midgap ratio evolution in front of the silicon pillar length for air (a, b) and water (c, d) background considering a bottom and top silicon oxide pillar of 500 nm. 120

Figure 5.1. Basic process flow carried out in the cleanroom. 125

Figure 5.2. Example of the dose variation carried out by the BEAMER® software for some combinations of radii and pitch of the pillars. The colours represent the different modulations. Blue represents the lowest modulation and red the largest. 129

Figure 5.3. SEM images of the resulting etched pillars using the original nano 1.42 recipe for 5 min. An Al mask with pillars of 100 nm radius and 500 nm pitch. 135

Figure 5.4. Image of a chip bonded on a Si wafer with Crystalbond™. 137

Figure 5.5. SEM images of the pillars etched during 5 min with the chip bonded on a silicon substrate (a) and a masked substrate (b). 138

Figure 5.6. Cross-sectional view of the pillars etched using the Bosch process bonded on a (a, c) silicon wafer carrier and on a (b, d) masked wafer. The top images show a general view of the pillars and the bottom row shows the detail of the scalloping effect. 139

Figure 5.7. Cross-sectional views of the etched pillars with different gas concentrations keeping the total flow to 113 sccm. The gas flows used for the diferent samples shown in the images are: (a) 67 sccm of C_4F_8 and 46 sccm of SF_6, (b) 69 sccm of C_4F_8 and 44 sccm of SF_6, (c) 71 sccm of C_4F_8 and 42 sccm of SF_6, (d) 73 sccm of C_4F_8 and 40 sccm of SF_6, and (e) 75 sccm of C_4F_8 and 38 sccm of SF_6. 144

Figure 5.8. Cross-sectional SEM images of the pillars after varying the gas proportions inside the chamber. (a) Corresponds to the 69 sccm and 46 sccm flows of C_4F_8 and SF_6 while (b) corresponds to 69 sccm and 48 sccm flows of C_4F_8 and SF_6. 145

Figure 5.9. Cross-sectional images for the different combinations of coil and platen powers used during the etching process: (a) 800 W and 20 W, (b) 1000 W and 20 W, (c) 1200 W and 20 W, (d) 800 W and 40 W, (e) 1000 W and 40 W and, (f) 1200 W and 40 W of coil and platen power respectively in all cases. 149

Figure 5.10. Cross-sectional images of the final tuning combinations of gases and powers. Resulting pillars of using (the conditions are expressed as C_4F_8 / SF_6 flows and platen / coil powers): (a) 71 sccm / 44 sccm flows, and 1000 W / 20 W powers, (b) 69 sccm / 46 sccm flows, and 1000 W / 20 W powers, (c) 69 sccm / 44 sccm flows, and 900 W / 20 W powers, (d) 69 sccm / 44 sccm flows, and 1000 W / 20 W powers, (e) 69 sccm / 44 sccm flows, and 1100 W / 20 W powers. 150

Figure 5.11. Graph representation of the etched depth in front of the etching time, indicating a linear relationship. 151

Figure 5.12. Cross-sectional SEM imatges of the different etched fillars for a time of (a) 1 min, (b) 9 min and (c) 12 min. In (d) a magnified image of the top part of the pillars etched for 12 min (c) can be observed. 152

Figure 5.13. Graphical representation of the etch tendencies for different radii pillars and loads for different etching times..... 153

Figure 5.14. Distribution of the radius evolution along the vertical axis for different pillars with nominal radius 40 nm, 60 nm, 80 nm, and 100 nm etched down for (a) 3 min, (b) 5 min and, (c) 7 min. 157

Figure 5.15. The set of four images to the left show top-view SEM images of pillars with 100 nm (top left), 80 nm (top right), 60 (bottom left), and 40 nm (bottom right) radius. The set of four images to the right show the same images but with the detection of the pillars performed by MATLAB® funcions. 157

Figure 5.16. Radii distribution obtained from the images shown in Figure 5.15. 157

Figure 5.17. Survey XPS spectra from the a substrate developed until the lift-off step. Two sample areas have been tested: (a) photonic crystal area, and (b) outside the photonic crystal area. In black the positions of the peaks for the different studied elements are marked. 160

Figure 5.18. High-resolution spectra of different elements for the sample that has not been etched and from the masked area. The spectra from oxygen (a), silicon (b), carbon (c), and aluminium (d). In the different spectra measurement is shown in red, the peak adjustmen in yellow, the envelope profile in blue and the spectra baseline in geen. 162

Figure 5.19. Survey XPS spectra from the a substrate submited to the dry etch step. In the same way as in Figure 5.17, two sample areas have been tested: (a) photonic crystal area, and (b) outside the photonic crystal area. In black the peaks for the different studied elements are marked. 164

Figure 5.20. (a) Oxygen, (b) silicon, (c) carbon, (d) aluminium, (e) fluor and (f) sulphur spectra. Each spectra has been taken individually during the XPS experiment on top of the photonic crystal area. In red the measured spectra can be seen. In blue the enveloping simulated spectra considering the measured peaks (in yellow). The spectra baseline is shown in green..... 166

Figure 5.21. SEM images ot the silicon etched pillars for 4 min and a silicon oxide etch for (a) 1 min and (b) 2 min. In red the different etched materials are indicated. 171

Figure 5.22. Images of the undercut pillars. (a) Overview of the pillars where the top and bottom undercut parts are etched according with the conditions described in Table 5.16; (b) and (c) show closer images of the transition between the regular pillar and the undercut and the undercut section, respectively. 173

List of Tables

Table 4.1. Summary of the optimal results considering the gap-to-midgap figure of merit in air and water backgrounds. In addition to the normalised radius-to-pitch value the actual configuration simulated is given as well. 85

Table 4.2. Summary of the photonic band gap (PBG) minimum and maximum positions obtained when considering a photonic crystal of 100 nm radius and 500 nm pitch in air and water background. Both the normalised positions as well as their equivalent wavelengths for the considered structures are shown. 86

Table 4.3. Summary of the boundaries of the primary band gap opened for the simulations carried out with FDTD method both in air and water background. This table contains the minimum and maximum of the measured band gaps (PBG) including the gap-to-midgap ratio for the different band gaps. In red, those boundaries falling outside the transparent region of silicon are marked. 93

Table 4.4. Summary of the bandgap positions and gap-to-midgap for a photonic crystal of 500 nm pitch and 100 nm radius in air and water backgrounds. The results of the two types of simulations done through the band diagram and the FDTD. 96

Table 4.5. Summary of the opening of the band created by the defect line when a row of pillars is missing. The resulting normalised frequencies and the equivalent wavelengths are indicated, as well. 99

Table 4.6. Summary of the opening of the new band due to the missing row as line defect for the two types of simulations carried out for both air and water backgrounds. These results correspond to a photonic crystal structure with 500 nm pitch and 100 nm radius. 100

Table 4.7. Summary of the band opening for different radius of the pillars creating the defect line in both air and water backgrounds. 102

Table 4. 8. Summary of the distance between the bottom of the introduced band and the bottom of the band gap (PBG) as well as the percentage of the band gap covered by the defect band. The results belong to the calculation done by introducing a line defect by varying the radius of one row of pillars down to 40 nm, 60 nm and 80 nm, both in air and water. 104

Table 4.9. Summary of the peak positions represented in Figure 4.19 b for air and water background depending on the displacement of the left pillar creating the cavity. 107

Table 4.10. Summary of the band gap openings for the band diagrams shown in Figure 4.21 considering the light cone limitations. 111

Table 4.11. Summary of the maximum and minimum values of the bandgap opened in air and water for a self-standing pillar. The optimal thickness found considering the gap-to-

midgap representation in Figure 4.22 is added as well. In addition, the theoretical value of the optimal thickness calculated with equations (4.4) and (4.5). 114

Table 4.12. Summary of the optimal silicon lengths for the configuration shown in Figure 4.23 a with their gap-to-midgap ratio. 117

Table 4.13. Summary of the optimal silicon lengths for the configuration shown in Figure 4.23 b with their gap-to-midgap ratio. 119

Table 4.14. Properties of the optimal band gaps for air and water backgrounds for a structure with a silicon oxide pillar at the top and the bottom of the silicon pillar. 120

Table 5.1. Considering the device nominal thickness of 1500 nm, the depth of silicon needed to be etched varies depending on the final thickness. Therefore the oxidised layer varies as well according to equation 3.6. Thanks to the oxidation curves of the furnace used the oxidation time can be estimated as well. 127

Table 5.2. Etching conditions of the original recipe nano 1.42. 134

Table 5.3. Summary of the calculation of the loads used during the dry etch step depending on the carrier wafer used. 136

Table 5.4. Summary of the etching conditions during the gas flow tests. 142

Table 5.5. Summary of the etching conditions fixed during the power conditioning. 145

Table 5.6. Results of the measurements carried out using SEM images of the diferent power conditions discussed. 146

Table 5.7. Summary of the resulting measurements using SEM images of the final tuning of the conditions to obtain the optimal etching of pillars. 147

Table 5.8. Summary of the measurements of the pillars' radii along the vertical depending on the etching time and the radii of the original pillar mask. 154

Table 5.9. Data obtained from the pillars measured using the MATLAB® code. 158

Table 5.10. Summary of the binding energies and relative atomic weight of the elements analised. This data has been obtained using the Avantage software analising the spectra shown in Figure 5.17. 161

Table 5.11. Summary of the different peak positions shown in Figure 5.18, for the non-etched sample and the measurement on top of the masked region. 163

Table 5.12. Summary of the binding energies and relative atomic weight of the elements analised. This data has been obtained using the Avantage software analising the spectra shown in Figure 5.19..... 165

Table 5.13. Summary of the peak binding energies of the spectra shown in Figure 5.20. The peak names correspond the to the ones labeled in the figure..... 167

Table 5.14. Binding energies of the different atom combinations used during the dry etch steps. 169

Table 5.15. Etching conditions used for testing the silicon oxide etch below the silicon pillars. 170

Table 5.16. Summary of the Bosch process conditions used for the etch of the top body of the undercut bottom body of the pillars for 10 cycles..... 172

List of Abbreviations

AFM	Atomic Force Microscopy
ALD	Atomic Layer Deposition
BHF	Buffered Fluorhydric acid
BOX	Buried Oxide
BSE	Backscattered Electrons
CCP	Capacitive Coupled Plasma
CSAR	AR-P 6200 electrosensitive resist
CVD	Chemical Vapour Deposition
DREM	Deposit, Remove, Etch Multistep
DTU	Danish Technical University
DUV	Deep Ultraviolet
EB	Electron Beam
EDS	Energy-Dispersive Spectrometry
FDM	Finite Difference Method
FDTD	Finite Difference Time Domain
FEM	Finite Element Method
HMDS	Hexamethyldisilazane
ICP	Inductively Coupled Plasma
IPA	2-propanol
ISO	International Organisation for Standardisation
LPCVD	Low Pressure Chemical Vapour Deposition
MEEP	MIT Electromagnetic Equation Propagation

MIT	Massachusetts Institute of Technology
NIR	Near Infrared
PAC	Photoactive Compound
PBG	Photonic Band Gap
PE	Proximity Effect
PEB	Post Exposure Bake
PEC	Proximity Effect Correction
PECVD	Plasma Enhanced Chemical Vapour Deposition
PML	Perfectly Matched Layers
PSF	Point Spread Function
PVD	Physical Vapour Deposition
RF	Radio Frequency
RIE	Reactive Ion Etching
SE	Secondary Electrons
SEM	Scanning Electron Microscopy
SOI	Silicon on Insulator
TE	Transversal Electric
TIR	Total Internal Reflection
TM	Transversal Magnetic
TMAH	Tetramethylammonium Hydroxide
UV	Ultraviolet
XPS	X-ray Photoelectron Spectrometry

CHAPTER 1.

INTRODUCTION, BACKGROUND AND GOALS OF THIS WORK

1.1. Framework of the thesis

1.1.1. The problem inspiring this thesis

The origin of this project is the need to better understand the mechanisms that drive the growth and regeneration of tissues. Nowadays, two main models are commonly accepted for the understanding of tissue growth and regeneration: one model is based on the biochemistry of the process and the other describes the mechanical tensions that change in the tissue [1]. However, a unified model that could explain these processes, benefitting from both approaches, has not been yet developed. This fact is due to the difficulty of experimentally measuring *in vivo* the evolution of the mechanical properties of the tissues. Several works have analysed the response of individual cells under mechanical stresses but studies quantitatively analysing the mechanical response of cell ensembles, such as tissues, are still lacking. The main difficulty for tissue measurements is the dimensions of the sensitive area to be evaluated. The studies done up to now on single cells have been carried out using atomic force microscopy (AFM) [2], [3]. AFM measurements, unfortunately, are characterised to be slow and to have a very limited scanning surface, in the range of 15 x 15 micrometre square.

A better understanding of the growth and regeneration of tissues would represent a step forward in the biomedical research. Questions such as how epithelia regulate their

normal size and the mechanisms that make them stop growing have been asked by the biomedical community for decades. These questions have been tried to be assessed with studies of cell-to-cell contacts and have been directly related to the mechanical properties of the tissue: tissue stretching, tensions and relaxation.

The proper knowledge of the mechanical processes in tissue regeneration will have a direct impact in medical practice. It is known that specific illnesses alter the elasticity of human tissue. This is the case of certain tumoral tissues, but also of some fibroses. The genes that operate on normal tissue growth are suppressed by the tumour suppressor genes and oncogenes. This provokes the uncontrolled proliferation of cells that is characteristic of cancer. The study of these processes is usually carried out by growing animal epithelia that can be easily manipulated in the laboratory. For decades, researchers have used genetically manipulated larvae of *drosophila melanogaster* (the wine fly) to investigate tumour growth in epithelia [4], [5]. Understanding how tumoral tissues grow will in the long term provide a better understanding on how they can be healed. For this reason, it is expected that the development of this type of sensors will be useful as well for the study of how drugs affect the tissue growth.

As already mentioned, one of the difficulties of the measurement of a real tissue evolution is the fact that the surface to be analysed is much larger than most of the techniques available nowadays. The tissues coming from the *drosophila* larvae can extend over hundreds of microns. For this reason, a system that would have multiple measuring sites with high spatial resolution and spanning over a large surface, will result in a larger measurement area. In this way an array of multiple measurement points, each of them with different properties, can be used as sensing setup. The tests with tissues, even being beyond the scope of this thesis work, can be performed with the so-called imaginal discs, the precursors of the different organs that can be found in the *drosophila melanogaster* larvae. The imaginal disc precursor of a wing will be put on top of the device and its temporal evolution studied.

1.1.2. The project behind the thesis

The overall goal of this thesis is the development of a mechanical sensor for *in vivo* monitoring of the growth and regeneration of living tissues using pillar-based photonic crystals.

Given the situation depicted in the previous section, there is a need for developing a mechanical sensor for *in vivo* monitoring of the growth and regeneration of living tissues. This sensor could be based on pillar-based photonic crystals. This project started as an ambitious one-year long Explora national project granted on 2017 [6]. The goal of this preliminary project was to start the research of a type of system that could be suitable for such sensor. The outcome of it oriented the research towards photonic crystals based on silicon nanopillars. The results of that project have been used as starting point for this thesis, where the research has been focused on further investigate such optical systems and, as well, to establish a robust process for their fabrication.

At the same time, some of the results of the work of this thesis have been used as background for the application of the granted H2020 FET-Open project StretchBio [7]. StretchBio is a challenging four-year project whose goal is to create and implement the mechanical sensor just described: to develop a working opto-mechanical sensor for *in vivo* monitoring of the growth and regeneration of tissues. Starting in October of 2021 it coordinates researchers from institutions from three different countries, among which experts in photonics, biology, medicine, and nanofabrication are working towards the creation of this sensor. This European project has been granted more than 3.8 M € and has an estimated working force of 343 person-month.

Therefore, research of this thesis should be contextualised between the grant of these two projects since this thesis research has served as bridge between them.

One of the preliminary questions about the research done both in the Explora and FET-Open projects is if it is possible to create a sensor as the one proposed and if it would behave as expected.

Some of the previously mentioned cell-based studies on mechanical tensions use long pillars for their tests [8], [9]. In these studies, the shift of the top position of pillars is

analysed while cells on top of them exert forces to bend them. The tracking of the pillars' tops is carried out by top view imaging the position of the pillars and of the cells. These studies show that the forces exerted by cells are in the order of nanonewtons (nN). The systems reported in these works require to be able to observe the pillars' tops and, therefore, the cells must be just on top of the pillars surface.

According to those studies, pillars with the correct geometry (length and radius) will be able to bend under the forces in the range as the ones expected from this project. Therefore, the system proposed in this work uses, as well, the property that pillars can bend under lateral tensions. However, for studying tissues the reported zenital observation of the pillars' tops is not feasible as in the previously mentioned due to the thickness of the tissue, that does not allow the visualisation of the pillars under the tissue. Consequently, a different approach is needed to measure the pillars bending.

The sensing system proposed in these projects is the one shown in Figure 1.1 a, which consists of and array of pillars, creating a photonic crystal with defects within it. Photonic crystals are periodic distributions of two or more dielectric materials that work analogously to solid ionic crystals [10], [11]. The dielectric distribution creates a system in which light can only be transmitted for specific wavelengths and directions in the crystal. Those wavelength ranges in which light cannot be transmitted through the structure are called photonic bandgaps. It is the use of these bandgaps what will be the base of this thesis.

The sensing system will consist of a photonic crystal based on pillars which cannot be bent under the tissue stresses. Within the periodic structure, line and point defects will be introduced. Line defects are created by changing some property of one line of pillars. This can either be done by changing the pillars' radii or their pitch, for instance [12], [13]. Properly designed line defects will allow a small range of wavelengths within the photonic crystal bandgap to propagate through the system. Additionally, point defects can be introduced as well [14]. These are created by adding one or multiple pillars whose radii or pitch are modified as compared to the reference photonic crystal. The effect of a point defect in a photonic crystal is the creation of a transmission peak within the photonic bandgap working like a cavity[15], [16].

The final device then will combine the three structures: a photonic crystal which creates a photonic bandgap, a line defect which will allow some wavelengths to be transmitted through the bandgap and a cavity whose resonance is within the transmitted wavelengths of the line defect [12]. This combination of elements will create a very specific transmission spectrum. To simplify it in Figure 1.1 b the outcoming light from the system is represented with one colour. If the pillar creating the cavity is small enough, under lateral forces exerted by a tissue this pillar will bent, resulting in the change of the cavities dimensions, and, consequently, the change of the transmission spectra outcoming of the device. This change in the transmission spectrum is represented in Figure 1.1 c with a different colour for the outcoming light [17].

In the final system the resulting transmission measurement will be analysed by observing how the different sensing points evolve over time while the tissues grow (shown in Figure 1.2). First tests using imaginal discs coming from *drosophila melanogaster* larvae will be used to analyse the response of the system under a living tissue. In Figure 1.2, a scheme of the tissue on top of the sensor is shown, the response of the system is shown, again by different output colours.

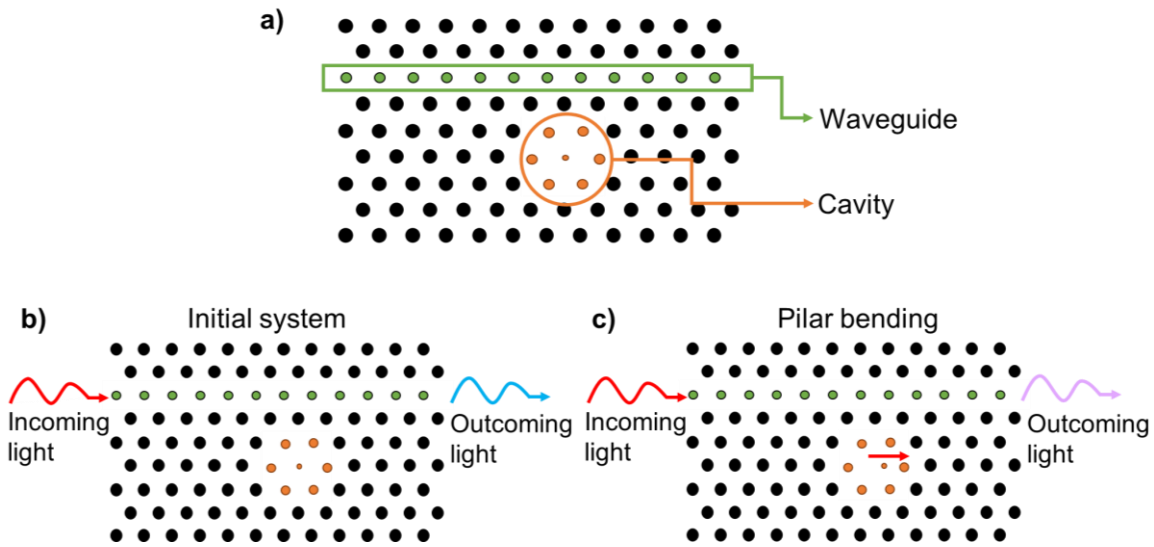

Figure 1.1. (a) scheme of the proposed sensing system. A waveguide acting as linear defect (in green) made with smaller pillars and a cavity (in orange) are introduced in the main photonic crystal structure (in black); (b and c) scheme of how the light is transferred in the initial system (a) and in a system where the central pillar of the cavity is bent from its original position. As a result the light outcome of the system changes due to the deformation of the cavity.

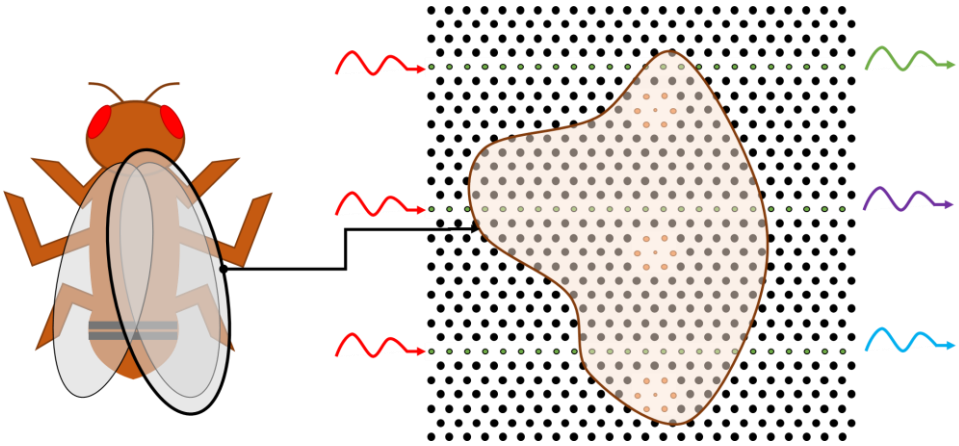

Figure 1.2. Scheme of a drosophila melanogaster fly and how an epithelium coming from its wing is placed on top of the proposed system for the measurement of the tensions in a large surface.

A system that can measure the evolution of the tissue's growth will constitute a first prototype. This will be upgraded later to a system that can measure the mechanical properties of human tumoral biopsies. Human biopsies can be cut into thin samples. A slice of tumoral tissue will be placed on top of the device to observe and analyse its evolution (Figure 1.3 a). This can be a starting point to analyse this same tissue but during (or after) the treatment with specific antitumoral drugs (Figure 1.3 b). Analysing the response of the tissue to different drugs will help identifying which is the most effective for a particular type of tumour of a particular patient. This, at the same time, can help developing new cancer treatments and providing a more patient oriented treatment for each case, helping to the well-known personalised medicine.

The use of tissues for this project requires to consider the conditions under which the device will work. First, using living tissues implies that the set up used should be biocompatible. This fact, combined with the need of adequate materials that can be used for producing a photonic crystal, limits the choice of materials to be used. In addition, the selected material should be suitable for the fabrication of pillars and, maybe, even more complex structures. For this reason, in this project silicon has been chosen to be used as pillar material. The wide knowledge about its fabrication and its use in both optical biosensing devices [18] and medicine [19] , together with its high refractive index (3.5 for wavelengths above 1 μm [20]), makes it the best material choice for the development of this project.

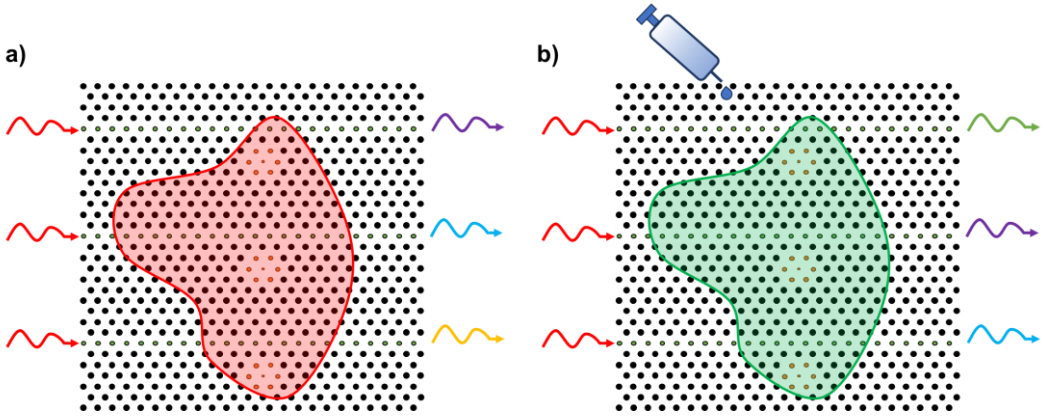

Figure 1.3. Representation of what is expected to happen when an ill tissue is placed on the system (a) and what would happen when an effective drug is applied on it (b).

In addition, the measurement of *in vivo* tissues requires an aqueous background that allows the tissue to survive during the experiment time. During the FET-Open project development, it is expected to consider two different types of background material (both on top and in between of the pillars): air and water. The air background will be mostly used for the first testing stage of the project where focus will be mostly on the photonic performance of the system. The water background will be the one used during the tissue stress testing. It is precisely this second type of background that brings another limitation to the system, which is related to the spectral range used for operating the structures.

The potential wavelength range where this system could work is within the near infrared (NIR) range of the electromagnetic spectrum. This range spans from wavelengths of 800 nm to 2500 nm. It is suitable for the use of photonic crystals based on silicon since this material has minimum adsorption for wavelengths above 1100 nm [20].

The wavelength range used during this project must, as well, be suitable for the biological application of the device. The water transmission spectrum presents some absorption windows that will limit the spectral ranges where the photonic system will be able to work when immersed in an aqueous environment [21]. Water has two main transmission windows in the NIR light spectrum. These ones are comprised between 8000 cm^{-1} and 7500 cm^{-1} (corresponding to wavelengths between 1250 nm and 1333 nm) and between 6500 cm^{-1} and 5500 cm^{-1} (corresponding to wavelengths between 1538 nm and 1818 nm) [21]. Therefore, the design of the system should take into account these wavelength ranges.

1.2. Goals of this thesis

Within this very ambitious framework, the purpose of this thesis is to set the theoretical and experimental basis for the implementation of the force sensing devices that will be developed in the StretchBio project. This will be achieved employing advanced simulation and nanofabrication techniques. It is important to indicate that other aspects, such as the biological compatibility of the structures and the feasibility of the photonic crystal characterisation, have been considered during the design and fabrication phases of the structures in this work, but they have not been analysed here, as they are beyond the scope of this thesis.

Therefore, the work carried out during this thesis can be divided into two main parts: the simulation of structures that fulfil the project requirements and the optimisation of the fabrication processes for their successful fabrication.

As starting point, the simulation of the structures under discussion has been considered. Two-dimensional photonic crystals based on pillars is something that has been predicted and mentioned in several theoretical works [22], [23]. The purpose of this thesis, however, is to analyse the structures theoretically keeping in mind a very specific purpose: to use them as bio-mechanical sensor.

For this reason, the results of the simulations must fulfil the following requirements:

- The system should work within the NIR region of the electromagnetic spectrum: this requirement is basically driven by the fact that we will be using silicon as material for the fabrication of the pillars.

- The fabrication of the simulated structures should be feasible: the goal of the StretchBio project is to have a system that can be used as a mechanical biosensor. For this reason, the research of this thesis must not be restricted to simulations but also should be (not excessively) complicated to be fabricated and characterised.

- The optical system should be operational in both water or air backgrounds. At the time of this work, it is not yet completely clear if the aqueous media required by the biological tissues will penetrate totally or partially between the pillar structure. For this

reason, the simulations must consider both air and water as backgrounds. Ideally, a configuration able to operate in both environments would simplify the fabrication and characterization of the structures.

On the other hand, a major part of the research carried out during this thesis has been focused on the fabrication of the structures. Based on the results obtained from the simulations, the fabrication of structures that should be measurable has been the focus of the second part of the work. The fabrication of silicon pillars has been reported in literature by research groups worldwide [24], [25], but the difficulty in reproducibly achieving mechanically stable devices requires well stablished fabrication processes. To obtain structures that can be used the requirements preset in this work are:

- To create pillars to form photonic crystals whose defects, such as surface roughness and shape discrepancies, are minimal. It is expected that these defects can highly affect the photonic performance of the system. For this reason, even though they are not completely avoidable, they should be as minimised as possible.

- To avoid the fabrication residuals on the surface of the pillars and of the surfaces. Some of the processes used during the fabrication create some residues on the surface that might affect the optical measurements and compromise the biocompatibility of the substrates.

- To create a fabrication route that can be used and that can be easily adapted to new requirements of the project. As the goal of this thesis is to set the basics for the fulfilment of the project, the fabrication will play a key role for its success. The use of multipurpose fabrication facilities with a large number of customers comes with a lot of variability in the process results when analysed over time. Therefore, an in-depth study and understanding of the impact of each parameter on the fabrication outcomes is paramount to quickly readapt the fabrication conditions to regain the optimal fabrication results.

With these considerations in mind the goals of this thesis have been determined. The simulation strategy has been focused on the evaluation of both the band diagrams and the transmission spectra of the structures while the fabrication has been oriented to stablish a well-defined and versatile fabrication process. The goals of this thesis are:

1. **To optimise the basic photonic crystal parameters,** such as the radius of the pillars and the interpillar distance, to obtain an optimal bandgap, while still having pillars thin enough to allow their bending.

2. **To evaluate the introduction of defects into the structure** and how they will affect the bandgap.

3. **To study the introduction of different types of claddings on top and below the nanopillars** to analyse their impact on the band diagrams and to evaluate the performance of the resulting photonic structure.

4. **To prepare and optimise a process flow** that permits the fabrication of the structures within the framework and requirements of the project.

5. **To optimise and evaluate the different parameters that affect the final shape of the silicon pillars.** Special importance has been given to the dry etch process.

6. **To fabricate structures that could be suitable for their use as photonic crystals,** taking under account not only the fabrication of the silicon pillars *per se*, but also the nanostructuring of the claddings according to the results provided by the simulation.

1.3. Structure of this thesis

Based on the purpose of the goals just mentioned, this thesis is organised in six chapters, which cover the introduction (this chapter), the two main blocks of the thesis (simulation and fabrication) and conclusions and outlook.

The first block (Chapter 2 and Chapter 3) are two chapters in which the basics and theory of the work done both on the simulation of the photonic crystals (Chapter 2) and on the nanofabrication (Chapter 3) are presented. The second block (Chapter 4 and Chapter 5) describe the experimental simulation (Chapter 4) and fabrication set ups and discusses the results obtained both for the design and fabrication of the photonic crystals (Chapter 5).

Chapter 2 is devoted to the description of the basics of two-dimensional photonic crystals and their properties. The theory of photonic crystals is well-known and broadly explained, but the aim of this chapter is to summarise those properties that are important for this thesis and relevant for the project. Special emphasis will be given on how band diagrams are constructed and how to interpret them. This chapter contains the description of the introduction of both line and point defects in the photonic crystal and their impact on the light propagation. These defects will have an important impact on the optical characterisation of the structures. In this chapter the simulation tools, later used in Chapter 4, are explained as well. The different methods available for the theoretical characterisation of photonic crystals are explained in the last section of Chapter 2.

In Chapter 3, the theory of the nanofabrication processes is summarised. In the cleanroom there are available many techniques and processes. In this chapter a quick overview of the main groups of fabrication techniques is given, with special emphasis on those used during this project. The chapter is structured in different sections explaining the groups of techniques distributed in lithography, thin film deposition, dry etching, and characterisation.

Chapter 4 is the first of the two chapters in which the results of this thesis are discussed. This chapter is devoted to the presentation and discussion of the simulations carried out within the framework of this thesis. All the discussions are done considering the framework of the StretchBio project, as explained in the section 1.1. Chapter's 4 goal is to analyse the behaviour of photonic crystals based on silicon pillars within the two different types of backgrounds mentioned: air and water. Even though the final real system is, obviously, a three-dimensional structure, the study begins with a much simpler approach in two-dimensions, considering only those directions that conform the periodic plane. This simplification of the system is used to carry out a first analysis on parameters, such as the radius and the interpillar distance. In addition, it has allowed the initial analysis of the introduction and effect of both line and point defects. To end the discussion, the introduction of a third dimension has been considered. This analysis has provided important practical information for the fabrication route and for the characterisation of the structures.

The last chapter with results of this thesis (Chapter 5) contains all the information about the fabrication route followed to fabricate the pillars and the simulated structures. As a bridge between the theoretical and experimental characterisation of the photonic crystals, the fabrication of the structures plays a key role in the success of the project. For this reason, in this chapter the main prerequisites that the fabrication must fulfil are included as well. An important part of this chapter is focused on achieving pillars that are suitable for their characterisation. This is directly related to the etching step of the pillars. Parameters such as their final shape, roughness and analysis of the residuals left after the fabrication process have been analysed in detail. The main part of the optimisation of the fabrication process has been carried out with bare silicon wafers, but part of the final discussion of this chapter has been done on silicon-on-insulator wafers, which are required for achieving devices suitable for performing photonic measurements and which are used in the StretchBio project.

CHAPTER 2.
THEORY OF PHOTONIC CRYSTALS

2.1. Photonic crystals theory

As explained in the introduction the device proposed for this project will be based on a photonic crystal structure with defects within it. To better understand how the system will work and interpret the results obtained from the simulations, background about photonic crystals is described in this chapter.

Photonic crystals are periodic distributions of two dielectric materials. The distribution of these two materials can extend in one, two or three dimensions. Their working principle is normally explained analogous to how solid crystals structures work. The solid-state theory describes the behaviour of a periodic distribution of atoms in the space. This distribution creates a periodic electrical potential where electrons can propagate as waves as a function of their wavevector direction and energy [26]. In the case of photonic crystals, it is the periodic distribution of the dielectric materials what describes how photons, depending on their wavevector and wavelength, will propagate [10], [11].

In the following subsections the specific conditions that the dielectric materials and the photons should meet are described.

2.1.1. Master equations in dielectric materials

To understand most of the phenomena related to photonic crystals, electromagnetic theory should be considered. Most of these phenomena can be described using the macroscopic Maxwell equations [27]:

$$\nabla \cdot B = 0 \quad \nabla \times E + \frac{\partial B}{\partial t} = 0$$

$$\nabla \cdot B = \rho \quad \nabla \times H - \frac{\partial D}{\partial t} = J$$

(2.1)

where $\boldsymbol{E}_{(\boldsymbol{r},\omega)}$ and $\boldsymbol{H}_{(\boldsymbol{r},\omega)}$ are the electric and magnetic fields, $\boldsymbol{D}_{(\boldsymbol{r},\omega)}$ and $\boldsymbol{B}_{(\boldsymbol{r},\omega)}$ are the displacement and magnetic induction fields, and ρ and $\boldsymbol{J}_{(\boldsymbol{r},\omega)}$ are the free charge and current densities, respectively. The goal of this section is to obtain a master equation that can describe how photons behave and propagate through the system. To derive this master equation, Maxwell equations will be used as starting point.

Photonic crystals are very complex systems and the materials conforming them are very complex, as well. For this reason, to derive the master equation, some approximations must be considered. These approximations are used to simplify the Maxwell equations. Several actions can be done to ease the problem [28]:

i) The medium in which the waver sill propagate will be considered as a mixture of homogeneous materials that are invariant over time (Figure 2.1 a). This means that each medium in the system is considered uniform. The spatial distribution of these materials can be expressed as function of their position through a vector ($\boldsymbol{r}$). This means that now the fields can be rewritten as $\boldsymbol{E}_{(\boldsymbol{r},\omega)}$, $\boldsymbol{H}_{(\boldsymbol{r},\omega)}$, $\boldsymbol{B}_{(\boldsymbol{r},\omega)}$ and $\boldsymbol{D}_{(\boldsymbol{r},\omega)}$.

ii) Another approximation is to consider that the free charge and current densities (ρ and $\boldsymbol{J}_{(\boldsymbol{r},\omega)}$, respectively) are zero. This approach can be done because a simple

system where only light propagates through it is considered and within it there are no light sources nor free charges. With this approximation the last two equations in (2.1) will be equal to zero.

iii) The materials considered are isotropic and macroscopic. This means that the proportionality between $\boldsymbol{E}_{(\boldsymbol{r},\omega)}$ and $\boldsymbol{D}_{(\boldsymbol{r},\omega)}$ is expressed by the dielectric permittivity (ε), which is expressed as:

$$\varepsilon_{(\boldsymbol{r},\omega)} = \varepsilon_0 \cdot \varepsilon_{\boldsymbol{r}_{(r,\omega)}}$$

(2.2)

where ε_0 ≈ 8.854 x 10^{-12} Farad/m, which is the vacuum permittivity, and $\varepsilon_{\boldsymbol{r}_{(r,\omega)}}$ is the scalar relative dielectric permittivity of the medium. The same can be derived for the magnetic permeability (μ):

$$\mu_{(\boldsymbol{r},\omega)} = \mu_0 \cdot \mu_{\boldsymbol{r}_{(r,\omega)}}$$

(2.3)

where μ_0 = 4π x 10^{-7} Henry/m and $\mu_{\boldsymbol{r}_{(r,\omega)}}$ is the scalar relative magnetic permeability function of the medium. However, for most dielectric materials this $\mu_{(\boldsymbol{r},\omega)}$ is equal to 1 and for simplicity this value will be assumed during the following mathematical developments.

iv) Because of the previous approximation, $\boldsymbol{E}_{(\boldsymbol{r},\omega)}$ and $\boldsymbol{H}_{(\boldsymbol{r},\omega)}$ are in the linear regime. Therefore, $\boldsymbol{D}_{(\boldsymbol{r},\omega)}$ and $\boldsymbol{B}_{(\boldsymbol{r},\omega)}$ can be expressed as proportional to $\boldsymbol{E}_{(\boldsymbol{r},\omega)}$ and $\boldsymbol{H}_{(\boldsymbol{r},\omega)}$, respectively as:

$$\boldsymbol{D}_{(\boldsymbol{r},\omega)} = \varepsilon \boldsymbol{E}_{(\boldsymbol{r},\omega)} \quad ; \quad \boldsymbol{B}_{(\boldsymbol{r},\omega)} = \mu \boldsymbol{H}_{(\boldsymbol{r},\omega)}$$

(2. 4)

For dielectric materials this proportionality can be expressed in terms of the refractive index, which correlates the dielectric permittivity, and the magnetic permeability as follows:

$$n = \sqrt{\varepsilon_{(\boldsymbol{r},\omega)}\mu_{(\boldsymbol{r},\omega)}}$$

(2.5)

v) The dielectric function will be assumed constant for the frequency range under study. Therefore, $\varepsilon_{(\boldsymbol{r},\omega)}$ can be expressed from now onwards as $\varepsilon_{(\boldsymbol{r})}$. In this way, the mediums under analysis will be considered non-dispersive. Therefore, during the study in Chapter 4 all the phenomena analysed will consider a system where the material's nature does not introduce any loss.

vi) Finally, the material absorption is considered zero, which implies that only transparent materials are under analysis. This is applied considering the dielectric function to be pure real and positive.

With these assumptions the Maxwell equations (equation (2.1) can be rewritten as:

$$\nabla \cdot \boldsymbol{H}_{(\boldsymbol{r},t)} = 0 \quad \nabla \times \boldsymbol{E}_{(\boldsymbol{r},t)} + \mu_0 \frac{\partial \boldsymbol{H}_{(\boldsymbol{r},t)}}{\partial t} = 0$$

$$\nabla \cdot \left[\varepsilon_{(\boldsymbol{r})}\boldsymbol{E}_{(\boldsymbol{r},t)}\right] = 0 \quad \nabla \times \boldsymbol{H}_{(\boldsymbol{r},t)} - \varepsilon_0\varepsilon_{(\boldsymbol{r})}\frac{\partial \boldsymbol{E}_{(\boldsymbol{r},t)}}{\partial t} = 0$$

(2.6)

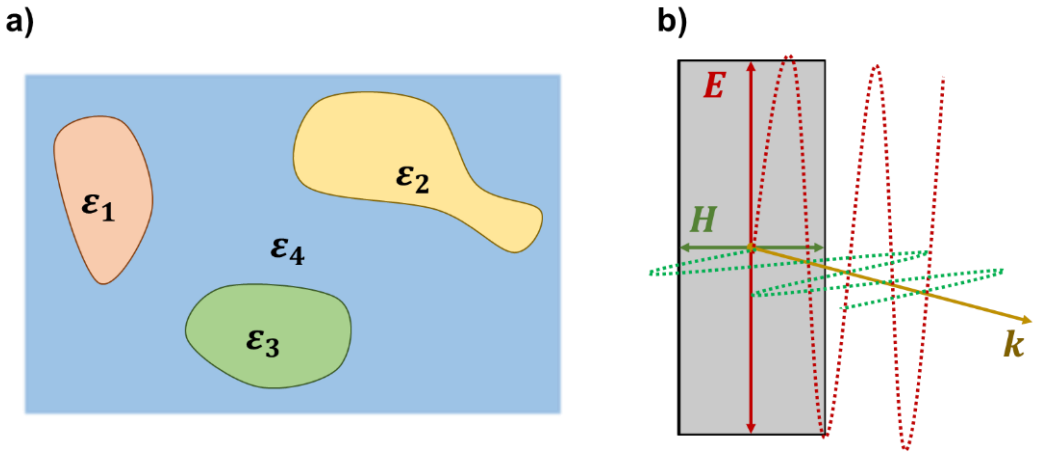

Figure 2.1. (a) Scheme of a system with different dielectric materials (represented by their dielectric permittivity ε_i); (b) Electric (red) and magnetic (green) fields propagating in the wavevector (yellow) direction as it is considered in this problem.

It is important to remember that these approximations are used to simplify Maxwell's equations and obtain a solvable master equation. But under this restricted system some physical phenomena might be missed. To evaluate more complex phenomena happening in the system, analysis of small perturbations can be done. However, this type of analysis is out of the scope of this section.

Maxwell equations are lineal equations. Therefore, both $\boldsymbol{E}_{(\boldsymbol{r},t)}$ and $\boldsymbol{H}_{(\boldsymbol{r},t)}$ fields can be expressed as the multiplication of two independent terms: one which is time dependent and another one which is spatial dependent. This can be done by expressing the fields in a set of harmonic modes. In this way, the fields will be considered to sinusoidally (harmonically) vary with time, oscillating on the transversal plane of propagation (Figure 2.1 b). With all these considerations the electric and magnetic fields can be written as:

$$\boldsymbol{E}_{(\boldsymbol{r},t)} = \boldsymbol{E}_{(\boldsymbol{r})} e^{-i\omega t} = \boldsymbol{E} e^{i\boldsymbol{k}\cdot\boldsymbol{r}} e^{-i\omega t}$$

$$\boldsymbol{H}_{(\boldsymbol{r},t)} = \boldsymbol{H}_{(\boldsymbol{r})} e^{-i\omega t} = \boldsymbol{H} e^{i\boldsymbol{k}\cdot\boldsymbol{r}} e^{-i\omega t}$$

(2.7)

where $\boldsymbol{k}$ is the wavevector, $\boldsymbol{r}$ is the spatial position in the system and ω is the frequency. In equation (2.7) the field's time dependent term is expressed as $e^{-i\omega t}$ and the space transversal term is expressed by $\boldsymbol{E}e^{i\boldsymbol{k}\cdot\boldsymbol{r}}$ and $\boldsymbol{H}e^{i\boldsymbol{k}\cdot\boldsymbol{r}}$ for the electric and magnetic fields, respectively. It is important to remind that $\boldsymbol{E}$ and $\boldsymbol{H}$ should fulfil the condition of transversality of the fields in relation to the propagation direction $\boldsymbol{k}$ (Figure 2.1 b).

The equations in (2.6) can be further developed by using the new expression of the fields in (2.7). The result of this development are the master equations, which describe the propagation of the fields through a system of dielectric materials:

$$\nabla \times \left(\frac{1}{\varepsilon_{(\boldsymbol{r})}} \nabla \times \boldsymbol{H}_{(\boldsymbol{r})} \right) = \left(\frac{\omega}{c} \right)^2 \boldsymbol{H}_{(\boldsymbol{r})}$$

(2.8)

in this master equation c represents the speed of light being the result of $c = 1/\sqrt{\varepsilon_0 \mu_0}$. With this result, the equation in (2.6) and using the fields expressions in (2.7), then the expressions for the spatial terms of the fields can be written as:

$$\boldsymbol{E}_{(\boldsymbol{r})} = -\frac{i}{\omega \varepsilon_{(\boldsymbol{r})}} \nabla \times \boldsymbol{H}_{(\boldsymbol{r})} \quad \text{or} \quad \boldsymbol{H}_{(\boldsymbol{r})} = -\frac{i}{\omega \mu_{(\boldsymbol{r})}} \nabla \times \boldsymbol{E}_{(\boldsymbol{r})}$$

(2.9)

The solution of these master equations is a so-called eigenvalue problem [29] and, thus, the field solutions and their frequencies are called eigenmodes for specific eigenfrequencies, respectively. The discrete or continuous character of these eigenfrequencies will allow the discussion of the band diagrams on later sections.

2.1.2. Translational symmetries

Up to now, a photonic crystal has been referred to be a periodic distribution of materials with different permittivities. This means that such a crystal consists of the repetition, in one, two or three directions, of a minimum unit. This minimum unit is called unit cell and is defined by the lattice vectors. Consequently, there can be one, two or three lattice vectors, depending on whether the photonic crystal has one, two or three periodic dimensions. Finally, the characteristic length of the unit cell is called lattice constant. All these definitions are similar to those used in crystalline solid materials [26].

These definitions are important because they imply that moving along any of the periodic directions by a discrete number of times the lattice vector, the dielectric distribution is the same [30]. This can be expressed as follows for a one-dimensional system:

$$\varepsilon_{(\boldsymbol{r})} = \varepsilon_{(\boldsymbol{r}+\boldsymbol{R})} \quad \text{where} \quad \boldsymbol{R} = l \cdot \boldsymbol{a}$$

(2.10)

where l is an integer and $\boldsymbol{a}$ is the primitive lattice vector.

In the previous section a system with two or more dielectric materials with random spatial distribution has been considered (Figure 2.1.a). However, the system under study here, a photonic crystal, is a well organised periodic distribution of two dielectric materials. Therefore, the eigenvalue problem faced in this case is a very specific one. The spatial term of the fields in a periodic distribution of dielectric material can be expressed, for instance, for the magnetic field, as:

$$\boldsymbol{H}_{(\boldsymbol{r})} = e^{i\mathbf{k}\cdot\boldsymbol{r}}\boldsymbol{u}_{(\boldsymbol{r})}$$

(2.11)

Expression (2.11) is predicted by the Bloch's theorem [31], which states that a transversal wavefunction in a crystal can be expressed as the product of a plane wave ($e^{i\mathbf{k}\cdot\boldsymbol{r}}$) and a periodic function which has the same periodicity as the lattice ($\boldsymbol{u}_{(\boldsymbol{r})}$). As a consequence, this periodic function will fulfil the same translational condition as the material:

$$\boldsymbol{u}_{\boldsymbol{k}_{(\boldsymbol{r})}} = \boldsymbol{u}_{\boldsymbol{k}_{(\boldsymbol{r}+\boldsymbol{R})}}$$

(2.12)

thanks to this, the problem can be restricted to solving the master equations only inside a single unit cell. In addition, the plane wave term of the wavefunction expressed in (2.11) must fulfil that:

$$e^{i\mathbf{k}\cdot\boldsymbol{r}} = e^{i\mathbf{k}\cdot(\boldsymbol{r}+\boldsymbol{R})} = e^{i\mathbf{k}\cdot\boldsymbol{r}}e^{i\mathbf{k}\cdot\boldsymbol{R}} = e^{i\mathbf{k}\cdot\boldsymbol{r}}e^{il\mathbf{k}\cdot\boldsymbol{a}}$$

(2.13)

where $\boldsymbol{k}$ is the wavevector, $\boldsymbol{r}$ is the position in the system and, similarly to equation (2.10), the value of $\boldsymbol{R}$ is $\boldsymbol{R} = l \cdot \boldsymbol{a}$, where l is an integer and $\boldsymbol{a}$ is the lattice vector (Figure 2.2 a).

The conclusion in equation (2.13) will only be true if:

$$\boldsymbol{k} \cdot \boldsymbol{a} = 2m\pi \;\rightarrow\; \boldsymbol{k} = \frac{2m\pi}{\boldsymbol{a}}$$

(2.14)

where m is an integer. As a result of the Bloch theorem, the translational symmetry applies as well to the wavevector behaviour, since $\boldsymbol{k} = \boldsymbol{k} + {}^{2m\pi}/_{\boldsymbol{a}}$.

Thanks to this result, to solve the eigenvalue problem, instead of using the positions space (direct space), the wavevector space (reciprocal space) can be used [26]. This space is called as well reciprocal space. In the direct space the dielectric function is represented depending on its position while in the reciprocal space the wavefunction is represented depending on its wavevector. This wavefunction is constructed by a set of planewaves that behave as the ones expressed in (2.11).

Several parallelisms between the direct space and the reciprocal space can be stated. One of them is the equivalence of the primitive lattice vector in the reciprocal space. According to the conclusion of equation (2.13), the limits of a unit cell in the reciprocal space can be defined as well. Considering the case in which m = 1, then a reciprocal lattice vector can be defined as $\boldsymbol{b} = 2\pi/\boldsymbol{a}$ (Figure 2.2 b). In an analogous way, the boundaries of the unit cell in the reciprocal space are defined by the Brillouin Zone [26], [30], which is described by all the points whose distance from the origin is smaller than $\boldsymbol{b} = 2\pi/\boldsymbol{a}$.

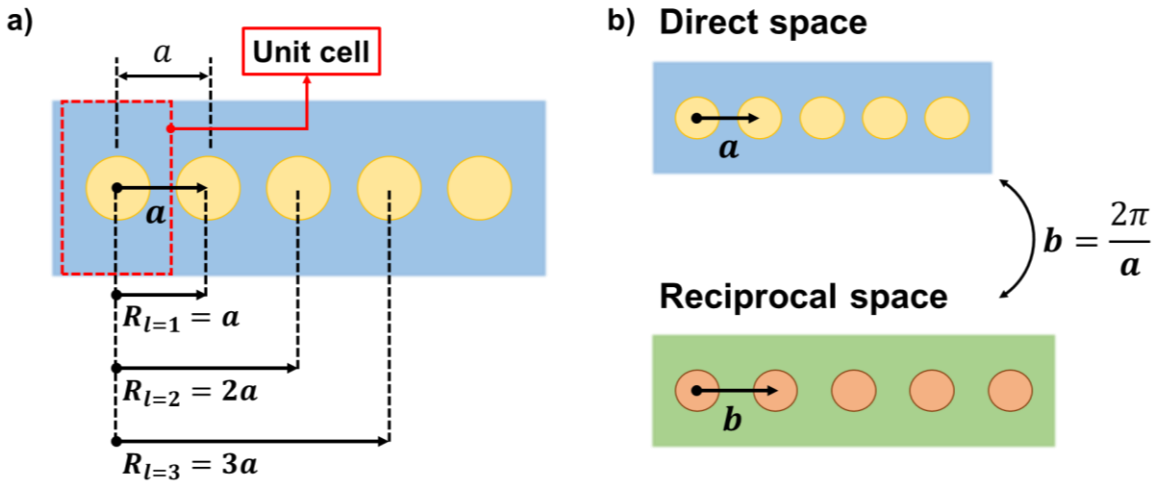

Figure 2.2. (a) Schematic representation of a one-dimensional photonic crystal in which several unit cells are depicted; both the lattice vector expressed as ***a*** *and the lattice constant expressed as a. (b) Representation of the relation between the direct and the reciprocal space of a one-dimensional photonic crystal.*

Until now, the solution of the master equations has only been considered for those directions in which there is periodicity. A photonic crystal, consequently, does not necessarily have to be periodic in all directions. For those directions where there is no periodicity $\varepsilon_{(r)}$ cannot be expressed as a function of a discrete number of unit cells and, consequently, its value is continuous in these directions and the Bloch theorem does not apply. As a result, the wavefunction can be expressed as:

$$\boldsymbol{H}_{(r)} = \boldsymbol{H}e^{i\mathbf{k}\cdot\boldsymbol{r}} \tag{2.15}$$

where $\boldsymbol{H}$ is a vector transversal to the propagation direction $\boldsymbol{k}$.

2.1.3. Photonic Band Diagram

Having defined the master equation and how the fields propagate in a periodic system, we can procced to solve the eigenvalue problem (Bloch theorem). Introducing the wavefunctions stated in equation (2.11) into the master equation (equation (2.8)), a

series of solutions within the unit cell can be found. These solutions will consist of an infinite series of functions or modes, ($\omega_{(\boldsymbol{k})}$), which are discretely spaced. Each of these modes will be continuous in $\boldsymbol{k}$ and will span from edge to edge of the Brillouin Zone. This set of modes creates a band structure, where each band correspond to one mode, and they are ordered according to increasing energy by a band number (n), starting at 0 [30].

The graphical representation of these bands for those $\boldsymbol{k}$ in the first Brillouin Zone is the band diagram of the photonic crystal (Figure 2.3 a). This visualization helps in a better comprehension and prediction of the light propagation within a photonic crystal. The bands will show which frequencies (wavelengths) will be transmitted and which not for specific directions in the photonic crystal. It is important to notice that the unit used to express the eigenvalues is dimensionless (in terms of $\omega a/2\pi c$), which helps generalising the situation to a scale-invariant problem and solution, only dependent on the basic unit of length of the system (a).

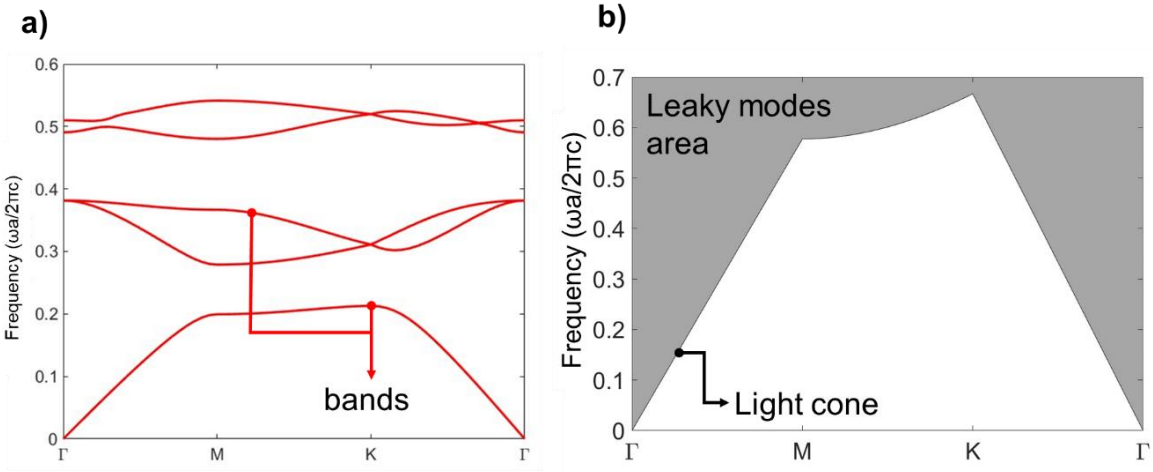

Figure 2.3. (a) Representation of a band diagram, where in red the different bands are shown. (b) Representation of a light cone. In grey the area of leaky modes is shown while in white the area of transmitted modes is represented.

The edges of the first Brillouin Zone will be defined by the symmetry points that will depend on the periodic geometry used [26]. These symmetry points (starting at the origin) will define which are the $\boldsymbol{k}$ directions used to represent the modes in the band diagram. Since the first Brillouin Zone is dependent on the geometry of the periodic

structure, the choice of the photonic crystal geometry will have an impact on the final band diagram and, thus, the light behaviour within it.

For those directions where the medium is homogeneous, this set of functions is infinite and continuous instead of discrete. These solutions fulfil the following restriction:

$$\omega \geq \frac{c \cdot |\boldsymbol{k}|}{\sqrt{\varepsilon_{(\boldsymbol{r})}}}$$

(2.16)

where c is the light velocity of propagation constant, and $\varepsilon_{(\boldsymbol{r})}$ is the dielectric permittivity of the medium and can be rewritten as the medium refractive index, since $n = \sqrt{\varepsilon_{(\boldsymbol{r})}}$. Those values at the border between the continuous and the discrete regime of modes create the so-called light line or light cone[30] (Figure 2.3 b). The modes above this light line are those that propagate into the homogeneous media and, therefore, are dispersive modes or extended states since they are not localised in the periodic structure. On the other hand, those below this line are guided modes or localised modes since they propagate only in the photonic crystal.

Previously it has been said that the mathematical solution of the eigenvalue problem is the obtention of an infinite set of modes discretely spaced. In this sense, it is important to emphasize the importance of expression (2.16), since it shows the physical limit to the number of guided modes that will be allowed within the photonic crystal.

From the previous explanation, the dependency of this light cone on the dielectric permittivity of the medium is clear. If this dielectric permittivity is small, the light line shifts towards higher frequencies, allowing more discrete modes to fall within the guided region.

The next question we rise is how light can be localised within the photonic crystal structure on those directions where no discrete translational symmetry exists. The strategy followed to keep the light propagation through the structure is the so-called index guiding [32]. Index guiding is based on the total internal reflection (TIR) phenomena predicted by Snell's law [33]. This law explains how an electromagnetic

wave behaves when it reaches the interface between two dielectric materials. The angle of the refracted wave in the second material will depend on the difference in refractive index between the two materials and the incident angle of the wave. The specific case here discussed happens when light propagates in a high refractive index material and reaches an interface with a material that has a lower refractive index. If the angle of incidence is large enough, above the so-called critical angle, the phenomenon of the TIR occurs. As a result of this phenomenon, the electromagnetic wave cannot propagate into the second material, staying confined within the high refractive index material.

Index guiding benefits from this phenomenon to prevent light loss from the guiding material. This principle is used by, for instance, optical fibres [34], which combine a high refractive index material (core) surrounded by a lower refractive index material (cladding) to efficiently transmit electromagnetic waves. A photonic crystal uses this principle as well to localize light within the crystal for those directions without discrete translational periodicity.

Another important consequence of all this development is that the photonic band diagrams are easily scalable [35]. This is possible because the master equation is scale invariant. This means that if a system is simulated under specific dimensions and we want to extend the calculation to a system in which the dimensions are scaled by a factor (s), called the scaling factor, the resulting modes can be scaled by the same factor (s) as follows:

$$\omega' = \frac{\omega}{s}$$

(2.17)

where ω' is the scaled mode and ω is the original mode. The same methodology can be applied if the dielectric constant of the new system can be scaled as well. In this case if the dielectric material is scaled by a l factor, then the mode scales as follows:

$$\omega' = l \cdot \omega$$

(2.18)

2.1.4. Photonic Band Gap

The fact that the solution of the eigenvalue problem is an infinite number of bands discretely spaced might give rise to frequency regions for which the system does not have any allowed mode. This means that one could encounter that for specific wavevector directions and frequency regions light might not be allowed to be transmitted through the system. If, in addition, this situation occurs for all the wavevector directions in the reciprocal space, this region is called photonic band gap (PBG)[36], [37].

There are two main driving factors that can influence in the creation of these band gaps. One of them is the dielectric permittivity difference between the two dielectric materials creating the periodic structure [36]. The band gap creation is primarily driven due to the concentration of the electric fields in one or the other materials and their profile depends on the particular mode. The lowest frequency mode (first band or dielectric band) tends to appear in the high dielectric permittivity materials because the electric field's energy tends to concentrate there. On the other hand, the next frequency mode (second band or air band) tends to appear in the low dielectric permittivity materials due to the high concentration of energy in the low refractive index material. Therefore, when the dielectric contrast, the ratio between the dielectric constants of both materials, is large, the band gap width will be larger. This will happen because the electric field localisation in one material is stronger if the contrast is larger. Therefore, the energy distribution in the material drives the band energy position and this energy difference is what creates the band gap [37].

Light can be polarised in different ways depending on the correlation of the phase and amplitude of the electric and magnetic fields [38]. In photonics typically linearly polarised light is used. Linearly polarised light can be transversal electric (TE), when the electric field oscillates parallel to the vertical direction of the pillars, or transversal magnetic (TM), when the magnetic field oscillates perpendicular to the vertical direction of the pillars.

The energy distribution in the different dielectric materials depends also on the interaction between the electric and magnetic fields with the system [37]. This interaction

depends on the polarisation of light. The direction at which the electric and magnetic fields intersect with the system will determine the opening of band gaps as well. In the case of two-dimensional photonic crystals, it is important to note which is the intersection between the oscillation direction of the electric field with the periodic plane direction and the dielectric material distribution. The previous discussion on where the energy will be concentrated just stated that it will depend as well on how easy it is for the electric field to be concentrated within the materials. For all these reasons, and as a rule of thumb explained elsewhere [37], TM band gaps will appear for material distributions where the high refractive index material is isolated (e.g., pillars), while TE band gaps will appear when the low refractive index material is isolated (e.g., slab with holes).

Summarising, the opening of band gaps will depend on the number of periodic directions in the structure, its geometry, the refractive index contrast of the two dielectric materials used, and the polarisation of the light used.

The next question that arises from this discussion is how these band gaps can be used and evaluated in a quantitative way. For this reason, a figure of merit is defined to evaluate the PBG. This figure of merit is defined as the ratio between the band gap width ($\Delta\omega$) and the band gap central frequency (ω_m) and is normally expressed in percentage. The characterization of PBGs, is therefore, done with the gap-to-midgap ratio [36].

Since this scalability mentioned above affects the band diagram, it affects as well to the band gap width and position. Even though the scalation of the system parameters affects the band diagram, the gap-to-midgap ratio, i.e., the figure of merit, remains constant.

Until the moment a general discussion of light behaviour in photonic crystals has been presented. However, the focus of this work, as explained in Chapter 1, is a particular case: to use a two-dimensional photonic crystal based on silicon pillars using air, first, and water, next, as dielectric background materials. The dielectric material choice for this project and the need of using pillars already limits the options for which periodic distribution and which light polarisation are the best to be used.

Previously in this section it has been explained that the opening of band gaps for either TE or TM polarised light strongly depends on both in the permittivity contrast between the two materials and their relative proportion within the unit cell. When using high

refractive index material for the pillars, the opening of band gaps is optimal for TM polarised light [37]. Therefore, in this project TM polarised light will be used in the following.

On the other hand, the choice of the periodic distribution is another important decision for the project. Elsewhere it is shown that a hexagonal periodic distribution promotes the creation of wider band gaps in comparison with similar structures but with different periodic distribution [39]. This is the result of the fact that the Brillouin Zone shape is very close to a circle. For this reason, a hexagonal distribution is chosen for this project. The creation of the Brillouin zone for this geometry is presented in Figure 2.4.

Choosing a polarisation and a periodic distribution, narrows down the design options of the devices proposed in this work. The structure described in Chapter 1, however, is not limited to the photonic crystal structure itself, but adds some modifications to the structure to further allow the control of the light transmission through the system.

In this section only the opening of band gaps has been considered as a priority. Due to the required sensing purpose of the system, the use of a uniform photonic crystal with only one band gap is just the starting point. As already explained, a band gap is a wide range of frequencies where the light is not transmitted through the photonic crystal for several or all directions. Even though this band gap is sensitive to geometrical changes in the system, it is not sensitive neither selective enough for the purposes of this project since the pillars that will be used will not bend under the lateral forces exerted by the tissues. To fulfil these needs, defects could be introduced in the photonic crystal structure. The nature of these defects and the changes that give rise in the photonic band diagram are explained in the following section.

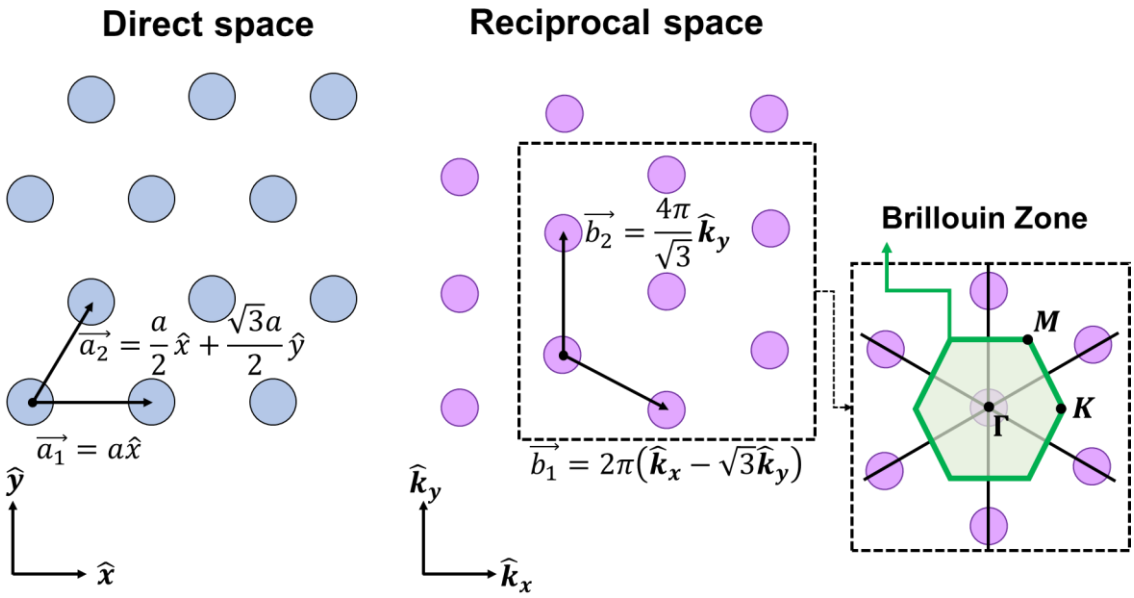

Figure 2.4. Representation of the direct space for a hexagonal distribution of pillars. The lattice vectors for a structure like this are represented by $\mathbf{a_1}$ *and* $\mathbf{a_2}$*. Then the reciprocal space representation of the same structure is shown with the reciprocal space lattice vectors represented by* $\mathbf{b_1}$ *and* $\mathbf{b_2}$*. Finally, the first Brillouin Zone calculation and symmetry points are shown as the intersection in the centre of the lines that connect the central point with the closer neighbouring pillars.*

2.2. Linear and point defects

The introduction of defects in a periodic system like the one described in the previous section will perturbate its periodicity. The effect of these perturbations, if they are properly designed, will be the generation of allowed states within the PBG structure [37].

Since the defects are surrounded by the photonic crystal structure, the light cannot leave the defect. This is thanks to the fact that, aside from the states created by the defect, the PBG still exists in the vicinity of this defect. This prevents the light in propagating in the photonic crystal and therefore, it is trapped inside the defect.

This is one of the strengths of photonic crystals and allows to trap and guide light in a very controlled way inside the photonic crystal for specific wavelengths and directions. In

this way, the photonic crystal works like a light conductor. Two different types of defects have been considered in this thesis: linear and point defects [37].

2.2.1. Linear defects

A linear defect is the alteration of a pillar row inside the system. This alteration can be a variation of the dimensions of the pillars, of the pillar-pillar distance or of the material that constitutes them. The variation of a line of pillars creates a discrete band inside the forbidden PBG. The newly allowed eigenfrequencies resulting from the presence of the linear defect inside the system still depend on the wavevector direction [40]. In addition, this new band will still be evanescent into the unaltered photonic crystal. This means that the modes corresponding to the defect's new band will only be localized inside the line defect but will not be transmitted through the rest of the system because the band gap still applies to the rest of the photonic crystal.

To better understand how this new bands are created, it should be noted that a line defect breaks the periodicity of the structure in a specific wavevector direction. This means that to evaluate how the defect behaves the guided modes in its wavevector direction are analysed.

To do so, a projection of the band structure is carried out [41]. This projection consists in collapsing the symmetry points in the Brillouin Zone onto the reciprocal space direction in which the defect is located. In the case of the structures discussed in this thesis, the first Brillouin Zone for a hexagonal periodic distribution contains three symmetry points Γ, K and M (Figure 2.5 a). Creating a linear defect in the direction shown in Figure 2.5 b, in the direction of $\boldsymbol{k}$, provokes the collapsing of the M point onto the $\Gamma - K$ direction. The projection of this M point creates a K' point which becomes the new edge of the Brillouin Zone.

When considering a real two-dimensional photonic crystal, one has to extend this problem to a three-dimensional system [42], [43]. In a three-dimensional system it must be expected that some modes will not be sustained by the photonic crystal and will propagate into the background materials (leaky modes). The real three-dimensional

system is the so-called photonic crystal slab. This slab considers a finite third dimension of, in this case, pillars. As explained in section 2.1.3 the light confinement is possible thanks to the TIR of light in this third non periodic direction.

The main consequence of having a slab is the limitation on the number of final allowed modes inside the slab because of the leak of modes into the claddings (limited by the refractive index of these claddings by the light cone – section 2.1.3 -). The introduction of the third dimenion in the problem affects as well the creation of linear defects and the modes that the defect can sustain. The ultimate effect of this limitation is the fact that, theoretically, a line of pillars could be completely removed in the system here discussed and still sustain a mode in the defect. However, having the same refractive index in the waveguide and in one of the claddings, makes this approach unrealistic because light will propagate into the background instead that staying in the slab [43].

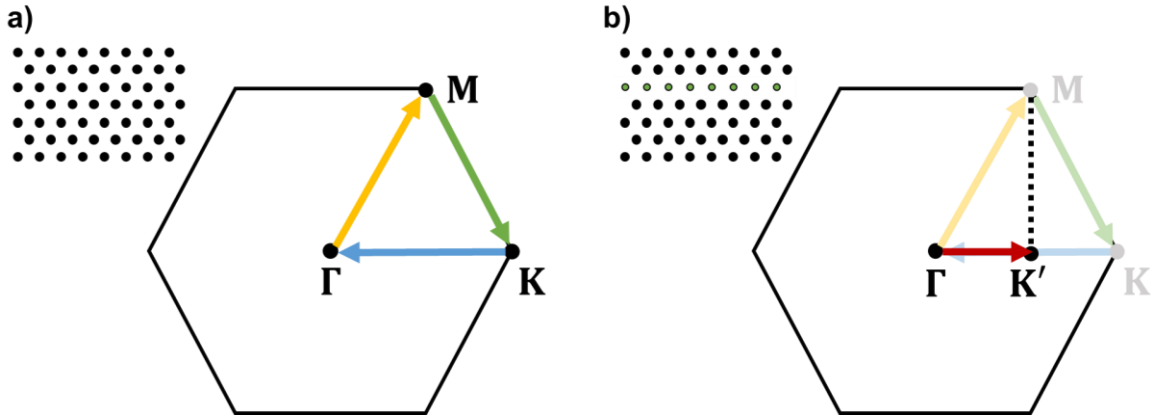

Figure 2.5. (a) First Brillouin Zone boundaries for a perfect two-dimensional photonic crystal structure. The arrows show the direction of the wavevector variation during the band gap evaluation. (b) Projection of the M symmetry point onto the defect direction creating a new symmetry point K' due to the creation of a line defect to the structure.

2.2.2. Point defects

Another type of defects are the point defects, which are punctual disruptions of the periodicity of the photonic crystal in one specific direction [44]. If the mode sustained by this point is one of the modes forbidden by the PBG, then the resonance is localized in the defect. This has very similar effects as those explained for linear defects. However, there is a key difference, and it is that the resonance frequency is independent of the

light wavevector [43]. This means that a band diagram cannot be used to explain the behaviour of the resonance, since it has no dependency on the directions of the first Brillouin Zone.

The main way to create a point defect is to increase or decrease the amount of one of the two dielectric materials in a specific spot or to change the pillar distance between the defect pillar and the ones in the nearest vicinity. In the case of this thesis, as described in Chapter 1, we are considering the former situation. If the size of the pillar creating the defect will be smaller than the ones creating the photonic crystal to allow it to be bent under the exertion of lateral forces at their top, i.e., reducing the pillar's radius (reducing the amount of high refractive index material), this will give rise to the appearance of a band of modes in the PBG just below the edge of the dielectric band. On the other hand, if the pillar's radius is increased (increasing the amount of high refractive index material), the new band will fall in the PBG just above the edge of the air band.

In the same way as explained for the linear defects, the impact of having slab instead of an ideal two-dimensional photonic crystal is by introducing some limitations on how these defects can be created. Even though, the creation of the mode is not dependent on the wavevector direction, if must be localized in the third dimension too. Again, this is possible thanks to the TIR phenomenon of light in the slab described above.

2.3. Computational methods

The solution of eigenvalue problems can be very complicated, especially when it comes to complex photonic systems like the one discussed in this work. For this reason, for solving these problems, the use of simulations is needed [45].

The fast growth of the research of photonic crystals can be explained thanks to the numerous computational methods developed during the last decades. It is precisely because of this wide range of simulation options that choosing the right one for the purposes of this research is a difficult task. Some methods have been created to solve more than one electromagnetic problem. However, the reality is that they present

strengths and weaknesses depending on their final application, making them more convenient to solve one or another problem.

In this thesis we will focus on two methods which will be applied to one or another situation depending on what is simulated. In Chapter 3 the discussion of the band diagrams and the transmission and reflection spectra will be analysed. For the analysis of the band diagrams, a Finite Element Method (FEM) has been used, while for the transmission reflection spectra, Finite Difference Time Domain (FDTD) method has been used. In the following subsections the principles of these two methods are described.

2.3.1. Finite Element Method

The FEM is a method that it is not exclusive for solving electromagnetic problems [46]. Among others, it is a method widely used to study and mathematically model problems related to heat transfer, fluid flow and, of course, electromagnetic fields.

This method is used to solve problems that can be described by partial differential equations (Maxwell equations, in the present case) and which can hardly be solved analytically. The solution given by the FEM method allows to track the evolution of a dependent variable among time and space (independent variables). The change evaluated can be made very small so it can be expressed by means of differential equations of the independent variables.

In this method, the system is divided into small elements (finite elements), simplifying a continuous and complex physical problem into a finite number of local, smaller, and easier problems (Figure 2.6). Even though the system is simplified the precision achieved is remarkable and can be further improved by increasing the number of elements into which the system is divided.

As already mentioned, to solve the problem the domain under study is divided (discretized) into finite elements, which are smaller parts of the system itself [47]. This term and concept resemble the term infinitesimal, name used in differential calculus to define a small part of a continuum. This division (discretization) can be performed in

several manners and depending on the geometrical and material complexity of the system. Thanks to the versatility of the method this subdivision can be done in an irregular way to fit in any geometry requirements (e.g., the system can be divided into triangles or tetrahedra). All these finite elements are part of a mesh whose nodes are the connections between the different elements (Figure 2.6). At these nodes the variables of the system will be evaluated.

After the discretization of the system the dependent variable can be explicitly defined at the nodes [47]. The solutions at these points can be considered as unknown constants. Next, the strategy to solve the variable behaviour within each element will be done by an interpolation of the results at each node enclosing each element.

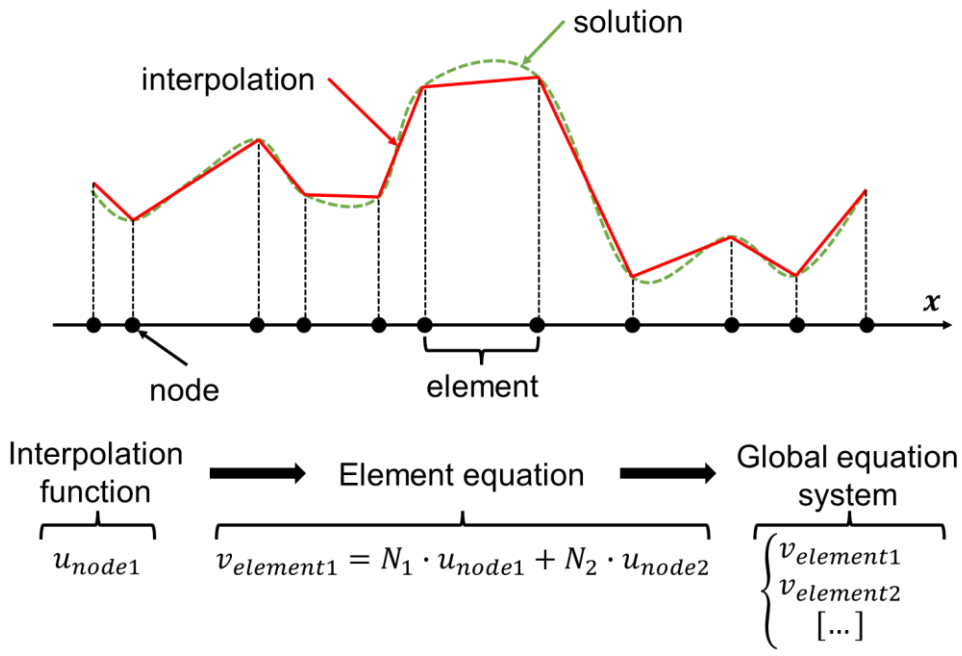

*Figure 2.6. Scheme of the approximation to the solution done with FEM methods. In dashed green the actual solution to the problem. In red the interpolation result obtained from a FEM simulation. On the **x** line are presented the nodes limiting the different space element in which the space is divided. An example of the flow followed by FEM simulations is shown too.*

The interpolation is done by using known interpolation functions, as well as shape functions [47]. On each node an interpolation function will be defined to describe the variation of the variable within the finite element. These functions should be continuous

across each element. They are normally defined as polynomial functions with different degrees whose number will depend on how complex the finite elements are (e.g., how many nodes they have). It must be kept in mind that the higher the polynomial order (order of interpolation) the better the accuracy but also the larger the computation effort.

After creating these interpolation functions the element equation can be constructed by linearly combining each interpolation function and imposing the boundary element conditions, i.e., the continuity, for the variable values at each node [47]. This equation can be obtained by using different approaches. For a differential system, such as the one discussed here, the Galerkin method is the most suitable [46].

After this a global equation system can be solved by assembling all the element's equations. This connects the local conditions of each element with the rest of the system. Imposing boundary conditions to the system and by computational iterative methods, this system can be solved, providing the system behaviour.

This method has been used during this thesis to solve the band diagrams of the samples. This method is useful because it allows the solution of the eigenvalue problem solving the master equation for the structures. To carry out these simulations, COMSOL Multiphysics® [48] has been used. COMSOL Multiphysics® is known to have several modules that allow the simulation and theoretical evaluation of problems with very varied origins. In this case the module used is the Electromagnetic Waves module. The detailed program used has been described in Chapter 3.

2.3.2. Finite Difference Time Domain Method

The FDTD method is known to be the most widely used for computing time variant electromagnetic systems, such as the transmission and reflection spectra of photonic crystals [45]. It is part of the group of computational methods of Finite Difference Method (FDM). FDTD method is a specific case of FDM methods that uses the fact that the electric and the magnetic fields are linked in a way that when the first varies in time the second varies in space, and vice versa [49]. This method is known as well as Yee method [50].

As already stated before, this method uses the fact that both the electric and magnetic field's time and space derivatives are correlated. Similarly, to the FEM methods, the FDTD method divides the space into a rectangular grid (Yee's lattice) that contains a finite number of nodes. In this lattice the electric field and the magnetic field are shifted half a cell in space and half the time step one from the other (Figure 2.7). At the same time, while the space is divided into a grid, the time evolution is divided in time steps [51].

With this construction the derivative Maxwell equations are solved iteratively for all the time steps using a leap-frog algorithm. This means that the magnetic field is calculated at some nodes, and, after that, the electric fields are calculated at the shifted nodes. In this way the electric and magnetic field are solved in time and space iteratively.

Even though this method has a less complex construction than the one explained in the FEM section, it is very sensitive to several parameters, such as the grid cells size (resolution), the dielectric materials in the system or the time step [51].

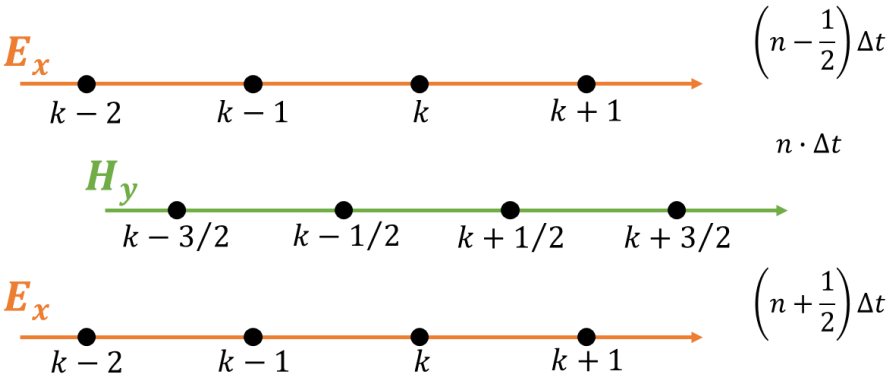

Figure 2.7. Scheme of the time and space dependent solution of the electric and magnetic fields depending on the time step considered. The offset by half a time unit is expressed by the shift in the position of the nodes in the magnetic field wavevector line relation to the electric fields line.

This method has been used in this thesis for the simulation of transmission and reflection spectra. To do so, open-source software, such as Python™, has been used to create the codes of the simulation. The FDTD method has been implemented in the code thanks to the use of the MEEP module [52]. The MEEP module (standing for MIT Electromagnetic Equation Propagation module) is an open access Python™ module developed by

researchers of the Massachusetts Institute of Technology (MIT). The structure of the code is further explained in Chapter 3.

2.4. Proposal of simulation activities

From the discussions in this chapter, it can be seen that the simulation of photonic crystals is a rather complex problem to solve. Even though several approximations can be applied to simplify the problem, still powerful simulation tools are needed to evaluate the system performance.

In this thesis, the simulation goals are:

1. To narrow down the photonic crystal parameters, both in air and water environments, to one single configuration that can be further fabricated and tested.

2. To evaluate the introduction of both line and point defects into the photonic crystal structure and obtain their allowed modes.

3. To investigate the use of different types of claddings for the three-dimensional structure to emulate the real system to be analysed.

To fulfil these goals, both simulations using FEM and FDTD simulation methods have been used, each of them providing different information that will be shown in Chapter 4 and which are organised into the following milestones:

1. Creation of simulation programs and files that can be easily tuned to the necessities of the project.

2. Evaluation of the photonic crystal pitch and radius values, considering air and water backgrounds. These simulations have been carried out in two-dimensional and with both FEM and FDTD simulation methods.

3. Introduction of line defects into the photonic crystals and discussion on the different parameters of the defect and their impact on both the band diagram and the transmission spectra.

4. Discussion on the introduction of cavities and how the potential pillar bending might affect the resonance peak frequency position.

5. Discussion of three possible scenarios for the cladding distribution in the real three-dimensional structure.

These five points summarise the simulations that will be shown in Chapter 4. In there, there is an in-depth explanation of the simulation programs used and the results obtained are detailed.

CHAPTER 3.
THEORY OF NANOFABRICATION

3.1. The cleanroom

The fabrication of the structures has been carried out at Lyngby campus of the Technical University of Denmark (DTU) within the facilities of the National Centre of Nano and Microfabrication and Characterisation of Denmark (DTU Nanolab) [53]. It houses a cleanroom (1350 m^2) as well as characterisation infrastructures inside and outside the cleanroom for both material and soft matter characterisation (Figure 3.1). With more than 100 staff members the mission of DTU Nanolab is to provide industry and academia a state-of-the-art infrastructure for carrying out their production and research. Furthermore, the combination of both worlds makes DTU Nanolab a perfect environment for knowledge transfer and education. DTU Nanolab has been rated as an ISO 9001 infrastructure, demonstrating the quality of the users' services and the facilities' conditions [54].

The cleanroom laboratory is primarily characterised by the monitoring and control of temperature, pressure, humidity, and the number of particles per cubic meter, with special emphasis on particles smaller than 0.5 µm [55]. The cleanroom facilities therefore provide a suitable environment for the controllable fabrication of micro and nanostructures.

Inside the cleanroom numerous processes can be carried out. These processes can be classified in the following fields:

- Wafer cleaning
- Lithography
- Thin film deposition, growth, and doping
- Etching
- Characterisation
- Back-end processing

A standard fabrication of samples inside the cleanroom typically involves using techniques across the fields listed above. The process described in this thesis is not an exception. In this project processes among the fields of lithography, thin film deposition, etching and characterisation have been widely studied and used.

To better understand the final process flow steps and conditions, the different fields are described in the following sections to provide context on the discussion carried out in Chapter 5.

Figure 3.1. Images of the DTU Nanolab cleanroom facilities: (top left) the cleanroom building; (top right) electron beam lithography cassette loading; (bottom left) automatic resist spin coaters; (bottom right) automatic electron beam resist developer.

3.2. Lithography

Lithography is a process used to transfer a pattern onto a flat surface. It uses a mask, a radiative source, and a resist that, under the radiation, changes its properties [56]. The minimum feature size that is possible to transfer onto the substrates strongly depends on the wavelength of the radiation used. At the same time this wavelength depends on the nature of the radiation and the source that creates it. The two main types of radiation used for lithography are photons and electrons [57].

But the radiation source and wavelength are not the only factor affecting the resolution and the result of the lithography. In the following subsections, step by step, the lithography process is detailed and discussed. In addition, one of the post-processing techniques used in this thesis will be discussed below, comprising the transfer of a metallic pattern on the surface after the regular lithography.

3.2.1. Resist deposition

This step consists of the deposition of a film of resist on top of the substrate. A good adhesion between the resist and the substrate is essential, as well as uniformity of the resist properties and thickness along all the surface of the substrate.

To understand the mechanics of lithography, though, first it must be understood the components of the resist. A resist is a combination of three components [58], [59] :

i) A resin based on polymers and monomers, which determines the mechanical and thermal properties of the resist.

ii) A photoactive or electroactive compound (PAC), which reacts with the radiation, provoking the chemical changes in the resin.

iii) A solvent that controls the viscosity of the resist, allowing to dispense it and which helps the resist spread on the substrate.

Depending on the polymers used as resin and PAC, the behaviour of the resist can be considered positive or negative, known also as the resist tone [58]. This means that the exposed areas will soften and be removed after development or they will harden and, therefore, remain after development, respectively.

For those resists that are positive, the exposed areas of the resist are soluble in the developer. In positive resists the PAC compound inhibits the solubility of the resin while it is not exposed. When exposed, the PAC compound reacts creating an acidic compound that breaks the polymeric chains of the resin and makes the exposed areas soluble [58]. Negative resists, however, become insoluble upon exposure. In this case, the exposure to light and the acidic compounds from the PAC promote the cross-linking of the resist polymers under the exposed areas, increasing their molecular weight and becoming less soluble [58].

Therefore, the mask design must consider the type of resist used during the process. The tone of the resist affects not only the final developed or remaining areas but also the

resolution. The resolution is affected by the length of the polymeric chains: the shorter the chain, the better the resolution. Other factors affecting the resolution are the dose and the development time, both of which are discussed in the following subsections.

The process of deposition of the resist involves several steps to ensure optimal conditions for the exposure. Adhesion of the resist deposition on to the surface is a critical factor and prone to humidity on the surface [58], [60]. To avoid the presence of the water radicals on the surface, a prebake at 100-200 ^{o}C can provoke the desorption of these radicals from the surface. However, and depending on the humidity levels in the cleanroom, water can be easily reabsorbed again. To help mitigate this, Hexamethyldisilazane (HMDS) vapour treatment can be applied on the surface, which makes the surface hydrophobic, preventing the reabsorption of water on the surfaces and thereby improving the resist adhesion. This process lasts for several days, whereas the prebake may last only up to 10 minutes.

After the surface preparation, the resist deposition is typically carried out using spin coating [61]. This is one of the most widely used approaches and was employed in this project. Other techniques include spray coating [62] or roll lamination [63].

The spin coating deposits the resist on a surface while rotating it at a high speed. The substrate is vacuum clamped at its backside on a rotatory chuck (Figure 3.2 a) [61]. Subsequently, the resist is dispensed on the wafer dynamically or statically, depending on whether the wafer is already rotating or not, respectively (Figure 3.2 b). After that, the rotation velocity is increased to a few thousand revolutions per minute (rpm) and rotates at this high speed for 30 to 60 seconds (Figure 3.2 c). During the acceleration and the first high speed moments, the resist is spread all over the wafer and thinned down, therefore more than 90% of the resist is wasted. The remainder time of the process at a high-speed spin velocity helps to evaporate the partially the solvent and provoke resist hardening.

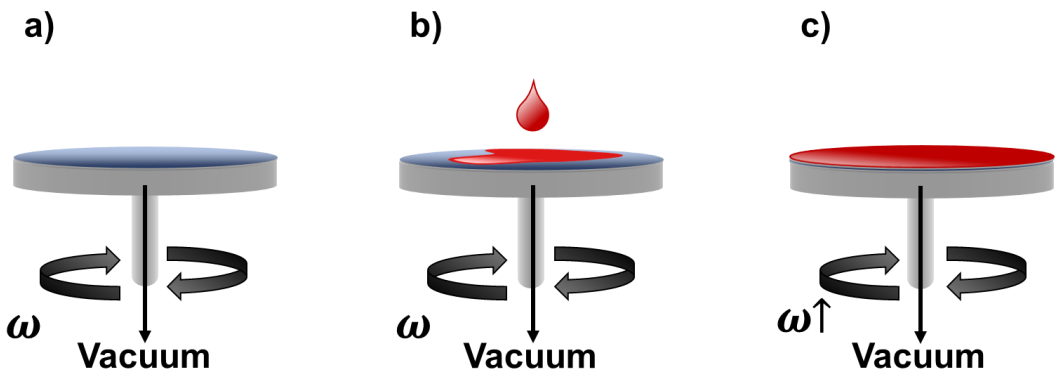

*Figure 3.2. Sketch of the three main steps of the spin coating process: (a) wafer clamp and beginning of rotation (**ω**); (b) resist dispense; and (c) increase of rotation spin and resist flatten.*

It is important to keep in mind that the typical final thickness of the resists used for lithography spans from several micrometres down to a few hundreds of nanometres, depending on whether they are used for Ultraviolet lithography (UV), or Electron Beam lithography (EB) and Deep Ultraviolet lithography (DUV), respectively. Several parameters play an important role to achieve these thin layers of resist. The final resist thickness (t) is correlated with the resist viscosity (η) and the spin speed (ω) [58]:

$$t \propto \sqrt{\frac{\eta}{\omega}} \tag{3.1}$$

however, the spin coating process and the resist spread is complex and depends on a large number of variables [58], [61]. For this reason, spin curves provided by the commercial suppliers are used to determine the conditions at which the resist should be handled and spined [64]. They serve as a starting point and need to be fine-tuned by the cleanroom technicians to ensure a controlled and repeatable thickness.

After the deposition, a post bake can be carried out at a resist-dependent temperature to harden the resist and evaporate the remaining solvent [58].

3.2.2. Exposure

Following the resist deposition, the exposure is carried out. The goal of the exposure is to promote the chemical changes of the resist on the desired areas of the substrate which enables the transfer of a pattern. To do so, the lithographic process must ensure that the pattern can be resolved on the substrate.

The primary condition for this to happen is to ensure that the resist gets enough energy to promote the reactions that help the polymers break or cross-link for positive or negative tone resists, respectively. The energy input by the system (defined as dose) is computed from the time of exposure at a specific location and the intensity of the source. The minimum dose required to promote the change on the resist behaviour is called resist threshold. This threshold depends on the resist used and its thickness as well as the substrate's material, since both photons and electrons interact with the material underneath the resist during the exposure. This interaction is material dependent and its use in EB lithography is discussed in detail later in this subsection. The pattern can be created by using a physical or a virtual mask that will determine which areas will be exposed and which will not.

In this subsection, two basic exposure processes are briefly discussed: optical lithography (UV and DUV) and EB lithography.

Both UV and DUV are lithography techniques based on photons and use physical masks with a limited resolution [65]. The widely used UV lithography is limited by the Fresnel diffraction limit that determines the minimum resolvable linewidth or the minimum separation between features as [58]:

$$w \approx \sqrt{\lambda \cdot \left(g + \frac{d}{2}\right)} \tag{3.2}$$

where w is the line width, λ is the light wavelength, g is the distance between the mask and the resist, and d is the resist thickness. This physical limit, together with the resist limitations, makes the UV lithography suitable for fabricating structures above a few micrometres.

Other approaches, such as the DUV, allow resolutions down to hundreds or even tens of nanometres because of the use of light sources with very short wavelengths, down to the deep UV. In this case, the resolution limit is determined by the Rayleigh equation [66]:

$$w \propto \frac{\lambda}{NA} \tag{3.3}$$

where w is the line width, λ is the light wavelength, and NA is the numerical aperture of the projection optics.

Despite the resolution limitations of these techniques, both are widely used in manufacturing because they allow fast exposure of large areas. Furthermore, some of these limitations can be overcome by combining the lithography with additional fabrication steps or more exotic lithographic strategies, as is used in the state-of-the-art commercial microelectronic devices [56], [66].

Alternatively, to the traditional photolithography, the EB lithography uses high voltage accelerated electrons for the exposure [57]. The main gain of this technique is the resolution achieved due to the use of electrons, which have a much shorter wavelength than photons. Therefore, the theoretical resolution limit is dependent on the wavelength of the electron [67]:

$$\lambda_{electron} = \frac{1.2}{\sqrt{V}} \tag{3.4}$$

where $\lambda_{electron}$ is the electron wavelength and V is the acceleration voltage. The wavelengths achieved for the voltages used in normal electron beam systems can reach values below 10 pm. However, the real resolution limit of this technique is much larger than the electron wavelength itself. The electromagnetic lenses used to drive and collimate the electron beam through the system have some intrinsic aberrations [67]. This can affect the final beam spot size and shape on the substrate playing an important limiting factor for this technique. Therefore, the real resolution of this technique depends on the beam spot on the substrate and extends to several nanometres. These limitations

can be controlled and optimised by changing the system's column settings and they are tool dependent.

The beam spot size is a consequence of both the intensity of the beam current in the column, the aperture used, and the acceleration voltage. Considering a fixed voltage, the correlation between the aperture, the beam current, and the spot size are normally depicted in logarithmic scales, where the larger the aperture and beam current, the larger the beam size (Figure 3.3). These curves are strongly dependent on the system used for the exposure. Regarding the tools available in the Nanolab cleanroom, the minimum beam diameter obtained is a spot of 4 nm in diameter.

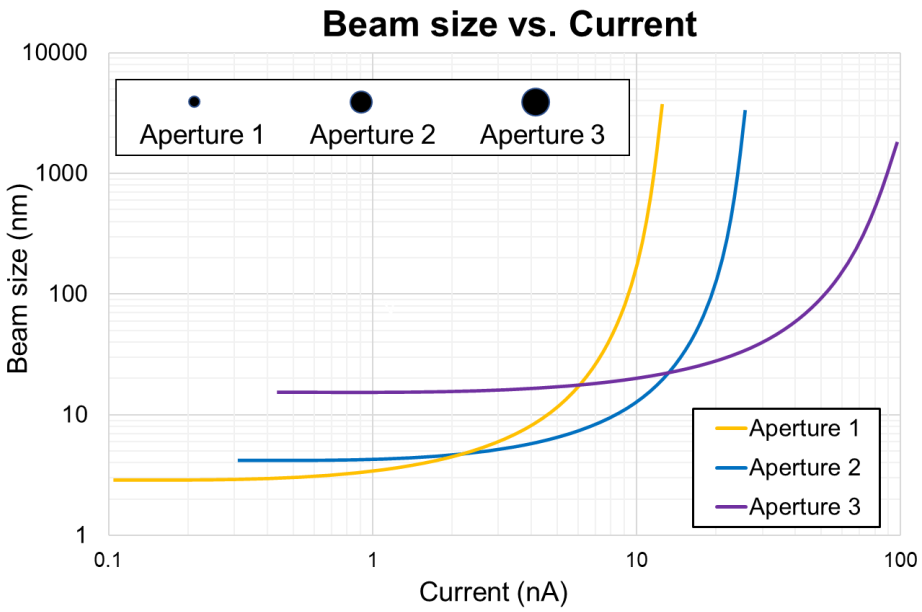

Figure 3.3. Sketch of the curves used to determine the beam spot size on the substrate depending on the aperture size and the current used during the exposure.

Nevertheless, the column settings and beam conditions are not the only parameters playing a role in the EB lithography exposure. The interactions of the electrons with the resist and the substrate also impact the resolution. These interactions are uncontrollable and intrinsic to the use of high energetic electrons, but they are predictable [68].

The electron-resist interaction provokes the reactions that promote the resist's behaviour change. However, when the electrons reach the resist the incoming beam spreads

(Figure 3.4 a), broadening the exposed area. This effect is known as forward scattering [67] and the range of affectation is in the order of nanometres depending on the resist thickness. Since the electrons involved in the forward scattering are still highly energetic the resist affected by this effect is exposed. The impact of the forward scattered electrons can be estimated by [67]:

$$d_{eff} = 0.9\left(\frac{t_r}{V}\right)^{1.5} \tag{3.5}$$

where d_{eff} is the effective beam diameter, t_r is the resist thickness, and V is the acceleration voltage. Therefore, the use of high acceleration voltage narrows the forward scattered electrons' dispersion.

Once the electrons reach the substrate, the effects of the electron-substrate interaction appear: the incoming electrons start interacting with the atoms in the material [67], [69]. The volume of interaction depends on the energy of the incoming electrons and the atomic number of the atoms in the substrate. The result of this interaction is depicted in the so-called teardrop diagram (Figure 3.4 a) and it gives rise to the creation of radiation, secondary electrons, and backscattered electrons. The electrons emitted from these interactions can expose parts of the resist if they reach the substrate-resist interface with sufficient energy. These electrons are called backward scattered electrons and have an interaction range of tens of microns [69]. This large deviation from the original incoming beam spot makes the contribution of these backward scattered electrons a problem for the exposure, since undesired adjacent resist areas can be exposed because of the effect of these electrons. The effect that these forward and backward scattered electrons have on the surrounding area is called Proximity Effect (PE) and can distort the resulting exposed pattern [67], [69].

As previously mentioned, these interactions between the electrons and the resist and the substrate are uncontrollable but can be predicted. If the energy of the incoming electrons, the substrate materials and their thicknesses for a given number of simulated electrons are known, Monte Carlo simulations can predict accurately the direction and

quantity of both forward and backward scattered electrons during these interactions. In addition, these simulations can provide information about the energy of these electrons. The result of the computation is represented with a Point Spread Function (PSF) [67], [69] that shows the energy of the forward and backward scattered electrons depending on the distance where they come back to the surface from the incoming beam (Figure 3.5 a). Commercial software offers the option to run these simulations in a straightforward manner, the one used in this thesis is the TRACER® [69], [70] simulator provided by GenISys®.

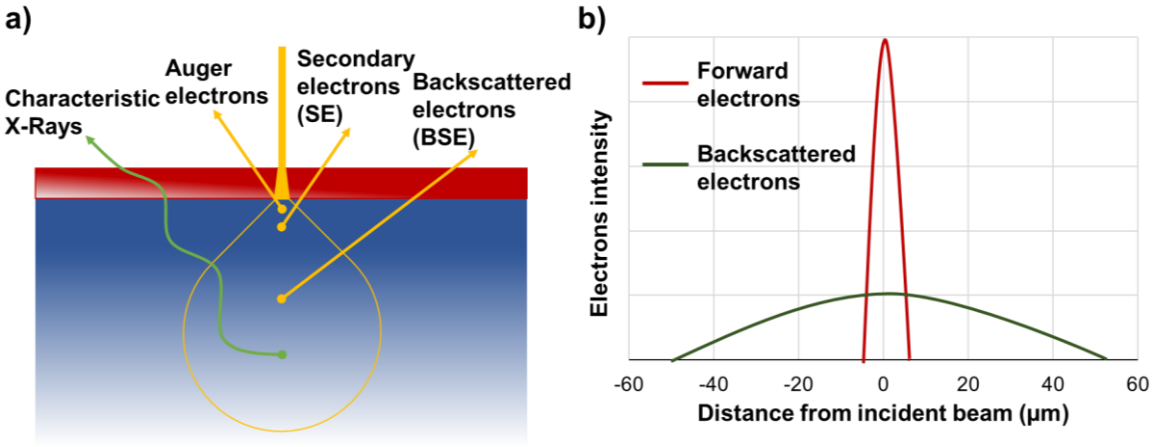

Figure 3.4. (a) Scheme of a teardrop diagram showing the interaction volume and the outcoming particles and photons of this interaction. (b) Sketch of the distribution of the forward and backscattered electrons as a function of the distance to the incident beam and the electrons energy.

The PSF of a specific combination of material layers can be used to know what areas of a specific pattern will receive extra electrons and if these electrons are energetic enough to expose the resist in these areas. Taking into account that this contribution cannot be avoided, the dose given at the different areas of the pattern can be modulated according to the PE contribution. This modulation of the doses is called Proximity Effect Correction (PEC) and allows to compensate the effect of the forward and backward scattered electrons. This correction is carried out with the commercial software BEAMER® [69], [71] provided by GenISys®. An example of a PEC pattern is observed in Figure 3.5 b where the different colours correspond to different modulations of the dose used during exposure.

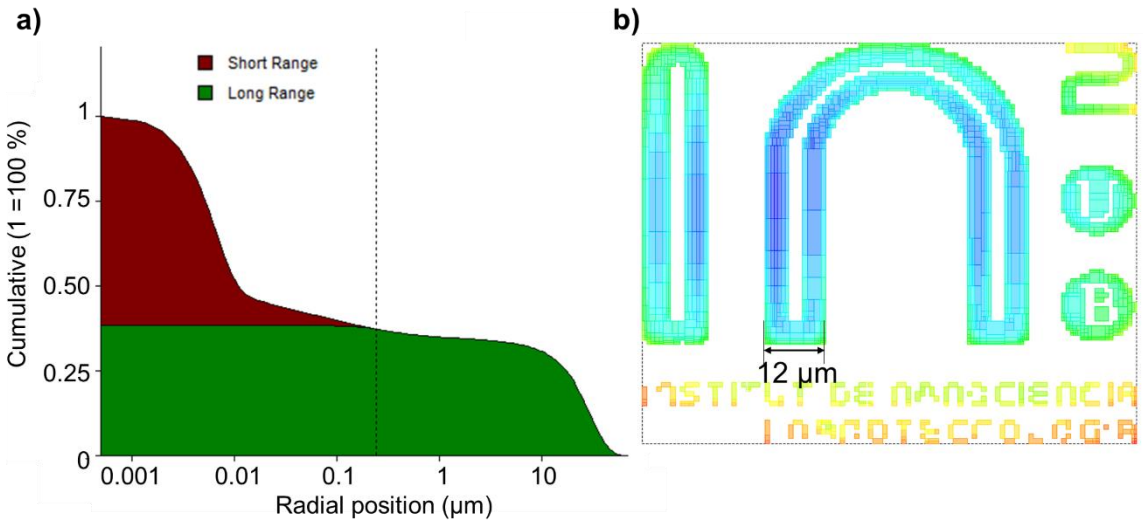

Figure 3.5.(a) Example of a point spread function for silicon-on-insulator (SOI) wafer with a buried oxide (BOX) layer of 1 µm, a device layer of 1.5 µm and a resist thickness of 180 nm. The simulation has been carried out assuming a beam energy of 100 keV (as used in this thesis) it has been done using TRACER® software. (b) Dose modulation of a mask after the proximity effect correction using the point spread function in the left image done with BEAMER®. The different colours correspond to different modulations of the base dose with blue representing the minimum modulation and red the maximum.

The electron-substrate interaction has been obtained neglecting the fact that during the beam interaction with the substrate material there are scattered electrons that cannot reach the resist, assuming their evacuation through the substrate material. This evacuation can be assumed for conductive and dielectric materials, but not for insulating materials. When the substrate contains insulating materials, the electrons created by the electron-surface interaction cannot be dissipated and remain in the material and – possibly – even in the resist. This can affect the exposure, creating undesired tree-like patterns. To avoid this effect, one of the most widely used strategies is the deposition of a conductive material, typically a light metal, on top of the resist that allows for electron dissipation. This deposition is carried out using thermal evaporation, a technique that will be explained later in this chapter.

EB lithography shows excellent results and good resolution for this project's applications. However, one of its main drawbacks is the difficulty of its application in mass production processes since it is a slow technique (in contrast to optical lithography), which allows serial processing. Nevertheless, it is an excellent technique to carry out preliminary

studies and research tasks that are necessary prior to moving forward to larger numbers of samples and mass production.

3.2.3. Development

After the exposure, the development – the final step of regular lithography processes – is carried out [58]. Sometimes a post exposure bake (PEB) [72] can be used to further harden the resist. For the development, the samples are submerged in, or covered by, a solvent liquid that dissolves the softer resist, keeping the harder one. The type of developer used in each case will depend on the type of resist. As mentioned before, it impacts the resulting pattern, and the development time must be optimised.

It has been discussed how the chemical changes of the resist are promoted or not depending on the energy given during the exposure. However, the different exposed areas do not have sharp boundaries giving different side walls profiles [58]. The surrounding areas also receive radiation and not only on the exposure plane but also deep into the resist. For this reason, there are areas that are susceptible to be developed even though they have not been, strictly speaking, exposed. Overdeveloping the substrates after the exposure might affect the final pattern dimensions and accuracy and the resist's remaining side walls.

On the other hand, under developing can prevent the correct removal of the exposed resist affecting the final pattern and resist side walls as well. One of the effects of the resist sidewalls is explained later in this chapter for the post processing of exposed samples.

3.3. Thin film growth and deposition techniques

Another group of techniques are the thin film growth and deposition techniques. These techniques are widely used inside the cleanroom and are used to create thin films that can be considered as two-dimensional materials [73].

There are different methods to create these thin films and they can be classified depending on the strategy used. The two main groups are the thin film growth techniques and the deposition techniques. The former use part of the material of the substrate's surface to grow a thin film, while the deposition techniques use a source whose material is deposited on the substrate's surface.

In this thesis different techniques of thin film growth and deposition have been used. The choice of one or the other method has been dependent on the thin film material and the purpose of the thin film.

The growth technique used in this thesis has been used to grow thin films of silicon oxide. The method used is the thermal oxidation of the top silicon layer of the wafer [74]. This oxidation process is carried out using water vapour, which reacts with the silicon of the surface creating silicon oxide:

$$Si(s) + 2H_2O(g) \rightarrow SiO_2(s) + 2H_2(g) \quad (3.6)$$

This process is known as wet oxidation and is carried out at temperatures over 1000°C in a horizontal furnace. The oxidation rates depend on the temperature and the time of the process among other parameters. Oxidation curves are created to provide an estimation of the time needed for the growth of an oxide layer of a specific thickness. One application of this growth process in this thesis is to reduce the silicon layer thickness of the device layer. For this, the amount of oxide to grow needs to be adjusted and one must take into account that the silicon oxide growth will consume part of the upper silicon, provoking the expansion of the top layer, as shown in Figure 3.6 b. The final silicon oxide thickness can be estimated by the following the relation[74], [75]:

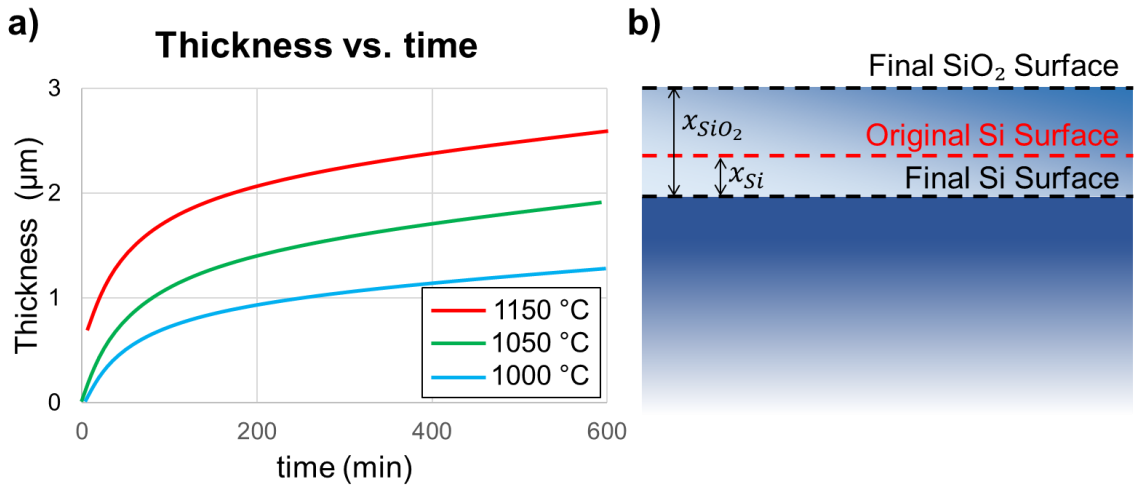

Figure 3.6. (a) Scheme of the silicon oxide growth curves used during a wet oxidation as a function of the oxidation time. (b) Sketch of the final oxidation layer and the upper silicon consumed during the oxidation.

$$x_{Si} = 0.45 \cdot x_{SiO_2} \tag{3.7}$$

where x_{Si} is the thickness of the consumed silicon layer and x_{Sio_2} is the final oxide thickness. In Chapter 5 specific information about the process will be further explained.

The deposition techniques can be classified in chemical or physical processes and are referred to here as: chemical vapour deposition (CVD) and physical vapour deposition (PVD) [73], [76]. The CVD processes can be divided into low pressure processes (LPCVD), plasma enhanced processes (PECVD), or atomic layer deposition (ALD). The main difference between the CVD and PVD approaches is how the layer is incorporated onto the surface.

In the case of CVD processes the gas species react on the substrate surface, producing the thin layer. This layer, therefore, is deposited everywhere and for this reason these techniques are known as non-directionals. On the other hand, in PVD processes, material is deposited on top of the surface after evaporating from a target. For this reason, the incorporation of material onto the substrate depends on the direction of the

evaporated material and the position of the substrate. These methods are also known as line-of-sight deposition or directional processes. In this thesis processes both LPCVD and PVD processes have been used.

Similarly, to the growth process, the LPCVD is carried out in a horizontal furnace where the gas species react or decompose on top of the surface at a very high temperature (above 500 °C). Several materials can be deposited using this approach, among them silicon. The deposition process involves a surface reaction of silane (SiH_4) with the surface silicon atoms, giving rise to the following reaction:

$$\mathrm{SiH4}(g) \rightarrow \mathrm{Si}(s) + 2\mathrm{H2}(g)$$

(3.8)

The creation of amorphous or polysilicon is dependent on the temperature since the incorporation rate changes. Below 600 °C the incorporation rate is 2 – 4 nm/s, producing amorphous silicon, while above 600 °C the rate increases up to 8-10 nm/s, giving rise to polysilicon [77], [78]. Since amorphous silicon is suitable for photonic applications, the amorphous silicon deposited by LPCVD processes has been used in this thesis for making pseudo-silicon-on-insulator (SOI) wafers.

On the other hand, the PVD processes used during this thesis are the thermal evaporation and the electron beam evaporation at ultra-high vacuum (10^{-6} - 10^{-7} Torr) of metals[76]. Both processes are based on heating a crucible that contains the material to be deposited. The main difference between these two methods is the strategy used for melting the material for its evaporation and, therefore, the materials that can be deposited. The thermal evaporation uses resistive heating of the crucible and the material, which makes this technique suitable to deposit metals with relatively low evaporation temperatures. In the case of aluminium, the evaporation temperature is 659 °C. In the e-beam evaporation method the heating is achieved by electron bombardment of the target, making it suitable for the deposition of metals that require a large amount of heat to be evaporated.

The thermal evaporation deposition technique has been used for the deposit of the discharge layer prior to the EB exposure. As already mentioned, for those substrates

containing insulator materials (as for the SOI wafers case) a metallic layer is deposited on top of the resist to ensure the correct evacuation of electrons during the exposure. The choice of using thermal evaporation is not arbitrary for to preserve the resist properties, the deposition technique should not involve the use of electrons. For this reason, thermally evaporated metals are suitable for the deposition of such a layer.

After the exposure, a lift-off process is carried out [79]. The lift-off process is used to transfer a metallic pattern onto a substrate. After the lithography a metal is deposited onto the open substrate areas and the remaining resist areas. After the metallisation, the substrate is submerged in a base solvent bath that dissolves the remaining resist and the metal on top of it leaving only the metal deposited on the substrate's exposed areas. The metallisation is carried out using evaporation methods because they do not have a good step coverage, i.e., they are directional. This ensures that the resist sidewalls will not be covered by metal, and, during the bath, the solvent will penetrate easily into the resist and dissolve it.

It is important to point out that the success of the lift-off is not only dependent on the deposition technique but also on the result of the lithography itself. Depending on the resist side wall profile, the side walls might be covered as well by metal preventing the resist dissolution during the chemical bath. The consequences of the different sidewalls are depicted in Figure 3.7, where it can be seen that for vertical and negative tapered sidewalls (Figure 3.7 b, c) the lift-off can be carried out successfully while with a positive tapered sidewall (Figure 3.7 a) the metal covers the surfaces completely.

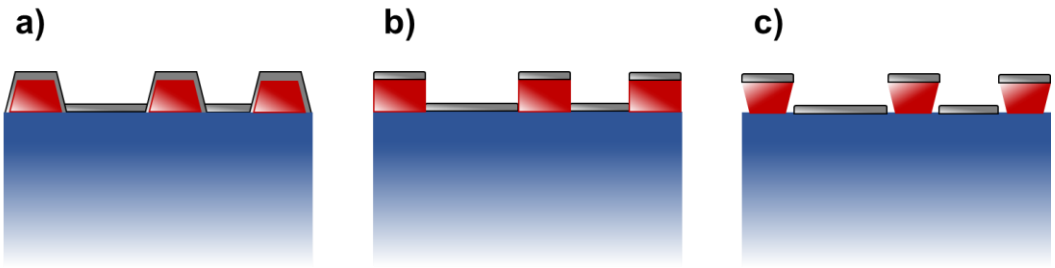

Figure 3.7. Schemes of the different metal coverage depending on the resist profiles.

3.4. Etching techniques

Several methods can be used for the etch silicon structures can be divided in two main groups: those performing an isotropic etch and those with an anisotropic etch. The main difference between these two groups is the etching profile and selectivity of the techniques [80].

An isotropic etch has an etching rate equal in all directions. This leads to etching profiles like the one sketched in Figure 3.8 a, where, in addition to the vertical etch, the masked areas are under-etched as the etching rate does not have a preferential direction. This type of etching is typical in wet- or gas-phase etching techniques. These techniques involve dipping the samples in a bath with the etching agent or in a chamber where the gas-phase etching agent is injected. Since the etching agent covers all the surfaces it will etch all of them equally.

An anisotropic etch is direction dependent and usually characterised by the etch in only one direction. The profiles of anisotropic etch are like the ones shown in Figure 3.8 b, where the etch is only carried out on the unmasked horizontal surfaces while the vertical sidewalls are not etched. The techniques that allow the anisotropic etch are commonly dry etch techniques although there are specific cases of wet etch where the etched rate is different depending on the crystallographic orientation of the etched material. However, these processes are characterised by reduced material selectivity and side wall control.

The anisotropic dry etch can be driven by physical phenomena, such as sputtering and bombardment of the exposed surfaces. This type of etching can be very suitable to etch deep structures with narrow widths (high aspect ratio structures) like the ones needed in this project.

Furthermore, while the isotropic etch is based on the chemical reaction of an etching agent with the etched material, the anisotropic etch can be more complicated: it can be a purely physical etch or a combination of a chemical and a physical etch [81]. While the chemical etch is based on the generation of volatile products of the reactions between the etched material and the etching agent, the physical techniques rely on the physical

bombardment of the opened areas with particles or molecules. In the same way that the chemical etching's limitation is the low selectivity in the etching rate and direction, the physical etch limitation is the material redeposition of the etched material on the sidewalls or on the already opened areas. All these factors constrain the size and depth that can be etched with techniques that purely use chemical or physical etch.

However, the combination of the two etching principles can become a powerful tool for the etch of high aspect ratio structures. This can be achieved using low pressure plasmas. This plasma is generated due to an electric field created inside the vacuum chamber. The positive side attracts the electrons in the gas atoms, creating ionised gas atoms and free electrons that, on their path to the positive side, collide with the other gas atoms, ionising them and creating new free electrons. Under the steady state conditions, the plasmas used for etching consist of a gas made of electrons, ions, and neutral particles. This mixture of species is what allows the combination of the physical and chemical etch in low-pressure plasma-based etching techniques. The dissociation of the chemical agents into smaller and charged molecules creates a larger amount and more reactive agents that can increase the etching rates compared with those obtained in wet etching techniques. On the other hand, the presence of charged particles and molecules allows a very precise control of the bombarding energy simply by tuning the applied electric field. Finally, due to the low-pressure conditions in the chamber, the mean free path of the species is long enough to ensure that they reach the surface to be etched.

However, this plasma can be created in different ways depending on what generates the electric field. In the following section the creation of this plasma and the parameters involved in it are discussed.

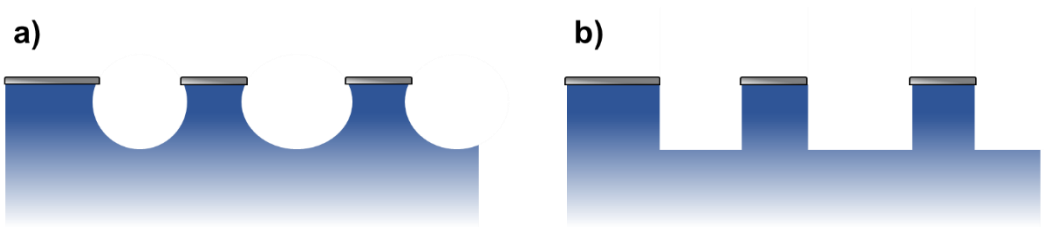

Figure 3.8. Sketches of the different etching profiles obtained with (a) wet etching processes and (b) dry etching processes.

3.4.1. Basics of RIE and ICP

The systems using this approach are called reactive ion etching (RIE) systems [81]. The classification of plasma-based etching systems can be divided in two methods depending on how the plasma is generated which, at the same time, means how the electric field is generated inside the processing chamber. The two systems are depicted in the Figure 3.9.

Capacitive coupled plasmas (CCP) create a plasma due to the application of a radio frequency (RF) voltage between an anode and a cathode situated inside the chamber. In this system the same electric field is used for creating the plasma and for driving-in the species towards the substrate. For this reason, the power used for the etching is limited: the larger the power, the higher the plasma density (more ionised species) and, therefore, less tunability and flexibility of the process.

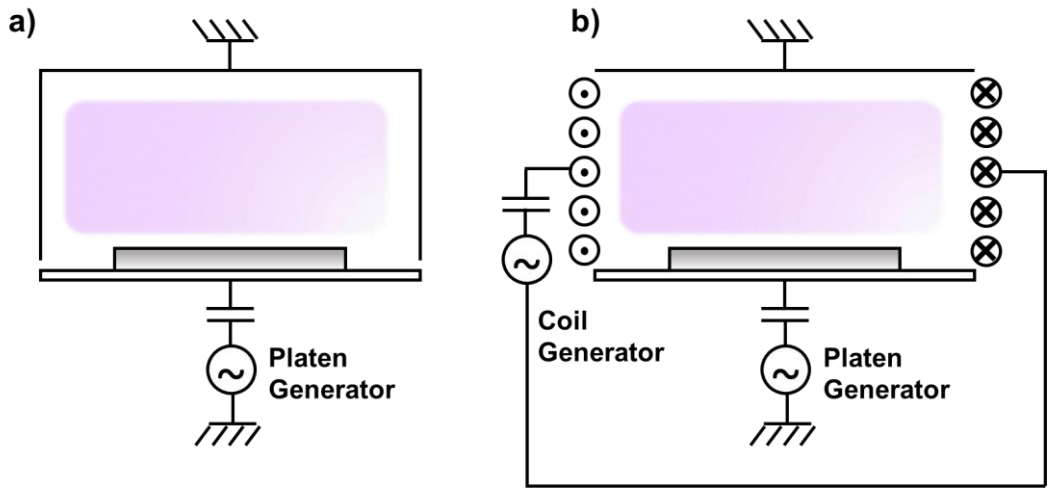

Figure 3.9. Scheme of the (a) CCP chamber and the (b) ICP chamber.

With the inductively coupled plasmas (ICP) the plasma is created by an external coil connected to an RF voltage, creating a time-varying magnetic field inside the chamber that, at the same time, creates a time varying electric field in the centre of the chamber and parallel to the substrate. In these systems there is still an RF power applied between an anode and a cathode that will generate an electric field towards the substrate. The combination of these two independent voltage sources decouples the creation of the plasma from the control of the etching over the substrate. As a general simplification, it

can be said that the coil voltage controls the number of ions in the chamber (density of the plasma) and, therefore, the chemical etch, while the voltage between anode and cathode controls the momentum of the ions and the energy at which they reach the surface, and therefore, the physical etch. The ICP approach was used in this project and will be discussed both in this section and in Chapter 4. In the remainder of this thesis, the voltage applied in the coil will be referred to as coil voltage (V_{Coil}) and the voltage applied between the anode and cathode as platen voltage (V_{Platen}) as well as their corresponding powers (P_{Coil} and P_{Platen}, respectively).

3.4.2. The Bosch and pseudo-Bosch processes

Until now the types of etching techniques have been presented and briefly discussed. The RIE systems using ICP generated plasma were found to be the most suitable for this project. However, selecting the gas species and how they are to be used is not trivial. In fact, depending on the chemistry used, either the chemical or the physical etch will dominate.

The etch of silicon structures has been well studied. Fluorine-based gases ensure a good reactivity of the silicon atoms and volatility of the products (enhancing the chemical etch) but will affect the physical etching. While the products of bromine and chlorine-based chemistries are less volatile, the ions themselves contribute more to the bombardment, which enhances the physical etch. This affects as well how anisotropic the final etch is. At this point an impasse has been reached and different strategies for each combination of chemistries should be considered.

The Bosch process is one of the most widely used strategies for the etching of silicon structures with fluorine-based chemistries. Known by the acronym DREM [82] (deposit, remove, etch multistep), it can yield highly anisotropic etch with high aspect ratio etchings. Other processes allow similar results using other chemistries or approaches such as the cryogenic etch.

The Bosch process is a cyclic process that combines etching and passivation steps [82], [83]. The passivation creates a conformal thin protective layer covering the substrate's

surface to prevent the side walls from being etched during etch step. These two actions are carried out by two different gases: the passivating gas used in the Bosch process is the octafluorocyclobutane (C_4F_8) and the etching gas is the sulphur hexafluoride (SF_6). The basic Bosch process can then be divided into three main steps: deposition, break, and etch steps (Figure 3.10) [83].

The deposition step involves dissociation of the C_4F_8 into the form of $(CF_2)_x$ in the plasma. During this step the coil power is on and the C_4F_8 is injected into the chamber in order to create the plasma to promote the dissociation. Some of these ions will deposit onto the surface creating a polymer chain of CF_2 that will protect the entire surface (including the horizontal areas).

The break step follows the polymer deposition. During this step the SF_6 gas is introduced in the chamber and the platen power is turned on at the same time as the coil. Thanks to the coil power the SF_6 will dissociate into ions and a high platen power will give them enough energy to vertically bombard the substrate. A highly directional bombardment ensures the polymer layer on the horizontal surfaces will be removed, while the side walls will still be protected.

The last step is the etch step in which the SF_6 is again injected into the chamber with the coil power on, but the platen power is reduced. As mentioned before, the fluorine-based etch enhances the chemical etch in silicon while the physical etch is minimal. For this reason, the platen power should be on to direct the ions towards the substrate without needing to be as large as during the break step.

These steps are repeated periodically in order to etch the structures. The etched depth will depend on the number of cycles carried out. The result of the Bosch process will depend on the volume of gases introduced into the chamber, the coil and platen powers, as well as the duration of each step. As a result, optimising the process can be challenging and time-consuming.

The optimisation will also depend on other characteristics related to the desired final result, such as the aspect ratio of the structures to etch, or the etch load. The aspect ratio is the ratio between the etched depth and the width of the etched structures. Depending on how deep and wide the opened material is, the diffusion of the gases into

the structures can limit the etch depth, shape and rate. On the other hand, the etch load is used to determine the open area to be etched. This parameter will affect the etching rates since the number of species for the etching will be distributed differently depending on how much of the surface will be etched.

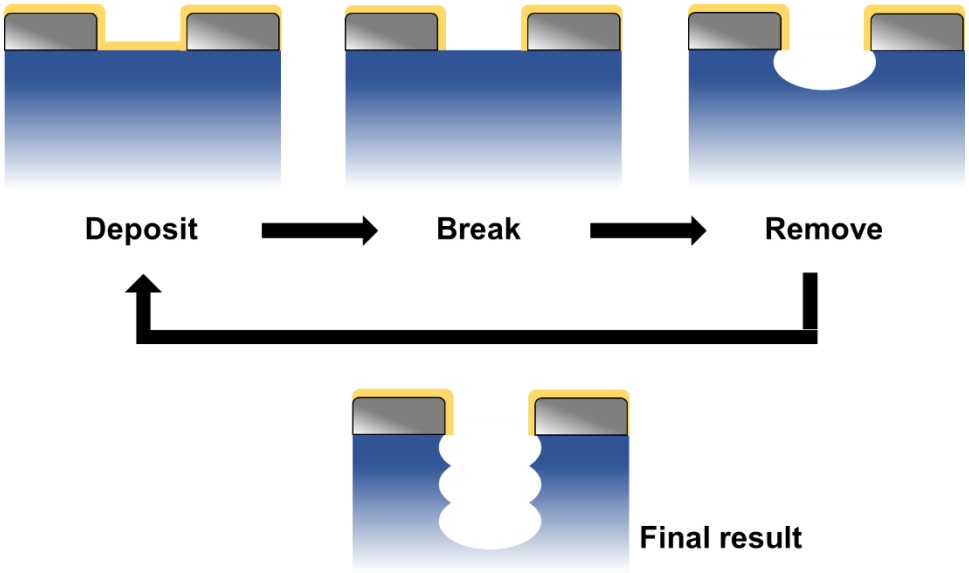

Figure 3.10. Sketch of the Bosch process. (Top) The three main steps are here described: deposit (left), break (middle), and etch (right). (Bottom) The final result sketch after the repetition of these three.

One of the drawbacks of the Bosch process is the difficulty to obtain smooth side wall surfaces due to scalloping, a product of the cyclic process. This can be solved by instead using a continuous process [84]. The continuous Bosch process, known also as the pseudo-Bosch process, uses the same chemistries as the cyclic Bosch process but instead of applying the etching and passivation as separate steps, both occur simultaneously inside the chamber.

During the pseudo-Bosch process both the SF_6 and C_4F_8 are continuously introduced inside the chamber and both the coil and platen powers are on during all the process (Figure 3.11 b). The balance between the passivation deposit and etch on the horizontal surfaces is important. Since both occur simultaneously, the breaking of the polymer should be faster than the redeposition of the polymer. This is possible because this

process relies not only on the physical milling of the polymer by the ionised SF_6 but also the recombination of the CF_2 polymer molecules into CF_4, which is a volatile product. This process is slower than the traditional Bosch process but, for our application, ensures a better control over the sidewalls profile and, especially, on the roughness, which is very important for this project.

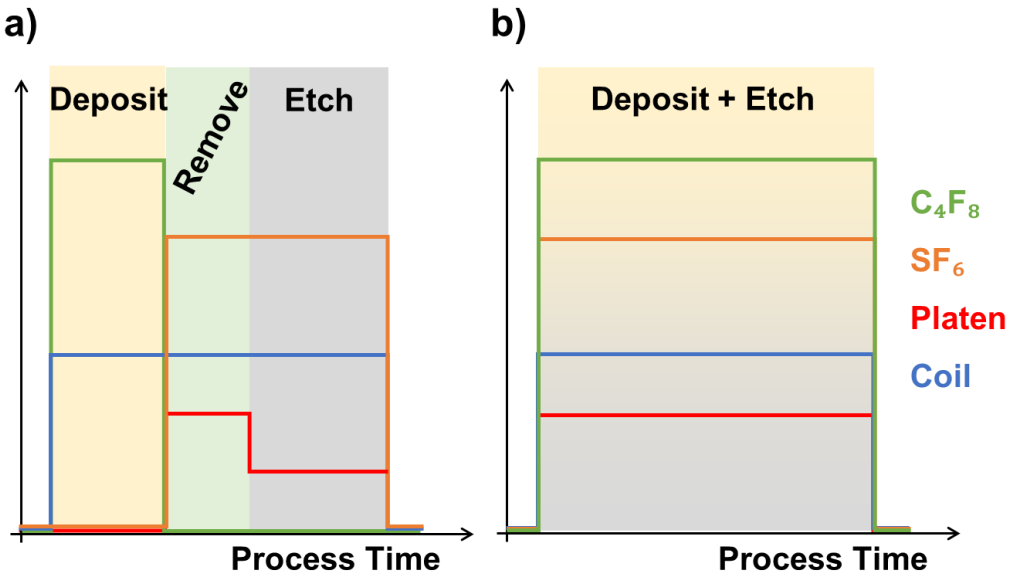

Figure 3.11. Schematic of the distribution of the gas flows and powers during the etch process. Representation of the variation of the parameters depending on time for (a) a (cyclic) Bosch process and (b) a pseudo-Bosch process.

3.5. Characterisation techniques

The final set of techniques used in this thesis are those used for characterising the samples. The techniques and their classifications used during this thesis can be classified according to whether they are used for imaging, layer characterisation or chemical information. The techniques used to carry out these measurements have been the scanning electron microscopy (SEM), ellipsometry and X-ray photoelectron spectrometry (XPS), respectively.

3.5.1. Scanning electron microscopy

SEM is one of the most widely used techniques for both topographical characterisation and chemical analysis at the nanoscale. It is based on the exposure of the analysed sample to an electron beam that interacts with the material on the sample[85]. This interaction gives rise to the emission of radiation and electrons whose generation is typically depicted by the teardrop diagram (Figure 3.4) [85]. The signals obtained from the substrate and the information they provide depend on the physics of their origin. The secondary electrons (SE) and backscattered electrons (BSE) are primarily used in this thesis, mainly for imaging.

The SE are generated close to the surface and bring topographic information about the sample. They are often generated due to the inelastic collision between the incoming electrons (primary electrons) with the outer electrons of the atoms which are loosely bonded to the atom (Figure 3.12 a). The SE can also be generated from a collision between backscattered electrons with the outer electrons of the atoms. Because of the low binding energy of these electrons when released they have a low kinetic energy and can travel a very short distance through the sample without colliding again (mean free path). Because of their short mean free path, the incoming electrons to the detector come mostly from the surface of the substrate. This fact implies that the number of detected electrons coming from the different parts of the sample depends on the relative orientation of the primary beam, the sample surface, and detector giving rise to the edge effect. The edge effect is a consequence of the detector receiving more electrons from the edges of the structures on the substrate than from the vertical or horizontal surfaces. Therefore, the images created using SE show the edges of the structures as brighter (because they provide more electrons) than other areas of the substrate (because they provide less electrons), giving topological information about the sample.

The BSE on the other hand are electrons coming from the primary beam but that have been elastically scattered because of their interaction with the atoms in the sample (Figure 3.12 b) [85]. Due to the elastic interaction with the atoms, these electrons are redirected back to the surface with almost the same energy as the primary electrons. Their high energy provides information from deeper layers of the substrate since their mean free path is larger. The number of these elastic events increases when the atomic

number is larger since the electromagnetic field of the nucleus is stronger. Therefore, those materials whose atoms have a large atomic number will provide more BSE that appears brighter than other materials whose atomic number is smaller. For this reason, the BSE are used to obtain information about the atomical distribution over the sample.

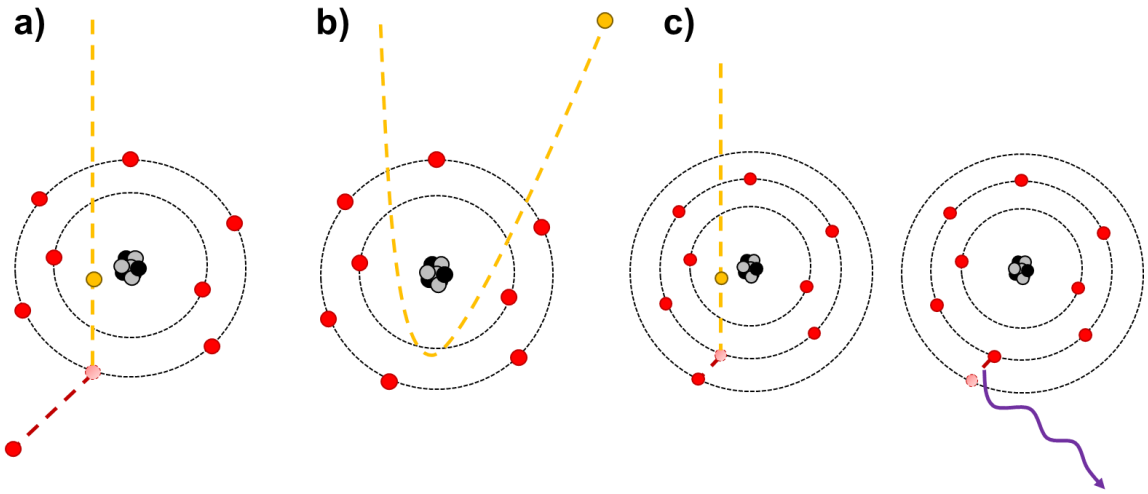

Figure 3.12. Representation of the interactions of the primary electrons with the substrate atoms: (a) the generation of SE when releasing an atom from the outer orbitals; (b) BSE electrons due to the atom nucleus electromagnetic potential; (c) creation of a photon due to the relaxation of an excited electron.

Aside from SE and BSE, the interaction of the electrons with the substrate generates other signals, such as X-rays. These photons are created due to the excitation of one electron of one atom to a higher energetic orbital. The relaxation of this electron going back to its original lower energetic orbital releases a photon whose energy corresponds to the difference between the two orbitals (Figure 3.12 c). The energetic transitions of the excited electrons are atom-dependent and are unique for each atom. These X-rays are therefore used for the chemical analysis of substrates: energy-dispersive spectrometry (EDS). Even though the signal emitted by these photons in an SEM system is not as accurate as the one given by other techniques, the EDS analysis offers a first approximation of the materials present on a sample.

In this thesis the SEM has been mainly used to characterise the samples nanofabricated at the different fabrication stages. These images have enabled the analysis of the shape

of the hard masks after the lithographic process to achieve the desired pillar size. In addition, it has been used to observe the pillars' characteristics after the dry etch. Since, in this thesis, a focus has been to obtain high-aspect ratio cylindrical pillars, the SEM has been a useful tool to analyse and obtain the desired results after the fabrication.

3.5.2. Thin film characterisation: Ellipsometry

Another group of techniques available in the cleanroom are those used for the determination of the film thickness and their optical constants. These techniques use the light interaction with the thin films either by reflection or ellipsometry.

Light propagation through different media is defined by the complex refractive index (ñ).

$$\tilde{n} = n + ik \quad \begin{cases} n = \dfrac{v}{c} \\ k = \dfrac{4\pi\alpha}{\lambda} \end{cases} \tag{3.9}$$

The real part of the refractive index (n) is defined as the ratio between the light's velocity in the medium (v) and in the vacuum (c), and the complex part (k) is the extinction coefficient of light in the medium, which depends on the material absorption (α) and the light's wavelength (λ). Techniques such as reflection and ellipsometry use these parameters to determine thin film parameters, especially their thickness.

In the case of ellipsometry [77], light is reflected on the surface and changes in the polarisation are analysed. Like the reflection techniques, the measurement depends on the optical properties and the thickness of the different layers forming the substrate. However, ellipsometry uses linearly polarised light and evaluates changes in polarisation to determine the material's thicknesses and other material properties that are related to the optical properties of the material, such as the refractive index or the surface roughness. In this thesis ellipsometry has been used mainly to determine the thickness of the buried oxide (BOX) and device layers of SOI wafers during the various fabrication steps.

In ellipsometry, light can be considered as an electromagnetic wave that travels through the space. It is important to notice that the field oscillates orthogonally to the propagation direction. Depending on the correlation between the amplitude and phase of these electromagnetic waves, light can be defined as polarised or not. Non-polarised light is a combination of waves whose field's amplitude, direction (on the plane perpendicular to the propagation), and phase are uncorrelated, whereas polarised light is a combination of orthogonal waves whose relative amplitude and phase are correlated. If, instead, the amplitudes differ and are out-of-phase, this is referred to as elliptically polarised, while circularly polarised light occurs in the specific case where both waves have the same amplitude and a phase of exactly 90°.

Ellipsometry uses linearly polarised light as incident light and measures the difference in phase and amplitude of the elliptically polarised light after interacting with the substrate (Figure 3.13) [86]. Linearly polarised light can be explained using the Maxwell equations boundary conditions. These conditions define the relationship between the reflection of electromagnetic waves and the oscillation direction of the incident wave. In the case of linearly polarised light, waves oscillate either perpendicular to the surface (p-plane) or parallel to the surface (s-plane). These p- and s-waves are originally in-phase and have a known amplitude and because they interact differently with the substrate, the outcoming light becomes elliptically polarised. The change in amplitude and phase (ρ) difference is written as [86]:

$$\rho = \tan(\Psi)\, e^{i\Delta} \tag{3.10}$$

where Ψ is the amplitude ratio between the orthogonal electromagnetic waves and Δ is the phase difference between the waves. This change can be explained due to the interaction of these waves with the material on the substrate. The outgoing light from the substrate comes not only from the surface reflection but also from the light reflected at the different material interfaces in the substrate (Figure 3.13).

If the film is thick enough the light is reflected multiple times in the different layers creating an interference pattern where the reflected wave will sometimes be in phase or not depending on the wavelength. The thickness of the layers can be calculated from the

angle of incidence of the polarised light, the different refractive indices, and the distance between peaks of the interference pattern.

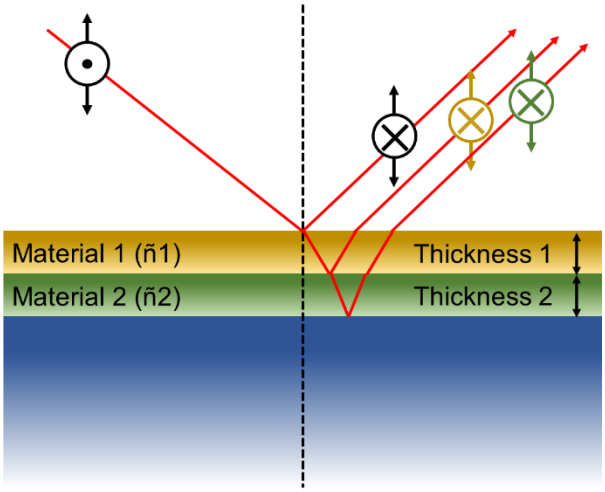

Figure 3.13. Schematic of how light interacts with the layers during ellipsometry measurements.

3.5.3. Atomic and chemical content analysis: X-ray Photoelectron Spectroscopy (XPS)

The last group of characterisation techniques, such as X-ray Photoelectron spectroscopy (XPS), use X-rays interaction with the substrate to analyse the atomic and chemical content of a sample. The interaction of high energy electrons and light with the substrate expel electrons which, respectively, provide information about the elemental composition and crystallography of the sample.

XPS has been used in this study to perform a composition analysis of the fabricated structures. The technique uses the electrons emitted due to the photoelectric effect when the sample is irradiated with X-ray photons. The kinetic energy of these electrons ($E_{Kinetic}$) will depend on the incoming X-ray photons energy (E_{Photon}) and the binding energy of the electron released ($E_{Binding}$):

$$E_{kinetic} = E_{photon} - E_{binding.} \tag{3.11}$$

The binding energy depends not only on the type of atoms present in the sample but also on other factors, such as the oxidation state or hybridisation due to bonds between different atoms. The relation expressed in equation (3.11) is valid while the electrons released do not lose part or their energy during the trip from the substrate to the surface and from the surface to the spectrometer. The minimum distance that an electron can travel without losing energy is the mean free path, which increases with increasing vacuum level. This limitation makes the XPS technique a surface technique, since the mean free path of these electrons is very short and, therefore, electrons released from atoms deeper in the sample, if they reach the spectrometer, do so with much lower kinetic energy.

3.6. Proposal of fabrication strategy

The fabrication possibilities in a cleanroom are wide and diverse. Depending on the application, resolution, and materials needed, the fabrication approach can vary drastically.

The fabrication goals of this thesis are:

- To correctly define a mask containing spots with radius down to 40 nm suitable for the etching step of the process.
- To etch nanopillars with high aspect ratio and under conditions that allow etching to different depths, ranging from hundreds of nanometres to few micrometres.
- To ensure repeatable results with different silicon-based substrates, so that systems that can assure the correct optical properties required can be fabricated.

To satisfy these three points, EB lithography was chosen as it resolves the feature sizes needed and provides a hard mask material for the dry etching. In addition, the use of SOI wafers has been needed to assure the correct optical confinement of the light in the upper silicon layer, the so-called device layer. Within these outlines the fabrication process has been adapted to overcome the challenges faced during this thesis.

The general strategy followed during this thesis reads as:

1. Pre-lithography process: deposition of an electron-sensitive and positive-tone resist for the EB exposure. In case of using substrates with insulating layers, an aluminium layer was deposited by thermal evaporation to ensure the proper electron discharge during the exposure.

2. EB exposure: exposition at a low current to resolve the required feature sizes, modulating the doses to account for the proximity effect correction.

3. Post-lithography process: removal of the thermal aluminium layer, if used, and development of the exposed resist areas.

4. Hard mask creation: deposition of an electron beam-evaporated aluminium layer followed by a lift-off process to transfer the hard mask onto the substrate prior to the dry etch.

5. Nanopillar etch: dry etch process to etch down the non-masked areas using a pseudo-Bosch process to ensure the correct aspect ratio etching of the structures.

6. Optional etching post-process: post processing of the substrates to make them suitable for both optical purposes and biocompatible for the tissue endurance on the pillars.

These six steps summarise the fabrication process, whose optimisations are detailed in Chapter 5. There, an in-depth explanation of the optimised conditions and steps are given. The optimisation of the dry etch step is also discussed there as it has been shown to be one of the most crucial steps for the final performance of the systems fabricated.

CHAPTER 4.
SIMULATION RESULTS

4.1. Two-dimensional photonic crystal

As already stated in Chapter 2, the simulation of photonic crystals based on pillars is a rather complex problem. The first strategy used in this thesis to evaluate the different parameters of the photonic crystal has been to reduce the simulations to a two-dimensional problem. In this manner, the number of parameters to be discussed is reduced to those affecting the two simulated dimensions. These parameters are related to the geometry of the photonic crystal and the two dielectric materials used.

The geometry of the system is defined by the radii of the pillars and the distance between the pillars' centres (from now and onwards, referred as pitch). These two parameters define the proportion of dielectric materials in the photonic crystal, which has a big impact on the band gap opening and position (Chapter 2 section 2.1.3). In addition, it determines the effective refractive index of the system which, later, when discussing the three-dimensional problem, will be key for the vertical light confinement.

Regarding the materials used, silicon has been selected as high refractive index material for the body of the pillars. As background material, either air or water have been used. The choice of these background materials is not arbitrary. Air is used for simplicity of the system, since it is expected that the first tests will be done in this environment and because it gives a large refractive index contrast. On the other hand, the water

background is considered due to the biological application of the project and the possibility of having aqueous liquid between the pillars.

The two-dimensional analysis has been carried out using two different strategies. The first approach consists in the simulation and evaluation of the band diagram of the photonic crystal. These simulations have been done using COMSOL Multiphysics® software and its specific modules devoted to the obtention of the eigenmodes and eigenfrequencies of photonic structures. The second approach consists in the simulation of the transmission and reflection spectra of the system using the FDTD method. To do these simulations, open-license software and self-made programs have been used.

4.1.1. Band diagram simulation

FEM method calculates the electromagnetic fields required to obtain both the resonant frequencies in the system (eigenfrequencies) and the normalized electromagnetic fields (eigenmodes) at these frequencies. COMSOL Multiphysics v5.2® has been used to simulate the band diagrams with the FEM method [87]. Specifically, this software offers an Electromagnetic Wave Module Eigenvalue solver module to carry out these simulations.

To start the simulation several parameters, must be set. Some of these parameters are related to the geometry or the materials used. In Figure 4.1 the representation of the unit cell done in COMSOL Multiphysics® is shown. The radius of the pillar and the pitch can be defined as parameters of the simulation to easily change them. The geometry is created by a circle to represent the pillar and a polygon representing the unit cell. These two structures will define as well the geometry domains. Each of these domains will take a material. In the Figure 4.1 these domains and the different materials are represented in grey and blue for the pillar and the background, respectively.

Once the geometry and the materials are defined, the electromagnetic simulation conditions must be set. Important parameters are the electromagnetic fields' polarisation and the boundary conditions. For a two-dimensional simulation the polarisation is defined depending on whether the electric field it is in- or out-of-plane. As stated in Chapter 2

section 2.1.4 polarised light can be described as for TE (Transversal Electric) and TM (Transversal Magnetic) depending on if the electric field orientation within the propagation plane or if it is perpendicular to it (Figure 2.1 b). In the simulations the definition of the electric field as in- or out-of-plane corresponds to TE and TM polarisations, respectively. In the simulations done in this work, TM polarised light has been used to analyse the performance of the different photonic structures.

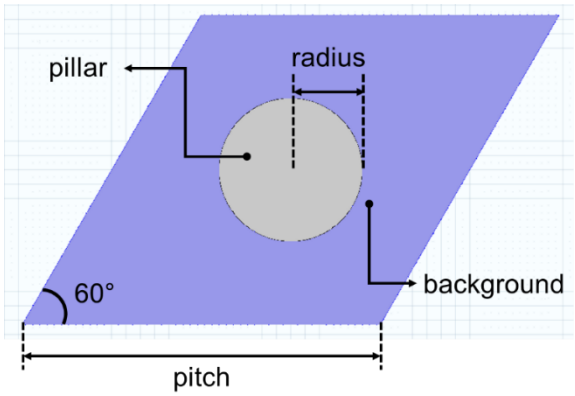

Figure 4.1. Image of the unit cell used for the simulation of band diagrams extracted from one of the COMSOL Multiphysics® programs created. In the figure the different geometry parameters are depicted as well as the different domains considered for the two-dimensional simulations.

To carry out this type of simulations, boundary conditions must be defined too. The boundary conditions are set at the edges of the primary cell. To create band diagrams, an infinite photonic crystal needs to be considered. For these reason periodic Bloch conditions (Chapter 2 section 2.1.3) are imposed at the edges. The boundaries in the simulated structure are distributed as shown in Figure 4.2 a. As it can be seen the different periodic conditions are set at the parallel boundaries of the cell. This construction will emulate an infinite photonic crystal created by the infinite repetition of the unitary cell in all the periodic directions.

As explained in Chapter 2 section 2.3.1, the domains of the simulation must be divided in smaller elements by a mesh. It is at the nodes of this mesh and at the boundaries of the elements where the Maxwell equations are solved locally. The software provides different options for creating this mesh. In this section a free triangular mesh has been used. This type of mesh adapts easily to most of the possible situations and to the

circular structure of the pillar, which can be truncated into a set of triangular shapes. Moreover, the boundary of the pillars and the background have a larger density of triangular elements since in these regions the fields are expected to behave differently from the bulk background. In Figure 4.2 b the mesh created for one of the structures can be seen.

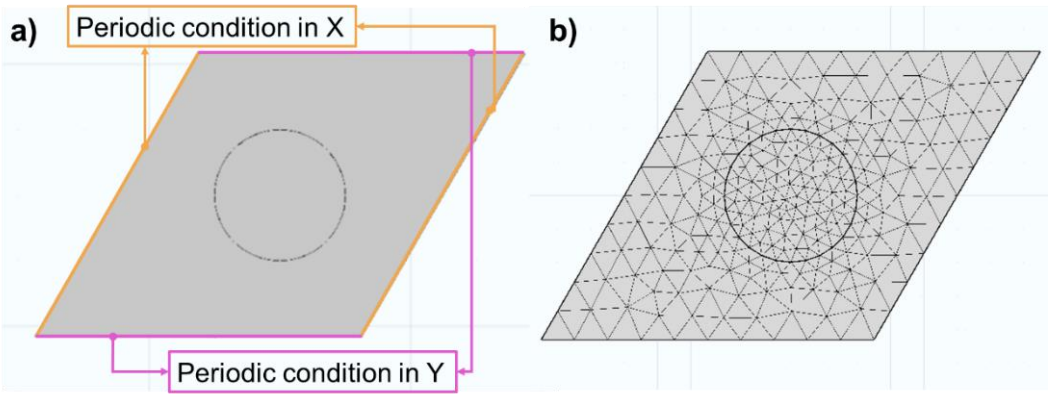

Figure 4.2. Image of the simulated unitary cell as shown in the COMSOL Multiphysics® software. (a) Delimitation of the periodic Bloch conditions for the two-dimensional simulations; (b) Example of the free triangular mesh created for the finite element division of the cell.

Once the simulation is set up, the solver calculates the eigenvalues and frequencies at the different $\boldsymbol{k}$ values within the first Brillouin zone. To get the full range of direction in the reciprocal space, an iteration of the $\boldsymbol{k}$ values for the reciprocal x ($\boldsymbol{k}_x$) and reciprocal y ($\boldsymbol{k}_y$) directions is done. To do so, the Bloch boundary conditions are iterated going over the three main reciprocal points in the hexagonal cell, as shown in Figure 2.5 a. At the different $\boldsymbol{k}$ values the eigenfrequencies are calculated.

$$\Gamma \rightarrow \mathrm{M}\ \ (if\ m \leq 1) \begin{cases} \boldsymbol{k}_x = \dfrac{\pi}{a} m \\ \boldsymbol{k}_y = \dfrac{-\pi}{\sqrt{3}a} m \end{cases}$$

$$\mathrm{M} \rightarrow \mathrm{K}\ \ (if\ 1 < m \leq 2) \begin{cases} \boldsymbol{k}_x = \dfrac{\pi}{3a} (m+2) \\ \boldsymbol{k}_y = \dfrac{-\pi}{\sqrt{3}a} (m-2) \end{cases}$$

$$\mathrm{K} \rightarrow \Gamma \ \ (if\ 2 < m \leq 3) \begin{cases} \boldsymbol{k}_x = \dfrac{4\pi}{3a}(3-m) \\ \boldsymbol{k}_y = 0 \end{cases}$$

(4.1)

In equation (4.1) the value of a represents the fundamental length equal to the pitch in the hexagonal structure discussed in this project, and the variable m takes values between 0 and 3. Equation (4.1) is constructed in the way that when m takes the value 0 or 3 the $\boldsymbol{k}$ vector corresponds the point Γ; when it takes the value 1 the $\boldsymbol{k}$ vector corresponds the point M; and when it takes the value 1 the $\boldsymbol{k}$ vector corresponds the point K.

4.1.2. Band diagram discussion

The program just described has been used to simulate the band diagram of different structures, repeating the calculations for the different values of the pillar's radius and the cell pitch. A representation of a band diagram is shown in Figure 4.3. Here, the evolution of the different band's frequencies as a function of the $\boldsymbol{k}$ direction in the reciprocal space can be observed.

This representation gives a good overview of the behaviour of the bands for a specific photonic crystal structure. However, it is difficult to make a systematic comparison and analysis of multiple photonic crystal structures with only the band diagram representation. To do such type of analysis, robustness maps are used.

A robustness map represents the evolution of the normalised frequency gap position and width depending on the radius-to-pitch ratio. They are plotted considering the maximum value of the fundamental band (or dielectric band) together with the minimum value of the first band (or air band). As explained in Chapter 2 in sections 2.1.3 and 2.1.4, the band diagram and band gap opening depend on the volumetric presence of the two dielectric materials. This proportion is determined by the ratio between the radii of the pillars and the pitch value, which is known as radius-to-pitch ratio.

Thanks to the use of the normalised frequency (units of $\omega a/2\pi c$) and the radius-to-pitch, the results that the robustness maps show can be easily extrapolated to any photonic crystal that has the same proportions. Therefore, robustness maps provide good information that can be easily adapted in case of need of changes in both the pillars radii and the pitch, simultaneously or independently.

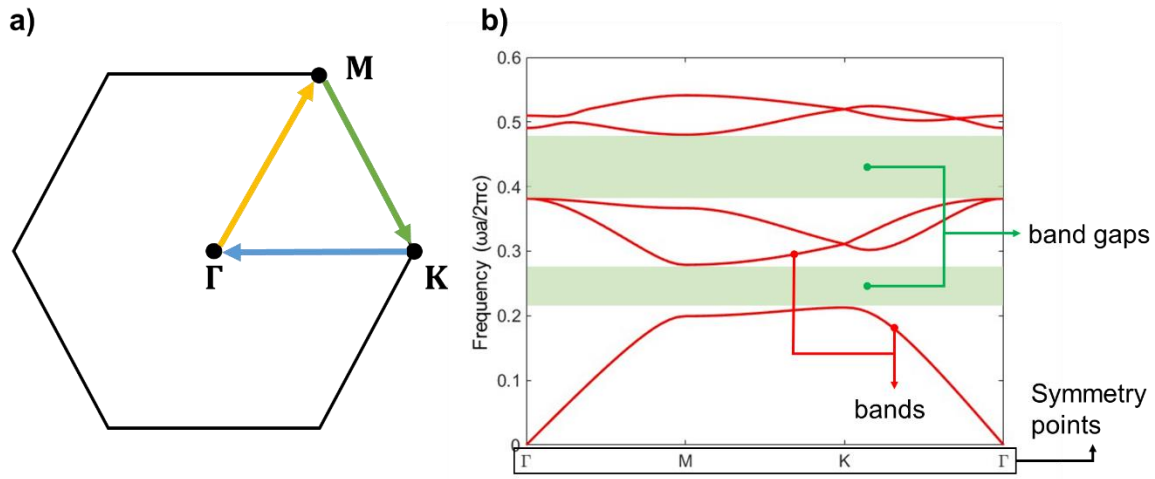

*Figure 4.3. (a) Scheme of the hexagonal structure of the reciprocal space and the three main points in the reciprocal space. With coloured arrows the m iteration path in the software is shown. (b) Band diagram corresponding to a photonic crystal structure with 100 nm radius pillars and 300 nm pitch for TM polarised light in air background. In red the different simulated bands are marked for the different **k** directions. In light green the bandgaps between the bands are shown too.*

In this thesis, robustness maps, both considering air and water backgrounds, have been analysed. These robustness maps have been obtained considering that the band gaps opened for transversal magnetic polarised light. The resulting maps have been created using the results of simulations considering a photonic crystal whose pillar's radius has been kept constant at 100 nm and whose pitch has been varied from 300 nm to 650 nm. In Figure 4.4 the resulting robustness maps both for air (Figure 4.4 a) and water backgrounds (Figure 4.4 b) are shown.

Even though, the robustness maps can represent more than one band gap evolution in Figure 4.4, for simplicity, only the main band gap has been considered. In this figure it can already be appreciated the importance of the background material.

As can be seen in (Figure 4.4 a and b), broader band gaps are obtained for air background in comparison to water background. This is a result of the larger contrast between the pillars and the background's refractive indexes. In addition, it can be observed that the radius-to-pitch ratio has a large impact on the variation of the band gap position and its width. The evolution of the band gap frequency position as a function of the radius-to-pitch ratio must be pointed out as well. For those radius-to-pitch combinations where the low refractive index material dominates (i.e., small radius of the pillars or larger pitch) the band gap is pushed towards higher frequencies, while in the reverse situation, when the high dielectric material is increased (i.e., larger pillar's radius or smaller pitch) then the band gap frequencies are pushed down. The extreme cases of a very small or a very large radius-to-pitch ratio, the tendency of the band gaps will be to close, with the disappearance of the band gap.

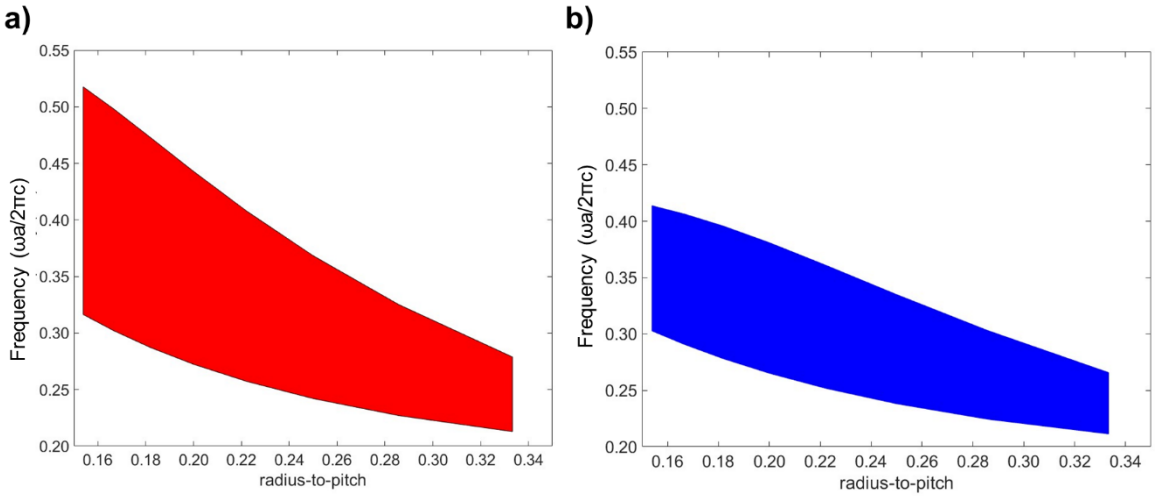

Figure 4.4. Robustness maps of the simulations carried out with a constant pillar radius of 100 nm and a pitch radius changing from 300 nm to 650 nm. The pillar material is silicon. These robustness maps correspond to (a) air and (b) water as background.

Similar discussions can be done when considering an aqueous background (Figure 4.4 b). The scale of the effects just discussed in the previous paragraph, such as the band width opening, is smaller. This is caused because of the smaller contrast between the pillars and the background refractive indexes. As explained in Chapter 2 section 2.1.4, the larger the difference between the two refractive indexes the more robust the band gaps that appear are. Consequently, it is expected that the band gaps opened when

considering an aqueous background are lower and narrower than those obtained with an air background. In addition, the frequencies of the band gaps for the liquid background are lower than the ones observed in air background. An interesting readout of the results for water background is the fact that the variation of the band gap as a function of the radius-to-pitch is less abrupt than the one observed in air. This could have a positive effect since small variations of the geometry of the system due to, for instance, fabrication requirements or issues, will not have an impact as large as it could have if an air background was considered. In Chapter 5 it will be seen that a tolerance should be added to the fabrication parameters. This means that the optimal dimensions will not be achieved during the fabrication and having a less abrupt variation of the radius-to-pitch is, in fact, a positive factor.

From the discussions just made the robustness maps provide a good two-dimensional overview of the evolution of the bandgaps, but it can be difficult, from them, to define what a “good” band gap is. The quality of a bandgap can be defined by the figure of merit of the gap-to-midgap ratio. This figure of merit, which is given in percentage, is the result of the ratio between the width of the band gap and the frequency of the centre of the band gap.

Using the results obtained from the simulations carried out with the program explained in section 4.1.1, the gap-to-midgap ratio dependence on the radius-to-pitch ratio can be evaluated. The results of the analysis are shown in Figure 4.5. As for the other figure of merit, the results are shown independently for each background that has been used for the simulations. Air or water background representations are shown in Figure 4.5 a and b, respectively.

This representation has a parabolic-like shape, being its peak the highest quality band gap and can be considered the optimal dielectric proportion for the highest quality photonic crystal. Again, due to the scalability behaviour of photonic crystals (Chapter 2 section 2.1.3) any configuration of radii and pitch that gives this ratio will be optimal. Consequently, the edges of this parabolic curve represent lower quality band gaps. This behaviour agrees with the discussion previously done where the extreme situations of either a very low or a very high radius-to-pitch ratio lead that the band gap will, eventually, disappear.

It must be noted that the information obtained from Figure 4.4 and Figure 4.5 are complementary. While the robustness map provides a visualisation of the gap evolution, the gap-to-midgap representation provides numerical information about this evolution. Therefore, and as expected, the resulting tendencies observed in the gap-to-midgap representation are in line with the ones discussed for the robustness maps. The parabola created by the evolution of the bandgap in air is sharper than the one in aqueous background. This agrees, again, with the consideration that a larger contrast between refractive indexes gives larger sensitivity of the band diagram to geometrical changes. The wider opening of the band gaps observed in Figure 4.4 a is reflected on Figure 4.5 a by a larger gap-to-midgap value than that in Figure 4.5 b. These optimal values are summarized in Table 4.1.

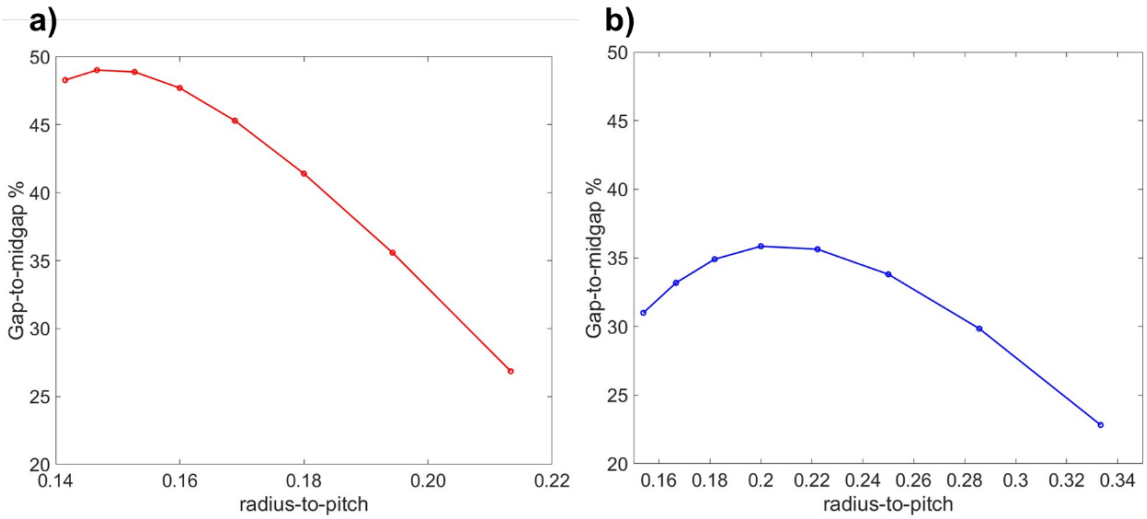

Figure 4.5. Evolution of the gap-to-midgap figure of merit as a function of the radius-to-pitch ratio of the simulated structures. The results obtained when considering an air or water background are shown in figures a) and b), respectively.

From the results summarized in Table 4.1 the optimal radius-to-pitch ratio for the simulated photonic crystals are 0.17 and 0.2 for air and water, respectively. This means that any radius and pitch combination giving these proportions will be optimal. Since the simulations analysed were carried out considering a fixed radius of 100 nm, the corresponding pitch for air and water to obtain the optimal radius-to-pitch ratio are 600 nm and 500 nm, respectively. To simplify the rest of the discussion, however, for both air and water, a pitch of 500 nm will be considered as optimal. This decision can be made

since the gap-to-midgap ratio for a radius of 100 nm and a pitch of 500 nm is still very high (47.7%). In this way the rest of the discussion in this thesis can be done considering the same fixed radius and pitch values for the two types of backgrounds. This proportion will be used as basic structure for the fabrication discussion in Chapter 5.

The band diagrams of transversal magnetic modes for structures of 100 nm radius and 500 nm pitch are shown in Figure 4.6 a and b for air and water backgrounds, respectively.

Background material	Optimal radius to pitch	Gap-to-midgap ratio (%)	Radius / pitch (nm / nm)
Air	0.17	49.02	100 / 600
Water	0.20	35.85	100 / 500

Table 4.1. Summary of the optimal results considering the gap-to-midgap figure of merit in air and water backgrounds. In addition to the normalised radius-to-pitch value the actual configuration simulated is given as well.

In Figure 4.6 it can be observed how a band appears between the fundamental and the first band for all directions and for both air and water backgrounds. As already analysed, for an air background, the band gap is wider and appears at higher frequencies than for the water one. The parameters of both these bandgaps are summarised in Table 4.2.

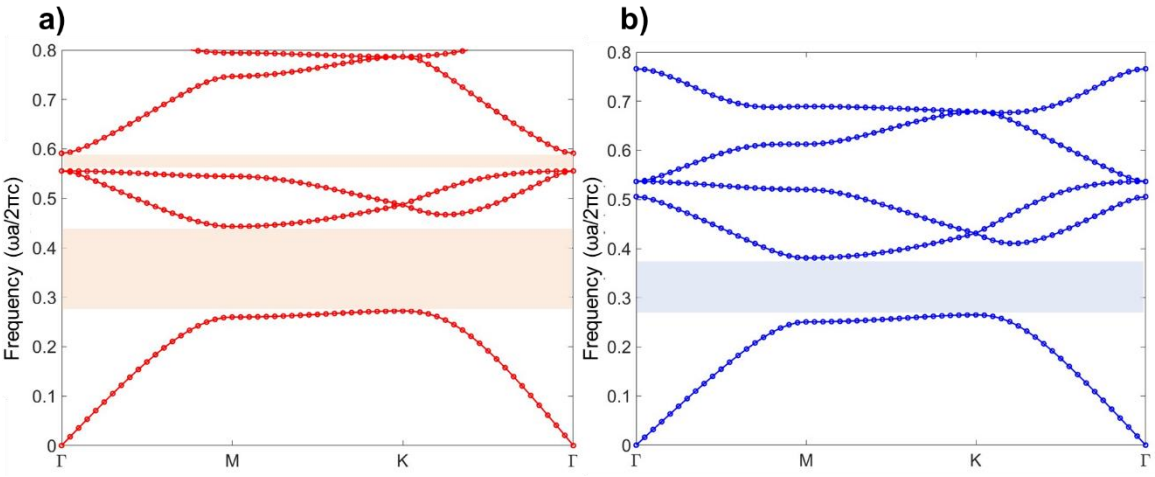

Figure 4.6. Band diagrams of a photonic structure of 100 nm radius and 500 nm pitch considering TM polarised light. In (a) an air background is considered while in (b) an aqueous background is used. The light red (a) and blue (b) bands correspond to the opened bandgaps.

In Table 4.2 both the normalised frequency and the real wavelength are added. Until now the normalised gap frequencies have been useful for the discussion. However, to evaluate experimental limitations, such as the transmission windows of the different materials, the real wavelength positions of these bandgaps must be considered. For the scope of this project, as described in the introduction (Chapter 1), it is expected that the light sources used will be within the near infrared (NIR) light spectrum. The values shown in Table 4.2 are within the NIR frequency range. Consequently, this shows that the structures considered would be useful for the project.

Background material	Gap-to-midgap ratio (%)	PBG min (ωa/2πc)	PBG max (ωa/2πc)	PBG min (μm)	PBG max (μm)
Air	47.70	0.272	0.443	1.130	1.841
Water	35.85	0.265	0.381	1.310	1.883

Table 4.2. Summary of the photonic band gap (PBG) minimum and maximum positions obtained when considering a photonic crystal of 100 nm radius and 500 nm pitch in air and water background. Both the normalised positions as well as their equivalent wavelengths for the considered structures are shown.

4.1.3. Transmission-Reflection spectra simulation

The second type of simulations employed in this thesis have been the ones based on the FDTD (Finite Difference Time Domain) method (Chapter 2 section 2.3.2). These simulations have been used to obtain the transmission spectra of a finite number of cells of the photonic crystal. This contrasts with the program described in section 4.1.1 where an infinite periodic structure is used.

The information provided by the transmission spectra is expected to be closer to the measurement of the experimental data. In this case, the band gaps will be observed as wavelength regions where the transmission is drastically reduced to almost zero values.

The construction of the FDTD simulations is completely different from the one used for the band gap simulations. The transmission simulations have been done using Python™ programming, employing standard Python™ modules and the MEEP module, developed by the Massachusetts Institute of Technology (MIT) [49], [52]. The MEEP module (standing for MIT Electromagnetic Equation Propagation module) is an open access module that uses the FDTD method to solve computational electromagnetic problems.

The choice of MEEP over other commercial software has been done due to its versatility and easy access compared to the others. However, one of the drawbacks of using this module is that it does not have a user-friendly interface, as commercial software programs do. To solve this problem, the simulations carried out have been done using two different self-developed programs: one creating the photonic crystal geometry of the system (now onwards geometry program) and another one using this geometry to carry out the simulations (now onwards analysis program).

The geometry program creates a figure like the one shown in Figure 4.8. Firstly, the simulation region is created given its dimensions and the refractive index of both the medium (silicon) and the background (air or water in this thesis). This has been done with one of the MEEP built-in functions. Then a grid of circles representing the pillars, using another MEEP function, is done. This grid is created by assigning circles to the positions of a hexagonal array with a defined radius and refractive index (silicon). This

hexagonal array has been done with Python™ basic functions centred in the centre of the simulation region and based on the size of the simulated Photonic crystal.

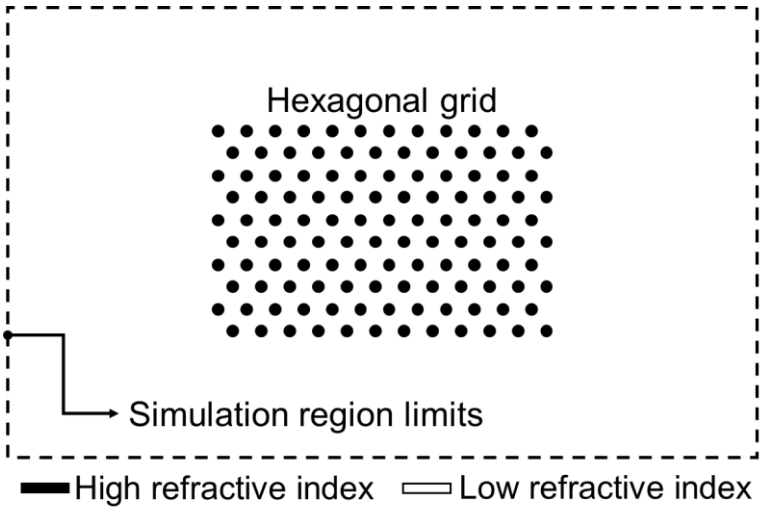

Figure 4.7. Scheme of the constructed geometry when using MEEP. In dashed lines the limits of the simulation region. Inside the simulation region, the representation in two dimensions of the photonic crystal using black circles. The black colour representing the areas of high refractive index while the white background represents the low refractive index area.

To ensure that the geometry of the system is as expected, using a built-in function of MEEP, a mapping of the refractive index distribution can be displayed. This mapping is done in black and white, being black the areas with a higher refractive index and white, the ones with a lower refractive index. In this way, since only two refractive indexes are used in the simulations, the background of the cell (air or water) will always appear in white and the circles representing the pillars will appear in black.

This geometry program has been programmed to make the introduction of defects in the photonic crystal more straightforward. In following sections, the introduction line and point defects will be discussed and for that similar programs have been used but changing the properties of some of the pillars in the array.

The analysis program uses the geometry created by the geometry program to run the FDTD simulation. In Figure 4.8, a scheme of the simulation structure can be seen. The elements added for the simulation are several.

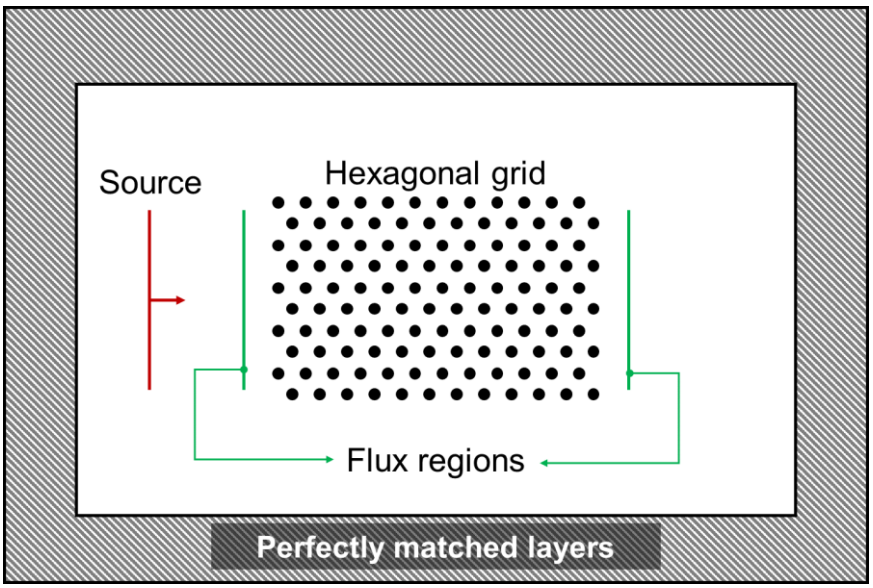

Figure 4.8. Scheme of the simulation built with the MEEP package. In red the source used shows the direction of the wavevector pointing towards the hexagonal grid created. In green the two flux regions used to evaluate the incoming and outcoming fluxes through the hexagonal grid. Surrounding the cell, the perfectly matched layer is shown dashed.

Firstly, a source is added to the simulation (in red in Figure 4.8). This will be the source sending the flux of light towards the photonic crystal. In the program it is constructed as a Gaussian source. This type of source is used to simplify the computation of the system response since only one broadband response must be analysed. In this way the spectral analysis of the response of the system can be done. This source is parametrised based on the central frequency of the spectrum to analyse and the Gaussian's width spanning until the spectrum limits. In addition, the polarisation can be set to TM by choosing the direction of the electromagnetic field.

Two flux regions are added to the program too (in green in Figure 4.8). These two regions are placed before (at the left-hand side of the photonic crystal in Figure 4.8) and after the photonic crystal array (at the right-hand side of the photonic crystal in Figure 4.8). They are designed to evaluate the energy that goes through them and can be created with a MEEP function. The input energy into the photonic crystal is captured by the detector before the photonic crystal and the output energy is detected by the detector region after the photonic crystal.

Finally, the boundaries of the simulation are added as well. The boundaries used in this work are the so called perfectly matched layers (PML) [88]. In Figure 4.8 they can be seen around the simulation region dashed in grey. These layers are absorbing layers. Their function is to absorb any incoming electromagnetic wave that reaches them at any angle and frequency. In this way, reflections resulting from the interaction of the electromagnetic waves with the boundaries of the simulation region will not return to the area of interest, which would alter the simulation results. For these layers to effectively work as absorbing layers, they should be large enough to absorb the electromagnetic fields gradually. As a rule of thumb, it is generally considered that they should be of the order of magnitude of half the largest wavelength employed in the simulation (between 1 and 1.5 μm in this work). In addition, these boundaries should be far enough from the analysed area not to block important electromagnetic fields. For this reason, in the simulations here shown there is a gap between the area where the photonic crystal is placed and the PML regions.

It is not shown in Figure 4.8, but as described in Chapter 2 section 2.3.2, FDTD simulations use meshing to divide the simulation region in smaller domains. This is done using another MEEP function which, given the mesh element size, creates a square mesh covering all the simulation region.

This second program is, at the same time, divided in two main blocks. To obtain the transmission spectra of the simulation, a similar approach as it is done in experimental measurements is carried out. The first block of the simulation runs without the photonic crystal structure between the two detection areas. This is equivalent to a blank measurement. The second block of the simulation runs with the photonic crystal structure introduced between the two detection areas, as shown in Figure 4.9.

The simulation stops when a certain condition is fulfilled. There are different strategies to stop the simulation from running. The more straightforward is to run the simulation for a given time. However, since there can be effects occurring in the simulation that last longer than the specified running time, they could be missed because of this strategy. In the simulations carried out in this work the strategy has been to wait until the amplitude of the fields falls decay below a specific value. In this way, once the source has sent the

Gaussian pulse, the simulation keeps running until the fields decay enough. Additionally, after this happens, an extra time can be set to ensure that the fields converge.

Once the simulation is done, the final transmission is calculated as follows:

$$T = \frac{P_{PhC}}{P_{blank}} \tag{4.2}$$

In equation (4.2) the transmission (T) is calculated as the ratio between the power obtained at the detector after the photonic crystal (P_{PhC}) and the blank power (P_{Blank}).

4.1.4. Transmission spectra discussion

Using the program described in the previous section, the analysis of the transmission spectra has been carried out. The strategy in this case has been slightly different from the one used for the bandgap discussion. While the bandgap discussion provided normalised information about the bandgap opening, the transmission discussion has been designed to simulate a closer to the real final structure and experimental set up. For this reason, again, several combinations of pillars' radii and pitch are considered. These combinations have been analysed independently from the results obtained for the band diagram in section 4.1.2 to observe if what we believe are closer-to-real simulations agree with the band gap simulations.

Here, photonic crystal structures combining 300, 400, 500 and 600 nm pitch and 40, 60, 80, 100 and 120 nm radii have been considered. It is important to note that the material construction used for this program does not consider the imaginary part of the refractive index of none of the materials. For this reason, the obtained spectra do not show the effects of the absorbing wavelength regions for the different materials. These regions have been marked in grey in the different spectra shown in the next figure (Figure 4.9). In addition, the existence of a bandgap has been considered in all those regions where the transmission drops to values below 10^{-4}. This bandgap is marked too, in this case in orange in Figure 4.9.

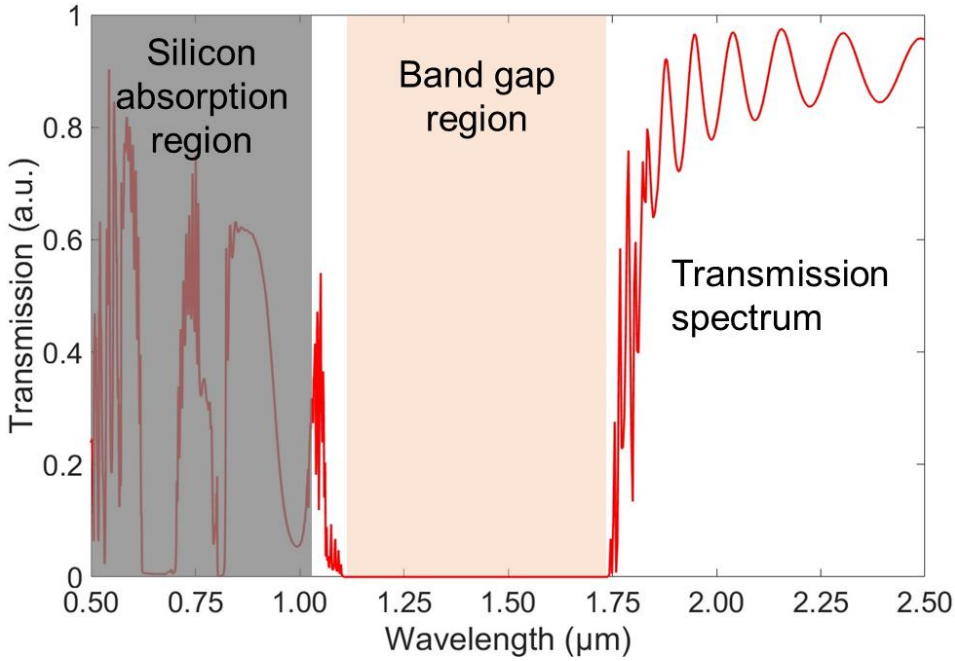

Figure 4.9. Example of one of the transmission spectra in air for a photonic crystal with a pitch of 600 nm and pillars with radii of 120 nm. In shadowed grey the absorption region of the silicon is delimited while the photonic crystal region is shown in orange.

Radius/ Pitch (nm/nm)	Air			Water		
	PBG min (μm)	PBG max (μm)	Gap-to-midgap (%)	PBG min (μm)	PBG max (μm)	Gap-to-midgap (%)
300 / 40	0.577	0.856	38.94	0.726	0.907	22.17
300 / 60	0.561	1.103	65.14	0.805	1.131	33.68
300 / 80	0.880	1.266	35.97	0.961	1.278	28.32
300 / 100	1.093	1.407	25.12	1.151	1.411	20.30
300 / 120	1.312	1.498	13.24	1.367	1.496	9.01
400 / 40	0.709	0.976	31.69	0.948	1.054	10.59
400 / 60	0.781	1.222	44.03	0.980	1.278	26.40

400 / 80	0.938	1.464	43.80	1.064	1.501	34.07
400 / 100	1.099	1.632	39.03	1.215	1.661	31.02
400 / 120	1.308	1.785	30.84	1.389	1.806	26.10
500 / 40	0.874	1.073	20.44	1.193	1.215	1.83
500 / 60	0.904	1.363	40.49	1.180	1.452	20.67
500 / 80	0.999	1.591	45.71	1.226	1.663	30.25
500 / 100	1.157	1.823	44.70	1.319	1.877	34.92
500 / 120	1.317	2.004	41.37	1.486	2.043	31.57
600 / 40	1.048	1.184	12.19	1.379	1.381	0.14
600 / 60	1.065	1.455	30.95	1.401	1.591	12.70
600 / 80	1.110	1.737	44.05	1.420	1.827	25.07
600 / 100	1.225	1.965	46.39	1.482	2.043	31.83
600 / 120	1.373	2.184	45.60	1.580	2.246	34.81

Table 4.3. Summary of the boundaries of the primary band gap opened for the simulations carried out with FDTD method both in air and water background. This table contains the minimum and maximum of the measured band gaps (PBG) including the gap-to-midgap ratio for the different band gaps. In red, those boundaries falling outside the transparent region of silicon are marked.

The oscillations observed in the transmission spectra are associated to ringing artifacts due to the use of Fourier transforms truncation for the solution of the electromagnetic equations in the FDTD simulation. This effect is known as Gibbs effect or overshoot [89].

In Table 4.3, the results of the simulation of the primary band gaps appear for all the pitch and radii combinations is summarized. Both the minimum and maximum values of the bandgap wavelengths are shown, together with their gap-to-midgap ratio. In grey are marked those calculated values that correspond to the spectral region where the absorption occurs in silicon. Consequently, it cannot be considered during the analysis of the system. It must be kept in mind that due to the width of some of these bandgaps they might overlap with other material's absorption ranges (i.e., water), but for simplicity they have not been added here.

Table 4.3's overview provides a good image of not only the quality of the bandgaps for the different structures but, at the same time, their position in the electromagnetic spectrum. Thanks to this a more realistic analysis of the bandgaps can be done. Some of the calculated bandgaps in the transmission spectra, even though having large gap-to-midgap values that are theoretically better than others, are not physically possible due to their position in the light spectrum. This happens specially when considering pillars with radii smaller than 100 nm. In these cases, all or part of the bandgap falls into the absorption regime of silicon [90]. This fact does not make these proportions best suited for the purposes of the project, where a stable and robust bandgap is desired. Therefore, and supporting the conclusion of section 4.1.2, the results confirm that a potential good configuration of photonic crystal is the use of pillars with radius of 100 nm. Even more, still the configuration with 500 nm pitch shows good gap-to-midgap ratio as well as a bandgap within the non-absorbing range of the light spectrum.

From the results in Table 4.3, it can be observed that the tendencies discussed in section 4.1.2 are followed in the FDTD simulations as well: larger gap-to-midgap values are obtained for air rather than for water and, as well, larger contrast among the different structures. Even more, those radius-to-pitch ratios for which the gap-to-midgap had a peak, the results of the FDTD simulations show maximum values too. For instance, the potential optimal configuration of 100 nm pillar's radius and 500 nm pitch shows a gap-to-midgap of 44.70 % and 34.92 % in air and water, respectively. These values are very close to the ones simulated in the bandgap discussion in section 4.1.2, which were 47.70 % and 35.85 %, respectively. In Figure 4.10 a comparison of the gap-to-midgap ratios simulated with the band diagram analysis and the transmission spectrum analysis is shown by overlapping both results. This overlap shows that the results of the FDTD simulations and the ones done with COMSOL Multiphysics® are in good agreement for both air and aqueous backgrounds.

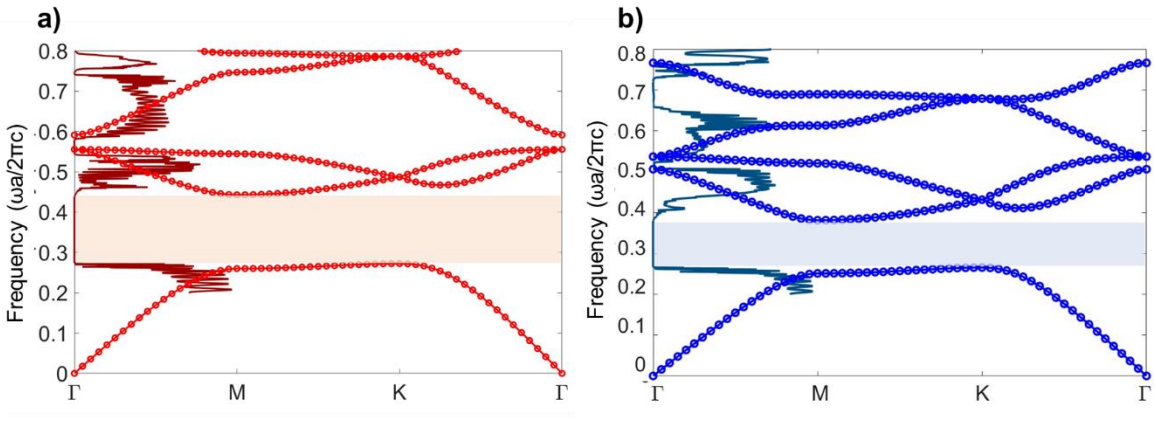

Figure 4.10. Overlap of the results of the bandgaps and the transmission spectra. Results for a photonic crystal with 500 nm pitch and 100 nm radius in (a) air and (b) water. Shadowed the principal band gap can be seen.

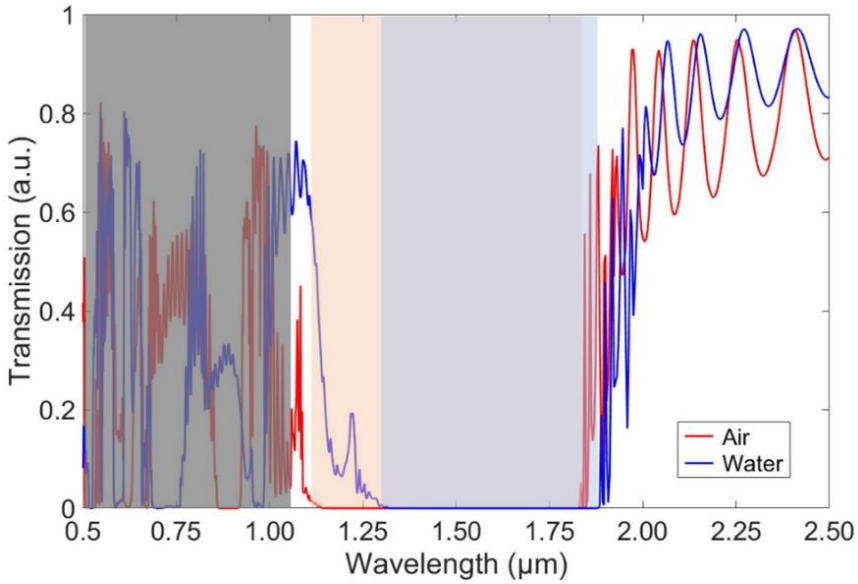

Figure 4.11. Transmission spectra of a structure of 14x14 unit cells of a photonic crystal with a 500 nm pitch and 100 nm radius. In red the transmission considering an air background and in blue considering a water background. Shadowed in grey the adsorbing region of silicon is marked. Shadowed in red and blue the bandgap regions for the air and water simulations are marked.

In Figure 4.11, the transmission spectra in air and water for the structure of 100 nm pillar radii and 500 nm pitch is shown, which is a combination of both Figure 4.11 a and b. In the figure in grey shadow the silicon absorption region is marked. In light red and light blue, the band gaps of, respectively, air and water are marked too.

To sum up the results obtained so far, from the FDTD simulation the configuration of 100 nm pillar radius and 500 nm pitch is still considered the best configuration for this project. The results obtained for this configuration using the COMSOL Multiphysics® and FDTD simulations are shown in Table 4.4. It can still be concluded that the results agree, even though there are small discrepancies between the results, as they have been obtained from two different methodologies and employing two different simulations packages.

Background material	Band diagram			Transmission Spectra		
	PBG min λ (μm)	PBG max λ (μm)	Gap-to-midgap (%)	PBG min λ (μm)	PBG max λ (μm)	Gap-to-midgap (%)
Air	1.130	1.841	49.02	1.157	1.823	44.70
Water	1.310	1.883	35.85	1.319	1.877	34.92

Table 4.4. Summary of the bandgap positions and gap-to-midgap for a photonic crystal of 500 nm pitch and 100 nm radius in air and water backgrounds. The results of the two types of simulations done through the band diagram and the FDTD.

4.2. Introduction of defects in two-dimensions

Until the moment only the full photonic crystal structures have been considered. However, as explained in Chapter 2 section 2.2 the introduction of defects to the structure creates alterations in the bandgap that can be interesting for this project. As discussed in Chapter 2, two main types of defects are considered in this work: line and point defects.

The simulations described in sections 4.1.1 and 4.1.3 can be modified accordingly to add the defects. Depending on which type of defect is added these modifications vary. In the following sections the results of the simulations with defects are depicted.

4.2.1. Line defects

The introduction of line defects is done by changing some parameters of one of the lines in the photonic crystal structure. One way to do it is by changing the radius of the pillars. This is the strategy that has been used in this thesis.

The starting point for this situation is the simulation of the band diagram. To do it the approach explained in section 4.1.1 using the primary cell is not valid anymore. In this case, a larger structure is needed for the simulation of the band diagram with line defects. The structure is shown in Figure 4.12 [91], [92].

In Figure 4.12 a, it can be seen how in the direction of the defect the primary cell can still be used. But in the perpendicular direction 5 cells are added at the top and 5 more at the bottom of the defect. This strategy must be used due to the use of periodic conditions at the top and the bottom of the simulation region. These periodic conditions applying in the vertical direction are equivalent to repeating infinitely vertically the line defect. For these reason, extra cells are needed to avoid the possibility of interaction between the infinite line defects, which would lead to a wrong result.

The simulation's discussion hereafter has been done considering a basic photonic crystal with pillars of 100 nm radius and 500 nm pitch. The discussion has been done within both water and air backgrounds. The representation of these new band diagrams is done in the direction $\Gamma K'$, which is the direction where the bands collapse for a lineal defect, as shown in Figure 4.12 b and which was explained in Chapter 2 section 2.2.1.

To begin the discussion, the projected band diagram of a photonic crystal structure in which a complete row of pillars has been removed is calculated. This structure is an extreme case of this type of defect but it clearly shows how the collapsed bands still create a band gap and a band appears in its centre. This band is created by the defect and appears for any reciprocal space directions. In Figure 4.13 the band diagram for a 100 nm radius and 500 nm pitch with a missing line for air (Figure 4.13 a) and water (Figure 4.13 b) backgrounds are shown. The results show, similarly to the results in the previous sections, that in the case of water background the projected band diagram

appears at lower frequencies than in the case of air background. The position of these two bands is summarised in Table 4.5.

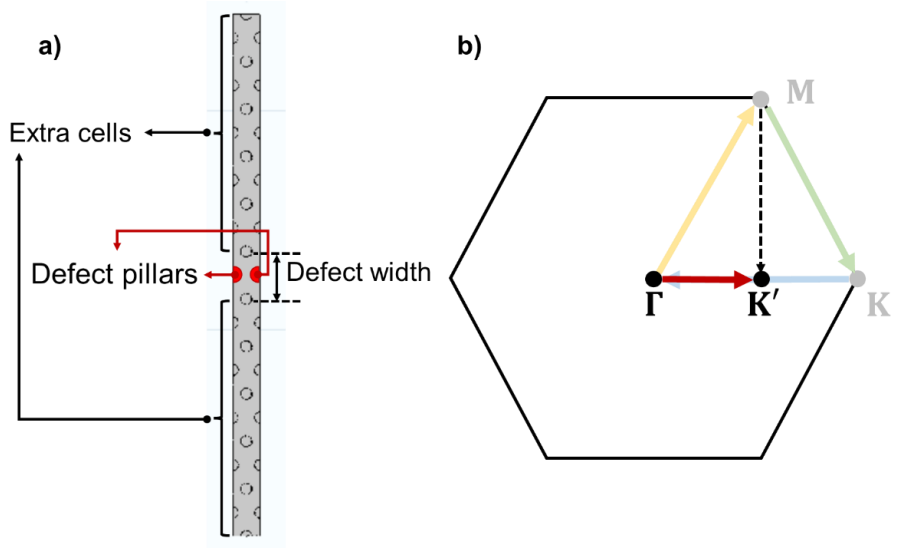

Figure 4.12. (a) Scheme of the supercell simulation carried out in COMSOL Multiphysics®. In red the pillars used as defect are marked; (b) Sketch of the projection of the M point onto the direction of the line defect. A new point of the reciprocal lattice is obtained from this projection (K').

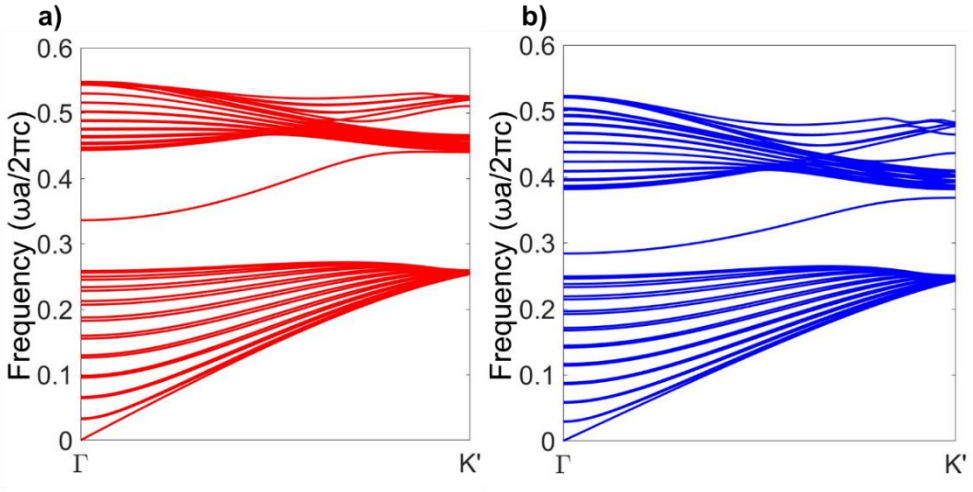

Figure 4.13. Projected band diagram of a missing row of pillars in a structure of 500 nm pitch and 100 nm radius in an air (a) and water (b) backgrounds.

Background material	Band min (ωa/2πc)	Band max (ωa/2πc)	Band min λ (μm)	Band max λ (μm)

Air	0.336	0.441	1.134	1.488
Water	0.284	0.369	1.355	1.761

Table 4.5. Summary of the opening of the band created by the defect line when a row of pillars is missing. The resulting normalised frequencies and the equivalent wavelengths are indicated, as well.

It is important to note that the resulting projected band gaps and the bands induced by the defect are in agreement with the results shown in the subsection 4.1.2.

This same simmulation has been done with the FDTD program described in section 4.1.3. In this case it can be seen how within the bandgap a transmission window is opened for both air and aqueous background (Figure 4.14).

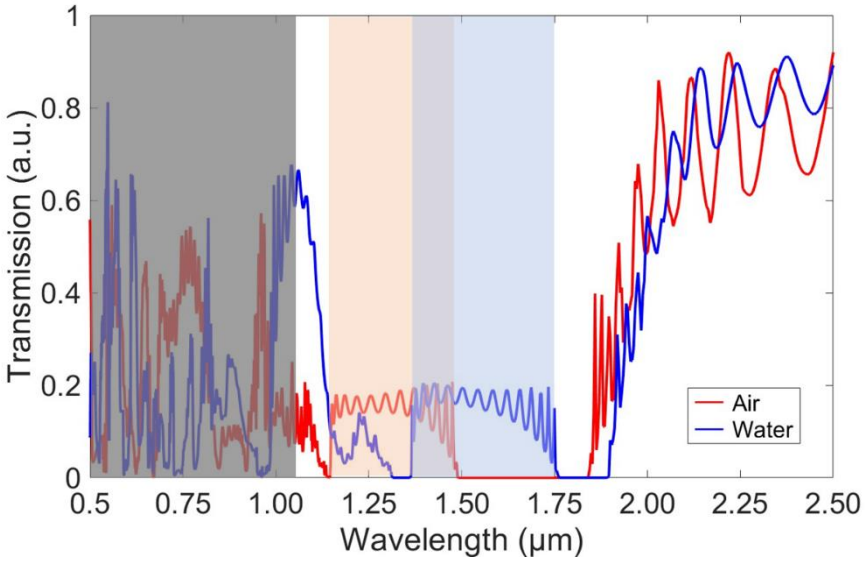

Figure 4.14. Transmission spectra resulting from the FDTD simulation of a photonic crystal with a row of pillars missing in air (red) and water (blue). It can be observed how within the bandgap a new transmission window is introduced thanks to the defect (shadowed in red and blue). In grey the area where silicon is adsorbent is shadowed.

A comparison between the results obtained with the band diagram and the FDTD simulation is shown in Figure 4.15. The overlap of the two results shows good agreement. It can be seen how the transmission window obtained for the FDTD simulation coincides with the band created within the band gap. The summary of the

band gap opening from the band diagram and the transmission spectra results are summarized in Table 4.6 and corroborate the good agreement shown in Figure 4.15.

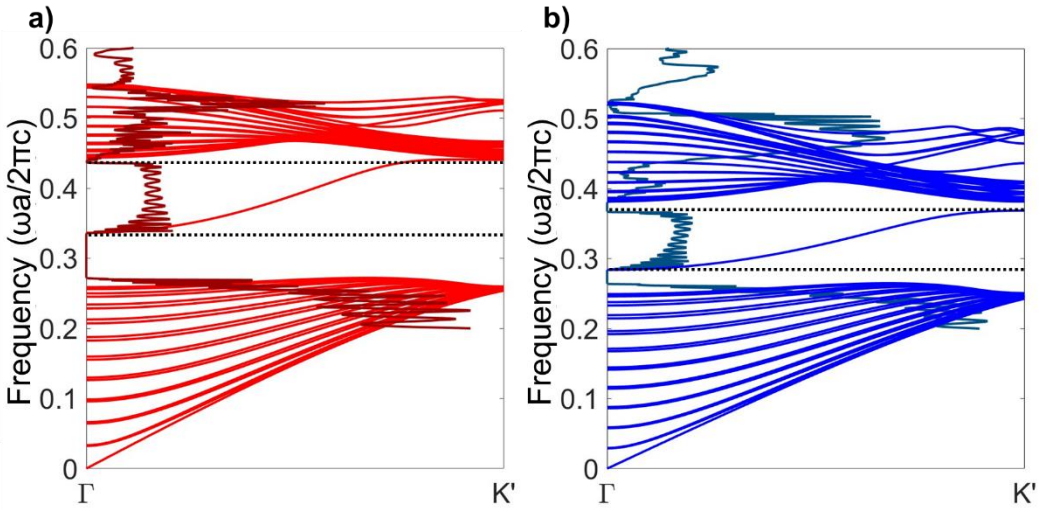

Figure 4.15. Overlapping of the results obtained both with the COMSOL Multiphysics® and FDTD simulations in air (a) and water (b). In dashed lines it can be seen how the transmission window resulting in the FDTD simulation and the band introduced in the bandgap agree as shown as well in Table 4.6.

Background material	Band diagram		Transmission Spectra	
	Band min λ (μm)	Band max λ (μm)	Band min λ (μm)	Band max λ (μm)
Air	1.134	1. 488	1. 146	1. 491
Water	1.355	1. 761	1.363	1. 759

Table 4.6. Summary of the opening of the new band due to the missing row as line defect for the two types of simulations carried out for both air and water backgrounds. These results correspond to a photonic crystal structure with 500 nm pitch and 100 nm radius.

However, this configuration with a missing row of pillars is physically impossible, as it would be equivalent to having an air (or water) waveguide within the pillars. Since in this case the top cladding, not taken into account in the calculations, will have the same

refractive index as the waveguide, the light would leak into the cladding instead of being transmitted through the system.

For this reason a discussion on the variation of the radius of one row of pillars in the main photonic crystal has been considered. The radius of the pillars of this line has been changed to 40, 60, and 80 nm, which is schematically depicted in Figure 4.12 a. The results of this variation in air and water are shown in Figure 4.16 and the position of the defect band summarised in Table 4.7. These plots clearly show how the new band inside the band gap raise from the dielectric band into the bandgap with decreasing pillar radius.

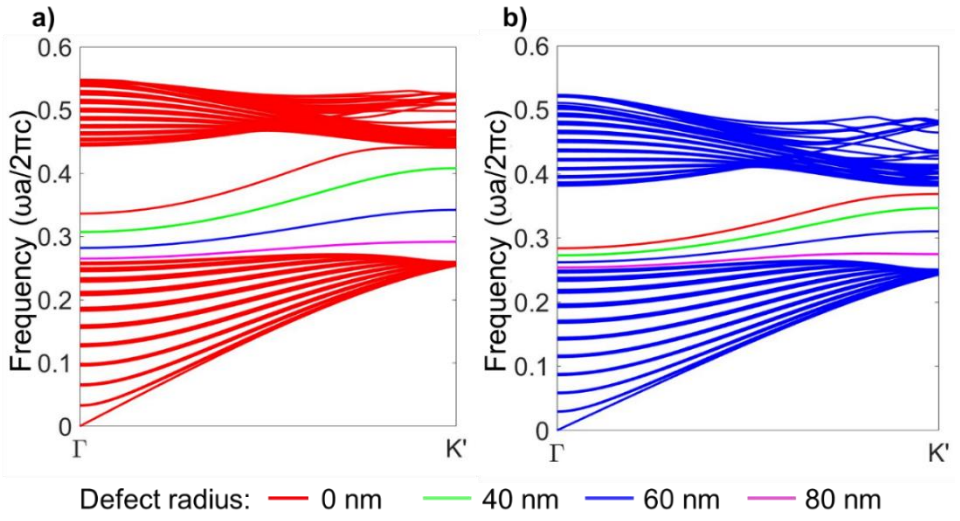

Figure 4.16. Projected band diagrams for different line defects in air (a) and water (b). The bands introduced in the bandgap resulting from a line defect of pillars with 80 nm radius (pink), 60 nm radius (blue), 40 nm radius (green) or no pillars (red) are marked.

For the purpose of this thesis a good option would be to have a line with pillars with radius 40 or 60 nm since they would create a band well within the photonic bandgap and their fabrication is technologically feasible. For the case of 80 nm radii pillars line a band is introduced but in very close vicinity to the bottom limit of the bandgap. This could give rise to a problem for the experimental characterisation of the devices since the transmission band might merge with the transmission signal through the photonic crystal. Because of this, the configuration with a row of pillars of radius 80 nm row would be more sensitive to errors during the fabrication process and other experimental issues

than in the case of rows of pillars of 40 nm or 60 nm. In Chapter 5 the discussion of fabricating simultaneously on the same sample pillars of different radius is discussed.

Defect radius (nm)	Air		Water	
	Band min (ωa/2πc)	Band max (ωa/2πc)	Band min (ωa/2πc)	Band max (ωa/2πc)
0	0.336	0.444	0.284	0.369
40	0.307	0.408	0.273	0.347
60	0.282	0.342	0.262	0.310
80	0.265	0.292	0.254	0.275

Table 4.7. Summary of the band opening for different radius of the pillars creating the defect line in both air and water backgrounds.

An alternative approximation to the creation of line defects is the variation of the defect width, which is expected to have a comparable effect as varying the radius of the defect line. This approach is also illustrated in Figure 4.12 a. This configuration has been attempted for different defect widths, ranging from 250 nm to 1000 nm. The results for the different simulated widths and for the defect pillars with radius 40 nm in air background are shown in Figure 4.17.

From the results in Figure 4.17 several conclusions can be exctracted. The most evident one is that for 250 nm width (Figure 4.17 a) no band is created by the defect inside the bandgap. This can be understood because the two rows of pillars on both sides of the defect ar too close one to the other when compared to the photonic crystal. When the line of the defect is increased to 375 nm, 500 nm and 625 nm (Figure 4.17 b, c and d, respectively), the band falls into the bandgap and expands with increasing defect width until it covers the complete bandgap. The consequence of this span is that the narrow transmission window created in the bandgap and observed in Figure 4.14 will end up covering the whole bandgap. This can be observed in Figure 4.17 e and Figure 4.17 f, where additional bands appear inside the bandgap. From all this we can deduce that there is a limitation on how wide the defect can be to confine the defect-created band

inside the band gap and avoiding to completely loose the light blocking properties of the photonic crystal.

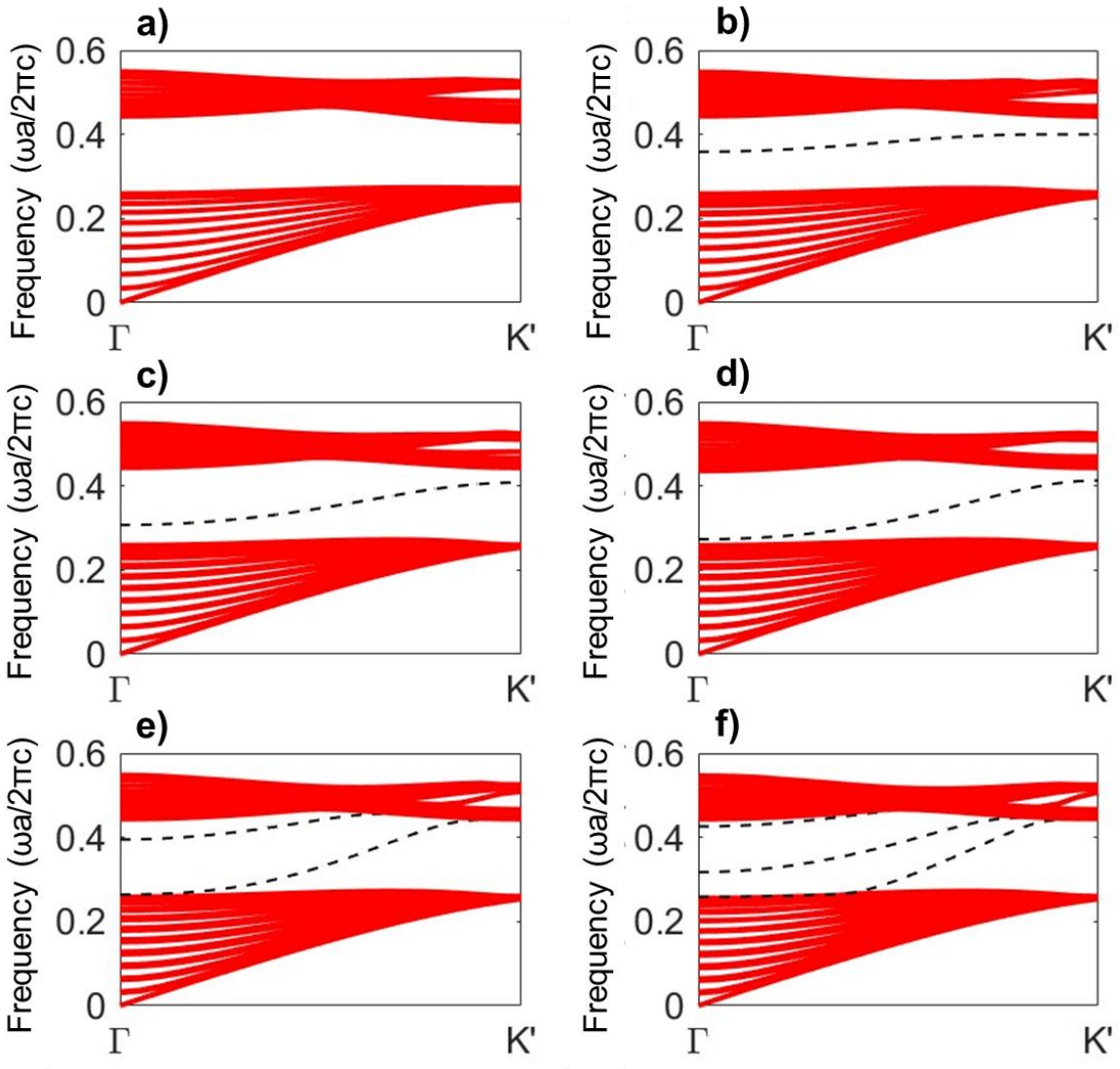

Figure 4.17. Projected band diagrams for a line defect created by pillars of 40 nm with widths of (a) 250 nm, (b) 375 nm, (c) 500 nm (corresponding to the green line in Figure 4.16), (e) 625 nm, and (f) 750 nm in air background. Dashed lines corresponding to the different bands created by the defect are marked.

The tendency shown in Figure 4.17 has been observed as well for line defects with a row of pillars of 80 and 60 nm, but their band diagrams are not shown here. Table 4. 8 summarises the results for line defects creating rows of pillars of 40, 60 and 80 nm both in air and water backgrounds. In this table both the distance of the introduced band to

the bottom of the band gap and the percentage of band gap coverage by this band are included. From the results in Table 4. 8, it is shown the distance of the bottom of the introduced the same tendency where a narrower band is created when the width is smaller and vice versa. This effect happens both in air and water background.

	Defect width	Defect radius 40 nm		Defect radius 60 nm		Defect radius 80 mn	
		Dist. to min PBG (ωa/2πc)	PBG coverage (%)	Dist. to min PBG (ωa/2πc)	PBG coverage (%)	Dist. to min PBG (ωa/2πc)	PBG coverage (%)
Air	375	0.087	25.65	0.048	11.89	0.019	6.26
	500	0.035	63.18	0.010	38.16	0.003	10.64
	625	0.001	87.58	0.000	50.67	0.000	16.89
Water	375	0.053	22.97	0.033	15.31	0.010	12.76
	500	0.009	62.94	0.000	40.83	0.000	18.71
	625	0.000	82.51	0.000	39.13	0.000	21.27

Table 4. 8. Summary of the distance between the bottom of the introduced band and the bottom of the band gap (PBG) as well as the percentage of the band gap covered by the defect band. The results belong to the calculation done by introducing a line defect by varying the radius of one row of pillars down to 40 nm, 60 nm and 80 nm, both in air and water.

From the results in Table 4. 8, it can be seen the same tendency where a narrower band is created when the width is smaller and vice versa. This effect happens both in air and water background. It can be seen that some of the combinations even though they do not completely cover the band gap they are start at its bottom. These combinations cannot be used since the band created would not be differenciated from the actual transmission of the photonic band gap. For this reason from the results in Table 4. 8, only those bands that are far away enough from the bottom of the bandgap but as well are narrower enough (small band gap coverage) are the ones suitable for this project. In this

case the best line defect found both in air and water background is the one considering 60 nm radius line of pillars and a defect width of 375 nm.

4.2.2. Point defects

Point defects are another type of structure that modifies the band structure. They consist on locally disturbing the periodicity of the structure. While the line defects consisted on changing some parameters for a row of pillars, point defects, on the other hand, consist on changing the properties of one or several pillars to create a cavity. These type of defects introduce a ressonance mode within the bandgap, giving rise to a peak in the transmission spectrum [93].

The possibilities of cavities in the system of a photonic crystal are huge. In this thesis the study of cavities has not been a major topic and they are described here only to prove their effect on the band diagram within the system. An example of the structure simulated using FDTD can be seen in Figure 4.18 a. The structure consists of a basic photonic crystal with a line missing and a cavity within it created by two pillars of the same size as the photonic crystal pillars. The resulting transmission spectra for this structure, both in air and in water, are shown in Figure 4.18 b. It can be seen that a transmission peak is introduced in the bandgap region. For an air background, the wavelength corresponding to this peak is 1.278 µm, while it is 1.565 µm for water background. The position of this peak falls within the transmission window opened by the waveguide (Table 4.6).

These results confirm that the combination of a waveguide and a cavity within the studied structure creates a transmission peak in the bandgap. This is a configuration that could potentially be used for the sensing purposes of the structure. The wavelength at which the peak occurs is mainly dependent on the size of the cavity and the background material[15], [16]. Therefore, if the position of one pillar is shifted, the size of the cavity will be changed, and the peak will shift. This is a simple way of emulating the bending of the pillars.

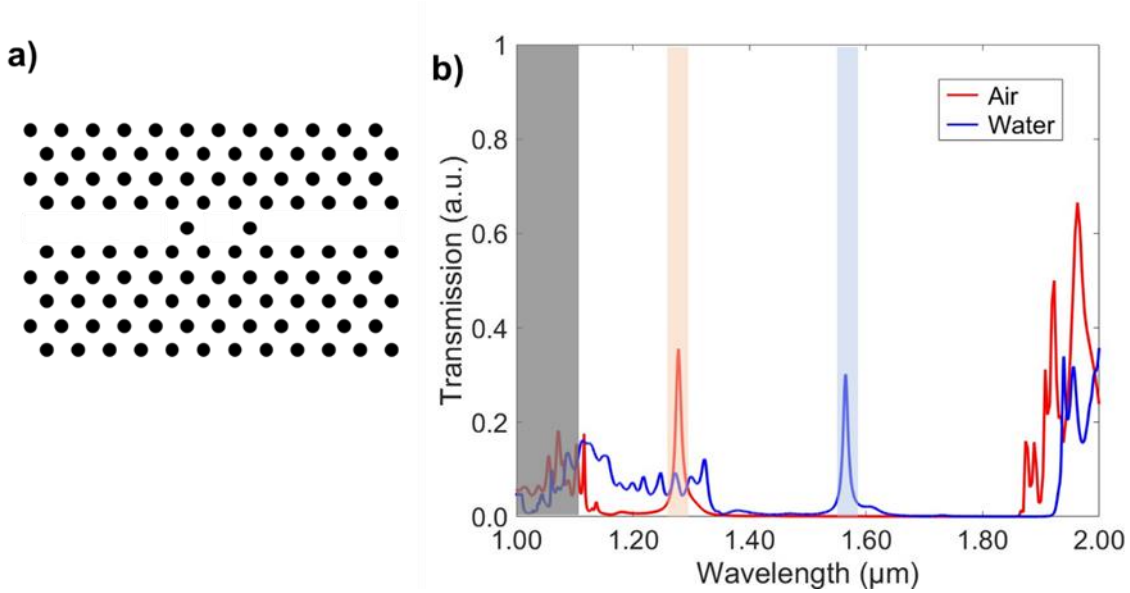

Figure 4.18. (a) Scheme of the structure simulated to evaluate the impact of cavities in the system. (b) The transmission spectra of the structure represented in figure a considering an air background (red) and water background (blue). Shadowed in grey the silicon absorption region is marked as well as shadowed in red and blue the resonance peaks for the cavities can be seen.

This simulation test has been carried out on the structure depicted in Figure 4.18, by moving the left pillar of the cavity to the left (making the cavity larger) and to the right (making the cavity smaller). The resulting transmission spectra for different pillar shifts and a water background are shown in Figure 4.19 a, while the peak evolution for both water and air backgrounds are shown in Figure 4.19 b. The positions of the peak are summarised in Table 4.9.

These results show that when the cavity size is reduced the peak moves towards lower wavelengths and vice versa. This makes sense if this is correlated with the frequency resonance of the system. A large cavity will resonate at lower frequencies (high wavelengths), while a small cavity will resonate at higher frequencies (lower wavelengths). In addition, this frequency change follows a lineal tendency both for water and air backgrounds. From these results we can conclude that the deflection of the pillar affects the peak position. And this is a promising result for the research project, because if it is experimentally confirmed, this configuration could work as an optical force sensor.

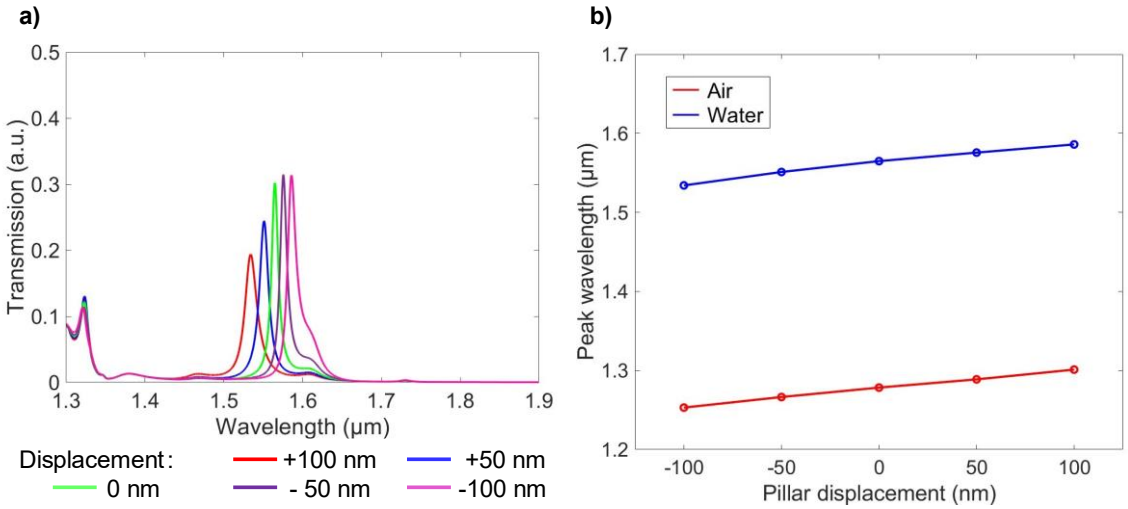

Figure 4.19. (a) Transmission spectra of the system shown in Figure 4.18 b for a water background. The displacements correspond to the movement of the left pillar creating the cavity to the left (negative values) and to the right (positive values); (b) representation of the peak position as a function of the displacement for both air and water background.

Displacement (nm)	Defect peak position in air (μm)	Defect peak position in water (μm)
-100	1.301	1.534
-50	1.289	1.551
0	1.278	1.565
50	1.266	1.576
100	1.253	1.586

Table 4.9. Summary of the peak positions represented in Figure 4.19 b for air and water background depending on the displacement of the left pillar creating the cavity.

4.3. Photonic crystal slabs

The simulations discussed until the moment in this chapter have considered ideal two-dimensional photonic crystals. These simulations have permitted to narrow down the parameters of the problem. But these simulations are not realistic since they only consider the directions in which the system is periodic. Until now infinitely long pillars were considered. However, the third dimension, vertical in this case, plays an important role in the problem and a finite slab needs to be simulated and will add some limitations to the results considered until now [22].

As explained in Chapter 2 section 2.1.3 the light confinement in the non-periodic direction occurs thanks to the TIR (total internal reflection) of light at the interfaces between the pillars and the top and bottom media. The light is confined within the silicon pillars if the refractive index on the top and bottom of the pillars is lower than the effective refractive index of the photonic crystal itself. These top and bottom materials will be, from now, referred as top and bottom claddings.

To depict this behaviour only COMSOL Multiphysics® simulations have been carried out under these conditions. Adding a third dimension in the simulations requires larger computation resources than the ones used in section 4.1.1 when only two-dimensional systems where considered. These computational costs are especially large for the FDTD simulations. For this reason, FDTD simulations have not been considered in this section and, therefore, only COMSOL Multiphysics® results have been used. The new configuration is shown in Figure 4.20.

In this figure, it can be seen how in these new simulations the real proportions of the pillar are considered. The scheme shown in Figure 4.20 a is an ideal situation in which only the pillar is represented but brings an idea on how the third dimension is added to the problem. In fact, this introduces new parameters to consider, such as the height of the pillar, the amount of top and bottom claddings added and the boundary conditions at the simulation region edges of the new dimension. The height of the pillar (or slab thickness) is a parameter that will be further discussed later in this section, as well as the cladding thicknesses.

Regarding the boundary conditions at the top and bottom of the simulation, periodic conditions cannot be used anymore. This is because in this direction the system is no longer periodic in this third dimension. As an alternative, PML layers are used. The construction and use of these layers in COMSOL Multiphysics® simulations is the same as the ones used in subsection 4.1.2 for FDTD simulations. These layers are designed to absorb the incoming wavelengths and prevent phenomena such as reflections at the limits of the simulation region that could twist the results. In the present simulation there is no source emitting light into the system, such as the one used in the FDTD simulations, but the FEM simulation still considers the propagation and behaviour of electromagnetic fields in the system. Again, similarly to what was explained in subsection 4.1.2, these PML layers should be thick enough to be able to absorb the incoming fields and, for this reason, it has been chosen to set them to be 1 µm thickness.

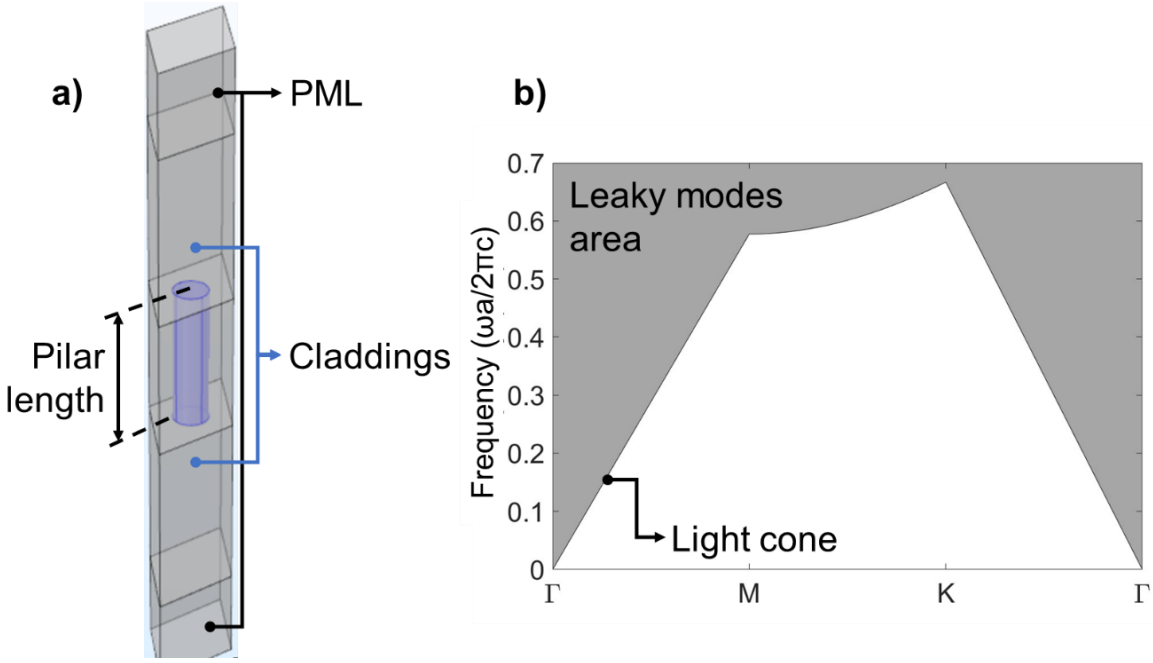

Figure 4.20. (a) Scheme of the three-dimensional simulation used in COMSOL Multiphysics®. In blue the pillar within the cell is shown. In addition, the areas acting as top and bottom claddings are marked as well as the PML top and bottom layer; (b) Sketch of one light cone considering an air cladding. In grey the region of leaky modes is marked while in white the area of guided modes can be seen.

The introduction of the third dimension into the problem adds some extra restrictions on the bandgap evaluation that have not been discussed in previous sections. The finite

structure and the presence of claddings at the top and bottom of it limits the number of modes that can be propagated through the silicon pillars. Those modes are called guided modes, while those which are not able to do so, are called leaky modes. These leaky modes cannot be sustained within the slab and propagate into the claddings (section 2.1.3). The boundary between the guided modes and the leaky modes is determined by the light cone (Figure 4.20 b), which is defined as [23]:

$$|\boldsymbol{k}_{||}| = \left(\frac{\omega}{c} n_{cl}\right)$$

(4.3)

where $\boldsymbol{k}_{\|}$ is the wavevector component parallel to the periodic structure, ω is the frequency, c is the light speed in air and n_{cl} is the refractive index value of the cladding. Therefore, depending on the material used as cladding, this light cone will vary. All those modes below the light cone will be modes that the photonic crystal slab will be able to sustain, while those ones above it will leak into the background.

In Figure 4.21 the represenation of the band diagram of one of the simulated structures is shown. In it, the light cone line is represented, and shadowed in red and blue the modes now considered leaky are shown. In this case it is the light cone considering an imaginary situation where the both the top and bottom cladding are the same: air (Figure 4.21 a) or water (Figure 4.21 b). As can be seen the light cone is pushed down to lower frequency values when a water background is considered as compared to an air background.

Aside from the limitations on the number of modes that are guided through the silicon pillars, the light cone limits as well the directions in which the band gap appears. In sections 4.1 and 4.2 the band gaps have been calculated considering to be opened in all the directions in the reciprocal space. However, due to the boundary of the light cone, the band gap is limited to those directions where the bandgap is determined by guided modes. Therefore, in this three dimensional system, the light direction is now important for the appearance of band gaps.

In this thesis the discussion on the evaluation of the response of the three dimensional system has been focused on the impact of the pillar height and the different claddings. The results are shown in the following subsections.

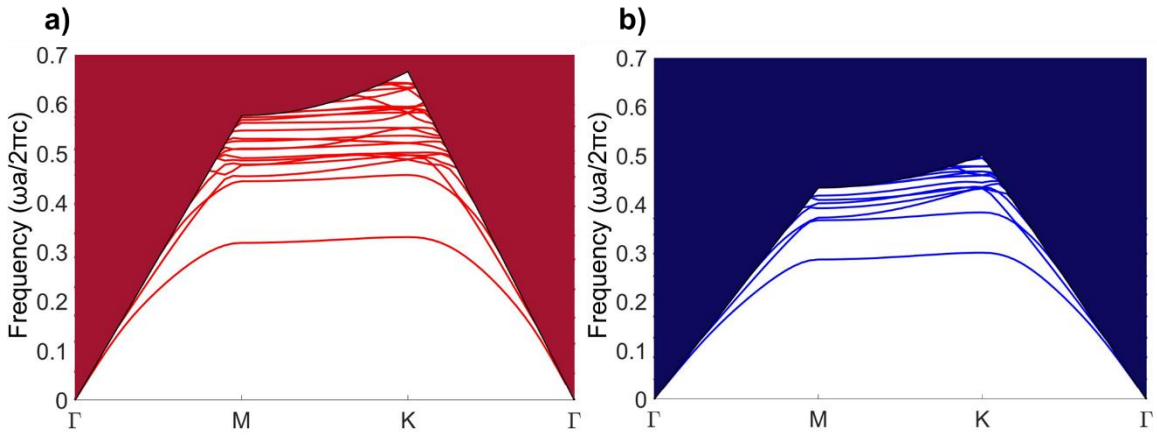

Figure 4.21. Band diagrams of a pillar of height 1000 nm and 100 nm radius in air (a) and water (b) considering a unit cell of 500 nm pitch. Above the light cone line, the areas shadowed in red, and blue correspond to the leaky modes' regions. Below the light cone line, the simulated guided bands can be seen.

Background material	PBG min (ωa/2πc)	PBG max (ωa/2πc)	PBG min λ (μm)	PBG max λ (μm)
Air	0.330	0.444	1.127	1.513
Water	0.301	0.368	1.360	1.663

Table 4.10. Summary of the band gap openings for the band diagrams shown in Figure 4.21 considering the light cone limitations.

4.3.1. Impact of the pillar height

Known the best radius and pitch configuration of the photonic crystal, their height is the final parameter to determine. In this thesis the focus has ben set on the optimisation of the bandgaps and this optimisation can be done as well depending on the pillar height.

For a too thin pillar a very weak perturbation of the overall dielectric constant would occur and, in the end, will have no measureable effect. On the other hand, considering a too thick pillar, the higher modes can be guided through the system, adding too many modes in the system. Similarly to what is aimed in other photonic problems, ideally, a monomode or close to monomodes system is seeked [23], [94].

Therefore to evaluate the quality of the opened photonic bandgaps, as done in section 4.1.2, the evolution of the gap-to-midgap and the robustness maps can be used. In the present case, however, instead of observing the evolution of these parameters depending on the radius-to-pitch ratio, the height of the pillar has been used. To do so an ideal configuration has been used where a floating pillar is considered whose height has been varied between 500 nm ad 1500 nm.

In Figure 4.22 the robustness maps and the gap-to-midgap representations of the bandgaps for air (Figure 4.22 a and b) and water (Figure 4.22 c and d) backgrounds are represented depending on the silicon pillar height.

The bandgap width has been measured using the maximum of the fundamental band and the minimum of the first band below the light cone.

From the results shown in Figure 4.22 it can be seen that the optimal bandgap is obtained for a 1000 nm height in air and 900 nm height in water. These values are in line with theoretical models that try to predict the optimal thickness of photonic crystal slabs. The model reads as follows:

$$h \sim \frac{a}{2\omega_{gap-bottom}\sqrt{\bar{\varepsilon}}} \tag{4.4}$$

where h is the theoretical optimal slab thickness, $\omega_{bap-bottom}$ is the lower value of the TM band gap of the 2D system, $\bar{\varepsilon}$ is the wheighted dielectric permitivity. Since we are considering a TM light polarization, the expression can be approximated by:

$$\bar{\varepsilon}_{TM}{}^{-1} = \frac{\langle H_0|\varepsilon^{-1}|H_0\rangle}{\langle H_0|H_0\rangle} = \langle\varepsilon^{-1}\rangle_H \sim \varepsilon_{low}{}^{-1}$$

(4.5)

Using the dielectric permitivity of air as ε = 1 and for water ε = 1.769, the theoretical results and the ones obtained thanks to the simulations are summarised in Table 4.11. It can be observed how the values are in good agreement.

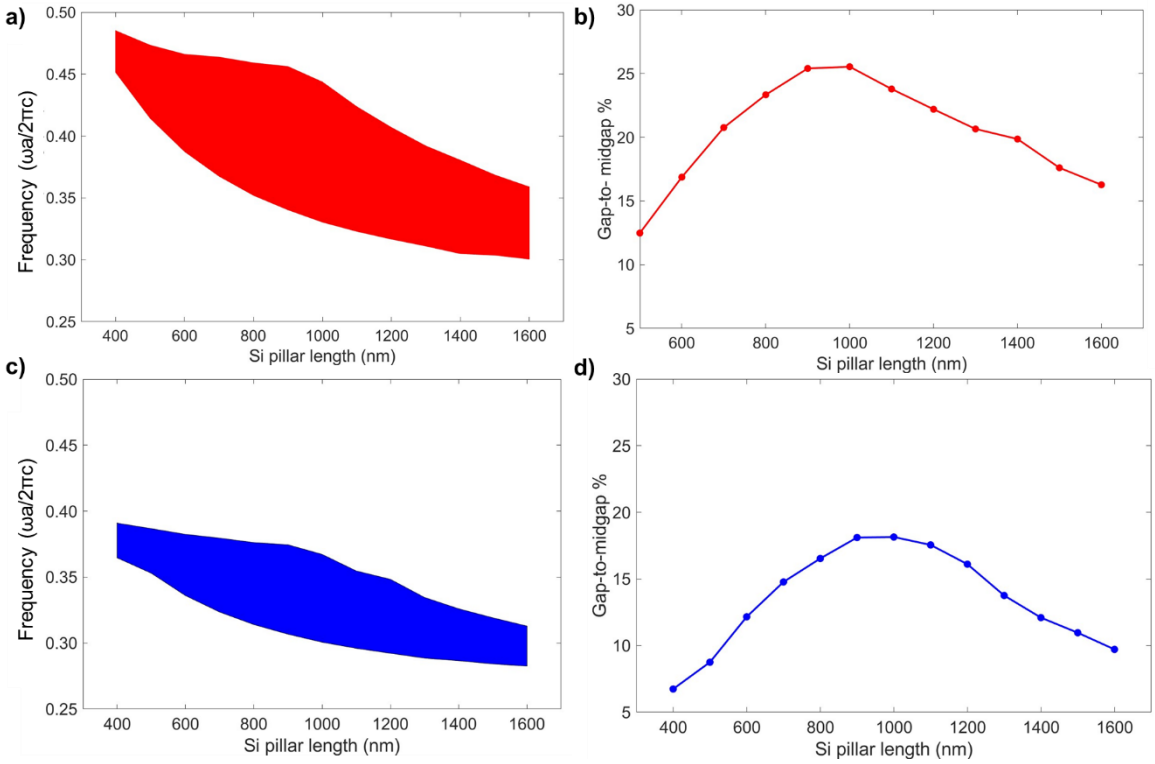

Figure 4.22. Resulting robustness maps and gap-to-midgap ratio evolution in front of the silicon pillar height for air (a, b) and water (c, d) background considering a structure with a stand-alone silicon pillar.

Background material	PBG min (ωa/2πc)	PBG max (ωa/2πc)	PBG min λ (μm)	PBG max λ (μm)	Theoretical thickness (nm)
Air	0.330	0.444	1.127	1.513	943

Water	0.307	0.375	1.335	1.630	767

Table 4.11. Summary of the maximum and minimum values of the bandgap opened in air and water for a self-standing pillar. The optimal thickness found considering the gap-to-midgap representation in Figure 4.22 is added as well. In addition, the theoretical value of the optimal thickness calculated with equations (4.4) and (4.5).

4.3.2. Impact of the claddings

In the previous subsection the analysis has been carried out considering strictly only the pillar height contribution. However, the real configuration will never be the case of a photonic crystal made of free-standing pillars, but the pillars must be standing on a substrate. The impact of this substrate is not trivial. As explained in the previous section, the materials conforming the top and bottom calddings play an important role on the light confinement within the pillar. The cladding material's refractive indexes should be smaller than the silicon refractive index to allow the light confinement within the vertical direction because of the TIR phenomenon. Here three different materials will be considered as claddings: silicon oxide, air and water.

In this thesis three configurations, shown in Figure 4.23, have been considered as possible top and bottom cladding distributions: one where there is a silicon slab below the silicon pillar, another one where there is a silicon oxide piller underneath the silicon pillar, and a final one where there is a silicon oxide pillar at the top and bottom of the silicon pillar. It must be pointed out that due to the complication of the structure in two out of these three cases, the bottom and the top claddings are not based on the same material (asymmetric claddings). This fact will affect the light cone shape since its boundaries are based on the refractive index of the claddings. For the results in this subsection always the most limiting light cone has been considered. This means that the light cone coming from the higher refractive index cladding material has been considered, therefore, silicon oxide light cone. In addition, this assymetry induces a less stable system where the leaks through the third dimension are larger [23].

The first configuration considered is the one depicted in Figure 4.23 a in which a silicon oxide slab is considered to sustain the pillars. This configuration is the simplest one from the simulation and the fabrication points of view. In this case, aside from the height of the

pillars, the thickness of the botom cladding silicon oxide has been considered as important parameter. A similar discussion to the one employed in the previous subsection while analysing the band diagram. Silicon pillar thicknesses between 250 nm and 2000 nm and silicon slab thicknesses 1000 nm have been simulated. The choice of these thicknesses has been done based on commercial SOI wafers available in the laboratory. The thicknesses of the device and buried oxide layers of the commercial SOI wafers span from few hundreds of nanometers to several microns. More precisely, the substrates purchased for this project had a 1500 nm device layer and 1000 nm buried oxide layer and where purchased based on the results of these simulations.

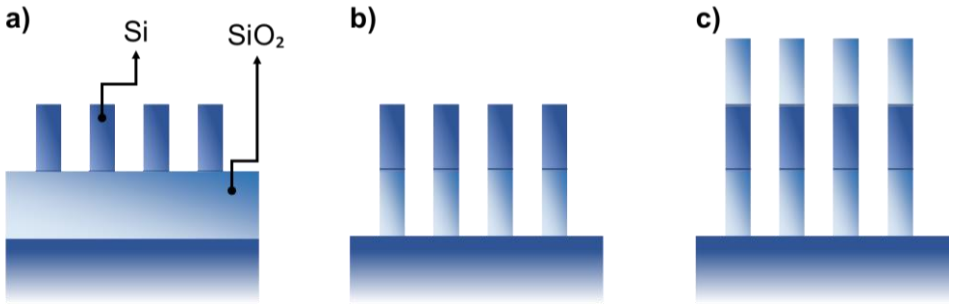

Figure 4.23. Sketches of the three configurations considered for the cladding distribution: (a) silicon pillars standing on a silicon oxide slab; (b) Silicon pillars on top of silicon oxide pillars and (c) silicon pillars in between two layers of silicon oxide pillars.

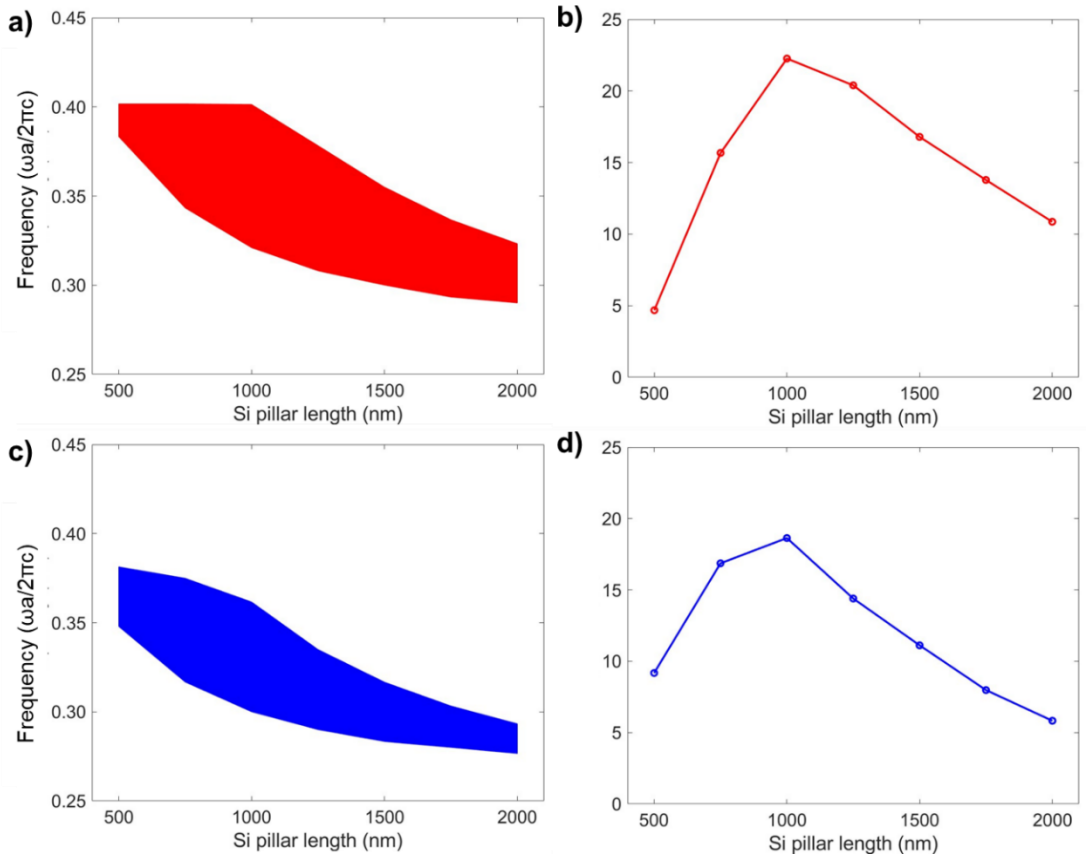

Figure 4.24. Resulting robustness maps and gap-to-midgap ratio evolution in front of the silicon pillar height for air (a, b) and water (c, d) background considering a structure with a bottom silicon oxide slab of 1000 nm with silicon pillars on top.

The simulation has been set to have a top layer of air (or water) cladding of 1000 nm and PMLs of 1000 nm as well. Based on this the values, the pillar height has been the only changed parameter among the different values already mentioned.

In Figure 4.24 the resulting robustness maps and the gap-to-midgap ratio are represented for both air and water backgrounds. In this configuration it can be seen how the tendency is similar to the one observed in the previous discussions. The robustness maps and the gap-to-midgap representations for air and water show a peak at around a height of 1000 nm. This result supports the versatility of the project since the fabrication of silicon pillars of 1000 nm height could work both for air and water backgrounds.

Background material	PBG min (ωa/2πc)	PBG min (ωa/2πc)	PBG min λ (μm)	PBG max λ (μm)	Gap-to-midgap ratio %
Air	0.321	0.402	1.250	1.560	22.26
Water	0.300	0.362	1.380	1. 667	18.64

Table 4.12. Summary of the optimal silicon heights for the configuration shown in Figure 4.23 a with their gap-to-midgap ratio.

For the second sketch shown in Figure 4.23 (Figure 4.23 b), a similar analysis has been carried out. In this case the silicon pillar thickness has been varied between 500 nm and 1500 nm. In addition, since the silicon oxide pillar etch can be total (down to the silicon substrate) or partial (a part of the silicon oxide will remain below the pillar), two different heights have been considered: 500 nm pillar height (etch of half of the buried oxide layer) and 1000 nm pillar height (full buried oxide layer etched). The resulting robustness maps and the gap-to-midgap ratio are represented for both air and water backgrounds for a bottom pillar of 1000 nm in Figure 4.25.

From the gap-to-midgap ratio representation the optimal silicon height value in air corresponds to a pillar of 1250 nm, while in the case of water background this optimal value is a pillar of 1000 nm. However, in this case, the bottom limit of the band gap for a water background falls within the absorption region of silicon. Consequently, according to the evolution of the robustness maps, the optimal silicon thickness should be larger than the 1000 nm of the optimal one even though for them the gap-to-midgap ratio already presents a certain decay. The values of the PBG for 1250 nm long silicon pillars in air and water and their gap-to-midgaps ratios are summarised in Table 4.13.

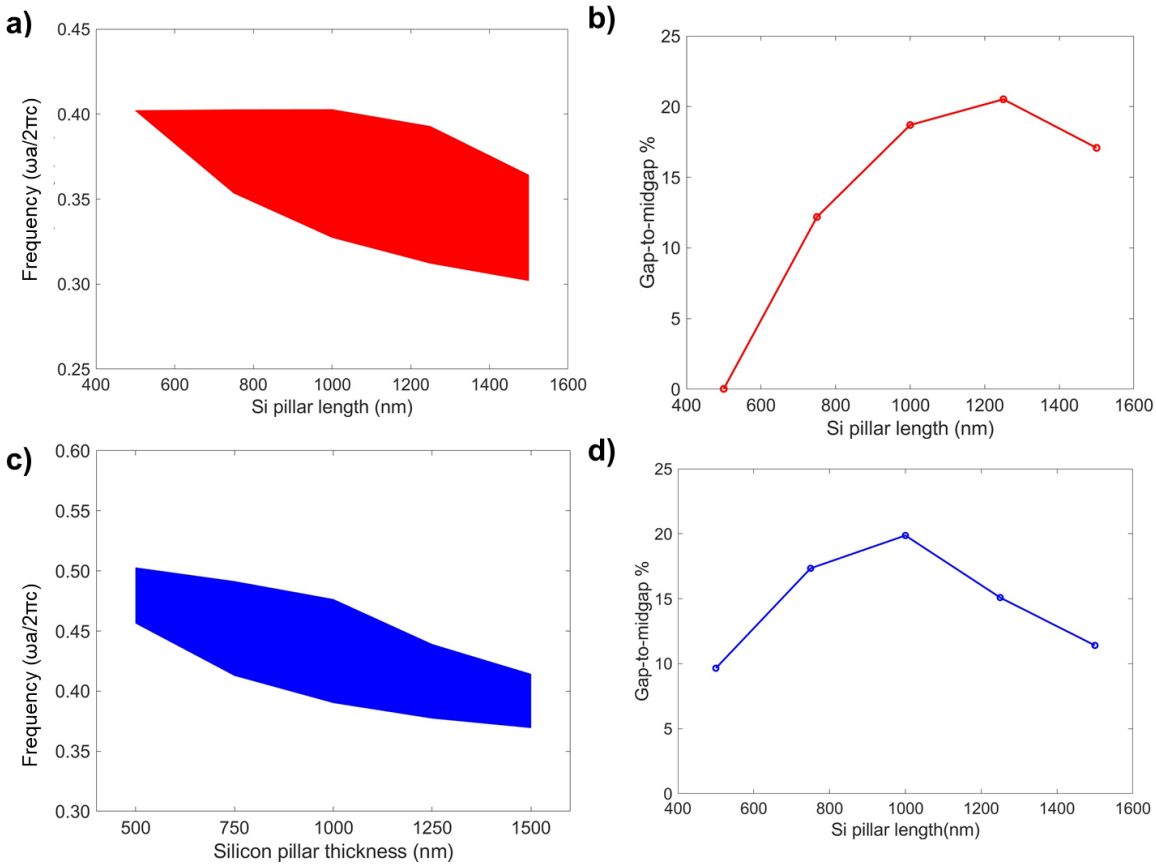

Figure 4.25. Resulting robustness maps and gap-to-midgap ratio evolution in front of the silicon pillar length for air (a, b) and water (c, d) background considering a bottom silicon oxide pillar of 1000 nm.

As already mentioned the same analysis as the one shown in Figure 4.25 has been carried out for the 500 nm cladding thickness. Surprisingly, the results for this thickness are very similar to the ones obtained for 1000 nm bottom cladding. This is a very interesting result since it provides room for the adjusting the etching of the silicon oxide as a continuation of the etching of the silicon pillar. This process is not straightforward from the fabrication point of view due to the different nature of these two materials. Further explanation of this process will be described in Chapter 5 in section 5.3.

Background material	PBG min (ωa/2πc)	PBG min (ωa/2πc)	PBG min λ (μm)	PBG max λ (μm)	Gap-to-midgap ratio (%)
Air	0.312	0.392	1.273	1.602	20.52

Water	0.377	0.439	1.139	1. 325	15.09

Table 4.13. Summary of the optimal silicon lengths for the configuration shown in Figure 4.23 b with their gap-to-midgap ratio.

The final structure which will be discussed here is the configuration with a top and a bottom cladding consisting on silicon oxide pillars (Figure 4.23 c). This is the only configuration where the cladding distribution is symmetric, as explained before. In theory this should help a better light confinement within the silicon pillar than for the other simulated cases. The construction of the simulation is symilar to the one described for a bottom cladding based on a silicon oxide pillar but adding the same configuration at the top. Given the results obtained in the previous analysis, here it has been chosen to keep the silicon oxide pillar top and bottom heights at 500 nm. Again, due to the potential fabrication challenges that this configuration could raise, the etching of a few hundreds of nm of silicon oxide would provide the versatility required by the tolerance of the different etching depths.

In Figure 4.26 the robustness maps for this last three-dimensional configuration are shown. The tendencies are very similar to the ones observed for the configuration with only a silicon oxide pillar at the bottom (Figure 4.23 b). In this case as well, the optimal band gaps are found for a silicon pillar with a height of 1000 nm both for air and water background. The gap-to-midgap in these cases is 22.31% and 19.37% respectively. The summary of these bandgaps can be found in Table 4.14. In this case all the bandgaps fall in the region of interest and the optimal heights coincide both for air and water. In addition, the gap-to-midgap ratios are slightly larger than the ones found for the configuration shown in Figure 4.23 b, but not as much as having a symmetrical cladding.

The summary of these results is that the optimal height of the silicon pillars should be around 1000 nm. This ensures in almost all the configurations a good quality PBG for both backgrounds. Regarding the cladding, the results do not show a clear winning configuration, but in all three discussed configurations a PBG is opened below the light cone delimitation.

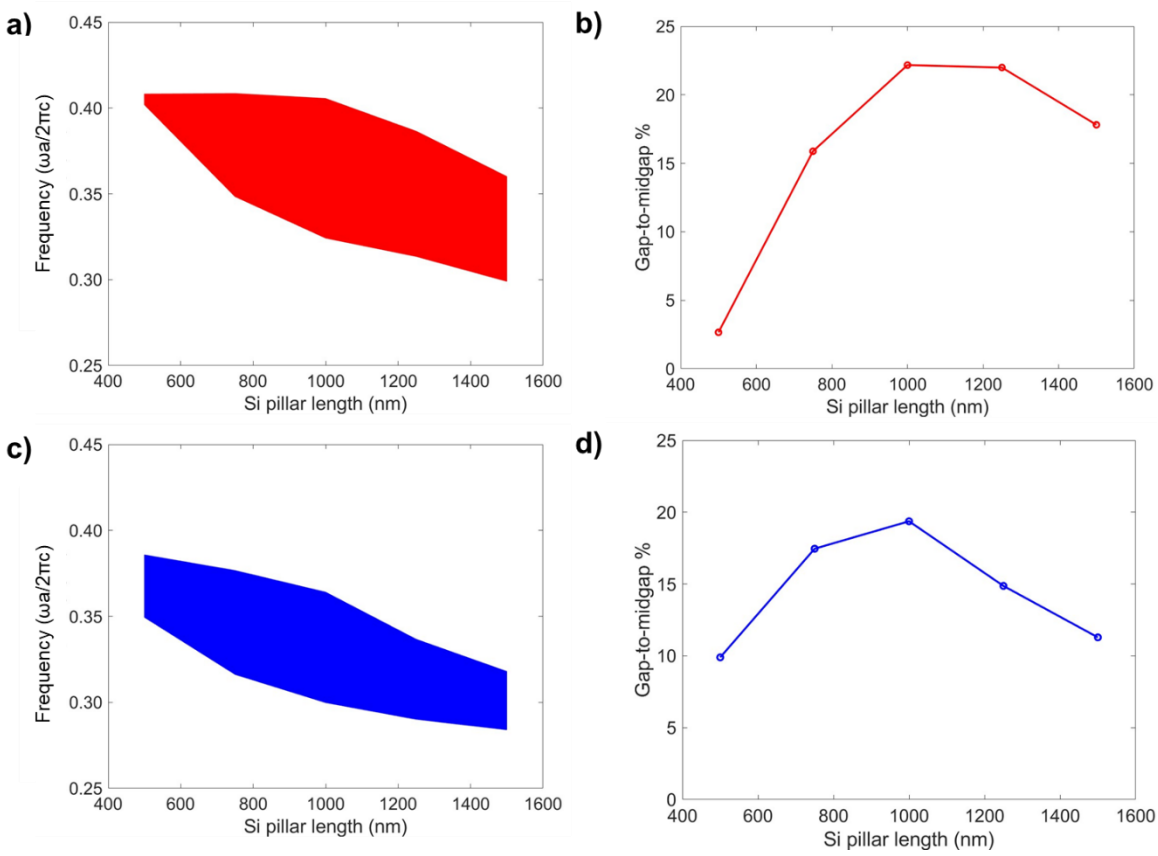

Figure 4.26. Resulting robustness maps and gap-to-midgap ratio evolution in front of the silicon pillar length for air (a, b) and water (c, d) background considering a bottom and top silicon oxide pillar of 500 nm.

Background material	PBG min (ωa/2πc)	PBG max (ωa/2πc)	PBG min λ (μm)	PBG max λ (μm)	Gap-to-midgap ratio (%)
Air	0.324	0.406	1.233	1.542	22.31
Water	0.300	0.364	1.373	1.668	19.37

Table 4.14. Properties of the optimal band gaps for air and water backgrounds for a structure with a silicon oxide pillar at the top and the bottom of the silicon pillar.

These results have been used for choosing the SOI substrates used in the fabrication in Chapter 5. In addition, it has motivated the exploration of combined dry etching processes of different materials, as will be shown in the next chapter.

CHAPTER 5.
FABRICATION RESULTS

5.1. Cleanroom processes

The processes used during this thesis have varied depending on the purpose of the different samples fabricated. The types of samples can be divided in two main groups. The first relates to the samples used for the optimisation of the different fabrication steps and first non-photonic related tests (e.g., biocompatibility, wettability). The second comprises those samples designed to be used for photonic applications. The main reason for this difference between these two groups of samples is the type of wafers processed: silicon in the first case and SOI in the second. Moreover, for photonic applications two different types of SOI wafers have been used: commercial monocrystalline SOI substrates and self-fabricated amorphous or polycrystalline SOI wafers (henceforth referred to as “pseudo-SOI” wafers). In either case, the use of SOI wafers increases the expense of either buying or processing them, as well as the time for preparing the samples for their further processing. For this reason, for the optimisation of processes in the cleanroom and tests that do not require a bottom SiO_2 cladding, Si wafers have been used.

In addition, depending on the type of optimisation and the possibilities of the different processing tools, these silicon wafers have been used either fully or cut into small chips, which were bonded to carriers to make the process more agile. These processes will be explained below in more detail. Depending on the minimum feature size of the designs

fabricated, different types of lithography have been used and, therefore, slightly different pre- and post-processes and conditions have been employed.

Therefore, while different process flows have been used, this thesis is limited to those that have been mostly widely used. Special attention has been paid to the optimisation of the process based on silicon wafers.

The keys steps are depicted in Figure 5.1. The processes carried out in the cleanroom can be divided in three main groups: the lithography, the masking, and the etching (Chapter 3 section 3.1). The lithography involves the deposit of the electron-sensitive resist, the pattern exposure, and the resist development (steps a, b, and c in Figure 5.1). This is followed by the process of the hard mask creation, which involves the metallisation of the developed samples and the subsequent lift-off for removing the remaining resist with metal on top (steps d and e in Figure 5.1). And finally, the anisotropic etch is carried out using dry etching techniques.

In the following section we will describe the process flow carried out with electron beam lithography.

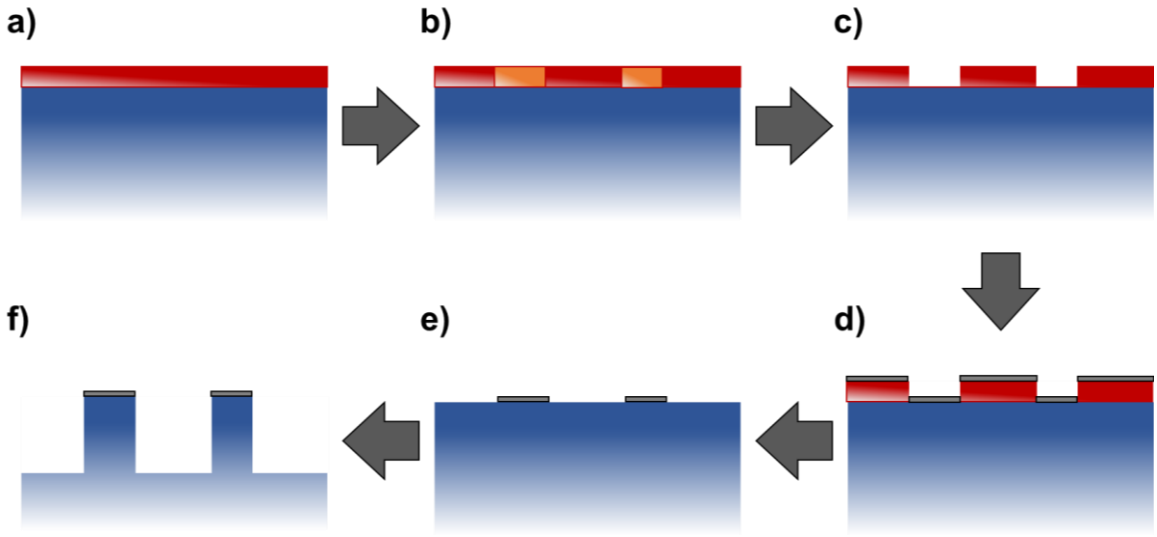

Figure 5.1. Basic process flow carried out in the cleanroom.

As explained in Chapter 3 section 3.2, the fabrication of structures below 1 µm feature size require lithographic processes with higher resolution than the common UV lithography. In this thesis the use of electron beam lithography has been employed to

expose areas containing the pillars with radii down to 40 nm. Here, the fabrication of photonic crystal structures on SOI substrates will be considered. It must be pointed out that the fabrication on silicon wafers is carried out in a similar way to the one described here. The steps required uniquely for SOI wafers are indicated where needed.

5.1.1. Pre-processing of SOI wafers

As previously mentioned, both commercial and pseudo-SOI substrates have been used in the fabrication. The commercial substrates have been provided by Siegert Wafer (Aachen, Germany). Several 6” wafers were purchased with a top silicon layer (device) of 1.5 µm nominal thickness with a tolerance of a 20% on top of a BOX of 1 µm nominal thickness with a tolerance of a 5%. The primary reason for using the commercial substrates was the possibility to use monocrystalline silicon with a resistivity suitable for the photonic applications (1 - 5 Ω·cm). However, as explained in Chapter 4 in section 4.3, the bandgap opened for 1.5 µm thick pillars is narrower than the one opened with shorter pillars. Therefore, the silicon layer had to be thinned down to the optimal thickness. The strategy used to do so has been a repeated combination of cycles of silicon thermal oxidation followed by wet etching of the top silicon oxide layer. Thanks to the oxidation process the part of the top silicon layer was converted into silicon oxide and then removed, leaving a silicon layer thinner than before the oxidation. This process was carried out at 1100 °C in water steam (wet oxidation) in an Anneal Oxide Furnace.

Considering the nominal value of the device layer and, according to the simulations shown in Chapter 4, a final layer between 800 - 1000 nm should be aimed for. The approximate grown oxide layer can be estimated according to the information provided by the theory and as schematically depicted in Figure 3.5 and estimated in equation 3.6 (Chapter 3 section 3.3). Thanks to the oxidation curve, the oxidation time can also be estimated (Table 5.1). However, these processes require time and to better ensure the desired device silicon thickness is reached, this oxidation step was divided into two different oxidation processes.

The etching of the silicon oxide has been carried out using a buffered hydrofluoric acid (BHF) bath at room temperature, where the etching rate is around 79 nm/s. To stop the BHF etching, after this process the sample was rinsed in water for 5 min and spin dried.

Final Si thickness	Si etched thickness	SiO_2 thickness to grow	Oxidation time
800 nm	700 nm	1515 nm	7 h 17 min
1000 nm	500 nm	1082 nm	3 h 45 min

Table 5.1. Considering the device nominal thickness of 1500 nm, the depth of silicon needed to be etched varies depending on the final thickness. Therefore, the oxidised layer varies as well according to equation 3.6. Thanks to the oxidation curves of the furnace used the oxidation time can be estimated as well.

On the other hand, the fabrication of pseudo-SOI wafers has been carried out using silicon wafers. In this case, thermal oxidation is used as well, but only to fabricate the BOX layer, on top of which the silicon layer is deposited. This layer must fulfil specific conditions to be suitable for photonic applications. Using LPCVD at low temperatures (around 560 °C) it is possible to obtain layers of amorphous silicon [78]. his silicon performance is suitable for photonic applications, as indicated in.

5.1.2. The lithographic process

The lithography process starts with the deposition of the resist. For this process the positive resist AR-P 6200 (CSAR) has been used. The CSAR resist is a positive tone resist widely used for e-beam lithography. The resist is spin-coated using a Süss Micro Tec Gamma 4M Spin coater. A resist layer of 180 nm thickness is achieved spinning the wafer at 4000 rpm for 60 s and soft baked at 180 °C for 180 s.

After the resist deposition and prior to the electron beam exposure, a discharge layer must be deposited on top of the resist to minimise the charge build-up in the isolating SiO_2 layer by promoting the electron evacuation towards the ground during the exposure. This step is carried out only for SOI samples. For this, a 20 nm layer of thermally

evaporated Al is deposited using a Nano36 Thermal Evaporator System. As explained in Chapter 3, the thermal evaporation allows the deposition of a metal without the presence of electrons, as is the case in electron beam assisted deposition, which could give rise to unwanted resist exposure.

The exposure is carried out using a Jeol JBX-9500-FS electron beam writer. This machine operates at 100 keV, allowing currents down to 0.2 nA and operates with a maximum man writing field of 1 x 1 mm^2 and sub-writing field of 4 x 4 μm^2. Depending on the minimum feature size of the design exposed, the current used during our exposures has been varied from 2 nA to 20 nA, corresponding to apertures of sizes of 60 µm and 110 µm, respectively. Under these conditions the minimum spot size attainable can be 4 nm and 20 nm, respectively. Doses of 300 $\mu C/cm^2$ yielded good results. However, depending on the design, PEC had to be used. This correction modulates the dose across the pattern taking into account that the exposure of the different features on the wafer affect the exposure of those in close proximity. To do so, the commercial BEAMER® software has been used to simulate the dose map. In Figure 5.2 the colour distribution shows the different doses across one of the masks used.

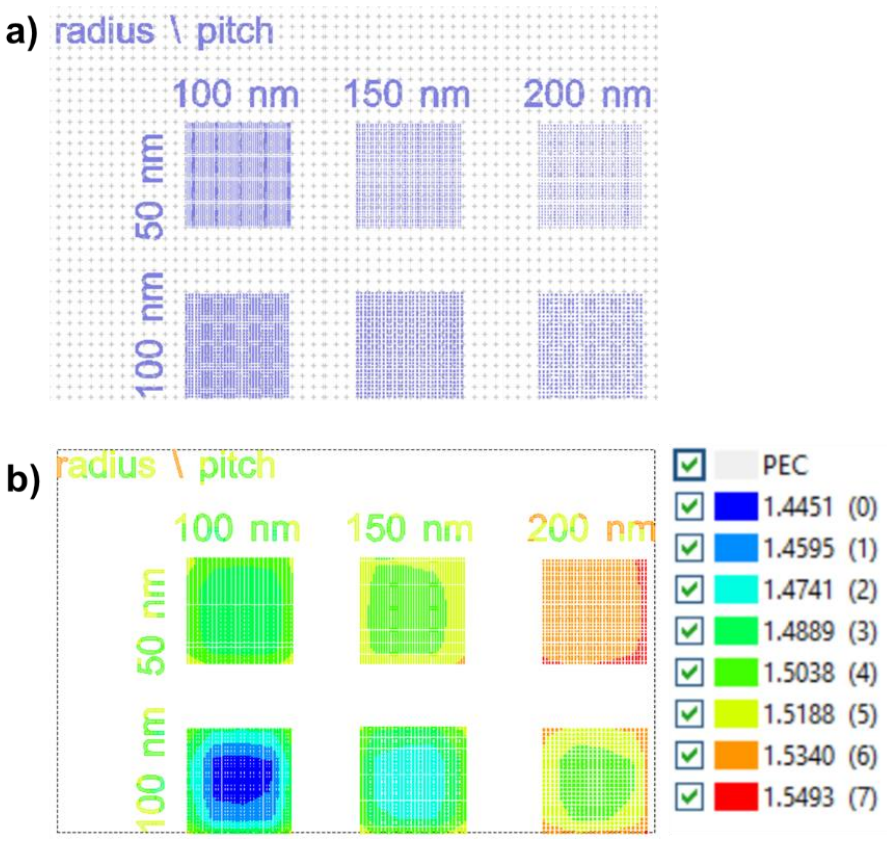

Figure 5.2. Example of the dose variation carried out by the BEAMER® software for some combinations of radii and pitch of the pillars. The colours represent the different modulations. Blue represents the lowest modulation and red the largest.

Alternatively, a Raith eLINE Plus electron beam lithography system has also been used for the exposure of samples with features larger than 40 nm but still smaller than 1 µm. This system operates similarly to SEM and can thus be used both as a SEM and as an electron beam writer. The operation conditions are slightly different from those used in the Jeol system. A maximum voltage of 30 keV can be used in this system, limiting the current and, therefore, the beam spot size, and making the writing much slower. To expose a layer of 180 nm of CSAR resist using a voltage of 20 keV and an aperture of 20 µm, doses of 100 µC/cm^2 have been successfully used.

After the exposure the discharge layer and the exposed resist are removed using two different Laurell EDC650 systems, each of them dispensing different solvents. The first sprays Tetramethylammonium Hydroxide (TMAH) for 60 s to remove the 20 nm of Al,

followed by a water rinse. The second develops the exposed CSAR resist using AR-60-546 developer for 60 s followed by 2-propanol (IPA) rinse.

5.1.3. Hard mask creation, etching and post-processing

After the exposure and development, the metal used to create the hard mask is deposited. A 20 nm Al mask is used throughout this thesis. This mask is deposited on top of the developed wafer and, thus, on top of the remaining resist and the opened areas using a Temescal e-beam evaporator set to a deposition rate of 2 Å/s. As discussed in Chapter 3, the use of a PVD technique is necessary since a directional deposition is required to prevent the coverage of the resist sidewalls.

Prior to the lift-off process the samples are left overnight at room temperature to ensure the correct adhesion of the metal both on the open substrate and on top of the resist. The lift-off process removes the resist underlying the aluminium layer and it involves placing the wafer in a Shipley Microposit® Remover 1165 [95] bath with ultrasound. This chemical is a mixture of several organic solvents capable of dissolving the resist. The use of ultrasounds helps the deadhesion of the resist and prevents the redeposit of parts of the metal on the substrate after the end of the process. The lift-off reaction is stopped by first rinsing in IPA and then water, before completing with a spin-dry.

Finally, the etching is carried out in a Deep Reactive Ion Etching of Si / SPTS-Pegasus. This step is crucial to achieve the final shape of the nanostructures and its use with silicon wafers is discussed in the following sections.

This applies as well to the post processing. The samples further used for optical measurements were postprocessed to remove the remaining e-beam deposited Al masking layer. To do so, the sample is placed again in the Laurell EDC 650 system and sprayed with TMAH for 40 s, followed by rinsing with water.

5.2. Fabrication requirements

The fabrication steps and the final resulting samples are paramount for the success of this project. For this reason, it has been decided that the fabrication results must fulfil specific criteria to consider the samples valid for the project. We divided these criteria into three categories in order of priority:

- Shape and reproducibility.
- Presence of fabrication residuals.
- Adaptability and scalability towards mass-production.

5.2.1. Shape and reproducibility

As discussed in the previous chapter, the shape of the pillars is fundamental for the performance of the photonic crystal. Therefore, the highest priority in the developed fabrication process is the final shape of the pillars. The key to obtaining the pillars is the reactive ion etching process. In the following we describe the multiple factors we have considered as quality control, listed in order of priority:

1. Side wall roughness: the roughness of the side walls can introduce undesired light scattering, resulting in the reduction and, even, the total loss of optical performance. For this reason, the target has been to obtain side walls as smooth as possible, avoiding the presence of scallops or irregularities. To this point, the Bosch and pseudo-Bosch processes have been discussed and evaluated.
2. Side wall verticality: the final shape of the pillars is important for the proper optical mode confinement in the structure. Pillars with as cylindrical shape as possible has been targeted and so much effort has been put into the vertical profile of the pillars. Specifically, the focus has been on the side wall angle and tapering achieve a 90° angle between the pillar side wall and the substrate, and to ensure the constant radius of the pillar in the vertical direction, respectively.
3. Dimension accuracy and repeatability: the homogeneity of the photonic crystal and across different samples is important for the correct characterisation and

further use of the samples fabricated. Here, two parameters have been prioritised: firstly, the obtention of the desired dimensions of the pillars and, secondly, the variability of these dimensions not only within one sample but, as well, across different samples.

These different requirements are broadly discussed later during the reactive ion etch optimisation process discussion.

5.2.2. Presence of fabrication residues

The presence of fabrication residues on the samples is important not only for the final optical performance of the samples but also for the biocompatibility of the substrates. For this reason, after fulfilling the previous requirements, the following have been taken under consideration.

1. Nanograss formation: the presence of nanograss is a side effect of the Bosch reactive ion etching step and a result of the gas combination[96]. Its presence not only perturbs the optical and mechanical performance of the photonic crystal but can also affect the tissue interaction with the system. Therefore, its presence is in all means to be avoided.

2. Fabrication remains: due to the processes carried out, several remains of them are left on the surface. Even though first compatibility tests have shown promising results, the actual impact of this remains to be studied. Nonetheless, their complete removal or the awareness of their presence is important to explain possible future problems. For this reason, analysis of the chemical composition of the final samples have been performed.

5.2.3. Adaptability and scalability towards mass-production

Despite being outside the core scope of this thesis, the scalability has, at least theoretically, been considered. Many of the processes described here have been carried out on relatively small surfaces to make their optimisation more agile. However, it is

expected that after this thorough process the fabrication should be transferable to larger surfaces, i.e., full wafers, and, therefore, scale the number of structures done per process. For this reason, the following have been taken under consideration during this project.

1. Flexibility of the process: even though most of the processes described here are developed with similar structures and surfaces in mind, it should be taken into account that in the future, and for the device integration, the process should be adaptable to new steps and configurations.
2. Process duration: the duration and optimisation of the fabrication is important for future potential mass-production of devices. The use of alternative systems carrying out the same process on larger areas or with faster performance have been considered: for example, e-beam lithography might be replaced by DUV. While this alternative has not been employed in this thesis due to the difficulty in creating new physical masks for each new pattern, theoretically, no practical obstacles that would significantly affect the shape and distribution of the nanostructures are expected.

With the requirements that the fabrication should fulfil, in the next sections the key parameters, especially in the reactive ion etch step, are discussed.

5.3. Optimisation of the RIE step

As described in Section 3.4, the reactive ion etch step offers many different approaches and processes. This step is key for the success of the fabrication and the final performance of the photonic crystal. For this reason, it is the process that has been the focus of discussion and optimisation. In this system, there are many parameters that affect the etching step. In this thesis special attention has been paid to two of them:

1. The etching/passivating gas flow ratios.
2. The platen and coil power values.

In the following sections the optimisation of the dry etching of the pillars has been performed by varying the values of these parameters. The optimisation has been carried out on chips coming from full 4" wafers of silicon processed as described in section 5.1. These chips contained a 1 x 1 mm^2 processed area containing pillars of 100 nm radius and pitch 500 nm, distributed in an hexagonal array.

The initial discussion is carried out modifying an already existing recipe in the system used for the etchings, henceforth referred to as nano1.42. The pre-set parameters of this recipe are summarised in Table 5.2.

	C_4F_8 (sccm)	SF_6 (sccm)	Coil Power (W)	Platen Power (W)	Pressure (mTorr)	Temperature (°C)
nano1.42	75	38	800	40	4	-19

Table 5.2. Etching conditions of the original recipe nano 1.42.

The result of this initial recipe for 5 min is shown in Figure 5.3. The pillars created using the nano 1.42 recipe are successfully etched. However, taking into account the requirements laid out in section 5.2, they are far from the desired results. The main issue is the roughness of the side walls and the over etch of the top part of the pillars which conflicts with the first requirement (subsection 5.2.1). As can be seen in Figure 5.3, this roughness is present across the entirety of the pillar's surface. Furthermore, the top part of the pillars has been over etched, likely due to an overly aggressive process. This

recipe has therefore offered a good starting point but required an iterative process of optimisation of the before mentioned parameters. In the following subsections a summary of the results obtained during this optimisation are depicted.

In addition, another major goal has been to prevent the raise of needle-shaped nanostructures, known as nanograss. This is a common side effect in the Bosch and pseudo-Bosch processes that occurs due to an incomplete passivation layer etching of the horizontal surfaces creating uncontrolled local micro masks, as briefly described in the subsection 5.2.2.

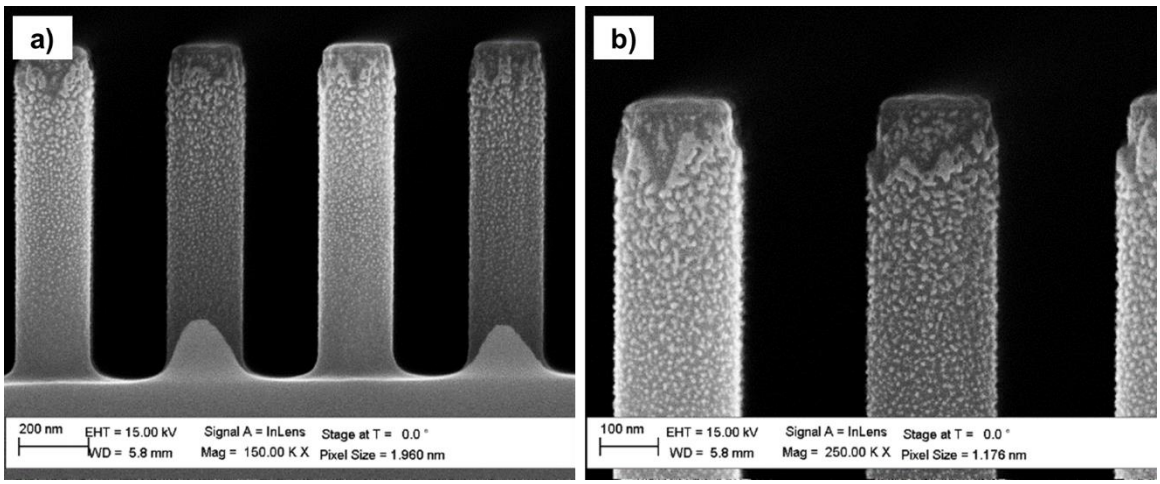

Figure 5.3. SEM images of the resulting etched pillars using the original nano 1.42 recipe for 5 min. An Al mask with pillars of 100 nm radius and 500 nm pitch.

5.3.1. Type of carrier and attaching approach

As described in the fabrication process section of this chapter (section 5.1), the chips have been attached to a carrier substrate to be able to introduce the sample into the etching chamber. This step already introduces two variables into the overall process: the type of carrier to be used and the type of bonding used. The impact of these two variables is the load introduced in the process and the proper clamping of the chip and cooling of the substrate, respectively.

Regarding the carrier wafers, two types of carriers have been used: silicon wafers and silicon wafers with a 940 nm top layer of silicon oxide. It is important to point out the

impact on the process of the use of the right carrier since the load of material to be etched will change. The load is defined as the substrate susceptible to be etched down expressed as a percentage of the overall substrate exposed in the chamber.

Substrate	Total exposed surface (cm^2)	Total masked surface (cm^2)	Total non-masked surface (cm^2)	Load percentage (%)
Chip	2.25	0.01	2.24	99.56
Chip on Si carrier	78.54	0.01	78.53	99.99
Chip on SiO_2 carrier	78.54	76.3	2.24	2.85

Table 5.3. Summary of the calculation of the loads used during the dry etch step depending on the carrier wafer used.

Considering that all the chips have roughly the same dimensions (1.5 x 1.5 cm^2) and their masked area is also constant (1 x 1 mm^2) the surface etched on each chip is approximately 2.24 cm^2 (first row of Table 5.3). Only 4" substrates have been used for testing (with a surface area of 78.54 cm^2), therefore the impact of the load introduced or not by the carrier entails a large amount of the overall surface. As shown in Table 5.3 the load of the substrate is an important factor for the etching and must be taken into account. The overall load when using a silicon 4" wafer as a carrier is close to 100%, while when using a silicon oxide covered wafer the load is below 3%.

The use of a silicon wafer as a carrier will impact the etching precisely because it is silicon that is etched during the process. This type of carrier will increase the load of material to be etched (almost to 100%) and, therefore, part of the gases introduced in the chamber will not only be used to etch the chip but also to etch the carrier. This redistribution of the gases across the full 4" wafer will impact on the etching rate of the structures, which will be slowed down. Thanks to the fact that the etching is slow and controllable, the etching of high aspect ratio structures is favoured using a silicon carrier, which fulfils most of the requirements listed in section 5.2. The only drawback of using silicon wafer carrier is the fact that the carrier is also etched during the optimisation and, consequently, working with chips, the carrier needs to be replaced frequently.

Nevertheless, the future of the project considers large production of chips which will be processed on full silicon wafers and, therefore, the load inside the etching chamber will be closer to the one using silicon carriers than to the one using silicon oxide layered carriers.

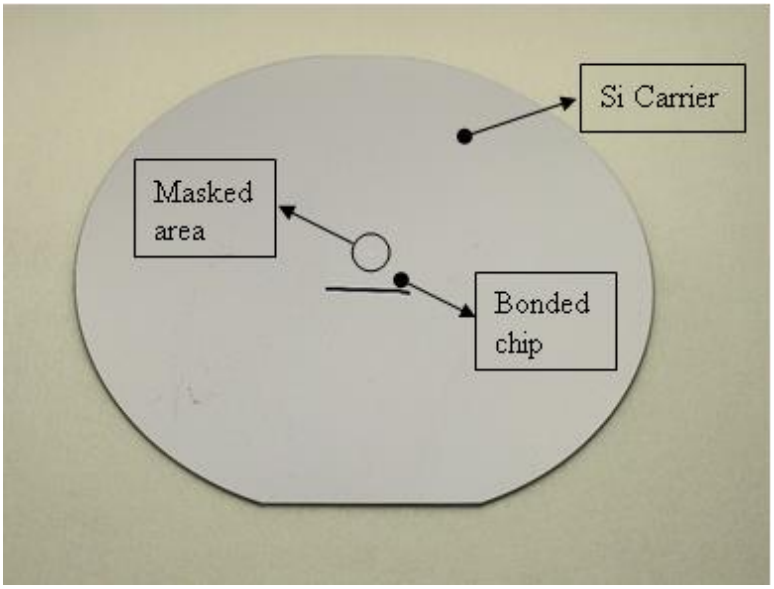

Figure 5.4. Image of a chip bonded on a Si wafer with Crystalbond™.

On the other hand, silicon oxide is used as a hard mask for dry etching of silicon. Therefore, the use of a carrier with a top layer of silicon oxide represents the opposite situation. The load is reduced to 3% and therefore the distribution of gases across the wafer is focused only on the non-masked area. This makes the etching more abrupt using this type of carrier and might become a problem when etching very narrow and high aspect ratio structures. However, it is suitable for etching wider structures, since the etching is faster and steeper side walls can be obtained.

A good example of the impact of the load can be seen in the Figure 5.5. The exact same process has been carried out using a silicon carrier wafer (left) and an oxidised silicon wafer (right). Both samples were first attached to the substrates using Crystalbond™ [97] a thermally conducting wax and etched for 5 min using a combination of C_4F_8 and SF_6 with flows of 71 sccm and 42 sccm, respectively, and powers of 1200 Watt and 20 Watt

in the platen and coil, respectively. The chiller temperature had been previously set and stabilised at -19 °C.

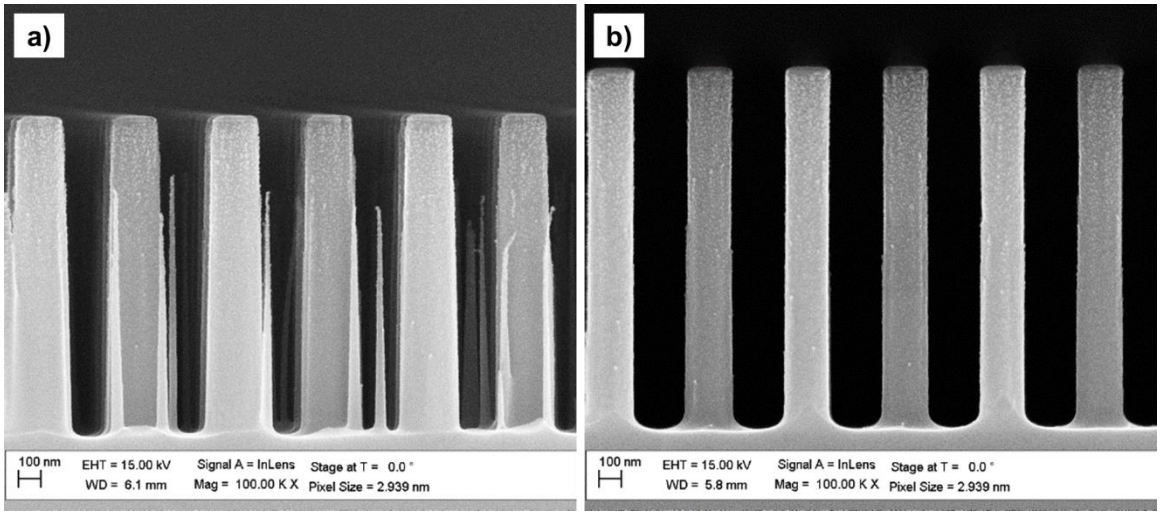

Figure 5.5. SEM images of the pillars etched during 5 min with the chip bonded on a silicon substrate (a) and a masked substrate (b).

The etching produces very different results between the two samples. Under the same conditions, when using a silicon oxide carrier, vertical side walls and an etching rate of 350 nm/min are achieved, while when using a silicon wafer as carrier, the etching rate drops to 320 nm/min and the side walls show a tapered profile. In addition, in this case when using a silicon carrier, nanograss is etched too, probably because the opening of the passivation layer on the horizontal surfaces is not wide enough.

This same test was carried out using the Bosch process to investigate the impact of the etching when using one carrier or another. The test has been carried out for 50 cycles of switching between the C_4F_8 and SF_6 flows of 25 sccm and 15 sccm for the deposition step and 5 sccm and 40 sccm for the etch step. The coil and the platen powers have been 1000 W and 0 W, respectively, during the deposit step and 1000 W and 0.1 W during the etch step, respectively. The deposit step time has been ramped from 4.8 s to 3.2 s and the etch step has been kept constant at 2.5 s during all the cycles. Throughout the process the temperature of the chiller has been kept at -19 °C and a pressure of 4 mTorr.

Thanks to the scalloping, characteristic of this process, the differences when using the different carriers are more noticeable. Figure 5.6 highlights the differences on the etching rate as a function of the load introduced by the carrier.

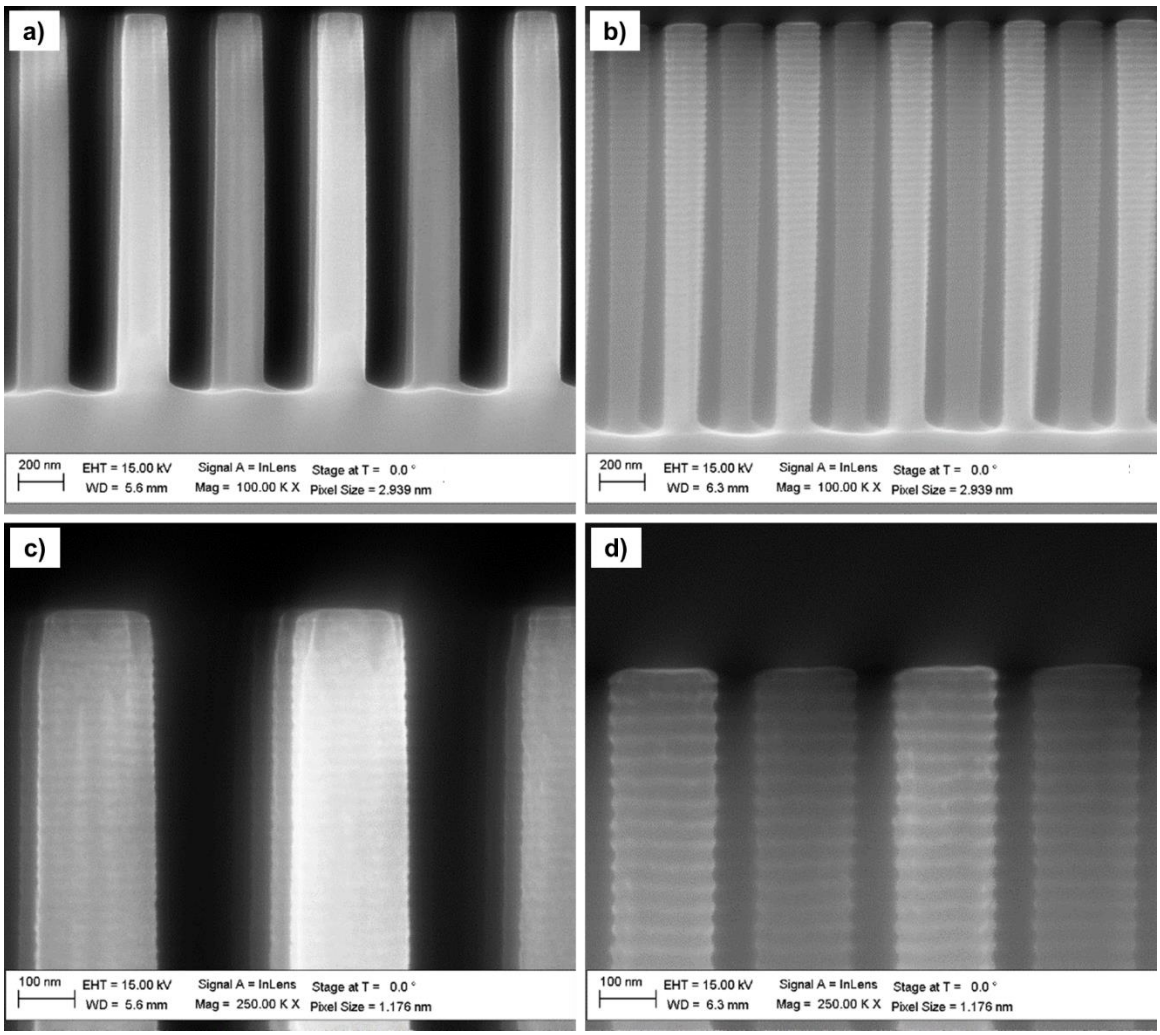

Figure 5.6. Cross-sectional view of the pillars etched using the Bosch process bonded on a (a, c) silicon wafer carrier and on a (b, d) masked wafer. The top images show a general view of the pillars and the bottom row shows the detail of the scalloping effect.

As for the pseudo-Bosch process, in the Bosch process and under the same conditions, the etching rate is slower, and the scalloping better controlled when using a silicon carrier (Figure 5.6 a, and c). On the other hand, the silicon oxide carrier gives rise to a faster etching process and the scalloping is more pronounced due to the etching being more abrupt (Figure 5.6 b, and d). The etching rates are 24 nm/cycle for the silicon carrier and 39 nm/cycle when using the masked carrier. The scallop's depth is, as well,

different for each carrier: 6 nm or 12 nm if using the silicon or the masked carrier, respectively.

During the rest of this thesis silicon wafers have been used as carriers. Even though it might seem that the silicon oxide approach is better for the final pillars' shape, two factors contributed to this decision. Firstly, as previously discussed, the future of the project will involve the use of full 4" wafers once the volume of the fabrication of chips increases. Therefore, the optimisation of a process on a substrate that matches the goals of the project prevailed over the results shown in Figure 5.5 and Figure 5.6. Secondly, regardless of the good results observed in the etched pillars shown, a fast and abrupt etching rate does not ensure the correct etch of smaller nanopillars or structures based on combinations of different nanopillar sizes. It is important to point out that the discussion of the carrier has been focused on the load introduced by the substrate, but locally, within the masked area, different loads will be considered too. Even though on a smaller scale, one must take into account that any variation of the mask layout will introduce a change on the load and, therefore, changes will occur during the etching process. The choice of using a slower but more controllable process, such as in the case when using silicon carriers, facilitates the control of nanopillar size variations. For these reasons, the parameter optimisation of the etching step has been carried out on silicon carriers (fulfilling the fabrication requirement outlined in 5.2.3).

Another factor that might have had an impact on the etching of the structures is the bonding strategy of the chips to the carrier. Again, two different options were available in the facilities: Crystalbond™ and Galden® HT fluid [98].

Crystalbond™ is a temporal adhesive that is used to bond together different types of materials for multiple purposes. The one used in this thesis (Crystalbond™ 555-HMP) consists of a solid bar at room temperature with a low melting point (90 °C) and provides good adhesion of the chips to the carrier wafers. It can be easily removed from the back of the chips and from the front of the carriers using water or acetone.

The Galden® HT fluid is an inert fluid that offers good heat transfer. This fluid is widely used for cooling systems. It is used as a bonder for the reactive ion etching systems because it can improve the heat transfer from the carrier wafer to the chip.

Tests carried out under the same conditions but using either Crystalbond™ or Galden® HT fluid did not show notable differences in their results. For this reason, throughout this thesis, the attaching system chosen for the samples shown has been Crystalbond™.

5.3.2. Gas flows in the chamber

The parameter discussion started by varying the etching and passivating gases ratios and flows inside the chamber. Firstly, we have established the variation of the relative percentage of the gases inside the chamber but maintaining the overall gas flow at 113 sccm, which is the original flow from the nano1.42 recipe. Once this step has been optimised, the variation of the overall gas flow has been fine-tuned to achieve the best conditions. The optimisation of the dry etch step has not been limited to the variation of the gas flows: the coil and platen powers have been tuned as well. In the following section the power impact is discussed.

The problems observed in the results, using the original recipe nano1.42, are both the presence of thick, rough grains on the surface of the pillars and the presence of nanograss. The origin of these grainy structures could be the remaining of passivation material on the pillars after the etching step. To minimise this grainy structure, the approach has been to impose a slight reduction of the passivation gas (C_4F_8) and the corresponding increase of the etching gas (SF_6). In Table 5.4 the conditions used during the testing are summarised:

Coil Power (W)	Platen Power (W)	Pressure (mTorr)	Temperature (°C)	Etching time (min)
1200	20	4	-19	5

Table 5.4. Summary of the etching conditions during the gas flow tests.

Comparing this table with Table 5.2 highlights differences in the powers between this approach and the original recipe. Following the recipe described elsewhere the power values were set above those of the original recipe.

Considering the results of Table 5.5 and the images in Figure 5.7, several tendencies can be deduced. On the one hand, the variation of the etching rates is inversely proportional to the amount of etching gas (SF_6) introduced in the chamber. This tendency can be observed in the pillar height measurements and, consequently, in the etching rate (Table 5.5, first and second columns).

The evolution of the pillar diameter along the vertical axis has been evaluated too. The analysis of this parameter already discards some of the gas flow combinations explored due to the large difference between the top and the bottom diameter values (Table 5.5, third and fourth columns). It must be kept in mind that one of the requirements of this project is to have pillars with side walls as vertical as possible. Large variations of the diameter along the vertical direction can be detrimental for the optical performance of the pillars.

Another feature to consider is the side wall roughness. In all cases some roughness appears on the side of the pillars. Even though the most prominent case is the wreck of the top pillar in the proportion 67 sccm of C_4F_8 and 46 sccm of SF_6, probably due to a too abrupt etching. Considering all these parameters it seems that the proportion of 69 sccm of C_4F_8 and 44 sccm of SF_6 (Figure 5.7 b) is the gas proportion that better fulfils all the requirements.

The most alarming feature, however, is that in all cases nanograss appeared in between the pillars. It is evident that when increasing the amount of C_4F_8 (the passivation gas) in the chamber, the density of nanograss increases. This observation is in line with the fact that nanograss appears due to the creation of uncontrolled micromasking in random areas of the silicon surface. Due to the increase of the passivating gas (and reduction of the etching gas), the passivation layer at the base of the nanopillars is not properly removed by the etching gas, resulting in the micromasking. The first strategy to avoid this micromasking is to maintain the flux of C_4F_8 but increase the flux of SF_6. This has been carried out using the C_4F_8 flow at 69 sccm and changing the SF_6 to 46sccm and 48 sccm (Figure 5.8 a and b, respectively).

It can be seen how this change does not eliminate the presence of nanograss completely. Therefore, the change of the gas proportions should be combined with a change in other parameters, such as the applied powers.

To summarise, the result of varying the gas ratios has shown to have an impact on the pillars' shape, the etching rates, and the presence of nanograss. Therefore, and after evaluating the different features and keeping in mind the fabrication requirements of the process, the ratio of 69 sccm of C_4F_8 and 44 sccm of SF_6 has been selected as the starting point for further optimisation and discussed in the following section.

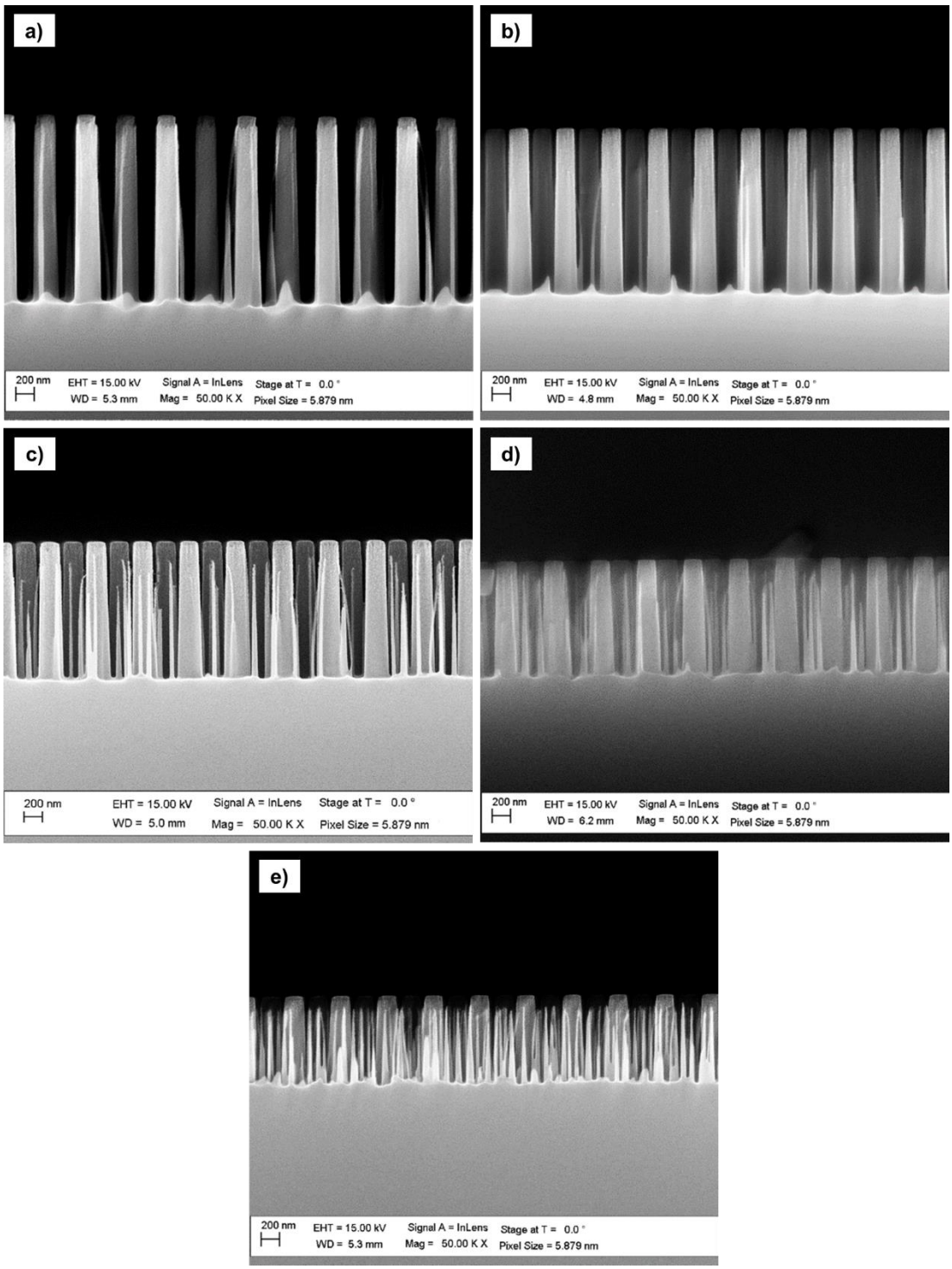

Figure 5.7. Cross-sectional views of the etched pillars with different gas concentrations keeping the total flow to 113 sccm. The gas flows used for the diferent samples shown in the images are: (a) 67 sccm of C_4F_8 and 46 sccm of SF_6, (b) 69 sccm of C_4F_8 and 44 sccm of SF_6, (c) 71 sccm of C_4F_8 and 42 sccm of SF_6, (d) 73 sccm of C_4F_8 and 40 sccm of SF_6, and (e) 75 sccm of C_4F_8 and 38 sccm of SF_6.

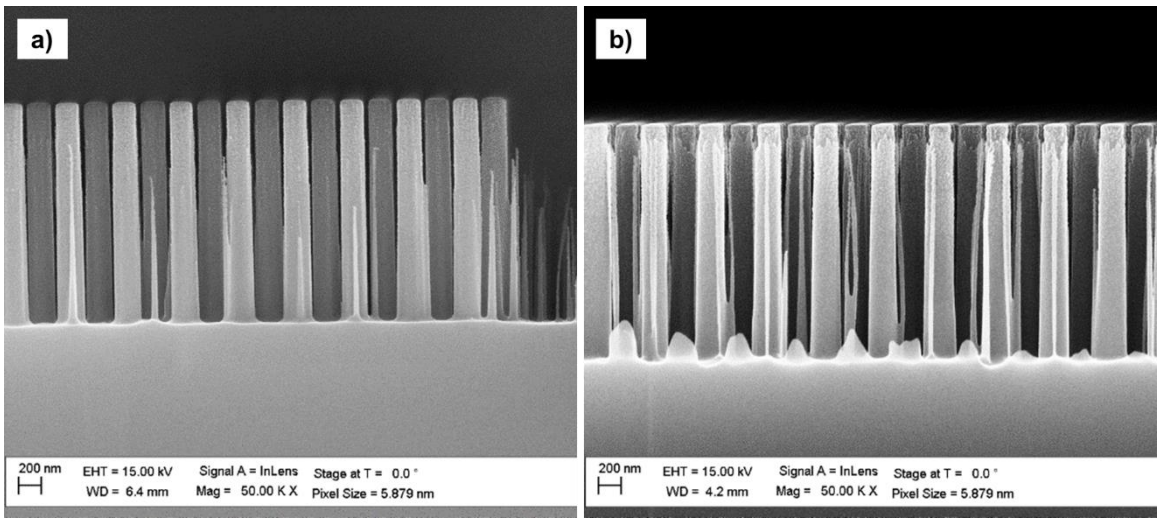

Figure 5.8. Cross-sectional SEM images of the pillars after varying the gas proportions inside the chamber. (a) Corresponds to the 69 sccm and 46 sccm flows of C_4F_8 and SF_6 while (b) corresponds to 69 sccm and 48 sccm flows of C_4F_8 and SF_6.

5.3.3. Platen and Coil powers

It is difficult to decouple the effect of the different parameters on the final etching result, but if in the previous section the gases played an important role in the balance between the passivation/etching, here the coil and platen powers will play a role on the chemical/physical etching processes. In Table 5.5 the parameters used are summarised:

C_4F_8 (sccm)	SF_6 (sccm)	Pressure (mTorr)	Temperature (°C)	Etching time (min)
69	44	4	-19	5

Table 5.5. Summary of the etching conditions fixed during the power conditioning.

The different power values used, and the corresponding results are summarised in Table 5.6 and the resulting pillars are shown in Figure 5.9. As one can observe, changing the power of the coil and the platen completely removes the presence of nanograss except for the power combination employed in the previous section (1200 W of coil power and 20 W of platen power) and the sample resulting from 1200 W coil power and 40 W platen

power. The rest of the samples, however, present some features which in the previous section were less prominent, such as the pillar tapering and top pillar over etch.

Coil / Platen power (W/W)	Pillar height (nm)	Etching rate (nm/min)	Top pillar diameter (nm)	Bottom pillar diameter (nm)	Nanograss density
800 / 20	1373	275	236	171	None
1000 / 20	1640	328	193	206	None
1200 / 20	1821	364	193	260	Low
800 / 40	1513	303	200	140	None
1000 / 40	2013	403	173	193	None
1200 / 40	2113	423	170	224	Low

Table 5.6. Results of the measurements carried out using SEM images of the different power conditions discussed.

From Table 5.6, and Figure 5.9, it can be seen that for coil powers of 800 W in both cases the tapering of the structures is pronounced (Figure 5.9 a and d). A variation up to 60 nm can be observed between the top and the bottom of the pillars meaning that the etching at the bottom is larger than at the top.

On the other hand, when applying a platen power of 40 W (Figure 5.9 d – f) the top part of the pillars is over etched or even wrecked. This can be explained because the platen power promotes the directionality of the etching, producing a stronger bombardment of the top part of the pillars, and destroying the mask and the passivation layer created. While this effect can also be observed in the images of the pillars etched with 20 W platen power, the damage created by the bombardment here is much less.

In summary, from the results of the variations of the coil and platen powers, it seems that the best power conditions are 1000 W and 20 W, respectively. The choice of these values over the other conditions tested has been motivated by the fact that the tapering of the pillars is minimal compared with the other conditions, the top pillar is mostly

preserved, even though it still suffers some over etch and damage, and the negligible presence of nanograss. The only persistent observation over all the etchings carried out is the presence of a consistent but light roughness on the side walls.

Even though the results after the tunning of first the gases and then the powers have yielded promising results, the impact of these variations cannot be decoupled. A final fine-tuning of both the gas ratios and the power values has been carried out to obtain the optimal etching conditions for the pillars. The different conditions considered for this optimisation are summarised in Table 5.7. Consistent with the previous tests, the pressure in the chamber has been kept as 4 mTorr, the chiller temperature at -19 °C, and the etching has been carried out for 5 min.

C_4F_8/SF_6 (sccm/sccm)	Coil/Platen Power (W/W)	Pillar height (nm)	Etching rate (nm/min)	Top pillar diameter (nm)	Bottom pillar diameter (nm)	Nanograss density
71 / 44	1000 / 20	1627	325	210	196	None
69 / 46	1000 / 20	1855	371	211	186	None
69 / 44	900 / 20	1629	326	208	174	None
69 / 44	1000 / 20	1939	388	237	217	Low
69 / 44	1100 / 20	1657	331	195	174	None

Table 5.7. Summary of the resulting measurements using SEM images of the final tuning of the conditions to obtain the optimal etching of pillars.

The results of the different conditions summarised in Table 5.7 are shown in Figure 5.10. At this stage of the optimisation, numerical evaluation might conclude that all the combinations are close to optimal. For this reason, a more subjective reasoning has been used to evaluate the quality of the fabricated samples. Focusing on the verticality of the walls, it seems that the two ideal combinations leading to non-tapered side walls are the those using coil and platen powers of 1000 W and 20 W, respectively, and C_4F_8 and SF_6 flows of 71 sccm and 44 sccm, and 69 sccm and 46 sccm on the other (Figure 5.10 a and b, respectively). In addition, under these two conditions, the side wall roughness is

similar. The condition chosen in this thesis has been 71 sccm of C_4F_8 and 44 sccm of SF_6 flows.

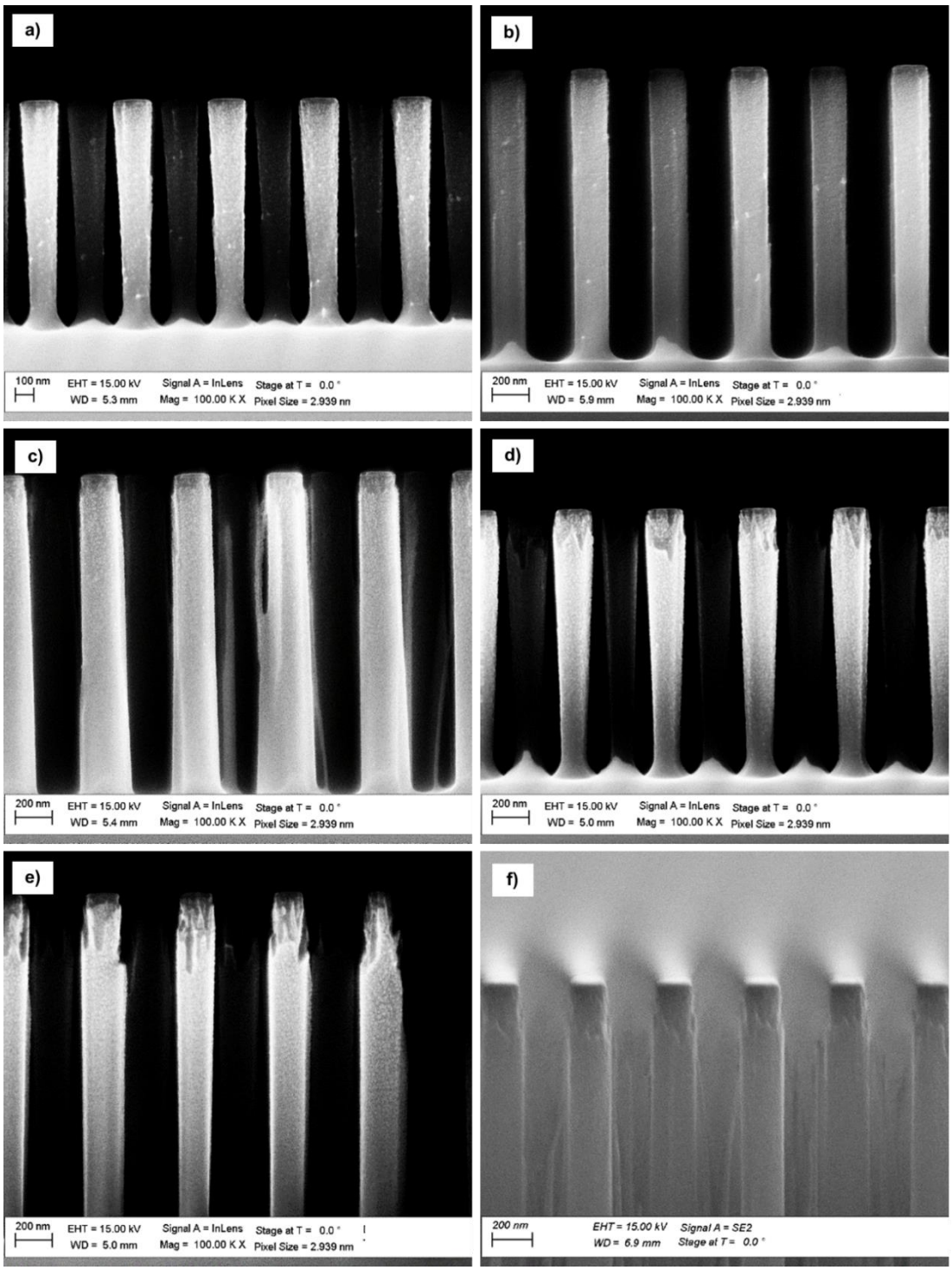

Figure 5.9. Cross-sectional images for the different combinations of coil and platen powers used during the etching process: (a) 800 W and 20 W, (b) 1000 W and 20 W, (c) 1200 W and 20 W, (d) 800 W and 40 W, (e) 1000 W and 40 W and, (f) 1200 W and 40 W of coil and platen power respectively in all cases.

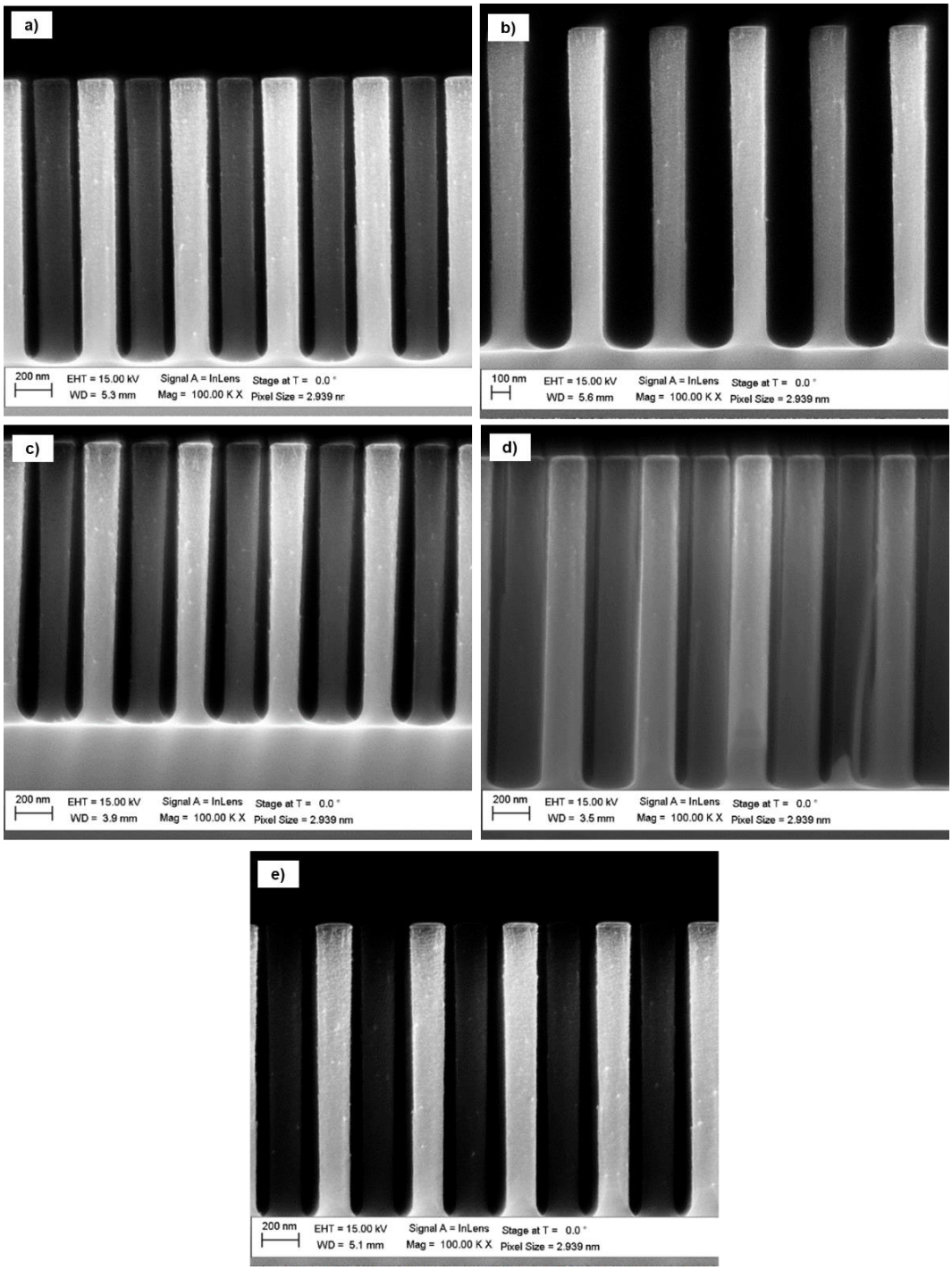

Figure 5.10. Cross-sectional images of the final tuning combinations of gases and powers. Resulting pillars of using (the conditions are expressed as C_4F_8 / SF_6 flows and platen / coil powers): (a) 71 sccm / 44 sccm flows, and 1000 W / 20 W powers, (b) 69 sccm / 46 sccm flows, and 1000 W / 20 W powers, (c) 69 sccm / 44 sccm flows, and 900 W / 20 W powers, (d) 69 sccm / 44 sccm flows, and 1000 W / 20 W powers, (e) 69 sccm / 44 sccm flows, and 1100 W / 20 W powers.

5.3.4. Etching rates

Once the etching conditions of the process have been optimised, other parameters have been considered, the first of which has been the evaluation of the etching rate. As shown in the previous chapter, the optimal length of the silicon pillars can vary, meaning control over the etching depth of the process is important. Under the pseudo-Bosch process, time is the control parameter over the etching depth. The etching depth for the optimised conditions has been tested for etching times of 30 s, 1 min, 3 min, 5 min, 7 min, 9 min, and 12 min. Figure 5.11 shows the etching depth rate.

The etching rate is constant across etching time with and is approximately 333.6 nm/min. This consistency of the etching rate among the different samples offers a positive indication that a high degree of accuracy can be achieved across different samples.

In addition to the etching rate, it is also important that the pillar shapes fulfil the requirements for various etching rates. In Figure 5.12 some of the etched pillars are shown, whose sidewalls remain close to vertical for the different etching times. However, as can be seen in Figure 5.12 d, the roughness of the sidewalls is present in all the cases and increases with the etching time.

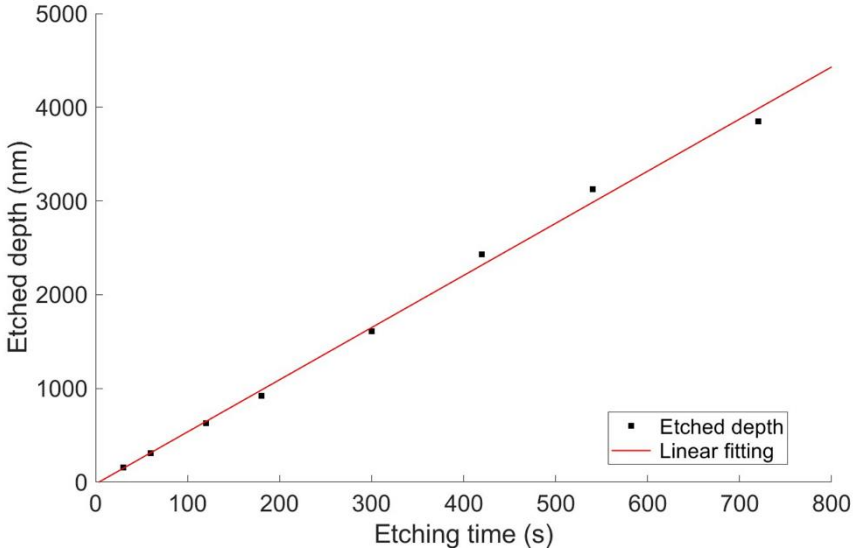

Figure 5.11. Graph representation of the etched depth in front of the etching time, indicating a linear relationship.

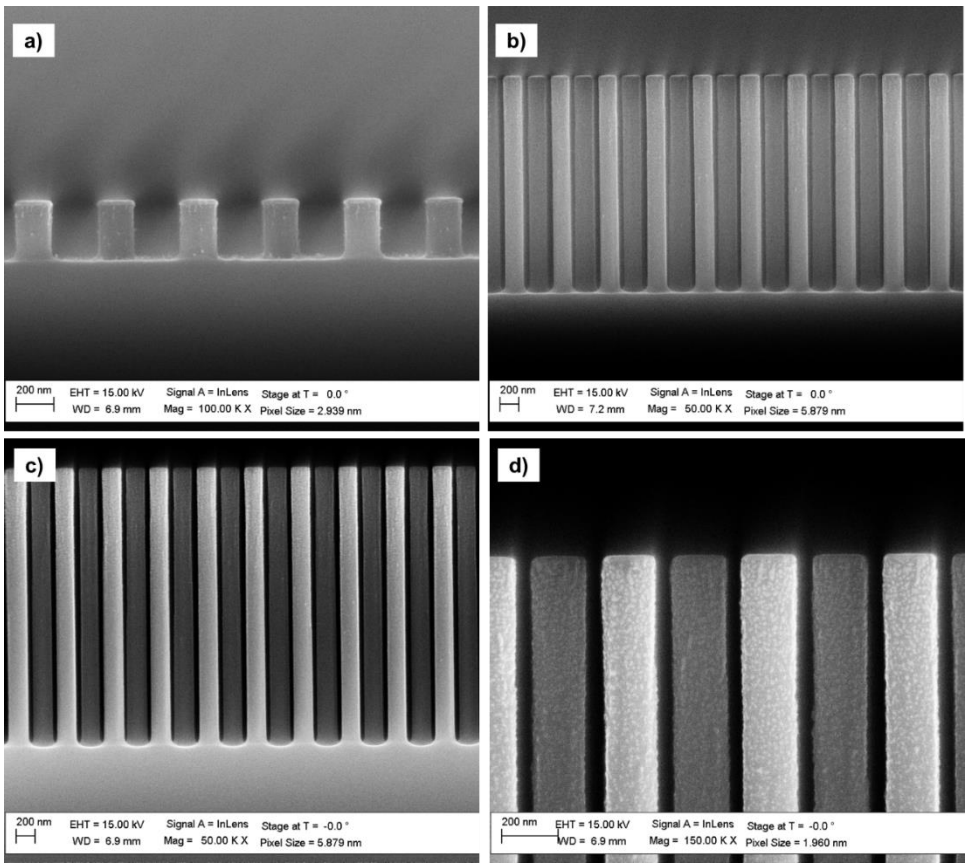

Figure 5.12. Cross-sectional SEM imatges of the different etched fillars for a time of (a) 1 min, (b) 9 min and (c) 12 min. In (d) a magnified image of the top part of the pillars etched for 12 min (c) can be observed.

5.3.5. The impact of the load

As discussed in the first part of this section (5.3.1), the impact of the load when using reactive ion etching processes has been demonstrated. That evaluation is an extreme case in which the load changed from a large value to a much smaller one. However, the effect of the load can also be observed at smaller scales. It is well known that changing the design of the masks will as well change the etching process, i.e., the depth and the shape. In this work the results of etching a hexagonal array of pillars with a pitch of 500 nm but with radii 40 nm, 60 nm, 80 nm, and 100 nm have been studied and displayed in Figure 5.13. Since the pitch has been kept constant the change in radii of the pillars implies a change on the load. The study of the etch of different loads is important for this

project to simulate the scenario in which the final chips need pillars with different dimensions. In addition, different etching times (3 min, 5 min and 7 min) have been considered to evaluate the evolution of the variation of the etching rates when considering different sized pillars.

One of the first parameters considered is the consistency of the etching depth of pillars with different radii. As discussed in the previous section it is important that the etching depth is well controlled across the different samples. If the etching depth changes between pillars of different radii, it will become a problem, since the final devices would have combinations of pillars with different heights. In Figure 5.13 the etching depth for pillars of different radii etched for different times are shown. The data indicates that the larger the pillars the lower the etching depth. This occurs because the space between the pillars is narrower and, therefore, the penetration of the gases between them is lower. This variation is larger in the case of longer etching times, since the gases have to penetrate deeper into the already formed trenches.

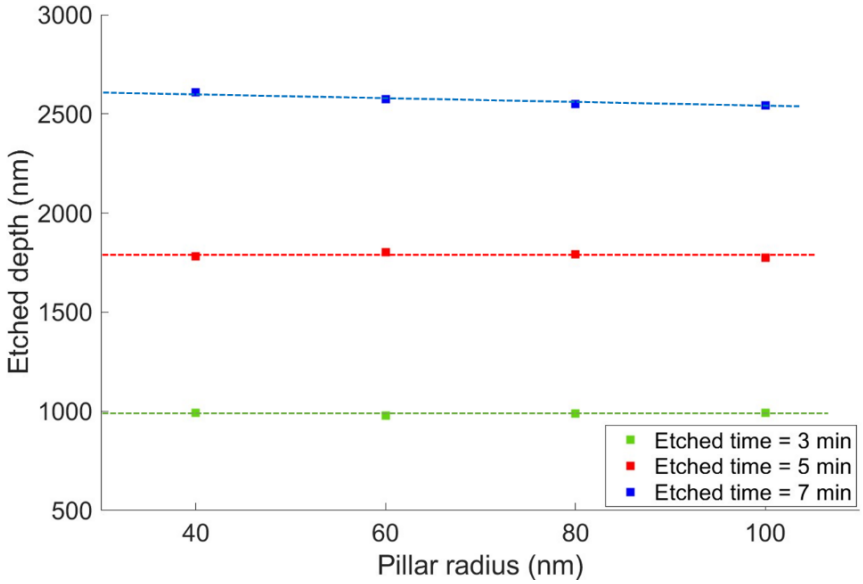

Figure 5.13. Graphical representation of the etch tendencies for different radii pillars and loads for different etching times.

Another consideration has been the radius variation along the vertical axis. This evaluation has been carried out to determine the optimal etching conditions. However, the gas penetration and the spacing between the pillars are expected to impact the

etching of the pillars. To evaluate the magnitude and range of this impact, the cross-sectional images of the etched pillars have been used to measure their shape. Pillars from different parts of the sample have been measured at different levels (top, middle and bottom), Table 5.8.

	Radii = 100 nm			Radii = 80 nm		
	Top	**Middle**	**Bottom**	**Top**	**Middle**	**Bottom**
3 min	150	136	136	154	139	132
5 min	210	198	203	167	156	156
7 min	210	214	268	166	168	210
	Radii = 60 nm			**Radii = 40 nm**		
	Top	**Middle**	**Bottom**	**Top**	**Middle**	**Bottom**
3 min	121	93	89	68	54	45
5 min	119	110	104	89	70	59
7 min	125	114	130	84	63	57

Table 5.8. Summary of the measurements of the pillars' radii along the vertical depending on the etching time and the radii of the original pillar mask.

Figure 5.12 visualises the data shown in Table 5.8. The variation across the height of the pillars, for short etching times, shows a positive tapering, while for longer etching times this tendency is reversed. It is important to point out, however, that this tendency is consistent among the different radii for the same etching times.

Finally, the reproducibility among the sample has also been evaluated in this thesis. As discussed in the fabrication requirements section, the performance of the photonic crystal will have a dependency on the homogeneity of the pillar structure across the sample. To evaluate this, MATLAB® [99] functions have been used to analyse the radii of the pillars from top-view SEM images. The analysis carried out by the program can be observed in Figure 5.15. It can be seen how the original images and the circles matching

the pillars have a high accuracy. In Figure 5.16 the distribution of the measured radii is displayed.

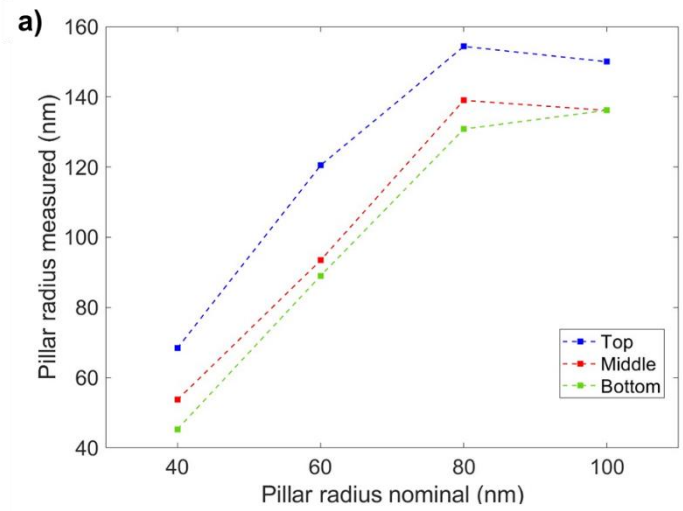
a)
Pillar radius measured (nm)
160
140
120
100
80
60
40
40
60
80
100
Pillar radius nominal (nm)
Top
Middle
Bottom

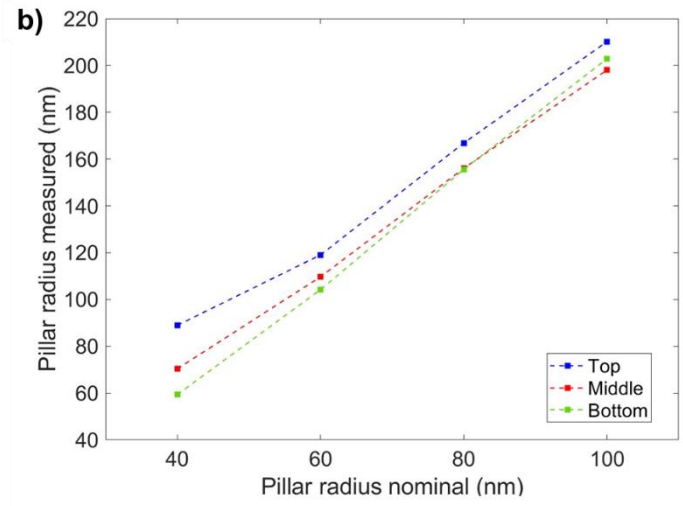
b)
Pillar radius measured (nm)
220
200
180
160
140
120
100
80
60
40
40
60
80
100
Pillar radius nominal (nm)
Top
Middle
Bottom

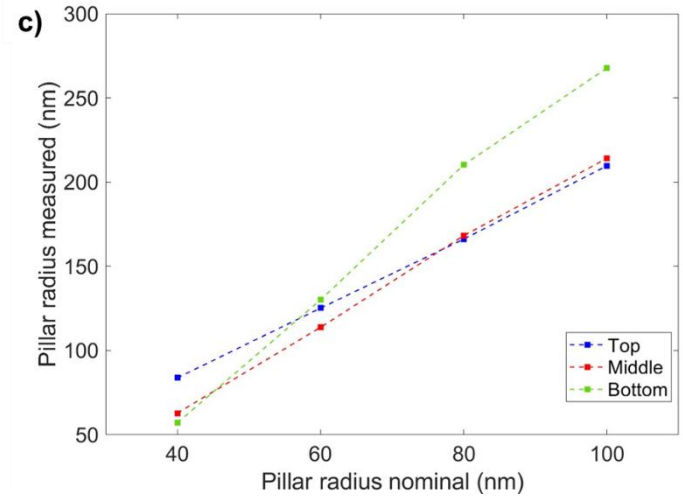
c)
Pillar radius measured (nm)
300
250
200
150
100
50
40
60
80
100
Pillar radius nominal (nm)
Top
Middle
Bottom

Figure 5.14. Distribution of the radius evolution along the vertical axis for different pillars with nominal radius 40 nm, 60 nm, 80 nm, and 100 nm etched down for a) 3 min, b) 5 min and c) 7 min.

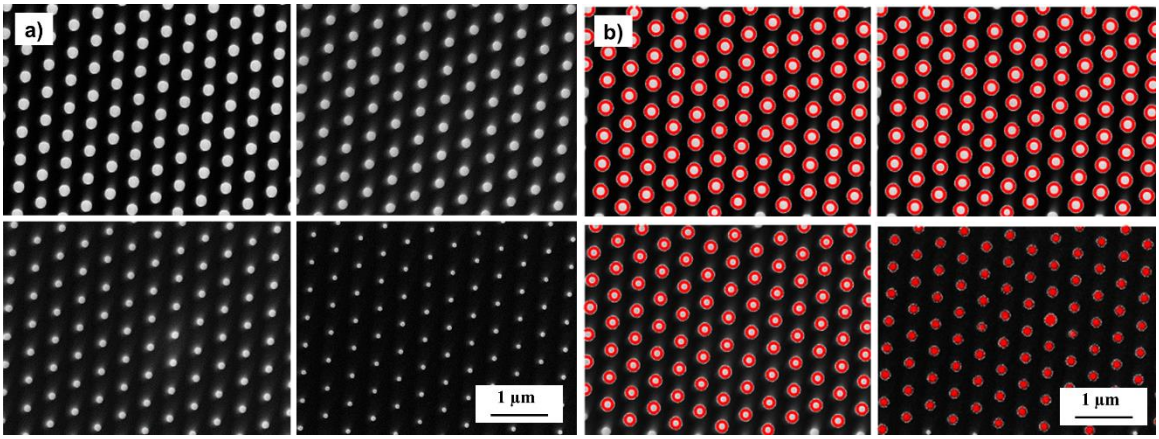

Figure 5.15. The set of four images to the left show top-view SEM images of pillars with 100 nm (top left), 80 nm (top right), 60 (bottom left), and 40 nm (bottom right) radius. The set of four images to the right show the same images but with the detection of the pillars performed by MATLAB® functions.

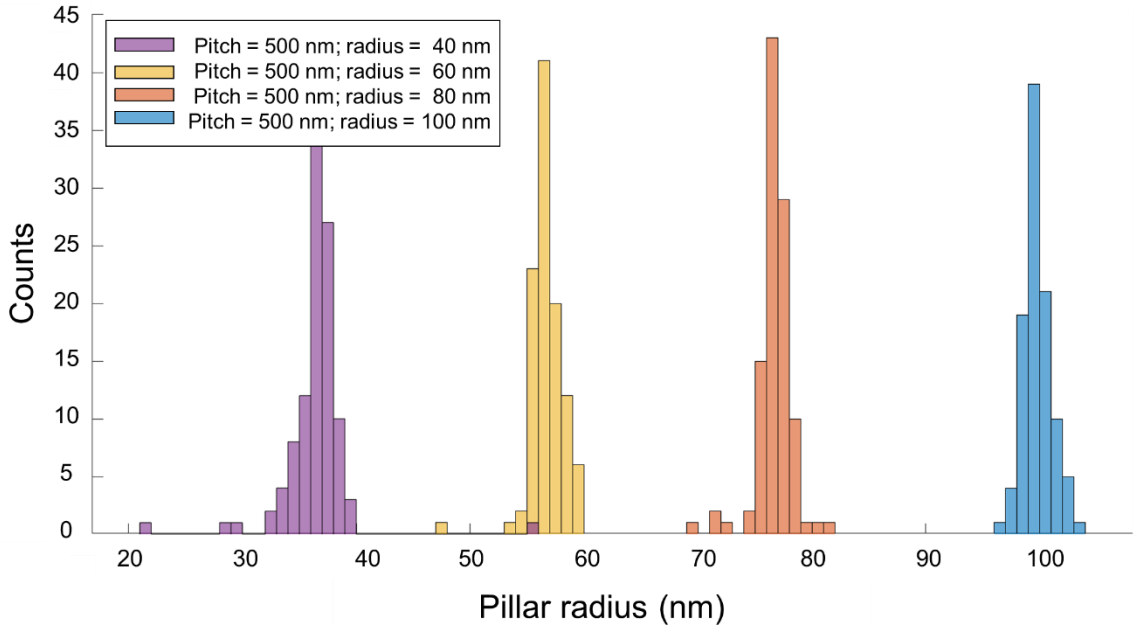

Figure 5.16. Radii distribution obtained from the images shown in Figure 5.15.

The results of the analysis on the pillars' radii show that for larger radii the discrepancy of the final size is lower (smaller standard deviations) than for smaller ones which tend to

be narrower than expected. The values displayed in Figure 5.16 can be found in Table 5.9 together with the results corresponding to extracted from different etching times. Despite this tendency, the deviation from the target radius value is very small (5.7 nm being the highest measured). It is important to keep in mind that this deviation might be affected by the quality and resolution of the SEM images and the automatic system of location and radii adjustment. For these reasons, we consider that the requirements in 5.2.1 are fulfilled and that the accuracy and homogeneity of the pillars among the same sample are sufficiently good for the further optical characterisation.

	Radii = 100 nm			Radii = 80 nm		
	Number of pillars	Average radius (nm)	Standard deviation (nm)	Number of pillars	Average radius (nm)	Standard deviation (nm)
3 min	100	99.8	1.2	106	76.7	1.5
5 min	104	97.3	0.8	105	78.6	1.2
7 min	100	101.1	1.1	105	80.9	1.5
	Radii = 60 nm			Radii = 40 nm		
	Number of pillars	Average radius (nm)	Standard deviation (nm)	Number of pillars	Average radius (nm)	Standard deviation (nm)
3 min	106	56.8	1.4	108	36.4	2.9
5 min	105	58.2	1.3	107	37.4	2.8
7 min	108	59.1	1.7	120	40.6	5.7

Table 5.9. Data obtained from the pillars measured using the MATLAB® code.

5.3.6. Impact of the dry etch on the surface materials

According to the fabrication constrictions described in section 5.2, the presence of residues might affect the biocompatibility of the fabricated samples and their photonic performance (subsection 5.2.2). Even though the core materials used for the fabrication – such as silicon, silicon oxide and aluminium – are biocompatible, both the passivating and etching gases used during the dry etch are fluorine-based. Remains on the surface of the sample and the pillar's walls of these two gases might compromise the biocompatibility of the samples. If a high concentration of fluor is present in the sample, it could become a hazard for the tissues' endurance on the sample.

Chemical analysis has been carried out on the surface of several samples to analyse the chemical composition of each of them. Each sample has been analysed both on top of the pillars' area and on the bare sample's surface. This analysis has been carried out with XPS technique (section 3.5.3). The results shown here have been obtained using an elliptical spot of the substrate of approximately 400 μm diameter and accumulating 4 scans for the survey analysis and 10 scans for the high-resolution spectra of each individual element.

Processed samples have been used for the analysis. To observe the variation of the chemical composition two types of samples have been analysed: a sample that has been processed until the lift-off step and another submitted to the dry etch step. The analysis of the spectra obtained has been done using the Thermo Avantage© software [100], which allows for the quick identification and evaluation of the peaks of the different elements and chemical states as well as with literature information [101]. For the analysis of the samples the peaks corresponding to atoms of silicon, oxygen, carbon, aluminium, sulphur, and fluor have been located. For all conditions both the survey and the individual elements have been analysed.

In Figure 5.17 the results of the analysis both on the photonic crystal (Figure 5.17 a) and on the bare surface (Figure 5.17 b) of a non-etched substrate are shown. It can be observed how the atoms present on both the photonic crystal and the bare surface of the chip are silicon, oxygen, and carbon. Aluminium is only found on the photonic crystal area because of the contribution of the masking material. A better comparison between the proportion of the different atoms and their oxidation state in each spectrum can be done observing the results shown in Table 5.10.

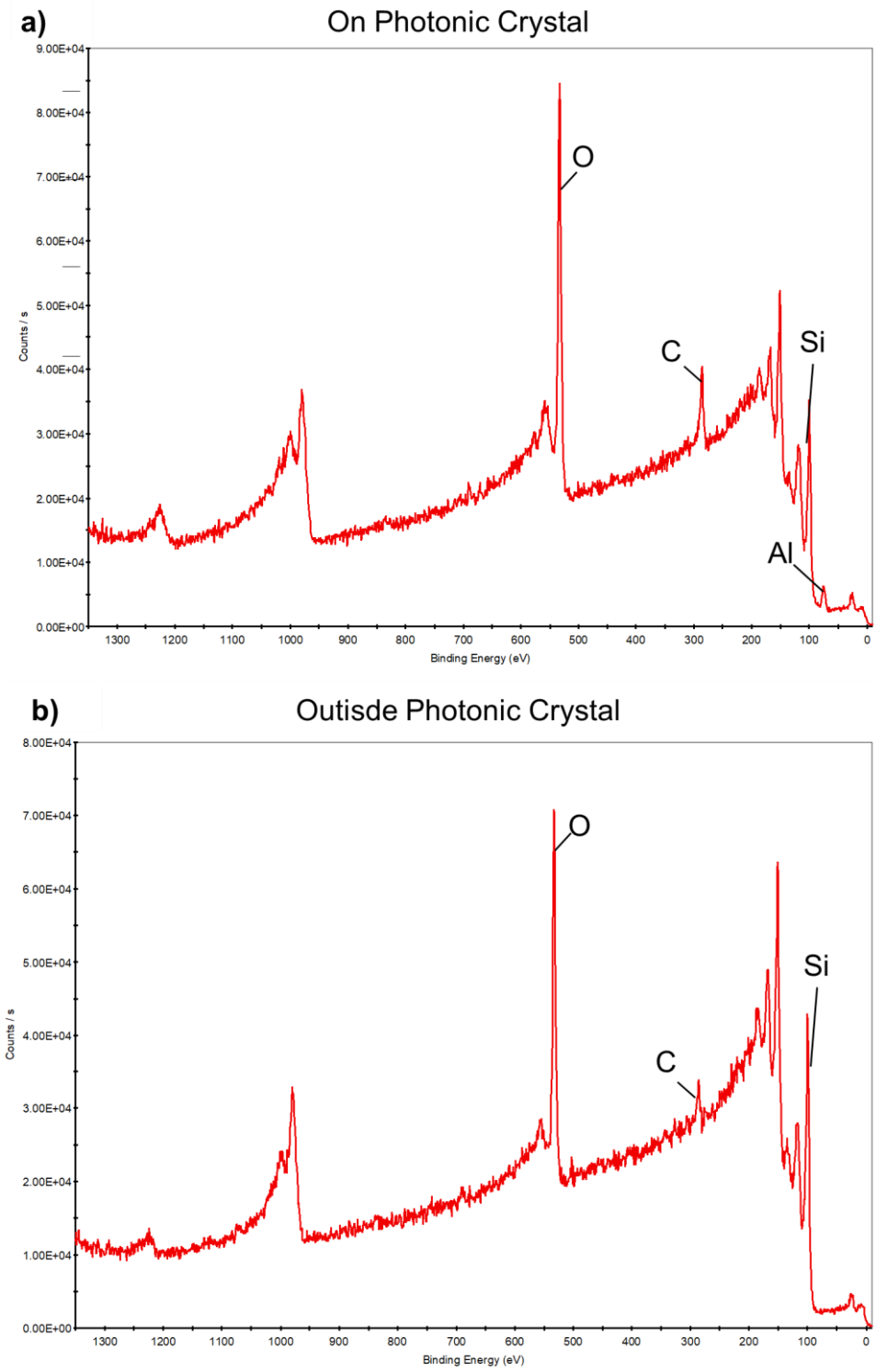

Figure 5.17. Survey XPS spectra from the substrate developed until the lift-off step. Two sample areas have been tested: (a) photonic crystal area, and (b) outside the photonic crystal area. In black the positions of the peaks for the different studied elements are marked.

Peak name	On Photonic Crystal		Outside Photonic Crystal	
	Peak binding energy (eV)	Atomic %	Peak binding energy (eV)	Atomic %
O1s	532.53	39.8	532.87	37.91
Si2p	99.73	31.53	99.94	50.85
C1s	286.01	17.90	286.21	11.24
Al2p	74.27	8.92	-	-

Table 5.10. Summary of the binding energies and relative atomic weight of the elements analysed. This data has been obtained using the Thermo Avantage® software analysing the spectra shown in Figure 5.17.

As expected from the survey analysis it can be seen that the non-etched sample has non presence of fluor on the surfaces of both the photonic crystal and the bare substrate. Regarding other atoms, it is important to notice the differences of the aluminium peaks comparing the two analysed areas. On top of the photonic crystal area an aluminium peak is detected while none appears on top of the bare substrate. To know the chemical state of the atoms a closer analysis with the individual elements should be carried out.

To better understand the different peaks origin of the spectra on top of the photonic crystal masking area, the high-resolution peaks can be analysed. In Figure 5.18 the high-resolution spectra for the oxygen, silicon, carbon, and aluminium are shown. The peaks positions are summarised in Table 5.11.

With this analysis the different peaks appear more detailed. The aluminium peak appears at the position of 76.08 eV. According to literature this peak corresponds to the position of aluminium oxide (alumina). The oxidation of the aluminium mask happens probably due to the contact of the layer with the environment.

Other elements such as silicon and oxygen support the presence of silicon oxide. These elements show a peak at 103.88 eV and at 525.08 eV, respectively. According to the current literature [101] these two positions correspond to silicon oxide. It is likely that the origin of these peaks is the native oxide layer created on the silicon because of its

contact with the atmosphere. This native layer is in the order of a few nanometres, which would explain the peak corresponding to the silicon remains (at 100.11 eV). Carbon peaks also appear between 286 eV and 290 eV. These peaks correspond to C-O-C and O-C=O components. The contribution to these peaks is probably due to contamination from the atmosphere.

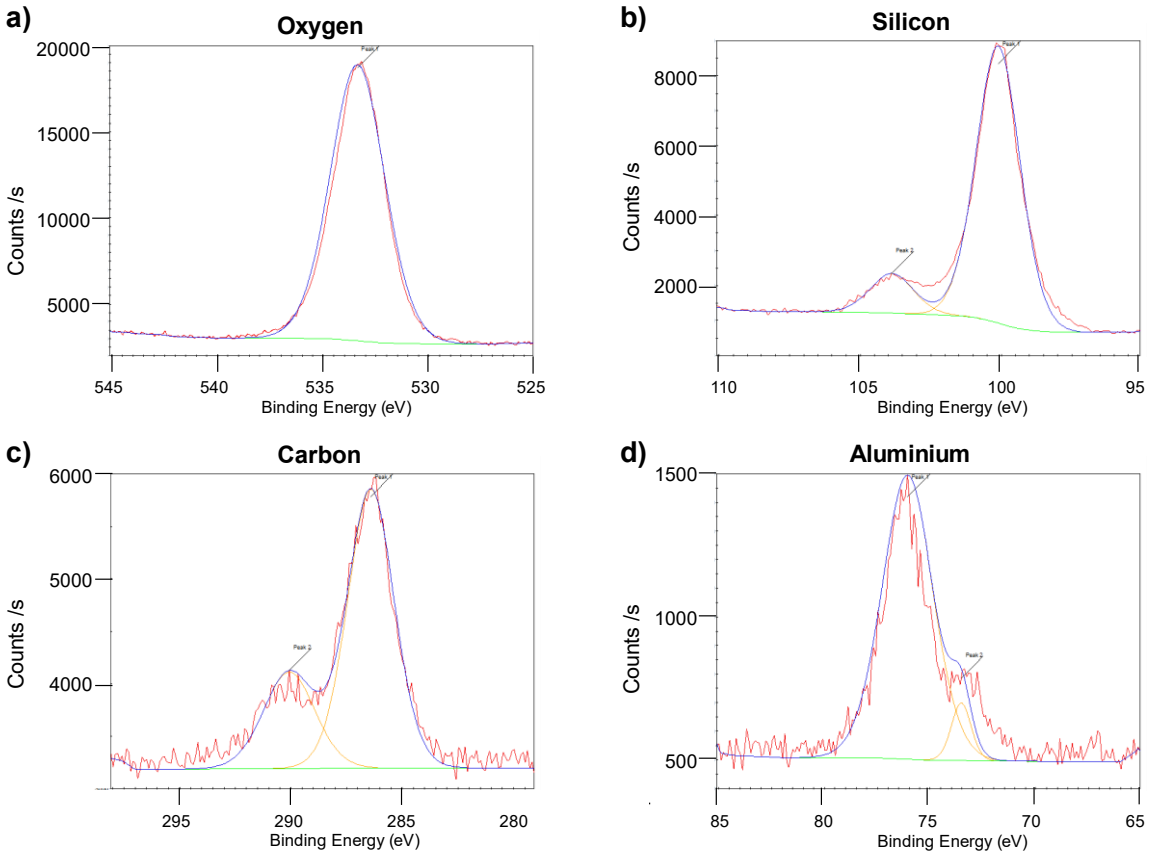

Figure 5.18. High-resolution spectra of different elements for the sample that has not been etched and from the masked area. The spectra from oxygen (a), silicon (b), carbon (c), and aluminium (d). In the different spectra measurement is shown in red, the peak fitting in yellow, the envelope profile in blue and the spectra baseline in green.

The analysis of the non-etched sample provides good information of the materials present on the sample prior the reactive ion etching. In this way the impact of the gases used during the etch step on the final substrate composition can be evaluated.

Element	Peak name	Peak binding energy (eV)
O1s	Peak 1	525.08
Si2p	Peak 1	100.11
	Peak 2	103.88
C1s	Peak 1	286.41
	Peak 2	290.08
Al2p	Peak 1	76.08
	Peak 2	73.53

Table 5.11. Summary of the different peak positions shown in Figure 5.18, for the non-etched sample and the measurement on top of the masked region.

The results of the analysis of the reactive ion etched sample shows interesting results that differ from the previous ones, as expected. In Figure 5.19, the survey spectra of the etched samples are shown again on the photonic crystal surface (Figure 5.19 a) and on the bare substrate (Figure 5.19 b). Again, the summary of the atomic weight and the peak binding energy positions obtained from the two surveys are summarized in Table 5.12.

Table 5.12 shows clearly how the fluor peak appears in both analysed areas. In addition, the sulphur peak raises too. Regarding the remaining elements, both the aluminium peak and the carbon peak are shifted compared to the results shown in Table 5.10, but only on the spectrum taken on top of the photonic crystal.

To better understand these shifts a closer look at the behaviour of each element is needed. In Figure 5.20, the spectra of aluminium (a), carbon (b) and fluor (c) and their fitting re shown. The corresponding positions of the peaks shown in Figure 5.20 are summarised in Table 5.13.

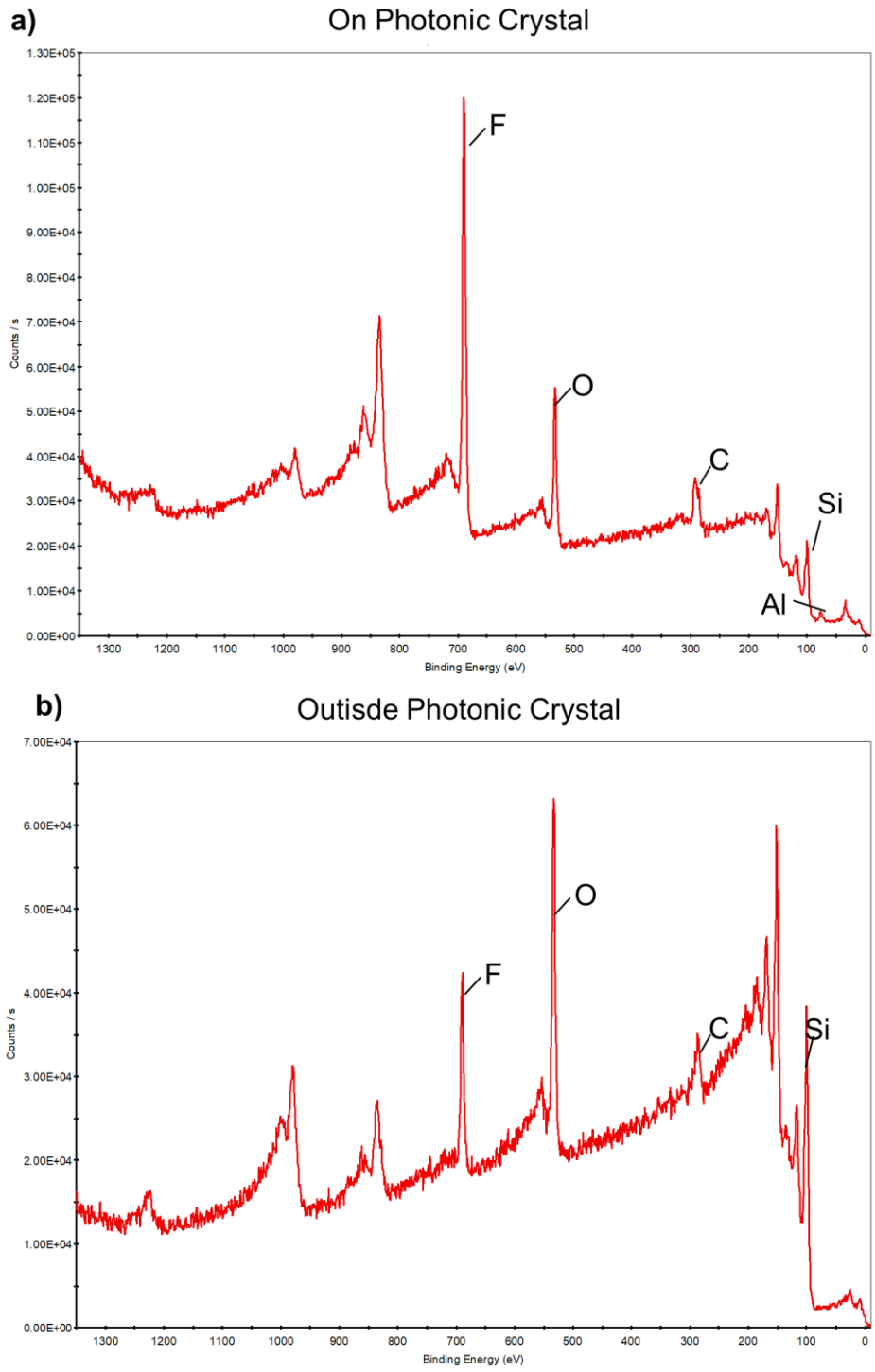

Figure 5.19. Survey XPS spectra from the substrate submitted to the dry etch step. In the same way as in Figure 5.17, two sample areas have been tested: (a) photonic crystal area, and (b) outside the photonic crystal area. In black the peaks for the different studied elements are marked.

Peak name	On Photonic Crystal		Outside Photonic Crystal	
	Peak binding energy (eV)	Atomic %	Peak binding energy (eV)	Atomic %
O1s	532.90	25.95	532.90	32.79
Si2p	99.92	4.96	100.20	48.25
C1s	291.29	25.46	286.10	12.56
Al2p	76.12	4.76	-	-
F1s	688.57	19.47	688.69	4.16
S2p	166.74	1.29	167.18	2.24

Table 5.12. Summary of the binding energies and relative atomic weight of the elements analysed. This data has been obtained using the Thermo Avantage® software analysing the spectra shown in Figure 5.19

From the results in Table 5.13 the aluminium signal two peaks can be extracted. Aside from the aluminium oxide peak at 73.18 eV, another peak at 77.06 eV can be observed. The origin of this peak is due to the presence of aluminium fluoride (AlF_3), according to literature. Both these signals come from the masking material which, probably, due to the ion bombardment during the dry etching step, has reacted with some of the fluor atoms, creating this new compound on the mask surface. A more detailed analysis could be done but it is out of the scope of this thesis.

Observing the carbon peaks, it can be seen that a peak at 292.51 eV appears (C1s-Peak 1 in Table 5.13). This peak is shifted by 2 eV from the original position of the carbonate at 290.08 eV. The position of this peak is correlated with the presence of CF_2 or CF_3. Probably the first is the one on the sample since this is the polymer created as passivation layer during the dry etch process (Chapter 2 section 2.4.2). This assumption is supported by the fluor peak whose position (689.39 eV) is assigned to the CF_2 compound [101].

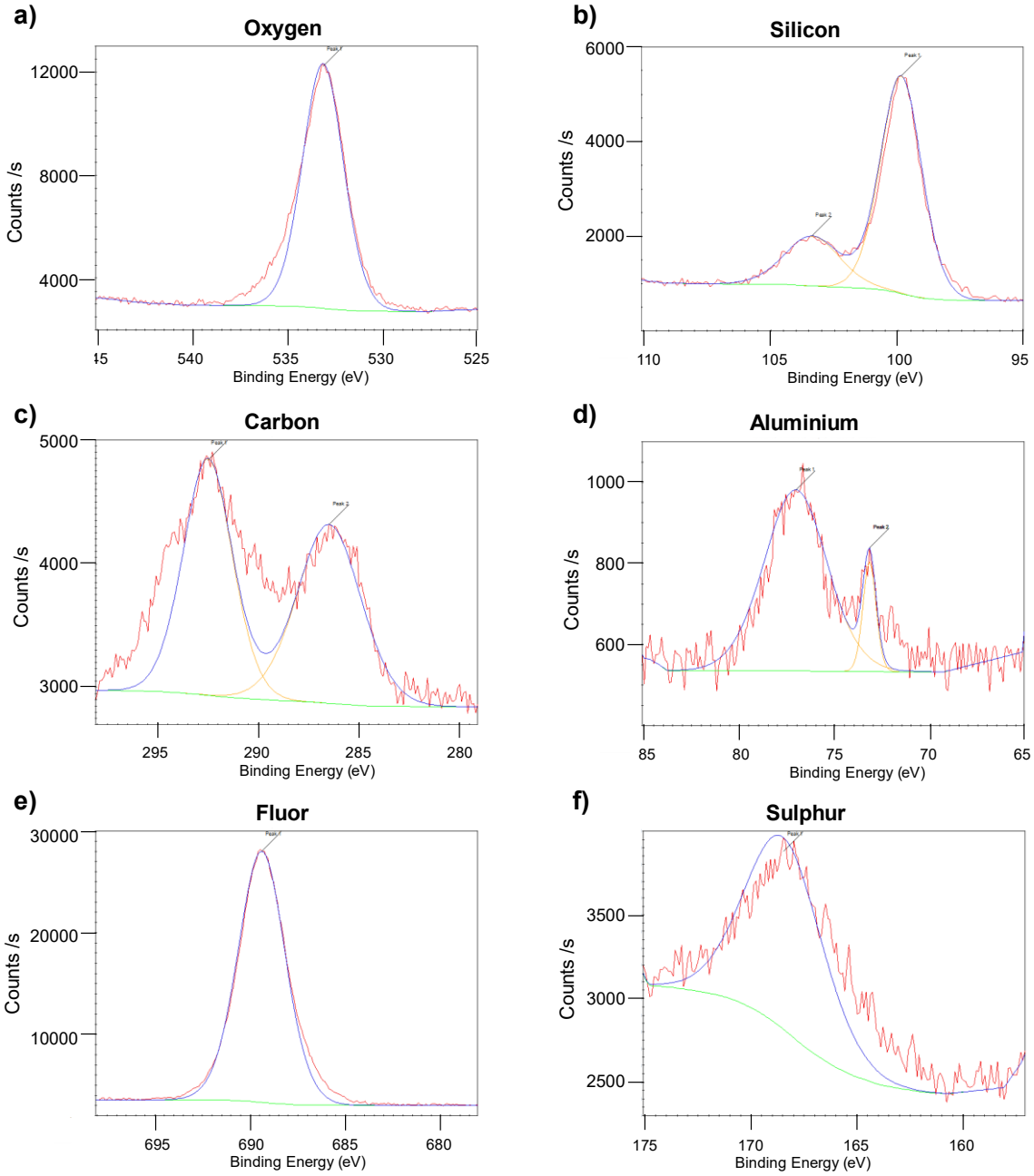

Figure 5.20. (a) Oxygen, (b) silicon, (c) carbon, (d) aluminium, (e) fluor and (f) sulphur spectra. Each spectrum has been taken individually during the XPS experiment on top of the photonic crystal area. In red the measured spectra can be seen. In blue the enveloping simulated spectra considering the measured peaks (in yellow). The spectra baseline is shown in green.

Element	Peak name	Peak binding energy (eV)
O1s	Peak 1	533.18
Si2p	Peak 1	99.88
	Peak 2	103.38
C1s	Peak 1	292.51
	Peak 2	286.48
Al2p	Peak 1	77.06
	Peak 2	73.18
F1s	Peak 1	689.40
S2p	Peak 1	168.60

Table 5.13. Summary of the peak binding energies of the spectra shown in Figure 5.20. The peak names correspond the to the ones labelled in the figure.

Therefore, what can be observed from this data is that after the dry etch process, fluor appears and remains on the photonic crystal area. This fluor appears in two different natures: creating AlF_3 and the passivation polymer CF_2. Finally, there is the sulphur peak which appears at 168.60 eV, which could be a consequence of the SF_6 gas use during the etch step.

From Table 5.12 it can be seen that the relative weight of fluor atoms is high. The large presence of fluor can be due to the large contribution of the pillar's sidewalls. Since this polymer is due to protect the pillars sidewalls during the dry etch, it probably remains on the side walls. Therefore, the surface contributing to the fluor XPS signal is larger due to the pillar's sidewalls.

5.4. Creation of bottom cladding

As explained in the photonic crystal chapters (Chapter 2 section 2.1.3 and Chapter 4 section 4.3), a top and bottom cladding are needed to confine light in the vertical direction and avoid leaking light into the silicon substrate. The top cladding is created by the air (or water) on top of the system. SOI wafers provide the possibility to have a bottom cladding thanks to the buried silicon oxide layer, whose refractive index is lower than that of silicon. However, the generation of a bottom cladding when using silicon pillars, as already mentioned, is more challenging. The complication comes from the fact that the effective refractive index of the photonic crystal because it is a combination of silicon and air (or water), is closer to the refractive index of silicon oxide than to that of silicon. This implies that the vertical confinement using a slab of silicon oxide under the pillars might not be enough to prevent the light leak through the substrate. The solution to this problem is to create a bottom cladding with an even lower refractive index than the refractive index of silicon oxide. This can be achieved by nanostructuring the bottom cladding, which can be achieved with two different approaches:

1. Using SOI wafers and continuing the etching of the pillars into the buried silicon oxide layer
2. Using silicon wafers, extending the etching of the pillars but with a smaller radius at the bottom

Both approaches are very challenging from the fabrication point of view due to the difficulties in fine tuning the dry etching step without affecting the already etched silicon nanopillars.

5.4.1. Etching of buried silicon oxide

The challenge of the first approach implies the etching down of two different materials. Until now only the etch of silicon has been considered. The complication of this approach is, in part, the fact that the binding energies are very different for silicon and silicon oxide. The binding energy of the Si-O atoms is larger than that of the Si-Si atoms (Table 5.14). This means that the ion energy needed to etch down the silicon oxide layer is larger than

the one used to etch down the silicon pillars. This is a drawback since there are high chances that the silicon pillar will be partially or totally etched away while etching the buried silicon oxide due to physical etch if it is not well protected.

However, as explained in Chapter 3 section 3.4, the etch step is not only driven by the physical etch but also the chemical etch. The balance between these two types of etchings will permit the proper etch of the silicon oxide pillar without affecting the top silicon pillar.

The difference in the binding energy affects not only the silicon etch but also the masking material. Until the moment 20 nm of e-beam evaporated Al has been used as masking material. With this approach this mask should stand, in addition, the silicon oxide etch step. From the chemical analysis discussed in the previous section, the top part of the mask has not only Al but Al_2O_3 and AlF_3 because of the oxidation of the surface in the cleanroom environment and the remains from the silicon etch. The binding energy of Al_2O_3 is larger than the one of silicon, making it a good mask for the silicon etch (Table 5.14). However, it is closer to the silicon oxide binding energy. This implies that during the silicon etch the Al_2O_3 will be sputtered as well by the ions, being damaged, and even completely removed, leaving the silicon pillar's top surface unprotected (Table 5.16). Something similar would happen with the AlF_3 present in the mask, even though the binding energy is closer to that of Si-O.

Atom bond	Bond Energy (kJ/mol)
Si-Si	327
Si-O	798
Al-Al	186
Al-O	512
Al-F	664

Table 5.14. Binding energies of the different atom combinations used during the dry etch steps.

Even though the binding energies of the different compounds on the sample play a role in the physical etching process, the configuration of the recipe such as the platen and coil powers and the gases used, have an even more important impact on the final result.

To test this approach, SOI wafer chips have been used which have followed the process described in the previous sections but with a 50 nm-thick Al mask. A mask with pillars with 100 nm radius and 500 nm pitch has been used. The dry etch of the silicon layer has been carried out using the recipe described in the previous sections for 4 min. This corresponds to pillars that are 1270 nm tall (number in accordance with Figure 5.11).

C_4F_8 (sccm)	O_2 (sccm)	Coil Power (W)	Platen Power (W)	Pressure (mTorr)	Temperature (°C)
40	5	1100	180	6	50

Table 5.15. Etching conditions used for testing the silicon oxide etch below the silicon pillars.

The silicon oxide etch has been tested using an STS MESC Multiplex ICP devoted to advanced oxide etching processes. The recipe used is summarised in Table 5.15. In this case the recipe uses C_4F_8 as etching gas and, at the same time, as passivation gas. Similar to the process explained for the silicon etch, in this case the fluorocarbon gas creates a passivation layer on the walls of the pillars. The key factor is that the thickness of the passivation layer is larger on the silicon than on the silicon oxide [102]. This difference on the passivation layer thickness makes the etch of the silicon oxide faster than the etch of the silicon. In addition, both the carbon and the fluor atoms form volatile products with the oxygen and silicon present in the substrate, respectively.

With this recipe the structures have been etched for 1 and 2 min and the result is shown in Figure 5.21 a and b, respectively. As it can be observed, the top part of the pillars remains quite untouched thanks to the use of fluorocarbon gases during the process. For 1 and 2 minutes of process a total of 435 nm and 964 nm of silicon oxide has been etched, respectively. This result is promising since it shows that the silicon oxide can be etched underneath the silicon pillar without varying its diameter while successfully reducing the effective refractive index of the bottom cladding.

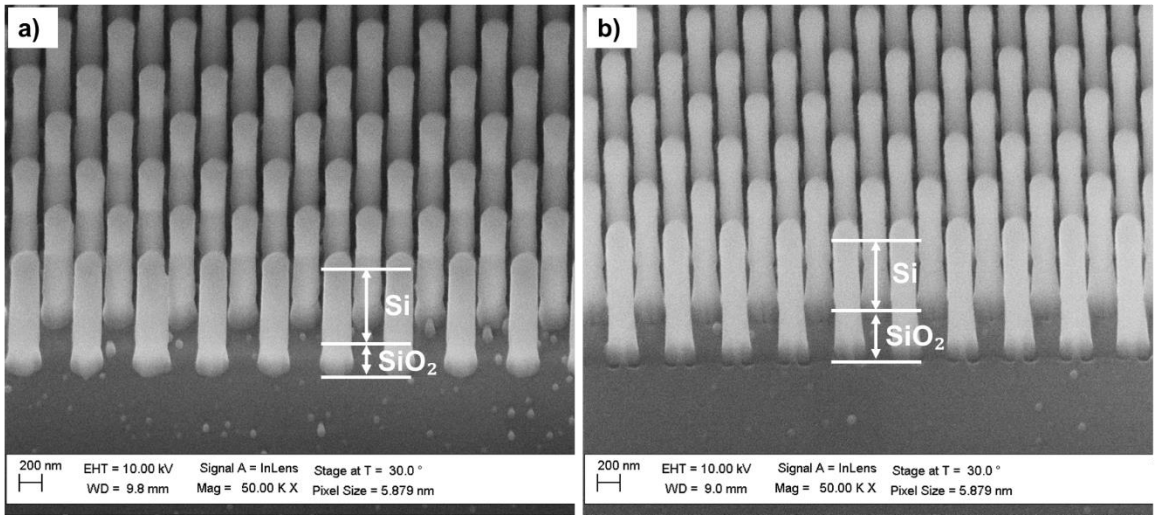

Figure 5.21. SEM images of the silicon etched pillars for 4 min and a silicon oxide etch for (a) 1 min and (b) 2 min. In red the different etched materials are indicated.

5.4.2. Undercutting silicon pillars

The second approach challenges as well the dry etch step established as reference process. It does not face the problem indicated in the previous paragraph, namely the binding energy of the different materials, since the etched material is silicon both for the pillar and for the undercut. However, the difficulty is the proper tunning of the experimental conditions to avoid damaging the top part of the pillars and to avoid lateral over etching when etching down the undercut, which could cause the nanopillars to fall down.

To carry out this approach it has been chosen to use the Bosch process. The benefit of this process is that both the etching and deposition steps are independent and ramping of their duration can be easily implemented, changing the conditions of the chamber cycle by cycle.

The final conditions of the Bosch process used for etching down the bottom part of the pillars (undercut) are summarised in Table 5.16. The top part of the pillars has been etched for 5 min using the optimised recipe for the nano1.42 recipe (section 5.3).

The Bosch process used for the undercut of the pillars has been designed to prevent the etch of the top part of the pillar and at the same time still provide a good base for the pillars not to collapse. The recipe summarised in Table 5.16 shows how the Bosch process evolves over time. While the etch step is kept constant the deposition step time is increased over the subsequent cycles. This increase of the passivation step will prevent the over etch of the top part of the pillars and the already etched parts of the undercut. At the same time, the over passivation reduces the scallop depth, giving the structure with a more stable base preventing the pillars to collapse.

	C_4F_8 (sccm)	SF_6 (sccm)	Coil Power (kW)	Platen Power (kW)	Pressure (mTorr)	Temperature (°C)	$t_{initial} \rightarrow t_{Final}$ per cycle (s→s)
Dep	25	15	1	0.1	4	-19	3.2 → 6.4
Etch	5	40					10 → 10

Table 5.16. Summary of the Bosch process conditions used for the etch of the top body of the undercut bottom body of the pillars for 10 cycles.

In Figure 5. 22, some images of the undercut pillars using the recipe in Table 5.16 are shown. It can be observed how the top part of the pillar has the smooth profile observed in the nano1.42 etched pillars (Figure 5. 22 b) and the undercut has the characteristic scallops of the Bosch process (Figure 5. 22 c).

Both fabricated structures have been tested experimentally in the research group proving their photonic performance, which confirms their suitability for such applications. These measurements are ongoing but are beyond the scope of this work.

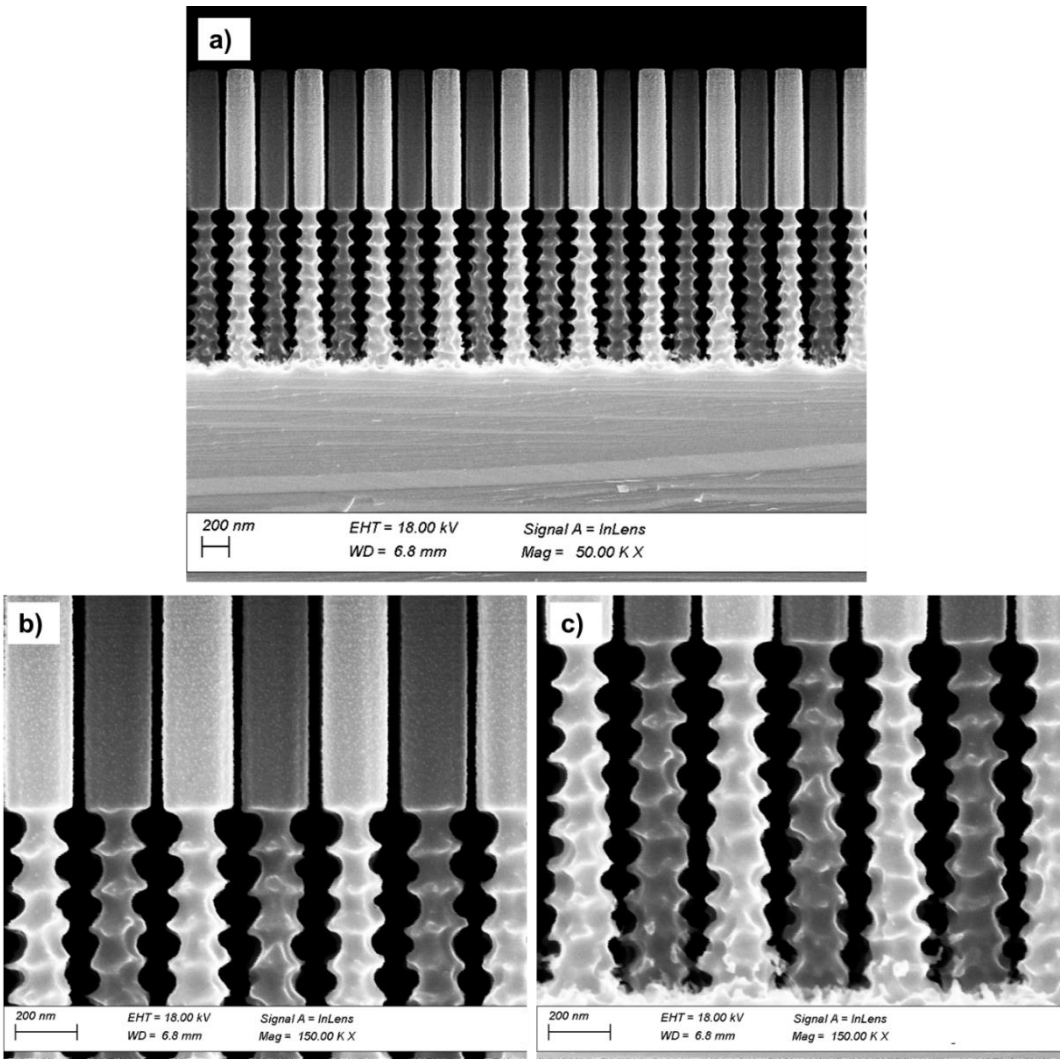

Figure 5. 22. Images of the undercut pillars. (a) Overview of the pillars where the top and bottom undercut parts are etched according with the conditions described in Table 5.16; (b) and (c) show closer images of the transition between the regular pillar and the undercut and the undercut section, respectively.

CHAPTER 6.
CONCLUSIONS

6.1. Conclusions of this thesis

As was presented at the beginning of this document, the aim of this thesis has been to set up the basis for the simulation and fabrication of photonic crystal structures based on silicon nanopillar within the scope of a larger H2020 FET-Open project, StretchBio, for the creation of a mechanical sensor for *in vivo* monitoring of the growth and regeneration of living tissues.

This thesis has been focused on establishing simulation and fabrication routes and guides that can be used in the future by the researchers willing to work in this topic and, especially, by researchers working in this research project. These routes have been developed with the intention to make them easily tuneable to any requirement and challenge that the forthcoming research might bring.

6.1.1. Simulation conclusions

The simulation route followed by this thesis has been mainly focused on the determination of a photonic crystal structure based on silicon pillars that matches the different requirements of the project. All these simulations have been done considering

two different types of backgrounds, air or water, because both scenarios could take place in the experimental working conditions of the final device.

To do so, simulations based on FEM and FDTD methods have been used to evaluate the photonic band diagrams and the transmission spectra of the structures, respectively. The FEM simulations have been carried out using COMSOL Multiphysics® software, while the FDTD simulation has been carried out using self-developed Python™ programs in combination with the MEEP module. This approach combining two different computational methods has permitted to robustly evaluate the theoretical behaviour of the simulated structures.

The principal characteristics of the photonic crystals (i.e., radius of the pillars and pitch) have been determined by two-dimensional simulations. The main goal of these simulations has been obtaining a photonic band gap with a high gap-to-midgap ratio, obtained as a function of the radius-to-pitch ratio of the simulated structure. The COMSOL Multiphysics® results show optimal gaps of 49.02 % for air and 35.85 % for water backgrounds. These optimal gap-to-midgap values are obtained for radius-to-pitch values of 0.17 and 0.20, respectively. Thanks to the scalability properties of photonic crystals and given the wavelength range limitations of this project, the dimensions chosen to be optimal for the photonic crystal structure have been pillars of 100 nm radius and pitch of 600 nm when considering an air background and pillars of 100 nm radius and pitch of 500 nm when considering a water background.

The evaluation of the transmission spectra obtained with FDTD simulations show good agreement with the band diagram analysis. For FDTD simulations the optimal band gaps have been obtained for the same radius and pitch values as the ones obtained with the band diagram analysis. The gap-to-midgap value for a 100 nm radius pillars and 600 nm pitch structure, considering air as background is 46.39%. And, on the other hand, pillars of 100 nm and pitch of 500 nm in water background has a gap-to-midgap value of 34.92%.

To simplify the situation and focusing on a solution suitable for both air and water backgrounds, the basic photonic crystal structure considered during the rest of the thesis discussion has been set to one structure with pillars of 100 nm radius and 500 nm pitch.

The analysis of how the two-dimensional system response is affected by the introduction of defects has been carried out during this work as well. Even though the goal of this thesis is not to prove the optical performance and neither to obtain a prototype of design of such structures, this exercise has provided useful information for the future.

The modification of a row of pillars from the main photonic crystal structure to create a line defect has proven that an allowed band will be introduced in the photonic bandgap. Tests varying the radius of the pillars of this row, both in air and water backgrounds, and varying the width of the line defect have been performed. These modifications have revealed the strong dependence of the transmission band on the properties and parameters of the defect. When decreasing the radius of the pillars of this row, the band is pushed into the band gap, increasing its frequency. These results show that a smaller line of pillars can create an independent band within the band gap.

Regarding the width of the defect, i.e., the distance to the next row of pillars, the wider the width is, the more bands are introduced in the bandgap, spanning over the whole band gap. This fact can be counter-productive for the application envisaged, since the band gap is completely covered by the defect bands and, consequently, the band gap disappears.

Under these conditions, the optimal defect for both backgrounds have been found to be a defect row constituted by pillars of 60 nm radius and with a width 375 nm.

Regarding the point defect analysis, it has been carried out by the removal of a full row of pillars and by creating a cavity within it enclosed by two pillars. This configuration allows the creation of a narrow transmission peak in the bandgap. In this case a clear difference between the use of air and water backgrounds arises for the former, the peak appears at 1.278 μm, while it is created at 1.565 μm for latter.

This simulation has been used as well to test how the transmission spectra would be affected by the shift of one of the pillars enclosing the cavity. These simulations have been done to emulate the bending of one of the pillars of the cavity. The results show that the transmission peak shifts almost linearly as a function of the displacement of the pillar. This result is very promising for the project’s sensing purposes since it shows that the transmission spectrum is sensitive to shifts (bendings) of one single pillar.

Finally, simulations considering three-dimensional structures have also been used to evaluate the effect of a stack of layers needed and their configuration. Three different configurations of top and bottom claddings have been analysed: silicon pillars directly on a silicon oxide slab, silicon pillars on top of silicon oxide pillars on a silicon oxide slab, and silicon pillars embedded between silicon oxide pillars at both their the top and bottom. All these configurations have shown that the introduction of the vertical dimension into the simulations produces a shrinkage of the band gaps as compared to two-dimensional situations. Even though with small variations, in all three cladding configurations the results prove that pillar heights of around 1000 nm give rise to an optimal band gap, while at least a 500 nm-thick BOX layer is needed to minimise leaking of the modes towards the background.

Therefore, the conclusions from the simulation study can be summarised as:

1. The photonic crystal structure parameters have been optimised, giving an optimal pillar radius of 100 nm and a pitch of 500 nm. This has been proven both in air and water backgrounds using FEM and FDTD simulations.

2. The introduction of defects has been analysed as well. The introduction of line defect has proven that varying the diameter of one line of pillars down to 60 nm with a defect width of 375 nm introduces a defect that allows proper transmission within the photonic band gap.

3. In addition, it has been demonstrated that the movement of one of the pillars creating the cavity induces a shift of the resonance peak. This promising result shows the sensing potential of such structures.

4. The introduction of the third dimension has provided useful information about the real structure needed for the project, not only from the simulation point of view but also for the fabrication. The three cladding structures considered have proven that silicon pillars with 1000 nm height and BOX layers of at least 500 nm will give rise to good claddings for the photonic crystal performance.

6.1.2. Fabrication conclusions

With all the described results of the simulations, the fabrication route has been set. The fabrication process, therefore, should be able to create nanopillars with the required dimensions and with the quality needed for such type of devices. In addition, this fabrication process should be tuneable, with minor changes, to almost any new configuration and geometry of the devices needed for the project.

The process flow proposed in this thesis is based on using electron beam lithography, followed by metallisation and lift-off, to finalise using dry etching to create the pillars. This optimisation has been mainly carried out on silicon wafers, but commercial SOI and self-made pseudo-SOI wafers have been used as well in advanced stages of the fabrication optimisation.

Each step of the process flow is important for the outcome, but the process which is more critical, and which determines most of the parameters of the final nanopillars and its arrays, is the dry etch process. The dry etch step plays an important role on the final geometry of the pillars, their roughness and the residuals that might remain after the process and that could be potentially hazardous for biological samples.

The dry etching of the pillars has been performed following a pseudo-Bosch process, consisting in a continuous supply of both C_4F_8 and SF_6. A thorough analysis of the C_4F_8 and SF_6 flow ratios and the coil and platen powers employed for the etching has been done. Other variables, such as the chiller temperature and the chamber pressure, have not been considered and have been kept constant. The aim of this analysis has been to provide a “map” of conditions in case that variations in the design or changes of the dry etching tool’s performance occur and that can be quickly redressed.

The optimised process recipe, with regards to the best pillar shape and smoothness, has been achieved with gas flows of 71 sccm C_4F_8 and 44 sccm of SF_6 and coil and platen powers of 1000 W and 20 W, respectively. A smooth surface of the pillars will prevent losses of the light through scattering at the pillars walls and an almost cylindrical shape will improve the experimental response of the system.

Once the etch recipe has been set, the etching rate for pillars of different radius has been measured and has been proven to be consistently constant over time, with an average value of 333.6 nm/min. In addition, even for long etching times, the pillar shape is kept constant. In addition, almost no variation in the etching rates have been obtained for pillars of different radii.

Aside from the shape of the individual pillars, the collective consistency about shape and dimensions has been sought. A MATLAB® script has been used to analyse the dispersion of the size of the pillars obtained after the etching process. Good consistency across the sample has been obtained with deviations of only a few nanometres in most of the cases. A homogeneous distribution of pillars is expected to help the photonic crystal performance. All these tests have been carried out on silicon wafers, which are not suitable for the photonic characterisation of the samples. The transfer of these results to SOI wafers has been smooth.

Due to the concern of the potential biocompatibility of the resulting samples, in this thesis an analysis of the impact of the fabrication processes on the surface materials of the samples has been performed. This analysis has proven that residuals from, probably, the dry etching step are still present on the pillar's surface. XPS analysis has shown that the etched samples present peaks that can be assigned to the presence of fluor at the samples' surface, which might compromise the biocompatibility.

Finally, the nanostructuring of the substrate has been studied to enhance the effect of the cladding. Two strategies have been followed to create a bottom cladding: etching the pillar into the silicon oxide layer and creating an undercut in the silicon below the main pillar. Both strategies have shown successful fabrication results keeping the top pillar geometry and integrity. These results show that different cladding strategies can be fabricated as a function of the requirements of the designed device. In addition, the results prove a good robustness and versatility of the process developed.

Therefore, the conclusions of the fabrication efforts are:

1. A robust process flow has been developed and fully detailed using electron beam lithography, lift-off, and dry etching processes, which leads to almost perfectly cylindrical pillars.

2. A thorough “map” of dry etching conditions has been carried out to obtain the optimal pillars with proper cylindrical shape and smooth side walls while preventing the creation of nanograss, which could affect the photonic behaviour.

3. The analysis of the sample surface’s chemical composition after the reactive ion etching process evidences the presence of fluor on the samples. This might compromise the biocompatibility of the samples.

4. The reduction of the light leakage through the substrate can be achieved by lowering of the bottom cladding’s refractive index, which has been addressed by two different successful strategies: etching part of the buried oxide layer underneath the silicon pillar and undercutting the silicon pillar to a lower depth. Both strategies employ reactive ion etching methods

6.2. Further work

Since this thesis has been developed within the scope of a broader and ambitious project, multiple lines of future work can be described here. As explained in Chapter 1 this thesis started as preliminary research for the development of the H2020 FET-Open project StretchBio.

Following the two main topics covered in this thesis future work could be carried out specially in the simulation side. This thesis has proven that photonic crystals based on pillars are viable when considering air and water backgrounds and initial tests on defect impact on the transmission spectra have been done. However, a broader and deeper simulation study of more advanced defect designs and distribution should be done. This will help directing the design towards a system that can be used as mechanical sensor.

One of the topics that has not been covered in this thesis, but which will be crucial for the experimental set up is the design of a coupling system that can guide and introduce light into the photonic crystal structure. Designing and testing a coupling system that can efficiently couple and decouple light should be one of the top priorities of the following work to do.

The aim of the StretchBio project is to use the photonic crystals as mechanical sensors. The bending of the pillars has been assumed based on data available in literature, however, proper simulations and experimental results on the pillars bending in the specific case of this thesis have not been added within the frame of this thesis. Experimental determination of the lateral forces for bending these pillars is rather difficult and, therefore, probably only theoretical approaches would bring numerical values about the bending of the pillars.

Finally, tests with tissues on top of the pillars to evaluate how they interact with the system should be performed. These tests will ensure that the materials on the surface after the fabrication are biocompatible and are suitable for *in vivo* testing of the samples.

Bibliography

[1] B. I. Shraiman, “Mechanical feedback as a possible regulator of tissue growth,” 2005. [Online]. Available: www.pnas.orgcgidoi10.1073pnas.0404782102

[2] A. Beaussart *et al.*, “Single-cell force spectroscopy of probiotic bacteria,” *Biophys J*, vol. 104, no. 9, pp. 1886–1892, May 2013, doi: 10.1016/j.bpj.2013.03.046.

[3] C. J. Wright, M. K. Shah, L. C. Powell, and I. Armstrong, “Application of AFM from microbial cell to biofilm,” *Scanning*, vol. 32, no. 3. pp. 134–149, May 2010. doi: 10.1002/sca.20193.

[4] C. Gonzalez, “Drosophila melanogaster: A model and a tool to investigate malignancy and identify new therapeutics,” *Nature Reviews Cancer*, vol. 13, no. 3. pp. 172–183, Mar. 2013. doi: 10.1038/nrc3461.

[5] U. Nienhaus, T. Aegerter-Wilmsen, and C. M. Aegerter, “Determination of mechanical stress distribution in Drosophila wing discs using photoelasticity,” *Mech Dev*, vol. 126, no. 11–12, pp. 942–949, Dec. 2009, doi: 10.1016/j.mod.2009.09.002.

[6] “Monitorización bidimensional de tensiones mecánicas en tejidos biológicos, Explora, TEC2014-62144-EXP, Ministerio de Economía, Industria y Competitividad”.

[7] “Continuous two-dimensional stretch monitoring of fresh tissue biopsies (StretchBio), Horizon 2020 FET-Open Project, Grant agreement 964808.” [Online]. Available: https://stretchbio.eu/

[8] P. Paulitschke *et al.*, “Ultraflexible Nanowire Array for Label- and Distortion-Free Cellular Force Tracking,” *Nano Lett*, vol. 19, no. 4, pp. 2207–2214, Apr. 2019, doi: 10.1021/acs.nanolett.8b02568.

[9] G. Piret, M. T. Perez, and C. N. Prinz, “Support of Neuronal Growth Over Glial Growth and Guidance of Optic Nerve Axons by Vertical Nanowire Arrays,” *ACS Appl Mater Interfaces*, vol. 7, no. 34, pp. 18944–18948, Sep. 2015, doi: 10.1021/acsami.5b03798.

[10] J. D. Joannopoulos, P. R. Villeneuve, and S. Fan, “Photonic crystals,” *Solid State Commun*, vol. 102, no. 2–3, pp. 165–173, Apr. 1997, doi: 10.1016/S0038-1098(96)00716-8.

[11] E. Yablonovitch, “Photonic crystals,” *J Mod Opt*, vol. 41, no. 2, pp. 173–194, Feb. 1994, doi: 10.1080/09500349414550261.

[12] T. Baba, D. Mori, K. Inoshita, and Y. Kuroki, “Light localizations in photonic crystal line defect waveguides,” *IEEE Journal on Selected Topics in Quantum Electronics*, vol. 10, no. 3, pp. 484–491, May 2004, doi: 10.1109/JSTQE.2004.829201.

[13] C. Jamois, R. B. Wehrspohn, L. C. Andreani, C. Hermann, O. Hess, and U. Gösele, “Silicon-based two-dimensional photonic crystal waveguides,” *Photonics and Nanostructures - Fundamentals and Applications*, vol. 1, no. 1. Elsevier, pp. 1–13, 2003. doi: 10.1016/j.photonics.2003.10.001.

[14] G. Tayeb and D. Maystre, “Rigorous theoretical study of finite-size two-dimensional photonic crystals doped by microcavities,” 1997.

[15] T. Xu, N. Zhu, M. Y. C. Xu, L. Wosinski, J. S. Aitchison, and H. E. Ruda, “A pillar-array based two-dimensional photonic crystal microcavity,” *Appl Phys Lett*, vol. 94, no. 24, 2009, doi: 10.1063/1.3152245.

[16] T. Xu *et al.*, “High-Q photonic nanocavity in a two-dimensional photonic crystal,” 2003.

[17] T. Yamamoto, Y. A. Pashkin, O. Astaflev, Y. Nakamura, and J. S. Tsai, “Demonstration of conditional gate operation using superconducting charge qubits,” *Nature*, vol. 425, no. 6961, pp. 941–944, Oct. 2003, doi: 10.1038/nature02015.

[18] A. F. Gavela, D. G. García, J. C. Ramirez, and L. M. Lechuga, “Last advances in silicon-based optical biosensors,” *Sensors (Switzerland)*, vol. 16, no. 3. MDPI AG, Feb. 24, 2016. doi: 10.3390/s16030285.

[19] D. Fine *et al.*, “Silicon Micro- and Nanofabrication for Medicine,” *Advanced Healthcare Materials*, vol. 2, no. 5. pp. 632–666, May 2013. doi: 10.1002/adhm.201200214.

[20] M. A. Green and M. J. Keevers, “Optical properties of intrinsic silicon at 300 K,” *Progress in Photovoltaics: Research and Applications*, vol. 3, no. 3, pp. 189–192, 1995, doi: 10.1002/pip.4670030303.

[21] P. S. Jensen and J. M. Y. Bak, “Near-Infrared Transmission Spectroscopy of Aqueous Solutions: In uence of Optical Pathlength on Signal-to-Noise Ratio,” 2002.

[22] T. Xu, S. Yang, S. V. Nair, and H. E. Ruda, “Nanowire-array-based photonic crystal cavity by finite-difference time-domain calculations,” *Phys Rev B Condens Matter Mater Phys*, vol. 75, no. 12, Mar. 2007, doi: 10.1103/PhysRevB.75.125104.

[23] S. G. Johnson, S. Fan, P. R. Villeneuve, J. D. Joannopoulos, and L. A. Kolodziejski, “Guided modes in photonic crystal slabs.”

[24] M. D. Henry, S. Walavalkar, A. Homyk, and A. Scherer, “Alumina etch masks for fabrication of high-aspect-ratio silicon micropillars and nanopillars,” *Nanotechnology*, vol. 20, no. 25, 2009, doi: 10.1088/0957-4484/20/25/255305.

[25] A. Pan, M. Samaan, Z. Yan, W. Hu, and B. Cui, “Fabrication of ultrahigh aspect ratio Si nanopillar and nanocone arrays,” *Journal of Vacuum Science & Technology B*, vol. 41, no. 2, Mar. 2023, doi: 10.1116/6.0002276.

[26] S. H. Patil, “Solid State Physics,” in *Elements of Modern Physics*, Cham: Springer International Publishing, 2021, pp. 255–315. doi: 10.1007/978-3-030-70143-7_8.

[27] V. Degiorgio and I. Cristiani, “Electromagnetic Optics,” 2014, pp. 1–23. doi: 10.1007/978-3-319-02108-9_1.

[28] J. D. Joannopoulos, S. G. Johnson, J. N. Winn, and R. D. Meade, “Chapter 2: Electromagnetism in Mixed Dielectric Media,” in *Photonic Crystals: Molding the Flow of Light*, (Second Edition)., Princeton University Press, 2008, pp. 6–24.

[29] J. Ning and E. Leong Tan, “Generalized eigenproblem of hybrid matrix for Bloch-Floquet waves in one-dimensional photonic crystals,” 2009.

[30] J. D. Joannopoulus, R. D. Meade, and J. N. Winn, “Symmetries and Solid-State electromagnetism,” in *Photonic Crystals: Molding the Flow of Light*, Second Edition., 2008, pp. 25–43.

[31] S. Fujita and K. Ito, “Bloch Theorem,” in *Quantum Theory of Conducting Matter*, 2007, pp. 85–95.

[32] F. Kusunoki, T. Yotsuya, J. Takahara, and T. Kobayashi, “Propagation properties of guided waves in index-guided two-dimensional optical waveguides,” *Appl Phys Lett*, vol. 86, no. 21, pp. 1–3, May 2005, doi: 10.1063/1.1935034.

[33] V. Degiorgio and I. Cristiani, “Optical Components and Methods,” 2016, pp. 25–80. doi: 10.1007/978-3-319-20627-1_2.

[34] J. Ballato *et al.*, “Advancements in semiconductor core optical fiber,” *Optical Fiber Technology*, vol. 16, no. 6, pp. 399–408, Dec. 2010, doi: 10.1016/J.YOFTE.2010.08.006.

[35] J. D. Joannopoulus, S. G. Johnson, J. N. Winn, and R. D. Meade, “Electromagnetism in Mixed Dielectric Media,” in *Photonic Crystals: Molding the Flow of Light*, (Second Edition)., Princeton University Press, 2008, pp. 6–24.

[36] J. D. Joannopoulus, R. D. Meade, and J. N. Winn, “The Multilayer Film: A One-Dimensional Photonic Crystal,” in *Photonic Crystals: Molding the Flow of Light*, Second Edition., 2008, pp. 44–65.

[37] J. D. Joannopoulus, R. D. Meade, and J. N. Winn, “Two-Dimensional Photonic Crystals,” in *Photonic Crystals: Molding the Flow of Light*, Second Edition., 2008, pp. 66–93.

[38] L. Nikolova and P. S. Ramanujam, “Light polarization,” in *Polarization Holography*, Cambridge University Press, 2009, pp. 1–12.

[39] J. D. Joannopoulos, R. D. Meade, and J. N. Winn, “Atlas of Band Gaps,” in *Photonic Crystals, Molding the Flow of Light*, Second Edition., 2008, pp. 242–251.

[40] A. Mekis, S. Fan, and J. D. Joannopoulos, “Bound states in photonic crystal waveguides and waveguide bends,” 1998.

[41] S. G. Johnson, P. R. Villeneuve, S. Fan, and J. D. Joannopoulos, “Linear waveguides in photonic-crystal slabs.”

[42] S. G. Johnson, S. Fan, P. R. Villeneuve, J. D. Joannopoulos, and L. A. Kolodziejski, “Guided modes in photonic crystal slabs.”

[43] J. D. Joannopoulos, R. D. Meade, and J. N. Winn, “Photonic-Crystal Slabs,” in *Photonic Crystals: Molding the Flow of Light*, Second Edition., 2008, pp. 135–155.

[44] J. Vučković, M. Lončar, H. Mabuchi, and A. Scherer, “Design of photonic crystal microcavities for cavity QED,” *Phys Rev E Stat Phys Plasmas Fluids Relat Interdiscip Topics*, vol. 65, no. 1, 2002, doi: 10.1103/PhysRevE.65.016608.

[45] J. D. Joannopoulos, R. D. Meade, and J. N. Winn, “Computational Photonics,” in *Photonic Crystals: Molding the Flow of Light*, Second Edition., 2008, pp. 252–264.

[46] S. M. Raiyan Kabir, B. M. A. Rahman, and A. Agrawal, “Finite element time domain method for photonics,” in *Springer Series in Optical Sciences*, Springer Verlag, 2017, pp. 1–37. doi: 10.1007/978-3-319-55438-9_1.

[47] A. C. Polycarpou, *Introduction to the Finite Element Method in Electromagnetics*. Springer International Publishing, 2006. doi: 10.1007/978-3-031-01689-9.

[48] “COMSOL Multiphysics®.” COMSOL AB, Stockholm, Sweden. Accessed: Oct. 02, 2023. [Online]. Available: www.comsol.com

[49] A. F. Oskooi, D. Roundy, M. Ibanescu, P. Bermel, J. D. Joannopoulos, and S. G. Johnson, “Meep: A flexible free-software package for electromagnetic simulations by

the FDTD method," *Comput Phys Commun*, vol. 181, no. 3, pp. 687–702, Mar. 2010, doi: 10.1016/j.cpc.2009.11.008.

[50] K. S. Yee, "Numerical Solution of Initial Boundary Value Problems Involving Maxwell's Equations in Isotropic Media," 1966.

[51] A. Taflove, S. C. Hagness, and M. Piket-May, "Computational Electromagnetics: The Finite-Difference Time-Domain Method," in *The Electrical engineering Handbook*, pp. 629–669.

[52] S. G. Johnson, A. Oskooi, D. Roundy, M. Ibanescu, and P. Bermel, "MEEP." Accessed: Oct. 02, 2023. [Online]. Available: https://meep.readthedocs.io/en/latest/

[53] "DTU Nanolab." Accessed: Oct. 02, 2023. [Online]. Available: https://www.nanolab.dtu.dk/

[54] "ISO 9001." Accessed: Oct. 02, 2023. [Online]. Available: https://www.iso.org/iso-9001-quality-management.html

[55] G. Horneck, "Clean Room," in *Encyclopedia of Astrobiology*, Springer Berlin Heidelberg, 2014, pp. 1–1. doi: 10.1007/978-3-642-27833-4_1907-2.

[56] C. Mack, "Introduction to Semiconductor Lithography," in *Fundamental Principles of Optical Lithography*, Wiley, 2007, pp. 1–28. doi: 10.1002/9780470723876.ch1.

[57] A. Roncaglia, "Advanced Lithography," in *Springer Handbooks*, Springer Science and Business Media Deutschland GmbH, 2023, pp. 279–308. doi: 10.1007/978-3-030-79827-7_8.

[58] S. Franssila, "Chapter 9: Optical Lithography," in *Introduction to Microfabrication* , Second Edition., 2010, pp. 103–113.

[59] MicroChemicals ®, "Notes on Fundamentals of Microstructuring ; Composition and properties of AZ ® and TI photoresists." [Online]. Available: www.microchemicals.com/downloads/application_notes.html

[60] MicroChemicals ®, "Notes on Fundamentals of Microstructuring: Substrate Preparation." [Online]. Available: www.microchemicals.com/downloads/application_notes.html

[61] S. F. Kistler and P. M. Schweizer, *Liquid film coating : scientific principles and their technological implications*. Chapman & Hall, 1997.

[62] K. Fischer and R. Süss, "Spray Coating-a Solution for Resist Film Deposition Across Severe Topography."

[63] F. Giacomozzi, V. Mulloni, G. Resta, and B. Margesin, “MEMS packaging by using Dry Film resist,” in *2015 XVIII AISEM Annual Conference.*, IEEE, 2015.

[64] MicroChemicals ®, “Notes on Fundamentals of Microstructuring: Spin-coating.” [Online]. Available: www.microchemicals.com/downloads/application_notes.html

[65] MicroChemicals ®, “Notes on Fundamentals of Microstructuring: Exposure of Photoresist.” [Online]. Available: www.microchemicals.com/downloads/application_notes.html

[66] T. Ito and S. Okazaki, “Pushing the limits of lithography,” Aug. 2000. [Online]. Available: www.nature.com

[67] M. McCord and M. Rooks, “Chapter 2: Electron Beam Lithography,” in *Handbook of Microlithography, Micromachining, and Microfabrication*, vol. 1, 1997, pp. 139–249. [Online]. Available: https://www.spiedigitallibrary.org/terms-of-use

[68] A. N. Broers, A. C. F. Hoole Andrew, and J. M. Ryan, “Electron beam lithography - Resolution limits,” *Microelectron Eng*, vol. 32, no. 1-4 SPEC. ISS., pp. 131–142, 1996, doi: 10.1016/0167-9317(95)00368-1.

[69] U. Hofmann and N. Ünal, “Slides on Proximity Effect in E-Beam Lithography: Overview,” Accessed: Oct. 05, 2023. [Online]. Available: https://www.genisys-gmbh.com/part-1-electron-scattering-and-proximity-effect.html

[70] “TRACER®.” Accessed: Oct. 02, 2023. [Online]. Available: https://www.genisys-gmbh.com/tracer.html

[71] “BEAMER®.” Accessed: Oct. 02, 2023. [Online]. Available: https://www.genisys-gmbh.com/beamer.html

[72] MicroChemicals ®, “Notes on Fundamentals of Microstructuring: Post Exposure Bake.” [Online]. Available: www.microchemicals.com/downloads/application_notes.html

[73] S. Franssila, “Thin-Film Materials and Processes,” in *Introduction to Microfabrication*, 2010, pp. 47–68.

[74] S. Franssila, “Thermal Oxidation,” in *Introduction to Microfabrication*, 2010, pp. 153–164.

[75] J. Blanc, “A revised model for the oxidation of Si by oxygen,” *Appl Phys Lett*, vol. 33, no. 5, pp. 424–426, 1978, doi: 10.1063/1.90409.

[76] O. O. Abegunde, E. T. Akinlabi, O. P. Oladijo, S. Akinlabi, and A. U. Ude, “Overview of thin film deposition techniques,” *AIMS Materials Science*, vol. 6, no. 2. AIMS Press, pp. 174–199, 2019. doi: 10.3934/MATERSCI.2019.2.174.

[77] G. Harbeke, L. Krausbauer, E. F. Steigmeier, A. E. Widmer, H. F. Kappert, and G. Neugebauer, “Growth and Physical Properties of LPCVD Polycrystalline Silicon Films.”

[78] by Apcvd, P. Zaka Ullah, S. Riaz, and Q. Li, “Structure and Properties of LPCVD Silicon Films You may also like A comparative study of graphene growth.”

[79] MicroChemicals ®, “Notes on Fundamentals of Microstructuring: Lift-off.” [Online]. Available: www.microchemicals.com/downloads/application_notes.html

[80] S. Franssila, “Etching,” in *Introduction to Microfabrication*, 2010, pp. 127–142.

[81] H. Jansen, H. Gardeniers, M. De Boer, M. Elwenspoek, and J. Fluitman, “A survey on the reactive ion etching of silicon in microtechnology,” 1996.

[82] V. Thi Hoang Nguyen *et al.*, “ The CORE Sequence: A Nanoscale Fluorocarbon-Free Silicon Plasma Etch Process Based on SF 6 /O 2 Cycles with Excellent 3D Profile Control at Room Temperature ,” *ECS Journal of Solid State Science and Technology*, vol. 9, no. 2, p. 024002, Jan. 2020, doi: 10.1149/2162-8777/ab61ed.

[83] R. Abdolvand and F. Ayazi, “An advanced reactive ion etching process for very high aspect-ratio sub-micron wide trenches in silicon,” *Sens Actuators A Phys*, vol. 144, no. 1, pp. 109–116, May 2008, doi: 10.1016/j.sna.2007.12.026.

[84] L. F. Voss, Q. Shao, A. M. Conway, C. E. Reinhardt, R. T. Graff, and R. J. Nikolic, “Smooth bosch etch for improved si diodes,” *IEEE Electron Device Letters*, vol. 34, no. 10, pp. 1226–1228, 2013, doi: 10.1109/LED.2013.2278374.

[85] W. Zhou, • Zhong, and L. Wang, “Fundamentals of Scanning Electron Microscopy (SEM),” in *Scanning Microscopy for Nanotechnology Techniques and Applications*.

[86] N. J. Podraza and G. E. Jellison, “Ellipsometry,” in *Encyclopedia of Spectroscopy and Spectrometry*, Elsevier, 2016, pp. 482–489. doi: 10.1016/B978-0-12-409547-2.10991-6.

[87] “The Finite Element Method.” Accessed: Nov. 01, 2023. [Online]. Available: https://www.comsol.com/multiphysics/finite-element-method

[88] Pekel and R. Mittra, “A finite-element-method frequency-domain application of the perfectly matched layer (PML) concept,” *Microw Opt Technol Lett*, vol. 9, no. 3, pp. 117–122, 1995, doi: 10.1002/mop.4650090303.

[89] J. Pond *et al.*, “A complete design flow for silicon photonics.” [Online]. Available: http://www.siepic.ubc.ca/GSiP

[90] M. A. Green and M. J. Keevers, “Optical properties of intrinsic silicon at 300 K,” *Progress in Photovoltaics: Research and Applications*, vol. 3, no. 3, pp. 189–192, 1995, doi: 10.1002/pip.4670030303.

[91] S. G. Johnson, P. R. Villeneuve, S. Fan, and J. D. Joannopoulos, “Linear waveguides in photonic-crystal slabs.”

[92] A. Mekis, S. Fan, and J. D. Joannopoulos, “Bound states in photonic crystal waveguides and waveguide bends,” 1998.

[93] J. Vučković, M. Lončar, H. Mabuchi, and A. Scherer, “Design of photonic crystal microcavities for cavity QED,” *Phys Rev E Stat Phys Plasmas Fluids Relat Interdiscip Topics*, vol. 65, no. 1, 2002, doi: 10.1103/PhysRevE.65.016608.

[94] J. D. Joannopoulos, R. D. Meade, and J. N. Winn, “Photonic-Crystal Slabs,” in *Photonic Crystals: Molding the Flow of Light*, Second Edition., 2008, pp. 135–155.

[95] “Shipley Microposit Remover 1165,” *Shipley*. Accessed: Nov. 05, 2023. [Online]. Available: https://kayakuam.com/wp-content/uploads/2020/10/Remover-1165-Data-Sheet.pdf

[96] K. B. Jung, W. J. Song, H. W. Lim, and C. S. Lee, “Parameter study for silicon grass formation in Bosch process,” *Journal of Vacuum Science & Technology B*, vol. 28, no. 1, pp. 143–148, Jan. 2010.

[97] “Crystalbond TM,” *Pelco*. Accessed: Oct. 06, 2023. [Online]. Available: https://www.tedpella.com/technote_html/821-1-2-3-4-6-TN.pdf

[98] Kurt J. Lesker, “Galden HT Fluid,” *Kurt J. Lesker*. Accessed: Oct. 06, 2023. [Online]. Available: https://www.lesker.com/newweb/fluids/pdf/11-012-fl-ds-galdenpfpe-heattransferfluiddatasheet.pdf

[99] MathWorks®, “MATLAB®.” Accessed: Nov. 05, 2023. [Online]. Available: https://se.mathworks.com/products/matlab.html

[100] ThermoFisher Scientific©, “Thermo Avantage©.” Accessed: Nov. 05, 2023. [Online]. Available: https://www.thermofisher.com/order/catalog/product/IQLAADGACKFAKRMAVI

[101] J. F. Moulder, W. F. Stickle, P. E. ’ Sobol, K. D. Bomben, and J. Chastain, “Handbook of X-ray Photoelectron Spectroscopy AReference Book of Standard Spectra for Identification and Interpretation of XPS Data.”

[102] A. Sankaran and M. J. Kushner, “Fluorocarbon plasma etching and profile evolution of porous low-dielectric-constant silica,” *Appl Phys Lett*, vol. 82, no. 12, pp. 1824–1826, Mar. 2003, doi: 10.1063/1.1562333.